UNIVERSITÀ DEGLI STUDI DI GENOVA
Facoltà di Scienze Matematiche Fisiche e Naturali

Tesi di Dottorato in Fisica

Sviluppo del sistema di acquisizione per CUORE e analisi di eventi a bassa energia in Cuoricino

Candidato:
Elena Guardincerri

Relatore:
Prof. Marco Pallavicini

Relatore Esterno:
Dott.ssa Maura Pavan

XVIII Ciclo di Dottorato di Ricerca

Settore scientifico-disciplinare: FIS/04

a mia nonna Erminia

Contents

Introduction

"It's a dangerous business going out your front door."
J.R. Tolkien

"Dear Radioactive Ladies and Gentlemen, [...] as a desperate remedy to save the principle of energy conservation in beta decay, I propose the idea if a particle of spin half". With these words Pauli gave birth to neutrino into the world of theoretical Physics: it was 1929.

Although neutrinos were experimentally detected only in 1956, they actually began to play a key role in the development of the theory of weak interactions many years before: by 1934 Fermi had indeed developed a theory of beta decay to include neutrino, at that time assumed to be massless and chargeless.

Evidence for only left handed neutrinos being emitted in double beta decay was later the main proof of the successful V-A theory of weak interactions, proposed by Sudarshan, Marshak, Feynman and Gell-Man, and the discovery of neutral current interactions in early seventies confirmed the theory of Glashow, Weinberg and Salam which succssfully unified weak and electromagnetic interactions under a general principle of gauge invariance.

During the past decades, and particularly during the last one, the research in the field of neutrino Physics was particularly intense and fruitful.
Neutrino flavour oscillations, already assumed as the most likely explanation to the results of the experiments on solar and atmospheric neutrinos, have been estabilished in 2001: neutrinos are now known to be massive and mixed, and the parameters involved in the mixing have been measured with great accuracy.

Moreover, the recent progress in Cosmology and Astrophysics has highlighted the critical dependance of our understanding of the Universe on our knowledge of neutrinos: these elusive particles are the most abundant form of matter in the Universe next to radiation, and they contributed to the origin of heavy elements playing a crucial role in nucleosynthesis.

Despite these last developments there is still much we don't know about neutrinos: the values of their masses, for example, are still to be determined, and their behaviour under the discrete CP symmetry is unknown.

One of the open issues concerns their nature: being neutrinos truly neutral particles, they could in principle be Majorana particles, that is, they could be their own antiparticles.

The only realistic way to determine whether neutrinos are Dirac or Majorana particles is to look for neutrinoless double beta decay: the observation of this rare event would estabilish for these particles a nonvanishing mass of Majorana nature, contributing moreover to the determination of the absolute neutrino mass scale.

The purpose of CUORE experiment, in the context of which my activity was carried on, is to search for neutrinoless double beta decay in ^{130}Te .

Using ^{130}Te crystals operated as bolometers at a temperature of about 10 mK, CUORE aims, in particular, to reach sensitivities of the order of 2.1 x 10^{26} y on the halflife of ^{130}Te against this decay: this would imply for $\langle m_{\beta\beta} \rangle$, the effective neutrino Majorana mass, values as low as 0.01 eV.

A prototype of CUORE, Cuoricino, is already running at Gran Sasso National Laboratories: the data it collected in the last two years demonstrated the feasibility of CUORE, setting at the same time the currently upper limit for ^{130}Te halflife against $0\nu\beta\beta$.

Although the main concern of Cuoricino and CUORE is the search for $0\nu\beta\beta$, the high intrinsic resolution achievable by these detectors allows other kinds of Physics to be be potentially addressed: the search for dark matter and for rare nuclear decays are some examples.

On the other hand, the choice to look for low energy events, such as those just mentioned, puts serious constraints on the detectors performances.

In particular, the analysis of the low energy range requires a sufficiently low energy threshold, an adequate energy resolution and a high stability of the system, since this is a region where any small change could affect significantly the quality of the data.

Another requirement concerns the accuracy of the whole signal conditioning and data acquisition chain: CUORE data acquisition system must guarantee an energy resolution at least equal to the bolometers' intrinsic one on the whole dynamic range, and this is perhaps the major challenge in its the realization.

Once these conditions are provided, and only then, low energy data become reliable, and a further analysis can be performed on them.

My doctoral thesis deals with both CUORE and Cuoricino, and with different aspects of the two experiments: I have been involved in the development of the data acquisition system for the CUORE experiment, which is in charge of the Genova group, and I participated to Cuoricino data analysis searching for a rare nuclear decay, the ^{123}Te electron capture to ^{123}Sb.

Even if CUORE is not a big experiment, its data acquisition system deserves some attention for the reasons I anticipated above.

Its project is now complete and a first reduced version has been built and tested.

At the same time the analysis of Cuoricino data at low energy, besides being physically significant in itself, is also necessary in view of the optimization of CUORE detector, which will allow much more statistics to be collected thanks to its greater size.

These two subjects, the development of CUORE DAQ and the search for ^{123}Te electron capture in Cuoricino data, will be the main topics of this work whose outline is sketched in the following.

After a general introduction, aiming to show the role of Cuoricino and CUORE in the context of neutrino Physics, and Neutrinoless Double Beta Decay in particular, I will review the principles of the bolometric technique and their applications to CUORE and Cuoricino, with particular attention to those aspects which maily influenced my activity.

I will then describe Cuoricino set-up, trying to point out those features which mainly affect the detection and analysis of low energy events.

CUORE project and its expected performances will be discussed afterwards: here the focus will be on the signals, from their generation to their amplification and conditioning.

The analysis performed to search for ^{123}Te electron capture in Cuoricino data will be presented in the next chapter.

After an introduction to CUORE and Cuoricino Physics at low energy, the problematics related to the analysis of low energy events will be shown, together with the results of a study on Cuoricino detector behaviour in this range.

Then the analysis performed to search for ^{123}Te electron capture in Cuoricino data will be presented.

The last part of this work will be dedicated to CUORE data acquisition and control system: its requirements will be discussed as well as their motivations; finally, the first prototype will be described and its measured performances shown.

Chapter 1

Neutrino Physics and Neutrinoless Double Beta Decay

Dolce e chiara è la notte e senza vento,
E queta sovra i tetti e in mezzo agli orti
Posa la luna, e di lontan rivela
Serena ogni montagna.

Giacomo Leopardi

Introduction

Neutrinos, discovered in 1956 by Reines and Cowan, are very light fermions participating only to weak interactions: they are included in the Standard Modelof Electroweak Interactions as massless left-handed particles belonging to one of the three known lepton flavours.

Very tight upper bounds for neutrino masses have been determined both in laboratory and cosmology experiments: the formers [1, 2] have obtained an upper limit of about 2.2 eV on the mass of the electron neutrino looking for a particular kinematic effect in nuclear beta decay; the latters [3] have determined an upper limit of 0.34 eV on neutrino mass, in the hypotesis of having three almost degenerate mass eigenstates; this last bound, however, is model-dependent.

During the last decade neutrino oscillations have been estabilished, and this necessarily implies the existence of a non-vanishing mass for these particles, and a mixing among the different neutrino species.

The characterization of neutrino flavour oscillations has allowed to measure parameters such as the differences between the mass eigenstates and the mixing angles entering the oscillation amplitudes, but our understanding of Neutrino Physics is far from complete: the absolute mass scale, for example, is still unknown.

An intriguing question concerns the form of the mass term which should account for neutrino masses: is it possible to accomodate a Majorana mass term in the Lagrangian describing neutrinos interactions? Or, stated in other words: is neutrino its own antiparticle?

This chapter will be devoted to an introduction to neutrino Physics and in particular to those issues concerning neutrino masses: after reviewing the status of neutrinos within the Standard Model, the last experimental developments will be shown.

A description of our current understanding on this subject will be followed by a review of the still open issues and of the experimental techniques which can be used to approach them.

1.1 Neutrinos and the Standard Model

As it is well known the Standard Model, which is at present the accepted theory describing the interactions between particles, is a gauge theory based on the $SU(3)_c \times SU(2)_L \times U(1)_Y$ symmetry.

Since neutrinos do not participate in strong interactions, only the $\mathrm{SU(2)_L \times U(1)_Y}$ model will be considered in the following.

Until the late ninties no evidence was found for an even tiny value of neutrino mass: neutrinos were thus believed to be massless chargless particles participating only to weak interactions.

According to the Standard Model neutrinos are in fact massless fermions, and the left-chiral components of neutrino fields are assigned to the $(2, -1)$ representation of $\mathrm{SU(2)_L \times U(1)_Y}$ together with the left-chiral components of the charged leptons.

The number of light flavour neutrinos is given by the invisible width of the Z boson [4, 5] and is equal to 3: there are no other neutrino flavours than ν_e, ν_μ, and ν_τ.

In the absence of a direct evidence of right handed neutrinos the right-chiral projections of neutrino fields are not included in the model.

The whole particle content of the Standard Model is reported below, together with the indication of the gauge group representation each fermion is assigned to.

$$\begin{array}{lll} q_L = \left(\begin{array}{c} u_L \\ \\ d_L \end{array} \right) & & \left(2, \frac{1}{3}\right) \\ u_R & & \left(1, \frac{4}{3}\right) \\ d_R & & \left(1, -\frac{4}{3}\right) \\ \psi_L = \left(\begin{array}{c} \nu_{eL} \\ \\ e_L \end{array} \right) & & (2, -1) \\ e_R & & (1, -2) \end{array} \tag{1.1}$$

The same assignments are repeated for the three known families of quark and leptons with the replacement of $(\mathrm{u, d, e}, \nu_\mathrm{e})$ with $(\mathrm{t, b}, \tau, \nu_\tau)$ and $(\mathrm{c, s}, \mu, \nu_\mu)$.

Denoting by $\mathrm{W}^\pm_\mu$ and W^0_μ the three gauge bosons of $\mathrm{SU(2)_L}$ and by B_μ the $\mathrm{U(1)_Y}$ gauge boson, the interactions between quarks, leptons and bosons are thus described by the following terms of the Standard Model lagrangian:

$$\begin{aligned} L_{CC} &= \tfrac{g}{\sqrt{2}}(J^{\mu\dagger} W^+_\mu + J^\mu W^-_\mu) \\ L_{NC} &= \tfrac{g}{cos\theta_W} K^\mu Z_\mu \end{aligned} \tag{1.2}$$

where

$$\begin{aligned} J^\mu &= (\overline{u^0 c^0 t^0})\gamma^\mu \tfrac{1}{2}(1-\gamma_5) \left(\begin{array}{c} d^0 \\ s^0 \\ b^0 \end{array} \right) + (\overline{\nu}_e \overline{\nu}_\mu \overline{\nu}_\tau)\gamma^\mu \tfrac{1}{2}(1-\gamma_5) \left(\begin{array}{c} e \\ \mu \\ \tau \end{array} \right) \\ K^\mu &= \textstyle\sum_f \overline{f}\gamma^\mu [I_{3L} L - \sin^2\theta_W Q] f \\ Z &= cos\theta_W W^0 - \sin\theta_W B \end{aligned} \tag{1.3}$$

$\theta_\mathrm{W} = \mathrm{arctg(g'/g)}$ is the Weinberg angle, $\mathrm{f} = \nu_\mathrm{e}, \mathrm{e, u, d}$ or the corresponding objects in higher generations, Q is the charge of f and $\mathrm{I_{3L}}$ is the value of the neutral generator of $\mathrm{SU(2)_L}$ for the left-chiral projection of each fermion fields.

The superscript '0' on quarks implies they are not mass eigenstates.

In particular, the interactions of first generation of neutrinos are described by:

$$L_{I\nu} = \frac{g}{\sqrt{2}}\overline{\nu}_{eL}\gamma^{\mu}eW^{+}_{\mu} + \frac{g}{2cos\theta_W}\overline{\nu}_{eL}\gamma^{\mu}\nu_e Z^0_{\mu} + h.c. \tag{1.4}$$

where the first term is responsible for charged current interactions and the second term for neutral current interactions.

The interactions of the remaining two families of neutrinos are described by similar terms with (e, ν_{e}) replaced by (μ, ν_{μ}) and (τ, ν_{τ}).

From equations (1.2) and (1.4) it can be seen that no mixing is allowed in the Standard Model between leptons (and in particular neutrinos) of different flavours.

1.2 Fermion masses in the Standard Model

1.2.1 Masses for quarks and charged leptons

The masses of quarks and leptons are generated in the Standard Model by the spontaneous breaking of the $\mathrm{SU(2)_L \times U(1)_Y}$ symmetry via the Higgs mechanism: bare masses are in fact forbidden for fermions by the gauge invariance.

In order to give masses to lepton, quarks and gauge bosons, a scalar field is introduced in the Standard Model and it is assigned to the (2,1) representation of $\mathrm{SU(2)_L \times U(1)_Y}$:

$$\phi = \begin{pmatrix} \phi_+ \\ \phi_0 \end{pmatrix}. \tag{1.5}$$

When the Higgs field aquire a non zero vacuum expectation value

$$\langle \phi_0 \rangle = \frac{v}{\sqrt{2}} \tag{1.6}$$

the mass terms for the quarks and the charged leptons are generated: they originate from the following Yukawa interactions, which are instead allowed by gauge symmetry

$$-L_Y = \sum_{a,b} \left[h^{(u)}_{ab}\overline{q}_{aL}\hat{\phi}u_{bR} + h^{(d)}_{ab}\overline{q}_{aL}\phi d_{bR} + h^{(l)}_{ab}\overline{\psi}_{aL}\phi l_{bR} \right] + h.c. \tag{1.7}$$

where a and b are generation indices.

On sobstituting eq (1.6) in (1.7) the following mass terms are generated:

$$-L_{mass} = \sum_{a,b} \left[\overline{u}_{aL}M^{(u)}_{ab}u_{bR} + \overline{d}_{aL}M^{(d)}_{ab}d_{bR} + \overline{l}_{aL}M^{(l)}_{ab}l_{bR} \right] \tag{1.8}$$

where

$$M^{(f)}_{ab} = h^{(f)}_{ab}\frac{v}{\sqrt{2}} \quad f = u, d, l \tag{1.9}$$

This kind of mass terms are named *Dirac mass* terms.

The matrices $h^{(u)}$ and $h^{(l)}$ can be chosen diagonal by a proper choice of the quark and lepton basis, so that the fields u_a and l_a are actually equal to the corrisponding mass eigenstates: $u^{(0)}_a = u_a$ and $l^{(0)}_a = l_a$.

As a result, however, the matrix $M^{(d)}$ is complex and non-diagonal. It can be diagonalized by a biunitary transformation

$$V_L M^{(d)} V_R^{\dagger} = D^{(d)} \tag{1.10}$$

The mass eigenstates of the down-type quark are then related to the interaction eigenstates by

$$(d_{L,R})_a = \sum_b (V_{L,R})_{ab} (d^{(0)}_{L,R})_b \tag{1.11}$$

The matrix V_L is the well known Cabibbo-Kobayashi-Maskawa matrix (CKM matrix for short): due to its presence the term describing charged current interactions between quarks

$$-L^q_{CC} = (\overline{u^0 c^0 t^0})\gamma^{\mu}\frac{1}{2}(1-\gamma_5)V_L^{\dagger}\begin{pmatrix} d \\ s \\ b \end{pmatrix} \tag{1.12}$$

gives rise to mixing between the different species of flavours.

This can be seen by noticing that in the term (1.12) quark fields of distinct flavours are coupled.

1.2.2 Masses for neutrinos

It turns out from the discussion of the previous sections that, due to the particle content and gauge symmetries of the Standard Model, neutrinos cannot have mass within this theory.

They cannot in fact have a Dirac mass, since such a mass term would require both the helicity states for neutrinos, and it has been pointed out that right-handed neutrinos are deliberately excluded from the Standard Model.

A different kind of mass term is the so called *Majorana* mass term: it is of the form $\nu_{\mathrm{L}}^{\mathrm{T}}\mathrm{C}^{-1}\nu_{\mathrm{L}}$ or $\nu_{\mathrm{R}}^{\mathrm{T}}\mathrm{C}^{-1}\nu_{\mathrm{R}}$ where C is the Lorenz conjugation matrix.

Considering the former term it is appearent that, although it requires only the left-handed helicity state for neutrinos and uses the opposite helicity state of antineutrinos, it is not gauge invariant, since it transforms as an $SU(2)$ triplet.

Both of the terms, moreover, violate lepton number conservation by two units: lepton number is conserved in the Standard Model at all orders in perturbation theory, even after symmetry breaking, therefore such terms cannot arise in perturbation theory.

One might wonder whether netrino masses can be induced by non-perturbative effects in the Standard Model: lepton number conservation is in fact broken non perturbatively through the axial anomaly of the lepton number current

$$L^{\mu} = \sum_{i=1}^{n_l} [\bar{e}_i \gamma^{\mu} e_i + \bar{\nu}_i \gamma^{\mu} \nu_i] \tag{1.13}$$

$$\partial_{\mu} L^{\mu} = \frac{1}{(4\pi)^2}\varepsilon^{\mu\nu\rho\sigma}[g'^2 B_{\mu\nu}B_{\rho\sigma} - g^2 W^i_{\mu\nu} W^j_{\rho\sigma}] \tag{1.14}$$

where

$$B^{\mu\nu} = \partial^{\mu}B^{\nu} - \partial^{\nu}B^{\mu} \tag{1.15}$$

$$W_i^{\mu\nu} = \partial^{\mu}W_i^{\nu} - \partial^{\nu}W_i^{\mu} + g\varepsilon^{ijk}W_j^{\mu}W_k^{\nu} \tag{1.16}$$

It can be shown that the anomaly contribution to the baryon number current conservation is identical, so that the $B-L$ current is conserved to all orders in perturbation theory.

Since the Majorana mass terms shown above violate also $B-L$, it follows that neutrino remains massless even in the presence of nonperturbative effects.

1.3 The evidence for neutrino mass: neutrino oscillations

The first hint on the true nature of neutrinos came from Ray Davis's discovery that the flux of solar neutrinos was lower than was expected from the knowledge of the nuclear reactions proceeding inside the Sun.

It is now known that this is due to *neutrino oscillations*, a macroscopic effect of the mixing between different neutrino flavours, direct consequence of the massive nature of these particles.

The first strong evidence in favour of neutrino oscillations was found by te Super-Kamiokande Collaboration [6, 7] and opened a new era in Particle Physics.

1.3.1 The formalism of vacuum oscillations

The concept of neutrino oscillation is based on the assumption that the neutrinos of definite flavour are not necessarily states of a definite mass.

Instead the left-chiral components of the neutrino fields $\nu_{\alpha L}$ ($\alpha = e, \mu, \tau$, s_1,s_2, ...) are linear combinations of the left-chiral components of the neutrino fields ν_k (k = 1, ...,n) with masses m_k.

With s_1, s_2... possible sterile neutrinos have been indicated.

Then:

$$\nu_{\alpha L} = \sum_{k=1}^{n} U_{\alpha k} \nu_{kL} \tag{1.17}$$

where U is an unitary matrix known as *neutrino mixing matrix.*

In the following only the case in which only three mass eigenstates and three active flavour neutrinos are present will be considered: then $n = 3$ in equation (1.17).

In this case only a 3×3 submatrix of U plays a role in neutrino oscillations, and it will be assumed unitary to a good approximation [8].

A convenient parametrization of the matrix U is [9]

$$U = \begin{pmatrix} c_{12}c_{13} & s_{12}c_{13} & s_{13}e^{i\delta_{13}} \\ -s_{12}c_{23} - c_{12}s_{23}s_{13}e^{i\delta_{13}} & c_{12}c_{32} - s_{12}s_{23}s_{13}e^{i\delta_{13}} & s_{23}c_{13} \\ s_{12}s_{23} - c_{12}c_{23}s_{13}e^{i\delta_{13}} & -c_{12}s_{23} - s_{12}c_{23}s_{13}e^{i\delta_{13}} & c_{23}c_{13} \end{pmatrix}$$

where $c_{ij} \equiv cos\theta_{ij}$ and $s_{ij} \equiv \sin\theta_{ij}$ and δ_{ij} is the CP violating phase.

If all neutrino mass differences are small, a state of a flavour neutrino ν_α produced with momentum $p >> m_k$ is described [10] by the coherent superposition of mass eigenstates

$$|\nu_\alpha\rangle = \sum_{k=1}^{n} U^*_{\alpha k} |\nu_k\rangle. \tag{1.18}$$

$|\nu_\alpha\rangle$ is the state of a neutrino with negative chirality, mass m_k and energy

$$E_k = \sqrt{p^2 + m^2} \simeq p + \frac{m_k^2}{2p}. \tag{1.19}$$

If a neutrino produced at time $t = 0$ is described by (1.18), the mass eigenstates will evolve in time with the phase factors $e^{(-iE_k t)}$, and at the time t their states will be

$$|\nu_\alpha\rangle_t = \sum_{k=1}^{n} U^*_{\alpha k} e^{-iE_k t} |\nu_k\rangle. \tag{1.20}$$

Since neutrinos are detected by observing weak interaction processes, it is useful to write 1.20 in the basis of flavour states:

$$|\nu_\alpha\rangle_t = \sum_\beta U_{\beta k} e^{-iE_k t} U^*_{\alpha k} |\nu_b\rangle = \langle \nu_\beta | \nu_\alpha \rangle_t |\nu_b\rangle. \tag{1.21}$$

The quantity $\langle \nu_\beta | \nu_\alpha \rangle_t$ is the amplitude of $\nu_\alpha \longrightarrow \nu_\beta$ transition at the time t at a distance $L \simeq t$ from the source.

As a consequence, the probability of this transition is given by

$$P_{\nu_\alpha \longrightarrow \nu \beta} = |\langle \nu_\beta | \nu_\alpha \rangle_t|^2 = \left| \sum_{k=1}^{n} U_{\beta k} e^{(-iE_k t)} U^*_{\alpha k} \right|^2. \tag{1.22}$$

Using the unitarity relation

$$\sum_{k=1}^{n} U_{\beta k} U^*_{\alpha k} = \delta_{\alpha \beta} \tag{1.23}$$

the probability (1.22) can be written as

$$P_{\nu_\alpha \longrightarrow \nu_\beta} = \left| \delta_{\alpha \beta} + \sum_{k=1}^{n} U_{\beta k} U^*_{\alpha k} \left[e^{\left(-i \frac{\Delta m^2_{kj} L}{2E}\right)} - 1 \right] \right|^2 \tag{1.24}$$

where $\Delta m^2_{kj} = m^2_k - m^2_j$.

Thus, the probability of the oscillation $\nu_\alpha \longrightarrow \nu_\beta$ depends on the mixing matrix, on *n - 1* independent mass squared differences and on the ratio L/E which is determined by the particular experimental set-up.

From (1.24) it can be seen that neutrino oscillations can occurr only if at least one Δm^2 is non zero.

In particular, they can be observed only if the condition

$$\Delta m^2 \gtrsim \frac{E}{L} \tag{1.25}$$

is satisfied, where Δm^2 is the neutrino mass-squared in eV^2, L is the distance between neutrino source and detector in m and E is neutrino energy in MeV.

The inequality (1.25) allows to roughly estimate the sensitivity to the parameter Δm^2 of different kinds of neutrino oscillation experiments (see section 1.3.2): these estimated are presented in table (1.3.1).

Experiment	L(m)	E(MeV)	$\Delta m^2 (eV^2)$
Reactor SBL	10^2	1	10^{-2}
Reactor LBL	10^3	1	10^{-3}
Accelerator SBL	10^3	10^3	1
Accelerator LBL	10^6	10^3	10^{-3}
Atmospheric	10^7	10^3	10^{-4}
Solar	10^{11}	1	10^{-4}

Table 1.1: Estimates of the values of Δm^2 which can be probed in reactor short-baseline (SBL) and long-baseline (LBL), accelerator SBL and LBL, atmospheric and solar neutrino oscillation experiments.

In the simplest case in which oscillations are assumed to involve only two neutrino types the transition probability for $\alpha \neq \beta$ (1.24) becomes

$$P_{\nu_\alpha \longrightarrow \nu_\beta} = \frac{1}{2}\sin^2 2\theta \left(1 - \cos 2.53 \frac{\Delta m^2 L}{E}\right) \tag{1.26}$$

where (1.3.1) has been used. This is a periodic function of L/E with an amplitude given by $\sin^2 2\theta$ and an oscillation length equal to

$$L^{OSC} = \frac{4\pi E}{\Delta m^2(eV^2)} \simeq 2.48 \frac{E(MeV)}{\Delta m^2(eV^2)} m \tag{1.27}$$

The oscillatory behaviour of the transition probability (1.26) is shown in figure (1.1): here the black curve represents the transition probability 1.26 averaged over a Gaussian energy distribution with standard deviation $\sigma = E/10$.

The averaged probability is the quantity which can be actually measured in neutrino oscillation experiments, since no monochromatic neutrino source can be found in nature or realized.

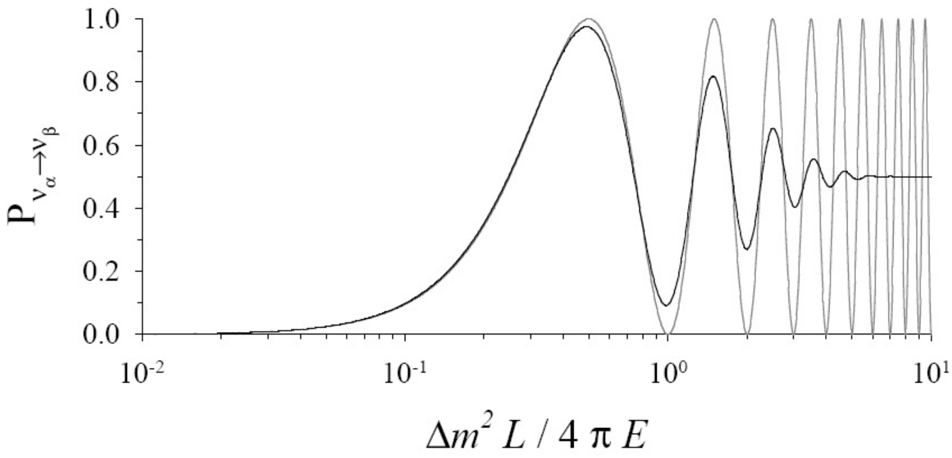

Figure 1.1: Transition probability for $\sin^2 2\theta = 1$. The grey line represents the oscillation probability (1.26) and the black one represents the same function averaged over a Gaussian energy spectrum with mean value E and standard deviation $\sigma = E/10$.

1.3.2 Neutrino oscillation experiments

Neutrino oscillation experiments are usually grouped into categories depending on the source of neutrinos exploited (which determines the energy of the neutrino beam) and by the distance between source and detector.

In the following section the basis of the main kinds of neutrino oscillation experiments will be explained: the synthesis of their results will be presented in section 1.3.3.

Further references are provided for details on the subject.

Solar neutrinos

The energy of the sun is produced in the reactions of the thermonuclear *pp* and CNO cycles (see, e.g., [11]).

The overall result of both cycles is the transition

$$4p + 2e^- \rightarrow^4 He + 2\nu_e + 26.74 \text{ MeV}. \tag{1.28}$$

Hence, the production of energy in the sun is accompanied by the emission of electron neutrinos.

Their total flux and energy spectrum is predicted by the Bahcall-Pinsonneault Standard Solar Model (SSM) [12]; in particular neutrinos produced in the *pp* cycle (which contributes over 92% of the flux) have energies lower than $\sim$ 15 MeV.

Homestake [13], GALLEX [14] and SAGE [15] are radiochemical experiments.

In the Kamiokande and Super-Kamiokande experiments, instead, electrons recoiling after elastic neutrino-electron scattering events are detected.

In these experiments the direction of neutrinos was determined and this allowed to confirm that the the source of the detected neutrinos was actually the Sun.

The detected event rates in all solar neutrino experiments were found significantly smaller than expected: the most natural explanation of this fact, known as the "solar neutrinos problem", was obtained in the framework of neutrino mixing.

If neutrinos are massive and mixed, in fact, solar ν_es can oscillate into neutrinos of different flavours on their way to the earth, so that they can't be detected by radiochemical experiments.

In Kamiokande and Super-Kamiokande experiment all flavours neutrinos are detected, but the cross section of $\nu_\mu(\nu_\tau)$ -e scattering is about six times smaller than the cross section of $\nu_e - e$ scattering.

The SNO solar neutrino experiment [16], could separately determine the flux of ν_e reaching the detector (through the charged current reactions) and the flux of all active neutrinos (through the neutral current reactions): thanks to this feature it made the conclusion that solar neutrinos certainly oscillate.

Solar neutrino data can be explained assuming that solar neutrino fluxes are given by the SSM and that there are oscillations between neutrinos of two flavours, controlled by two parameters: a mass square difference Δm^2 and a mixing angle $\sin^2 2\theta$.

In this hypothesis solar neutrinos experiment could jointy contribute to determine the values of Δm^2 and $\sin^2 2\theta$: the results of this analysis will be briefly presented later on.

Atmospheric Neutrinos

Atmospheric neutrinos are produced mainly in the decays of pions and muons

$$\pi \rightarrow \mu + \overline{\nu}_\mu \qquad \mu \rightarrow e + \overline{\nu}_e + \nu_\mu$$

pions being produced in the interaction of cosmic rays in the Earth atmosphere.

At small energies, ≤ 1 GeV, the ratio of the numbers of ν_μ's and ν_e's is equal to two (notice that in the existing detectors neutrinos and antineutrinos can't be distinguished).

At higher energies this ratio is larger, because not all the muons decay in the atmosphere, but it can nevertheless predicted with accuracy better than 5%.

The results of the measurements of the atmospheric neutrino flux are usually presented in the form of a double ratio

$$R = \frac{(N_\mu/N_e)_{data}}{(N_\mu/N_e)_{MC}} \tag{1.29}$$

where $(N_\mu/N_e)_{data}$ is the ratio of the total number of observed muon and electron events and $(N_\mu/N_e)_{MC}$ is the ratio predicted from Monte Carlo simulations.

The earlier indications for atmospheric neutrino oscillations came from the measured values of R, which were, according to most experiments [17, 18, 19], significantly lower than expected.

The important evidence in favour of neutrino oscillations was obtained by the Super-Kamiokande collaboration [7] with the discovery of a significant up-down assimmetry of multi-GeV muon events.

For atmospheric neutrinos the distance between production and detection region is about 20 km for down-going neutrinos ($\theta = 0$, θ being the zenith angle) and it changes up to about 13000 km for up-going neutrinos ($\theta = \pi$).

In the hyptesis of having no mixing among neutrinos, only a little (few %) dependence on the zenith angle is expected for neutrinos with energies larger than 2-3 GeV (due to the magnetic field of the Earth): the Super-Kamiokande collaboration found instead a value for the integral up-down assimmetry of multi-GeV muon neutrinos equal to:

$$A_\mu = 0.311 \pm 0.043 \pm 0.010 \tag{1.30}$$

having defined

$$A = \frac{U - D}{U + D} \tag{1.31}$$

where U is the number of up-going neutrinos ($\cos\theta \leq -0.2$) and D is the number of down-going neutrinos ($\cos\theta \geq -0.2$).

No assimmetry was found for electron neutrinos events:

$$A_e = 0.036 \pm 0.067 \pm 0.020 \tag{1.32}$$

The best explanation of Super-Kamiokande data is obtained assuming that there are $\nu_\mu \longrightarrow \nu_\tau$ oscillations: atmospheric neutrino oscillations can in fact be described in a two-neutrinos framework, and their pattern is therefore controlled by a mass square difference and a mixing angle.

The results of the analysis of atmospheric neutrinos data will be shown in section 1.3.3.

Artificial Neutrinos

Laboratory experiments to search for neutrino oscillations are performed with neutrino beams produced at either accelerators or nuclear reactors.

In *disappearence* experiments, one looks for the attenuation of a neutrino beam primarily composed of a single flavour due to the mixing with other flavours.

In *appearence* experiments, one searches for interactions by neutrinos of flavours not present in the original neutrino beam.

Early experiments of this kind were short baseline experiments (SBL) at accelerators, with characteristic distances of the order of hundreds of meters.

Conventional neutrino beams from **accelerators** are mostly produced by π decays, with the pions produced by the scattering of the accelerated protons on a fixed target:

$$\begin{aligned}
p + \text{target} \longrightarrow & \pi^\pm + X \\
& \pi^+ \longrightarrow \mu^+ \nu_\mu \\
& \qquad \mu^+ \longrightarrow e^+ \nu_e \bar{\nu_\mu} \\
& \pi^- \longrightarrow \mu^- \bar{\nu_\mu} \\
& \qquad \mu^- \longrightarrow e^- \bar{\nu_e} \nu_\mu
\end{aligned} \tag{1.33}$$

The beam can therefore contain both μ_νs and μ_νs and their antiparticles.

The final composition of the neutrino beam is determined by selecting the sign of the decaying π and stopping the produced μ in the beam line.

All SBL experiments (E776 [20] and KARMEN [21]) produced null results, with the exception of the LSND experiment [22] which reported an evidence for both $\nu_\mu \longrightarrow \nu_e$ and $\overline{\nu_\mu} \longrightarrow \overline{\nu_e}$ oscillations.

Such experiments, however, cannot probe values of Δm^2 much smaller than 10^{-2} eV^2.

On the other hand, data on atmospheric and solar neutrinos definitely indicated that the interesting region lies at smaller values of Δm^2.

Hence, reactor sources were preferred in later experiments, where the average energy is in the region of a few MeV.

Alternatively, long baseline accelerator (LBL) experiments can be set up to probe small values of Δm^2 relying on the large distance between the source and the detector.

Nuclear **reactors** produce $\overline{\nu_e}$ beams with $E_\nu \sim$ MeV; due to the low energy, e's are the only charged leptons wich can be produced in the neutrino CC interactions.

If the $\overline{\nu_e}$ oscillated to another flavour, its CC interaction could not be observed, therefore oscillation experiments performed at reactors are disapparence experiments.

All reactors experiments (Gosgen [23], Kranoyarsk [24], Budjey [25], CHOOZ [26]) reported negative results with the exception of Kamland [27], which observed a 34% depletion of the expected flux, thus providing evidence for oscillation.

Similarly, the K2K LBL experiment, using a multi-GeV muon neutrino beam from an accelerator, also sees evidence of a depletion of flux [28], providing evidence for $\nu_\mu \longrightarrow \nu_\tau$ oscillation.

The results of these experiments will be discussed in the framework of a three-flavours scenario in the next section.

1.3.3 Results from neutrino oscillation experiments

Before looking at the results obtained by oscillation experiments, it is worthwhile to understand how two-neutrinos transition probabilities, such as those used to describe experimental data, can contribute to the determination of the parameters characteristic of a three neutrinos oscillation framework.

To do this it is necessary [29] to consider the case in which the two mass differences appearing in (1.24) have very different values:

$$m_1 \ll m_2 \ll m_3 \tag{1.34}$$

this is true for the oscillations of solar and atmospheric neutrinos (from the analysis of the experimental data it follows that $\Delta m^2_{sol} \simeq 10^{-5} eV$ and $\Delta m^2_{atm} \simeq 10^{-3} eV$, see later).

One can suppose, for example, that for a certain experimental set-up the largest neutrino mass squared difference, which will be named Δm^2_{31}, is relevant, and that

$$\Delta m^2_{12}\frac{L}{2E} \ll 1. \tag{1.35}$$

Then (1.24), in the particular case in which $\alpha \neq \beta$, becomes

$$P_{\nu_\alpha \longrightarrow \nu_\beta} = 1 - 2|U_{\alpha 3}|^2(1 - |U_{\alpha 3}|^2)\left(1 - \cos \Delta m^2_{31}\frac{L}{2E}\right). \tag{1.36}$$

Since, due to the unitarity of U:

$$|U_{e3}|^2 + |U_{\mu 3}|^2 + |U_{\tau 3}|^2 = 1 \tag{1.37}$$

the probability (1.36) has a two-neutrino form and is described by three independent parameters: $\Delta m^2_{31}, |U_{e3}|^2$, and $|U_{\mu 3}|^2$.

It can be shown [29] that, in the case in which Δm^2_{12} is the relevant squared mass difference, the survival probability (e.g. the quantity $P\nu_\alpha \longrightarrow \nu_\alpha$) depends on Δm^2_{12} and all the $|U_{\alpha i}|^2$ where $i = 1, \ldots, 3$: in the particular case in which $\alpha \equiv e$, the probability $P_{\nu_e \longrightarrow \nu_e}$ takes the form

$$P\nu_e \longrightarrow \nu_e = (1 - |U_{e3}|^2)^2 P^{(1,2)} + |U_{e3}|^4 \tag{1.38}$$

where

$$P^{(1,2)} = 1 - \frac{1}{2} \sin^2 2\overline{\theta}_{12} (1 - \cos^2 \Delta m^2_{21} \frac{L}{2E}) \tag{1.39}$$

and

$$\cos^2 \overline{\theta}_{12} = \frac{|U_{e1}|^2}{\sum_{i=1,2} |U_{ei}|^2} \qquad \sin^2 \overline{\theta}_{12} = \frac{|U_{e2}|^2}{\sum_{i=1,2} |U_{ei}|^2} \tag{1.40}$$

Thus, it also has a two-neutrino form and it is characterized by two parameters: Δm^2_{12} and $\overline{\theta_{12}}$. The only element that connects oscillations of atmospheric, LBL and solar neutrino is $|U_{e3}|^2$.

Equations (1.36) and (1.38) can be used to describe neutrino oscillations in atmospheric and LBL neutrino experiments as well as in solar neutrino experiments: for the former kind of experiments equation (1.35) holds, while for the latters equation (1.38) is satisfied.

From LBL reactor experiment CHOOZ and Super-Kamiokande it follows that θ_{13} is small: thus oscillations of atmospheric, LBL and solar neutrinos are described by different elements of the neutrino mixing matrix and have a two-neutrino behaviour.

This must be kept in mind in order to understand the results of oscillation experiments, which are, in fact, presented in a two-neutrino oscillation framework.

In the remainder of this section the results of those experiments contributing to the determination of the oscillation parameters will be presented: in particular, the results of the analysis performed accomodating the various experimental results in a three neutrinos scenario (hence ignoring the results of the LSND experiment) will be shown.

For further details and for a description of the adopted experimental set-ups some references will be provided.

In section 1.3.2 it has been shown how solar neutrino oscillations can be explained in terms of two parameters, which are now understood to be Δm^2_{12} and $\overline{\theta}_{12}$.

The KamLAND experiment, detecting $\overline{\nu}_e$ produced from several reactors at distances of 150-200 km, has independently shown that $\overline{\nu}_e$ neutrinos oscillate as well, and moreover, the oscillation parameters extracted from that experiment agree with those from solar ν_e experiments, as expected by CPT invariance.

Based on the combined analysis of these data the parameters Δm^2_{12} and θ_{12} have been determined with great accuracy: they are shown in figure 1.2 in the hypothesis $\cos\theta_{13} \sim 1$ (see later).

Their best fit values are:

$$\Delta m^2_{21} = 8.0 \times 10^{-5} \mathrm{eV}^2 \qquad \sin^2 \theta_{12} = 0.28 \qquad \sin^2 \theta_{13} = 0.004 \tag{1.41}$$

Oscillations of the atmospheric neutrinos have been mainly observed in the Super-Kamiokande [6, 7] experiment.

As mentioned in section 1.3.2, Super-kamiokande atmospheric neutrino data are best described in terms of dominant two-neutrino $\nu_\mu \longrightarrow \nu_\tau$ ($\overline{\nu}_\mu \longrightarrow \overline{\nu}_\tau$) vacuum oscillations with maximal mixing. The analysis of the collected events, in the hypothesis $\cos\theta_{13} \sim 1$ leads to the following range for the oscillation parameters:

$$1.5 \times 10^{-3} < \Delta m^2 < 3.4 \times 10^{-3}\text{eV}^2 \qquad \sin^2 2\theta > 0.92 \qquad \text{at} \qquad 90\%\ \text{C.L.} \tag{1.42}$$

These results are shown in figure (1.3).

The same range of oscillation parameters which was obtained from the analysis of the atmospheric neutrino data has been probed by the first long baseline accelerator neutrino experiment K2K [28]: the picture described above has been confirmed, and this has provided the first test of the oscillation model in the atmospheric sector.

Further data from long-baseline experiments will enable more precise determination of these two-flavours mixing parameters.

The result of the first LBL reactor experiment, CHOOZ, has found no indication [26, 32] in favour of the transition of $\overline{\nu}_e$ into other states, thus allowing to constrain θ_{13} from above:

$$\sin^2 2\theta_{13} < 0.11 \qquad \text{for} \qquad \Delta m^2_{atm} = 2 \times 10^{-3}\ \text{eV}^2 \tag{1.43}$$

The results of the global analysis of neutrino oscillation data are summarized in table 1.2.

1.4 Open issues related to neutrino masses

It has been shown in section 1.1 that the Standard Model of particle physics offers no explanation for neutrino masses and mixing: accordingly, neutrino oscillations are the first indication

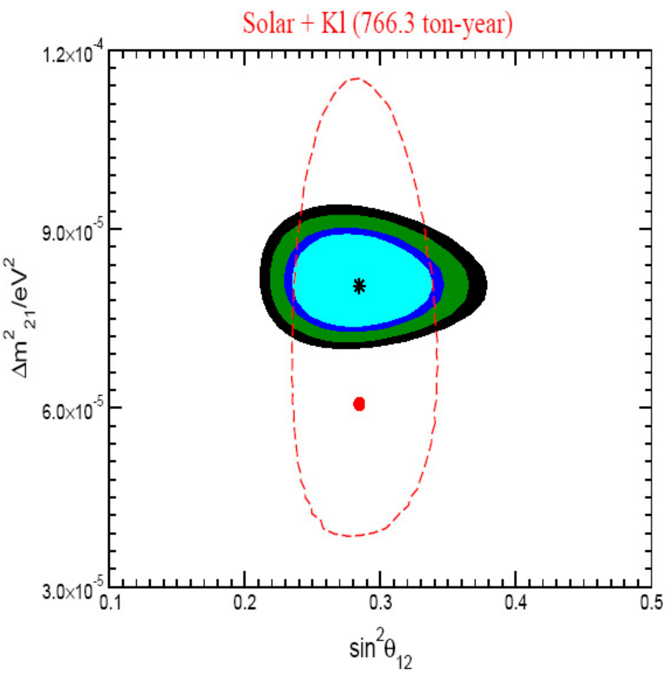

Figure 1.2: The 90%, 95%, 99% and 99.73% C.L. alowed regions in the Δm^2_{12} - θ_{12} plane, obtained in a three-neutrino oscillation analysis of the global solar and reactor neutrino data, including the data from the Kamland and CHOOZ experiments [30].

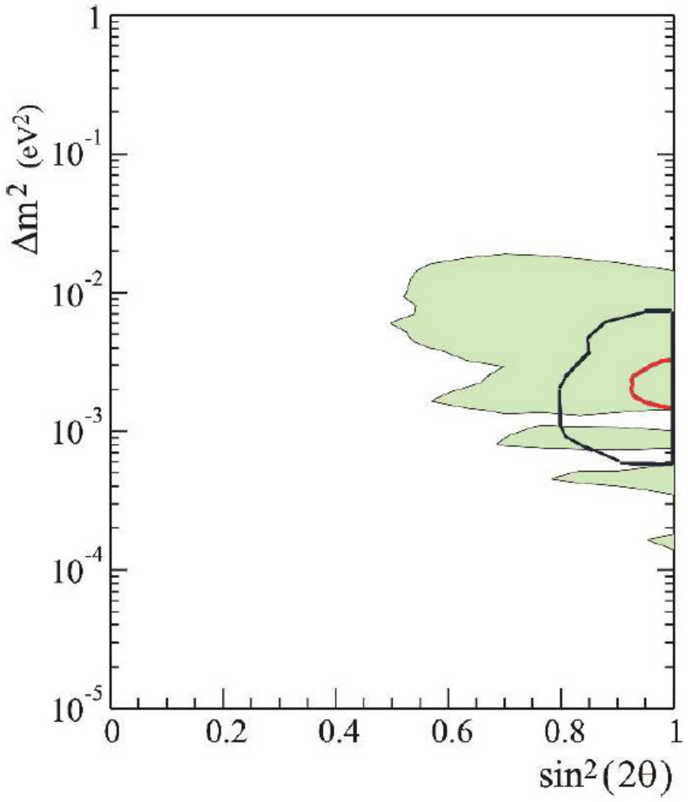

Figure 1.3: Allowed oscillation parameters from different atmospheric neutrinos oscillationsexperiments [31]: the shaded region shows the results of Soudan 2; the outer unfilled black contour shows the allowed region from MACRO upward-going muons; and the inner solid red contour shows the results from Super-Kamiokande.

for physics beyond the Standerd Model.

Many theories exist which explore the origins of neutrino masses and mixing.

The mechanisms exploited to generate neutrino masses are different: a large number of models use the so called see-saw effect [33, 34, 35], other theories are based on different possible origins of neutrino masses, such as radiative corrections arising from an extended Higgs sector [36].

Many of them rely on Supersimmetry as a way to naturally give masses to neutrinos.

All these models can be grouped into two different classes, leading either to a hierarchical pattern for the neutrino mass eigenvalues m_i

$$m_1 \ll m_2 \ll m_3 \tag{1.44}$$

or to a nearly degenerate pattern

$$m_1 \approx m_2 \approx m_3. \tag{1.45}$$

Furthermore, two different scenarios are possible within a hierarchical pattern.

If Δm^2_{12} is the mass squared difference which is extracted from oscillation experiments, and Δm^2_{23} is the value obtained from atmospheric neutrino experiment, both the following situations

Parameter	Value $\pm 1\sigma$	Comment
Δm^2_{21}	$8.2^{+0.6}_{-0.5} \times 10^{-5} eV^2$	
θ_{12}	$32.3^{\circ +2.7}_{-2.4}$	For $\theta_{13} = 0$
$\|\Delta m^2_{32}\|$	$2.4^{+0.6}_{-0.4} \times 10^{-3} eV^2$	
$\sin^2 2\theta_{23}$	> 0.94	For $\theta_{13} = 0$
$\sin^2 2\theta_{13}$	< 0.11	For $\Delta m^2_{atm} = 2 \times 10^{-3} eV^2$

Table 1.2: Neutrino oscilation parameters determined from various experiments (2004 status)

are allowed by the experimental data at present: the so called *normal hierarchy* scenario

$$m_1 \lesssim m_2 \approx \sqrt{\Delta m^2_{12}} \ll m_3 \approx \sqrt{\Delta m^2_{23}} \tag{1.46}$$

and the *inverted hierarchy* scenario

$$m_3 \ll m_1 \approx m_2 \approx \sqrt{\Delta m^2_{32}}. \tag{1.47}$$

In section 1.3 it has been shown that neutrino oscillation experiments cannot access absolute values of neutrino masses, since the are only sensitive to squared mass differences.

Therefore they do not distinguish between these classes of models, and only allow to set a lower bound on neutrino mass: at least one of the neutrino mass eigenvalues should in fact be non zero, and in particular:

$$m_i \geq \sqrt{|\Delta m^2_i|}. \tag{1.48}$$

The numerical value of this lower limit can be obtained by the current results of Super-Kamiokande:

$$m_3 \geq \sqrt{\Delta m^2_{atm}} \sim (0.04 - 0.07) \text{ eV}. \tag{1.49}$$

This doesn't allow, however, to discriminate between hierarchical and degenerate mass scenarios, since the fundamental mass scale of neutrinos can be located orders of magnitude above this bound (e.g. around 1 eV): for this reason a measurement of the absolute value of neutrino mass with a sensitivity in the sub-eV range is required.

Another important issue related to neutrino masses concerns their nature: theoretical models come to different conclusions of whether neutrino masses are of the Dirac or Majorana type (see sections 1.2.1 and 1.2.2).

In order to determine the nature of neutrino mass it is necessary to study processes which are affected by it: at present the best sensitivities are atteinable in experiments focusing on neutrinoless double beta decay.

Incidentally, a Majorana nature of neutrinos might also help us understand the smallness of neutrino masses through the see-saw mechanism: as neutrino masses are much smaller than the masses of the other fermions, their knowledge is crucial for our understanding of the fermion masses in general.

1.5 Absolute measurement of neutrino mass

Direct measurements of the neutrino mass can be performed relying on its kinematic effects.

In principle two approaches can be pursued: either the time-of-flight of neutrinos emitted from supernovae can be measured [37] or the kinematics of weak decays can be investigated.

Since the expected sensitivity of the first method will not reach values below 1 eV [38], all the expectations are reposed in the experiments based on the second one, and in particular on the investigation of the electron spectrum of tritium β decay.

1.5.1 Kinematic tests and beta decay

The investigation of weak decays is based on the measurement of the charged decay product of weak decays.

For the masses of ν_μ and ν_τ the following upper limits have been obtained:

$$\begin{array}{lll} m(\nu_\mu) < 190 \text{ keV} & \text{at} & 90\% \text{ C.L.[39]} \\ m(\nu_\tau) < 18.2 \text{ MeV} & \text{at} & 95\% \text{ C.L.[40]} \end{array} \tag{1.50}$$

Both limits are much larger than those atteinable in beta decays spectra studies, which turn out to be the most sensitive technique for the determination of neutrino mass.

The process investigated in these experiments is

$$^3H \rightarrow {}^3He + e^- + \overline{\nu}_e \tag{1.51}$$

It is a superallowed decay: the electron spectrum is determined only by the phase-space factor and the Coulomb interaction of the final e^- and ^3He and it is given by

$$\frac{dN}{dT} = CF(Z,E)pE(Q-T)\sum_i |U_{ei}|^2[(Q-T)^2 - m_i^2]^{\frac{1}{2}}\Theta(Q-T-m_i) \tag{1.52}$$

where p and T are respectively electron momentum and kinetic energy, $E = m_e + T$ is the total electron energy, $Q = m_{^3He} - m_e \simeq 18.6$ keV is the energy release, $C = const$, m_i are the eigenvalues of the neutrino mass eigenstates and *F(Z,E)* is the Fermi function, which describes the Coulomb interaction of the final particles.

The step function $\Theta(Q-E-m_i)$ ensures that a neutrino state ν_i is only produced if the energy available is larger than its mass.

The Kurie function is determined as follows

$$K(E) = \sqrt{\frac{dN}{dT}\frac{1}{pEF(Z,E)}} = \sqrt{C}\sqrt{(Q-T)|U_{ei}|^2\sqrt{(Q-T)^2 - m_i^2}} \tag{1.53}$$

If all the m_i are zero the Kurie function is a straight line $\sqrt{C}\sqrt{(Q-T)}$ and $T_{max} = 0$.

If at least one m_i is nonzero, the β spectrum ends at $T' = Q - m_1$, where m_1 is the lightest mass in the neutrino mass spectrum (see figure 1.4).

Moreover, if more than one m_i's are nonzero, some "kinks" appeare at the electron energy $T_e^i \approx Q - m_i$, with sizes determined by the mixing elements $|U_{ei}|^2$.

Current beta decay experiment are not sensitive enough to look for the kinks: they aim to observe a deficit of events in the end point part of the spectrum.

In this case the quantity which is determined is

$$m^2(\nu_e) = \sum_{i=1}^{3} |U_{ei}|^2 \cdot m_i^2. \tag{1.54}$$

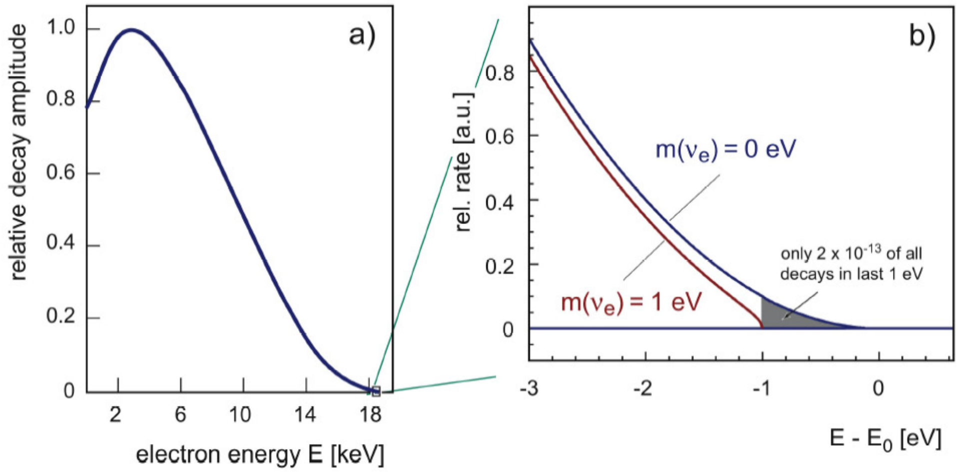

Figure 1.4: The electron energy spectrum of tritium β decay: (a) complete and (b) region around the endpoint. The spectrum is shown for neutrino masses of 0 and 1 eV

Experiment	$m^2_{\nu_e}$	m_{ν_e}
Mainz	$-1.2 \pm 2.2 \pm 2.1$ eV^2	$m_{\nu_e} < 2.2$ eV
Troitsk	$-2.3 \pm 2.5 \pm 2.0$ eV^2	$m_{\nu_e} < 2.1$ eV

Table 1.3: Measured values of $m^2_{\nu_e}$ and consequent upper limits on m_{ν_e} obtained by the Mainz and Troitsk groups. The negative values obtained for the best fit values of $m^2_{\nu_e}$ mean that some excess of events have been observed instead of a deficit.

No positive indications in favour of $m^2(\nu_e) \neq 0$ have been found at present [1, 2]: the measured values of $m^2(\nu_e)$ and the following upper limits are shown in table 1.3.

Next generation tritium β-decay experiments will measure the mass of the neutrino with sub-eV sensitivity [41].

1.6 Neutrinoless double beta decay

The decay

$$(A, Z) \rightarrow (A, Z+2) + e^- + e^- + \overline{\nu}_e + \overline{\nu}_e \tag{1.55}$$

is a second order Standard Model process, called *double beta decay* ($2\nu\beta\beta$).

Since its amplitude is proportional to G_F^2 such a process is very rare.

Moreover, this decay can occurr only if, for the neighbouring Z-values nuclei, single beta decay is energetically forbidden, and this restricts the choice of the candidate decaying isotope to a limited group of even-even nuclei.

$2\nu\beta\beta$ conserves lepton number.

The decay

$$(A, Z) \rightarrow (A, Z+2) + e^- + e^- \tag{1.56}$$

($0\nu\beta\beta$) violates lepton number by two units: if detected it would provide a clear evidence of new Physics beyond the Standard Model.

Isotope	Half-life Limit (y)	$\langle m_{\beta\beta}\rangle$ (meV)
^{48}Ca	$> 1.4 \times 10^{22}$	<7200-44700 [47]
^{76}Ge	$> 1.9 \times 10^{25}$	<350 [48]
^{76}Ge	$> 1.6 \times 10^{25}$	<330-1350 [46]
^{76}Ge	$= 1.2 \times 10^{25}$	=440 [45]
^{82}Se	$> 2.7 \times 10^{22}$ (68%)	<5000 [49]
^{100}Mo	$> 5.5 \times 10^{22}$	<2500 [50]
^{116}Cd	$> 1.7 \times 10^{23}$	<1700 [51]
^{128}Te	$> 7.7 \times 10^{24}$	<1100-1500 [52]
^{130}Te	$> 5.5 \times 10^{23}$	<370-1900 [53]
^{136}Xe	$> 4.4 \times 10^{23}$	<1800-5200 [54]
^{150}Nd	$> 1.2 \times 10^{21}$	<3000 [55]

Table 1.4: Summary of the recent $0\nu\beta\beta$ results. All limits, which are deduced by the authors, are 90% confidence level unless otherwise indicated

It can be recognized by its electron sum energy spectrum: since the nuclear masses are much larger than the decay Q value, the nuclear recoil can be neglected and the spectrum is simply a peak at $T_{e1} + T_{e2} = Q$.

Several experiments (see e. g. [42, 43, 44]) have searched for neutrinoless double beta decay (this is the name of the process (1.56)) but no evidence for it has been uncovered yet[1].

The best limit[2] on $0\nu\beta\beta$ comes from ^{76}Ge experiments [46], which set the limit:

$$\tau_{0\nu}(^{76}\mathrm{Ge}) \geq 1.57 \times 10^{25} \text{ y}. \tag{1.57}$$

In table 1.4 the current bounds on the life-times of some isotopes against $0\nu\beta\beta$ are shown.

The $0\nu\beta\beta$ process involves a vertex changing two neutrons into two protons with the emission of two electrons and nothing else.

It can proceed through many different mechanisms: almost any physics that violates the total lepton number can cause it (see, e.g. [56, 57]); however, no matter what the vertex is, **the decay is possible only is neutrinos are massive Majorana particles** [58].

The simplest way to obtain $0\nu\beta\beta$ is to have a Majorana mass term of the form $m_\nu \nu_L^T C^{-1} \nu_L$, which violates lepton number: this would lead to $0\nu\beta\beta$ through the diagram of fig. 1.5.

It can be shown that, if the exchange of a light Majorana neutrino were the dominant mechanism contributing to $0\nu\beta\beta$, the amplitude for such process would be proportional to the so called *effective neutrino mass*:

$$\langle m_{\beta\beta}\rangle = |\sum_i |U_{ei}|^2 m_{\nu_i} e^{i\alpha_i}|. \tag{1.58}$$

where α_i are the Majorana phases [3].

[1] Actually observation of $0\nu\beta\beta$ has recently been claimed by part of the collaboration of the Heidelberg-Moskow experiment [45], as will be descussed in section 1.6.1. The claim drew strong criticisms within the scientific community and it is still controversial.

[2] Halflives of different isotopes against $0\nu\beta\beta$ cannot however be compared without a large uncertainty, given their dependance on different nuclear matrix elements, see equation 1.59.

[3] The 3×3 unitary matrix U has 9 independent parameters: 3 of them are angles, and 6 parameters are phases. However, not all the phases have physical a meaning: if neutrinos with definite masses are Dirac particles thenumber of physical phases is equal to 1 (the so called Dirac phase, responsible for CP violation effects). If they are Majorana particles their number is equal to 3 (1 Dirac phase + 2 Majorana phases). In the former case, in fact, five phases can be rotated away by a proper ridefinition of the neutrino and lepton fields in (1.17). This is possible only for three phases with Majorana neutrinos because of the further constraint on neutrino fields posed by the Majorana condition $\nu_i^C = \nu_i$.

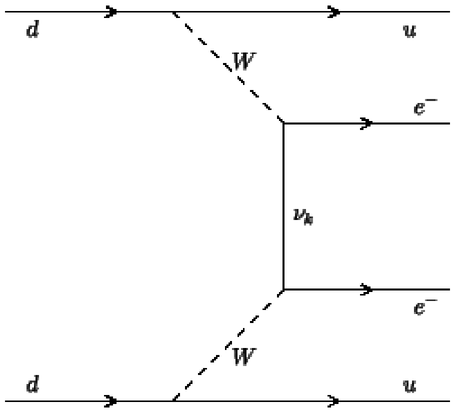

Figure 1.5: Feynman diagram of neutrinoless double beta decay mediated by the exchange of a light Majorana neutrino.

The decay rate would in fact be given by

$$[T^{0\nu}_{1/2}]^{-1} = G^{0\nu}(Q,Z)|M^{0\nu}|^2\langle m_{\beta\beta}\rangle^2 \tag{1.59}$$

where $G^{0\nu}$ is the accurately calculable phase space integral, and $|M^{0\nu}|$ is the nuclear matrix element, which accounts for the contributions of the nuclear physics involved in the decay.

If the $0\nu\beta\beta$ decay is observed, and the nuclear matrix element is known, it is then possible to obtain the value of $\langle m_{\beta\beta}\rangle$ from (1.59).

Since the quantity $\langle m_{\beta\beta}\rangle$ is in turn related to the oscillation parameters, its measured value could be further constrained by the results of the oscillation experiments.

Figure 1.6 shows the allowed region for $\langle m_{\beta\beta}\rangle$ and $m_{\nu_{min}}$, where $m_{\nu_{min}}$ is the value of the mass of the lightest neutrino; the plot has been obtained from the fits to the oscillation data.

It is evident that the determination of $\langle m_{\beta\beta}\rangle$ could considerably contribute to the determination of the absolute neutrino mass scale [59] reducing the allowed range of values for $m_{\nu_{min}}$ and for the oscillation parameters and possibly discriminating between the three hierarchy patterns (see section 1.4).

Next generation beta decay experiments aim at a sensitivity of $\sim 0.2\ eV$, on $m^2(\nu_e)$, and a value of $m^2(\nu_e)$ can immediately be converted into an upper bound on $m_{\nu_{min}}$.

The goal of the next $0\nu\beta\beta$ experiments is instead to reach sensitivities of few tens of millielectronvolts on $\langle m_{\beta\beta}\rangle$: this will allow to probe the region of the inverse hierarchy scenario.

Although the occurrence of $0\nu\beta\beta$ implies the existence of massive Majorana neutrinos, the connection between the half-life and the neutrino mass relies on the assumption that the diagram in fig 1.5 dominates $0\nu\beta\beta$.

While the exchange of a light massive neutrino is perhaps the most plausible mechanism, there exist many additional diagrams (involving the exchange of supersymmetric particles, higgs particles, leptoquarks, heavy neutrinos [56, 57]) which can play a role in generating double beta decay.

These alternative mechanisms, if dominant, would not allow to extract the effective mass from the observed $0\nu\beta\beta$ rate.

Indications for estabilishing whether the exchange of light Majorana meutrinos is the dominant mechanism could come from the study of the lepton flavour violating processes $\mu \to e$ and

[c]

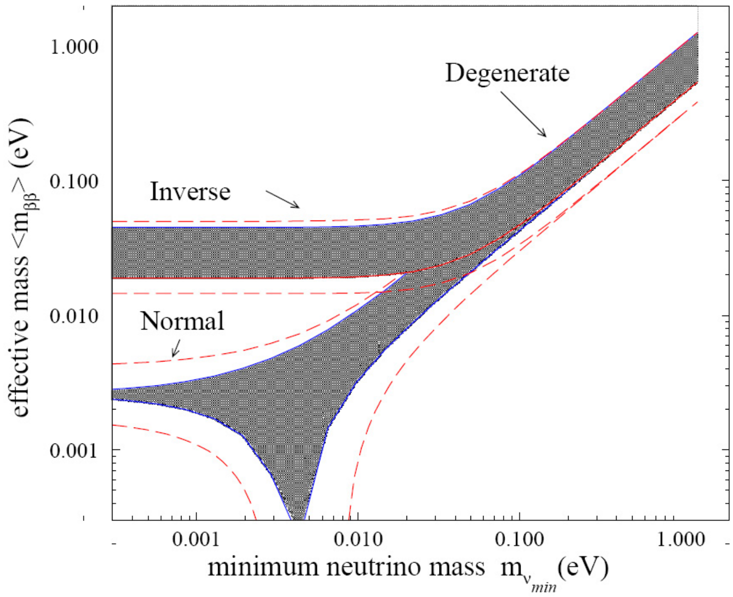

Figure 1.6: Effective Majorana mass versus the minimum mass $m_{\nu_{min}}$. The shaded region corresponds to the best values of oscillation parameters and $\theta_{13} = 0$. The dashed lines indicate the range corresponding to the 1σ errors of the oscillation parameters and the maximum allowed θ_{13}.

$\mu \to e + \gamma$ [60]: in particular the ratio of the branching fractions of these processes could possibly tell if the determination of $\langle m_{\beta\beta} \rangle$ from $0\nu\beta\beta$ is possible.

1.6.1 Main strategies for double beta decay searches

Given the expected rareness of $0\nu\beta\beta$, the basic requirements for all experiments looking for it is to have a large amount of at least one $0\nu\beta\beta$ candidate isotope (the most used are listed in table 1.4).

The experimental signatures of the nuclear double beta decays are in principle very clear: in the case of the neutrinoless decay, a peak at the $Q_{\beta\beta}$ value is expected in the two-electron summed energy spectrum, whereas a continuous spectra will characterize the two-neutrino decay mode.

In spite of such characteristic imprints, the rarity of the processes under consideration make their identification very difficult.

Such unlikely signals have to be disentangled from a background due to natural radioactive decay chains, cosmogenic-induced activity, and man-made radioactivity, which deposit energy on the same region where the $\beta\beta$ decays do, but at a faster rate.

Consequently, the main task in $\beta\beta$-decay searches is to diminish the background and identifying the signal.

Two general approaches have been followed so far to investigate $0\nu\beta\beta$ decay:

- indirect methods
- direct or counter methods

Indirect methods are based on the measurement of anomalous concentrations of the daughter nuclei in selected samples, characterized by very long accumulation times.

They include geochemical and radiochemical methods and can only give indirect evaluations of the $0\nu\beta\beta$ and $2\nu\beta\beta$ lifetimes, being completely insensitive to different $\beta\beta$ modes.

Counter methods are based instead on the direct observation of the two electrons emitted in the decay, and can therefore measure different features of the event (energies, momenta, topology, etc.).

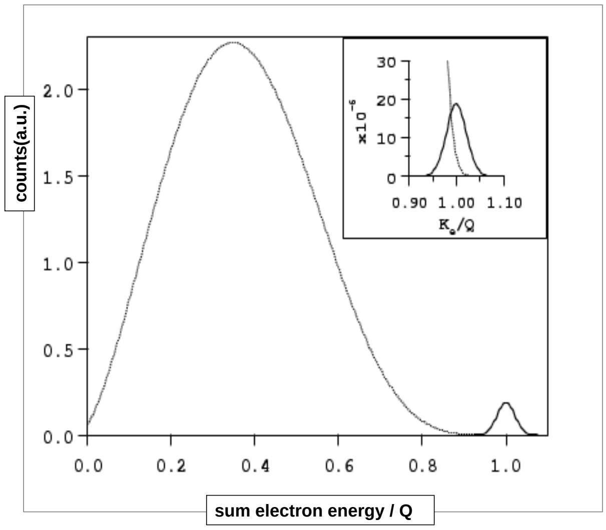

Figure 1.7: Electron sum energy spectra for $2\nu\beta\beta$ and $0\nu\beta\beta$. The inset shows the relative insensity of the two modes, underlining the contribution of $2\nu\beta\beta$ to $0\nu\beta\beta$ background.

Experiments exploiting direct methods keep nowadays the stage because of their evident advantages.

They can distinguish between the various $\beta\beta$ by the differences in their electron sum energy spectra 1.7.

Since a sharp line at the transition energy is expected for $0\nu\beta\beta$ electron sum energy, a very good energy resolution is the basic requirement for direct counting experiments: the ultimate irreducible background source when looking for $0\nu\beta\beta$ decay is in fact that due to the standard $2\nu\beta\beta$ decay, and only an adequate energy resolution will allow the discrimination between the two kinds of decays.

The types of detectors currently used are [61]:

- Calorimeters, where the detector is also the $\beta\beta$ source [62] (Ge diodes, scintillators, - CaF_2, $CdWO_4$ -, thermal detectors -TeO_2 -, Xe ionization chambers, ..).

  They are calorimeters which measure the two-electron sum energy.

- Tracking detectors in which the $\beta\beta$ source doesn't coincide with the sensing element (Time Projection Chambers TPC, drift chambers, electronic detectors), but is instead placed within the detector tracking volume, in the shape of a plane.

Leading examples of tracking devices are the Irvine TPC's and the NEMO and ELEGANTS series.

- Tracking calorimeters. They are tracking devices where the tracking volume is also the $\beta\beta$ source, for example a Xenon TPC (CALTECH/PSI/Neuchatel) and the future EXO.

The advantages of the various methods are different.

Calorimeters have good energy resolutions and almost 100 % efficiency, but they lack the tracking capabilities to identify the background on an event-by-event basis.

On the contrary, the identification capabilities of the various types of chambers make them very well suited for $2\nu\beta\beta$ and $0\nu\beta\beta$ searches, but their energy resolution is rather modest and the efficiency is only of a few percent.

Another advantage of modular calorimeters is that they can accomodate large quantities (like CUORE, Majorana and GENIUS) of $\beta\beta$ emitters: tracking detectors, instead, are limited by the requirement to shape their sources in plates: only recent versions of tracking devices have 10 kg and more (NEMO3).

TPC devices, on their side, are planning to reach one ton and more of active mass (EXO).

The general strategy followed to perform a neutrinoless double beta decay experiment is simply dictated by the expression of the half-life

$$T^{0\nu}_{1/2} \simeq \ln 2 \times \frac{N \cdot t}{S} \tag{1.60}$$

where N is the number of $0\nu\beta\beta$ emitter nuclei and S the number of recorded counts during time t (or the upper limit of double beta counts consistent with the observed background).

In the case of taking for S the background fluctuation (when that might be possible), one has the so-called detector factor-of-merit or neutrinoless sensitivity (1σ) which, for devices in which the source is also the sensitive element (for which the background rate scales with the detector mass) reads

$$F_D = 4.17 \times 10^{26} \frac{f}{A} \sqrt{\frac{Mt}{B\Gamma}} \varepsilon_\Gamma \text{ y} \tag{1.61}$$

where B is the background rate (c/(keV kg y)), M the mass of $0\nu\beta\beta$ emitter (kg),ε_Γ the detector efficiency in the energy interval Γ around $Q_{\beta\beta}$ (Γ is the FWHM energy resolution), t the running time measurement in years, a f is the isotopic abundance and A the mass number.

A slightly different behaviour is expected when the background rate is very low ("zero background" or $B\Gamma Mt << 1$ hypothesis)

$$F_D \sim fMt\varepsilon_\Gamma/A \text{ y}. \tag{1.62}$$

The other guideline of the experimental strategy is to choose, according to equation 1.59, a $0\nu\beta\beta$ emitter of large nuclear factor of merit $F_N = G^{0\nu}|M^{0\nu}|^2$, where the kinematical factor qualifies the goodness of the $Q_\beta\beta$ value and $M^{0\nu}$ the likeliness of the transition.

Notice that the upper limit on $|\langle m_{\beta\beta}\rangle|$ is given by $|\langle m_{\beta\beta}\rangle| \leq m_e/\sqrt{(F_D F_N)}$, or in terms of its experimental and theoretical components

$$|\langle m_{\beta\beta}\rangle| \leq 2.5 \times 10^{-8} \times \sqrt{\frac{A}{f}} \times \sqrt[4]{\frac{B\Gamma}{Mt}} \times \frac{1}{\sqrt{\varepsilon_\Gamma G^{0\nu}}} \times \frac{1}{|M^{0\nu}|} \tag{1.63}$$

1.6.2 Overview of main experiments an synopsis of results

In this section a briefing of the main techniques will be sketched together with a summary the current experimental situation.

The first isotope used for the search of $0\nu\beta\beta$ was ^{76}Ge: the search for the nuclear double beta decay of ^{76}Ge started as earlier as in 1967 by the Milano group [63] which is now leading the CUORE Collaboration.

Other groups both from USA (USSB-LBL-UCB, Caltech, PNL-USC) and Europe (Zaragoza, PSINeuchatel, Heidelberg-Moskow) continued this search with germanium detectors.

Thanks to the continuous reduction of radioactive background achieved steadily since the first prototypes (PNL-USC and USSB-LBL), the effective neutrino mass bound has been steadily improving along the last decades, and now the current most stringent limits are led by the results obtained with Germanium experiments (IGEX, Heidelberg-Moskow).

Two recent experiments have looked for the double beta decay of ^{76}Ge.

They both employ several kilograms of enriched^{76}Ge (86%) in sets of detectors: the IGEX Collaboration experiment [64] (a set of three detectors of total mass 6.0 kg) in the Canfranc Underground Laboratory (Spain) and the Heidelberg/Moscow Collaboration experiment [65] (a set of five detectors amounting to 11 kg) in Gran Sasso and (2.1 kg) in the Baksan Neutrino Observatory (Russia).

Very efficient shieldings, both active and passive, were used in the two experiments.

As a result, in the case of **IGEX** the background recorded in the energy region between 2.0 and 2.5 MeV is about 0.2 c/keV/kg/y prior to Pulse Shape Discrimination and most of the background in the relevant $Q_{\beta\beta}$ region of 2039 keV is accounted for by cosmogenic activated nuclei (^{76}Ge and ^{76}Ge).

This background level is further reduced through Pulse Shape Discrimination, which successfully eliminates multisite events, charac teristic of non-$\beta\beta$ events, leading to less than ~ 0.07 c/keV/kg/y.

IGEX data corresponding to 8.87 kg y in ^{76}Ge provided a half-life lower bound of $T_{0\nu}^{1/2} \geq 1.57 \times 10^{25}\ y$ at 90% C.L. for the complete data set with PSD [46].

Accordingly, the limit on the neutrino mass parameter is 0.33-1.31 eV, where the uncertainties originate from the spread in the calculated nuclear structure parameters.

The **Heidelberg-Moscow** experiment operated five p-type HPGe detectors of enriched ^{76}Ge (86%) with a total active mass of 10.96 kg, corresponding to 125.5 mol of ^{76}Ge.

To derive the neutrinoless decay half-life limit from the H-M experiment, the raw data of all five detectors as well as data with pulse shape analysis are considered.

No indication for a peak at the $Q_{\beta\beta}$ energy is seen in the data, corresponding to 35.5 kg $\cdot$ y of exposure and its background in the energy region between 2000 and 2080 keV is (0.06 ± 0.01) c/keV/kg/y.

Following the method proposed by PDG, the limit on the half-life is [48] $T_{0\nu}^{1/2} \geq 1.9 \times 10^{25}\ y$ at 90% C.L.

No evidence for $0\nu\beta\beta$ has been reported so far [66] with the exception of the claimed discovery of the decay of ^{76}Ge reported by a subset of the Heidelberg-Moscow collaboration [67].

This claim has been contested by various authors [46, 68] and also by other members of the same Heidelberg-Moscow Collaboration [69].

A new analysis in favour of the previous claim has however been published recently [45].

Another technique employs Time Projection Chambers.

An example of a TPC, successfully operated along many years, was the Time Projection Chamber of the **UC Irvine** group, which played an historical role in the discovery of the conventional double beta decay.

It was a rectangular box filled with helium and located underground at 290 m.w.e. (Hoover Dam).

A central $\beta\beta$ source plane divides the volume into two halves, whereas a magnetic field is placed perpendicular to the source plane.

Electrons emitted from the source follow helical trajectories from where the momentum and the angles of the β-particles are determined.

The $\beta\beta$ signal is recognized as two electrons emitted from a common point in the source, with no other associated activity, during some time before and after the event.

The $\beta\beta$ source is thin enough (few mg/cm^2) to allow a-particles to escape and be detected for tagging the background.

The UCI TPC series of experiments, finished more than five years ago, had the merit of having obtained the first direct observation of the double beta decay (^{82}Se).

They also successfully measured the two-neutrino double beta decay of ^{100}Mo , ^{150}Nd and ^{48}Ca.

The **NEMO** series of detectors are [70] electron tracking devices (with open Geiger cells) filled with helium gas.

An external calorimeter (plastic scintillator) covers the tracking volume and measures the β energies and time of flight.

The $\beta\beta$ source is placed in a central vertical plane and is divided in two halves, one enriched and another of natural abundance (of about 150 grams each), to monitor and subtract the background.

To identify a $\beta\beta$ signal, one should have a 2e-track with a common vertex ($\cos\alpha < 0.6$) in the source plus two fired plastic scintillators ($E_{deposition} > 200$ keV each).

The two-electron events are selected by time of flight analysis (in the energy range of $\beta\beta$).

For instance, NEMO 2 has been operating for several years at the Modane Underground Laboratory (Frejus Tunnel) at 4800 m.w.e and has measured the $2\nu\beta\beta$ decays of ^{100}Mo, ^{116}Cd, ^{82}Se and ^{96}Zr.

A new, bigger detector of the NEMO series, NEMO 3, has recently started its data taking with sources of up to 10 kg of ^{100}Mo and other emitters [71].

The **ELEGANTS V** detector of the University of Osaka (placed successively in Kamioka and Oto) is an electron tracking detector which consists of two drift chambers for β-trajectories, sixteen modules of plastic scintillators for β energies and timing measurement, and twenty modules of NaI for X- and γ-rays identification.

The $\beta\beta$ signals should appear as two tracks in the drift chamber with the vertex in the source plus two signals from two plastic scintillator segments.

Both enriched and natural sources (of about 100 grams) are employed in the detector for background monitoring and subtraction.

This detector has measured the $2\nu\beta\beta$ decay of ^{116}Cd, ^{100}Mo, and several other emitters [72].

A new variant of ELEGANTS is searching for the double beta decay of ^{48}Ca.

The **Caltech/PSI/Neuchatel** Collaboration [73] has investigated the double beta decay of ^{136}Xe in the Gotthard Tunnel (3000 m.w.e.) by using a time projection chamber where the Xenon, enriched up to 62.5% in ^{136}Xe, with a total mass of $m = 3.3$ kg, was both the source and the detector medium, i.e. a calorimeter plus a tracking device.

It had a cylindrical drift volume of 180 fiducial litres at a pressure of 5 atm. The $\beta\beta$ signal appears as a continuous trajectory with distinctive end features: a large angle multiple scattering and increase charge deposition (charge "blobs") at both ends.

As usual, the $\beta\beta$ topology gives powerful background rejection, leading to a figure of $B \sim 10^{-1} - 10^{-2}$ c/keV/kg/y (at 2480 keV).

Other results worth mentioning are those of the ITEP and Florence-Kiev groups.

The **ITEP** group measured [74] the double beta decay of ^{150}Nd (40 g) with a TPC of ~ 300 litres filled with CH_4 at atmospheric pressure, in a 700 gauss magnetic field.

On the other hand, the group of **INR at Kiev** [75] is investigating the double beta decay of 116Cd with cadmium tungstate ($^{116}CdWO_4$) scintillator crystals.

The results obtained by the various experiments in terms of both neutrinoless half-life and Majorana neutrino mass bounds and are summarized in table 1.4.

1.6.3 Next generation experiments

The requirements for a next-generation experiment can easily be deduced by reference to equations 1.60 and 1.61: to improve the sensitivity of $|\langle m_{\beta\beta}\rangle|$ by a factor of 100, the quantity Nt/S must be increased by a factor of 10^4.

The quantity N can easily be increased by a factor of $\sim 10^2$ over present experiments, so that t/S must also be improved by that amount.

Since practical counting times can only be increased by a factor 2-4, the background should be reduced by a factor 25-50 below the present levels.

These are approximately the target parameters of the next-generation neutrinoless double-beta decay experiments.

CUORE experiment, which will be described in detail in chapter 5, is a proposed cryogenic experiment with 19 towers of 52 detectors, each one being a 750 g TeO_2 bolometer.

It will be the only future detector not requiring isotopic enrichment: this means that it would utilize natural abundance Te, containing 33.8% ^{130}Te.

A pilot experiment, **Cuoricino**, comprising one CUORE tower, is now taking data at LNGS (chapter 3.

With equivalent background, CUORE would be as sensitive as 400-950 kg of Ge enriched to 86% ^{76}Ge, depending on the nuclear matrix elements used to derive $|\langle m_{\beta\beta}\rangle|$.

EXO is a large proposed TPC, either high-pressure gas or liquid, of enriched ^{136}Xe: its plans include, in particular, the use of 1 to 10 tons of Xenon.

This novel technique involves schemes for locating, isolating, and identifying the daughter $^{136}Ba^+$ ion by laser resonance ionization spectroscopy: EXO is planned as a zerobackground experiment.

A program of research and development is underway at the Stanford Linear Accelerator (SLAC) [76].

GENIUS is a proposal to use between 1.0 and 10 tons of "naked" germanium detectors, isotopically enriched to 86% in ^{76}Ge, directly submerged in a large tank of liquid nitrogen functioning both as a cooling medium and a clean shield.

In ref. [77] the authors claim a sensitivity range of 1-10 meV for $|\langle m_{\beta\beta}\rangle|$, using $10^3 - 10^4\ kg$ of enriched Ge.

A research and development program is underway in the Gran Sasso Laboratory to develop the techniques for cooling and operating "naked" Ge detectors in liquid nitrogen for extended periods [78].

The **Majorana** project is a proposed significant expansion of the IGEX experiment, utilizing newly developed segmented detectors along with pulse-shape discrimination techniques.

It proposes 500 fiducial kg of Ge isotopically enriched to 86% in ^{76}Ge in the form of 200-250 detectors.

Each detector will be segmented into electrically independent volumes, each of which will be instrumented with the new PSD system.

The **MOON** experiment is a proposed major extension of the ELEGANTS experiment.

It will utilize between 1 and 3 tons of Mo foils, isotopically enriched to 85% in ^{100}Mo, inserted between plastic scintillators.

It will have coincidence and tracking capabilities to search for $0\nu\beta\beta$ decay as well as solar neutrinos.

This novel technique for detecting solar neutrinos depends on the special properties of the nuclear decay schemes of ^{100}Mo and its daughters, allowing both event and background identification [79].

Chapter 2

The bolometric technique

"Ce qui m'émeut si fort de ce petit prince endormi,
c'est sa fidélité pour une fleur,
c'est l'image d'une rose qui rayonne en lui
comme la flamme d'une lampe, même quand il dort..."
Antoine De Saint-Exupéry

Introduction

The expression "thermal detector" is generically used to designate a sensitive calorimeter which measures the energy deposited by particles through the corresponding temperature rise.

Here the attention will be focused on a particular class of single particle interaction detectors: bolometers, or Low Temperature Detectors, which take advantage of being operated at low temperatures for achieving very high sensitivities and energy resolutions.

In this chapter the general principles of operation of bolometric detectors will be exposed, and the main detector components and their charecteristics properties will be described.

In view of the last chapters, dealing with CUORE data acquisition, a particular attention will be devoted to semiconductor thermistors, which are the sensors adopted by Cuoricino and CUORE experiments, and to the features which mainly contribute to determine their response.

2.1 General Principles

In a very basic approach a thermal detector is a calorimeter with heat capacitance C: the energy E released by a particle interaction is determined by measuring the temperature increase $\Delta T = E/C$.

In order to follow this approach the heat capacitance of the calorimeter must be minimized, and this is accomplisher by using suitable materials (dielectric crystals, superconductors below the phase transition, etc.) and operating the detector at low temperatures.

The main components of a thermal detector are an *absorber*, where the particles to be detected interact, a *sensor*, which collect the excitations produced by the particle interactions generating a signal, and a thermal coupling to a heath bath, with the purpose of mantaining the detector at the proper temperature.

A scheme of the thermal structure of a bolometer is drawn in figure 2.1.

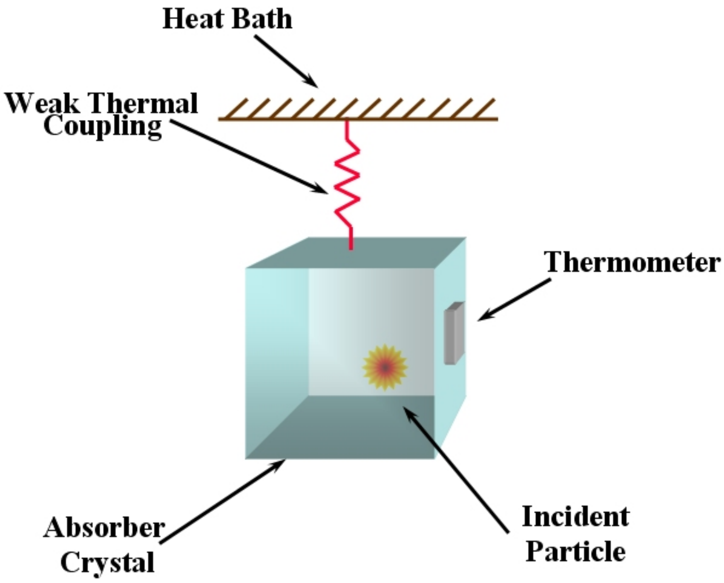

Figure 2.1: Thermal structure of a bolometric detector

The energy deposited by particles in the absorber is initially converted in phonons whose energy is very high compared to that of the tehermal bath (about the Debye energy): they are out of the thermodynamic equilibrium (athermal phonons) and they degrade their energy returning to an equilibrium distribution (thermal phonons) at a temperature still higher than the that of the thermal bath.

The time requires for phonons thermalization is of the order of microseconds, and the processes responsible for it depend on the material constituting the absorber and they are quite complicate.

If the response of the sensor is fast enough the detector can be sensitive to athermal phonons, and this is the case, for example, of the Superconducting Phase Transition thermometers.

If the sensor is slow it will be only sensitive to thermal phonons; in this case it measures the temperature of the absorber and it is a calorimeter.

Semiconductor doped sensors belong to this second class, and only thermal detectors operated as calorimeter will be considered in the following.

The distinction between thermal and athermal phonons detectors is not sharp, since the sensitivity of sensor to athermal phonons in some respects depends on its coupling to the absorber.

One of the main qualities of low temperature detectors is their good energy resolution, which is much better than that achieved by conventional detectors.

These are in fact only sensitive to the energy deposited in the form of ionization (about 30% of the total energy deposit) and their resolution is further reduced by the statistical fluctuations in the number of the produced pairs.

The resolution of a semiconductor detector, for example, can be estimated by

$$\Delta E_{FWHM} = 2.35F\sqrt{\epsilon E} \tag{2.1}$$

where F is the Fano Factor [80], ϵ is the energy required to create an electron-hole pair and E is the energy deposit.

A silicon detector, for example, can achieve energy resolutions of about 150 eV at 6 keV, mainly limited by ϵ, which is about 1 eV.

The intrinsic energy resolution of a bolometric detector (see section 2.5) can be expressed as

$$\Delta E = \sqrt{k_B C(T) T^2} \tag{2.2}$$

For 1 kg of TeO_2 working at 10 mK, the energy resolution is about 10 eV, and it is independent from the energy: so, at least in principle, bolometers have more than an order of magnitude better resolutions than conventional detectors.

2.2 The energy absorber

The absorber of a bolometer can be realized with any material whose specific heat is low enough at the working temperature.

The specific heat of a crystal at low temperatures is given by

$$c(T) = c_r(T) + c_e(T) \tag{2.3}$$

where c_r is the lattice contribution to the specific heat and c_e is the electron one. The lattice contribution is in turn expressed by the Debye law:

$$c_r(T) = \frac{12}{5}\pi^4 k_B K_A \left(\frac{T}{\Theta}\right)^3 = \beta\frac{m}{M}\left(\frac{T}{\Theta}\right)^3 \tag{2.4}$$

where N_A is the Avogadro number, Θ_D is the Debye temperature, $\beta = 1944$ J K^{-1}mol^{-1}, m is the absorber mass, and M is the molecular weight.

The electron contribution is

$$c_e(T) = \frac{\pi^2}{\Theta_D} ZR \frac{T}{\Theta_F} \tag{2.5}$$

where Z, R, and Θ_F are the number of conduction electron for each atom, the gas constant and the Fermi temperature.

Since for dielectric diamagnetic materials only the lattice contribution is present, they are preferred as energy absorbers, because they guarantee a lower specific heat.

Furthermore, since the Debye temperature depends on the mass number A and on the material density ρ according to $\Theta_D \propto A^{-\frac{1}{3}} \times \rho^{-\frac{1}{6}}$ low atomic mass number and low density materials would provide lower heat capacities; it must be kept in mind, however, that high A values guarantee higher detection efficienies for electrons and gammas.

2.2.1 Thermalization process

When a particle passes through a crystal it releases its energy interacting with nuclei and electrons.

Such energy is then converted into high energy phonons, which in turn relax, via different processes, onto an equilibrium Bose-Einstein distribution of thermal phonons.

In case the thermalization process occurs via the *nuclear channel*, the energy is released to the lattice via nuclear scattering.

This can result in the production of phonons, but also in the production of structural defects in the absorber: in this case the statistical fluctuation of the number of the produced defects can worsen the energy resolution.

The fraction of the energy which is lost in this way is negligible for photons and electrons, but it can cause a FWHM resolution of hundreds of eV in the case of α particles of some MeVs energy.

The contribution of the nuclear channel is negligible for primary electromagnetic radiation, for which the energy is released predominantly via the *electronic channel*.

When a ionizing particle interacts in an insulating or semiconductor material, in fact, its kinetic energy E is mainly spent for producing electron-hole pairs, whose spatial density and energy is high at the beginning of the particle's track.

The number N_{eh} of pairs produced is given by

$$N_{eh} = E/\epsilon_{eh} \tag{2.6}$$

where ϵ_{eh} is the average energy of the pairs.

These charge carriers interact first with each other and spread very quickly in the crystal and when a quasi equilibrium situation is reached they undergo their final degradation interacting with the lattice site: this interaction produce phonons.

Unfortunately this mechanism, whose timescale is $\sim$ 10 ps, has to compete with other undesirable processes: a fraction of the pair energy can leave the crystal or can be stored in stable or metastable states instead of being converted into phonons, and this results in fluctuations on the number of pairs contributing to generate the thermal signal, leading to a degradation of the energy resolution.

It is indeed possible to have radiative recombinations of the pairs, non-radiative recombinations over timescales longer compared to the signal developing time, or even trapping of carriers in impurity sites or lattice defects: the efficiences of these processes depends on the pairs density and energy.

Let's consider now the phonon thermalization processes.

The initially produced phonons have high energies and low momenta, and they belong to the optical branches (see figure 2.2).

They depart from the particle interaction region and decay in the longitudinal acoustic (LA) branches in a very short time (10 - 100 ps): the result of this process is a phonon system, mainly belonging to the LA branches, having energies of the order of $\hbar\omega_D/2$ (where $\omega_D = 2\pi\nu_D$ and where ν_D is the Debye cut-off frequency of the crystal), hence higher than the average energy of thermal phonons (for example, at T= 10 mK, the average energy is $\sim \mu$eV).

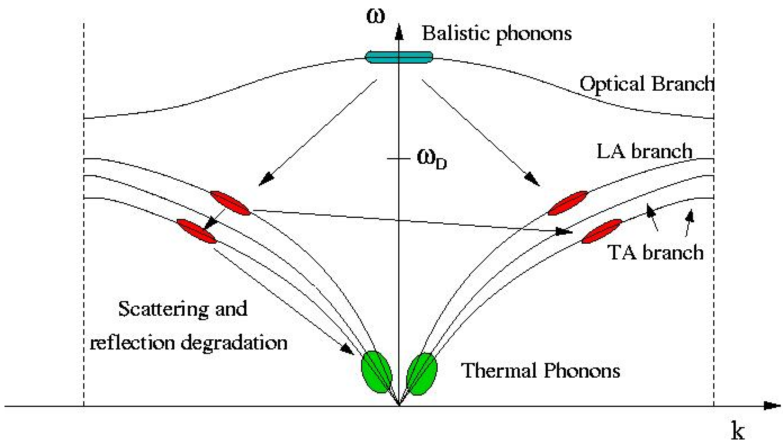

Figure 2.2: Mono-dimensional representation of the pnonon dispersion curve

The thermalization proceeds through phonon-phonon interactions, scattering on impuritues and on crystal surfaces.

The first mechanism is possible thanks to the an-harmonicity of the lattice potential, and leads also to the production of phonons in the transverse acoustic (TA) branches.

This anharmonicity becomes however less efficient as long as the energy of the phonons decreases (the rate of this decay channel is proportional to E^5), and at energies ~ 10 meV the dominant mechanism becomes the scattering on impurities.

At this stage, further conversions towards lower energies require times of the order $0.1s$.

After a certain number of decays, the mean free path becomes larger than the crystal dimensions: at this point, phonons propagate balisitically until they reach the crystal surfaces [81]: if fast sensors are used, it is in principle possible to detect athermal phonons and to determine the particle interaction point using their relative times [82].

Phonons that are not absorbed by a sensor ill be reflected by surfaces and undergo decay processes until they interact with the background thermal phonons and thermalize.

2.3 The phonon sensor

The phonon sensor is basically a device that collects phonons and generates an electric signal whose amplitude depends on the phonons' energy.

The devices which in the common practice give the best results are semiconductor thermistors (STs) and transition edge sensors (TESs): both kinds of detector rely on the temperature dependence of their resistance, which has different origin in the two cases.

Thermistors are usually characterized by their "logarithmic sensitivity" A:

$$A = \left| \frac{dlogR(T)}{dlogT} \right| \tag{2.7}$$

The typical sensitivity of a ST is in the range $1 \div 10$, while TESs have higher sensitivities, in the range $10^2 \div 10^3$.

In the following the attention will be focused on STs, since these are the sensors used in Cuoricino and CUORE experiments.

These detectors are intrinsically slow: they cannot hold signal rates higher than some Hz, and they are meinly sensitive to thermal phonons.

They consist of heavily doped semiconductor crystals with an impurity concentration slightly lower than the critical concentration N_C, for which the transition from insulator to metal occurs.

The region around this concentration is named metal-insulator transition region (MIT) [83].

If $T << 10$ K, the resistivity of such crystals exhibits a strong dependance on the temperature, since in this regime the conduction proceeds through the *hopping* or *variable range hopping* (VRH) mechanisms [84]: in both cases the electrons migrate due to quantum-mechanical tunneling through the potential barrier which separates the dopant sites.

It has been experimentally proved that the MIT can be traversed varying not only the concentration of the majoritary dopants, but also the compensation ratio (which is the ratio between the acceptor concentration N_A and the donor concentration N_D), and this is what is actually done in practice.

STs are in fact obtained exposing intrinsic semiconductor crystals to thermal neutron beams [85]: the bombarding neutrons induce nuclear reactions on the target isotopes leading to the formation of n- and p- dopants.

The compensation level can be controlled by changing the neutron flux, thus leading to different behaviour of the sensor.

For typical values ok K in the range $0.23 \div 0.41$ the resistivity depends on the temperature according to

$$\rho = \rho_0 \times e^{(\frac{T_0}{T})^\gamma} \tag{2.8}$$

where ρ_0, T_0 and γ are parameters depending on the doping and compensation levels. In particular, the value of γ is $1/4$ for thermistors operated in the VRH regime.

2.4 Detector operation

In order to obtain the best performances from semiconductor thermistors they must be properly biased: this is accomplished by means of a circuit whose working principle is sketched in figure 2.3.

The bias current I is produced by a voltage generator closed on a load resistance R_L in series with the thermistor, whose resistance R(T) is negligible in comparison to R_L.

In this condition a voltage drop $V(T) = I \cdot R(T)$ appears across the thermistor causing the dissipation of a power $P = I \cdot V$ on the same, with a consequent temperature raise.

The thermistor resistance (and consequently the voltage drop across it) decreases until the electrical power dissipated on the bolometer is equal to the thermal power absorbed from the detector by the heat bath: at this point an equilibrium is reached and the absorber temperature T_b is given by

$$T_b = T_0 + \frac{P}{G} \tag{2.9}$$

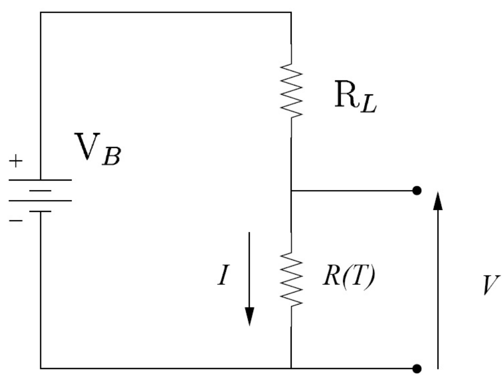

Figure 2.3: Electric scheme of the bias circuit used for the read out of a thermistor. R_L is the load resistance

where T_0 is the heat sink temperature and G
the thermal conductance to the bath.

Because of this behaviour the V-I curve deviates from linearity and leads to a non-ohmic behaviour, as can be seen from figure 2.4 (left). It the bias current is increased,the slope of the

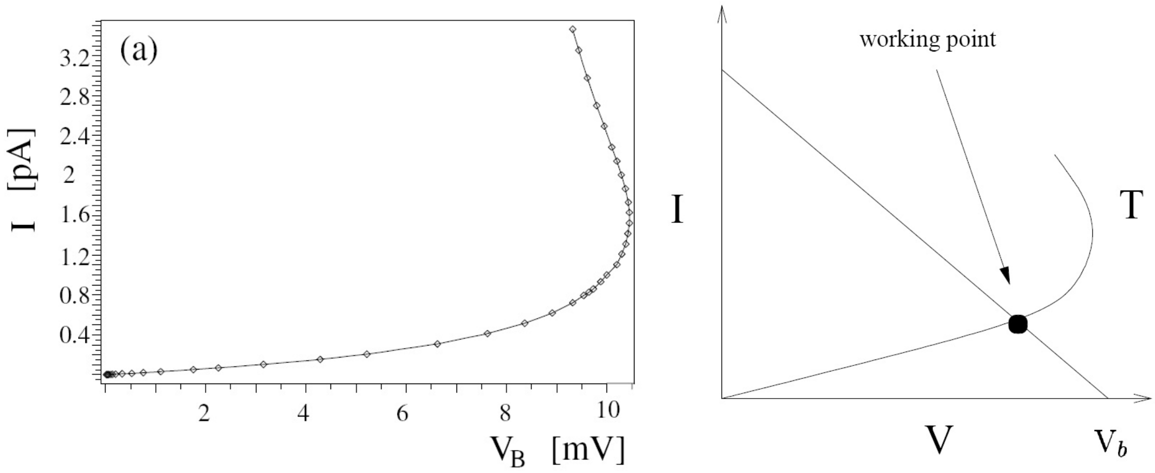

Figure 2.4: Typical load curve of a thermistor (a). The working point is the intersection of the curve with the line of equation $V = V_b - I$ (b)

I-V curve (also named "dynamic resistance" of the thermistor) raises until the so called inversion point is reached, where it becomes negative.

The I-V characteristic of a thermistor is named "load curve": in static conditions the thermistor working point is found at the intersection of the load curve with the straight line of equation $V = V_b - I$, determined by the thermistor biasing circuit.

Usually it is chosen in order to maximize the signal to noise ratio: the corresponding bias current is slightly lower than that at the inversion point.

Figure 2.5 shows some R-P load curves obtained at different temperatures: a combined fit to a set of such curves allows to determine the thermistor parameters R_O, T_0 and γ.

2.4.1 Signal amplitude

In the approximation of considering the phonon thermalization process much faster than the time taken by the bolometers to reach the temperature of the heath bath again, the relationship between the electric pulses height ΔV and the energy deposit E can be obtained as follows

$$\Delta V = I \cdot \Delta R \simeq \frac{V_B}{R + R_L} \cdot \frac{dR}{dT} \cdot \Delta T = \\ = \frac{V_B}{R + R_L} \cdot \frac{R}{T} \cdot A \cdot \Delta T \simeq \sqrt{P \cdot R} \cdot A \cdot \frac{E}{C \cdot T} \tag{2.10}$$

where A is the logarithmic sensitivity defined in eq 2.7, P is the power dissipated in the thermistor by Joule effect and R is the thermistor resistance.

The signal amplitude as a function of the thermistor working point is sketched in figure 2.6 Since the electronic noise decreases with the resistance of the thermistor, the best working

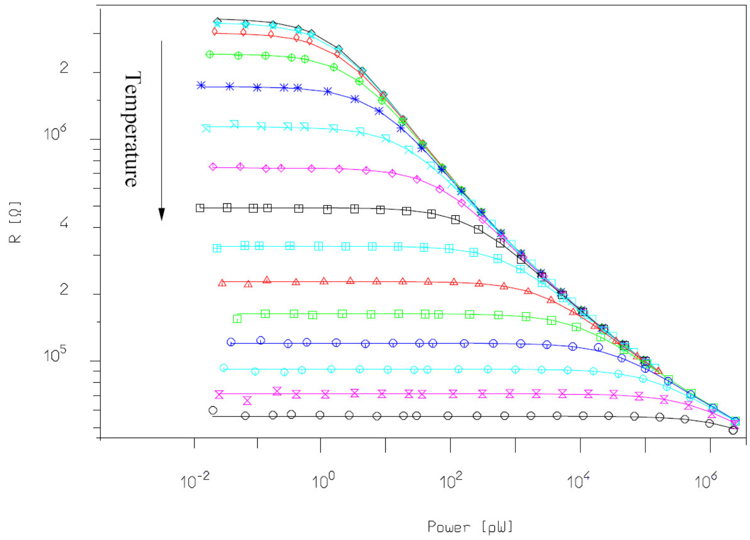

Figure 2.5: Typical R-P characteristics of a semiconductor thermistor at different base temperatures

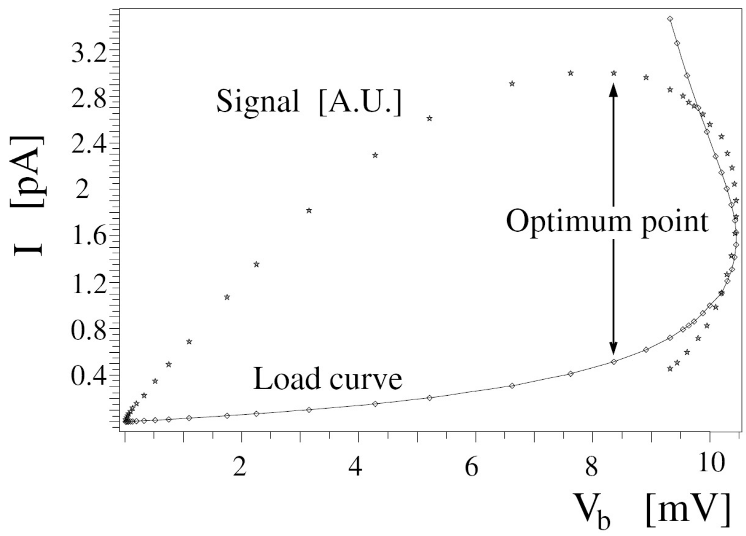

Figure 2.6: Signal amplitude as a function of the thermistor working point

point (*optimum point*) corresponds to a voltage slightly higher than the one for wich the signal amplitude is maximum.

2.5 Detector noise and energy resolution

In an experient using bolometers noise has different origins: it may be due to the physical characteristics of the absorber and of the sensor, and in this case it can't be completely eliminated, or it may depend on the details of the experimental set-up, for example it can be generated by the cryogenic, electronic and read-out systems.

These last contributions to the noise, which are in practice the main responsibles for the signal degradation, will be described in the following chapters.

In this section only the main uneliminable sources of noise will be considered: they are the thermodynamic fluctuations in the number of thermal phonons and the Jonson Noise, which is always associated to electrical resistances.

Although their contribution is negligible compared to other sources, they represent the intrinsic theoretical limit to the energy resolution.

Thermodynamic noise In case the energy deposited by particles in a bolometer undergoes complete thermalization, the intrinsic energy resolution of a bolometer is limited by the thermodinamic fluctuations int the number of thermal phonons exchanged with the heat bath.

A quantitative estimate of this effect can be obtained by the following simplified argument.

The number of phonons in the absorber at thermal equilibrium is given by

$$N = \frac{E}{\epsilon_a} = \frac{C(T) \cdot T}{k_B \cdot T} = \frac{C(T)}{k_B} \tag{2.11}$$

where $\epsilon_a = k_B \cdot T$ is the average phonon energy and E is the internal energy of the absorber.

The fluctuations of E can be estimated assuming that the number of phonons obeys Poisson statistics:

$$\Delta E = \Delta N \cdot k_B T = \sqrt{N} \cdot k_B T = \sqrt{\frac{C(T)}{k_B}} \cdot k_B T = \sqrt{k_B C(T) T^2} \tag{2.12}$$

In practice a dimensionless factor ξ must be introduced in 2.12 in order to account for details of the sensor, of the heat sink, and of the dependance of the heat capacity on the temperature:

$$\Delta E = \xi \sqrt{k_B C(T) T^2} \tag{2.13}$$

The value of ξ is of order 10 and can be lowered with a proper optimization work.

It should be stressed that according to eq (2.13) the resolution of a bolometer is independent on E: as stated in section 2.1, for 1 kg of TeO_2 working at 10 mK, the energy resolution achievable is about 10 eV.

Equation 2.13, however, doesn't take into account other sources of energy fluctuations (e. g. metastable electron-hole states, long lived non-thermal phonons), which contribute to worsen the detector energy resolution.

Johnson Noise Every resistance kept at a temperature T_b generates a white noise whose power spectrum is given by

$$e_R = \langle V^2(t) \rangle_t^{\frac{1}{2}} = \sqrt{4 k_B R T_b} \tag{2.14}$$

For a resistance of 150 MΩ working at a temperature of 10 mK the Jonson noise is $\sim 10^{-8}$ V/$\sqrt{\text{Hz}}$.

Cuoricino signal bandwidth is $\sim$ 10 Hz and the amplitude of a pulse generated by 1 MeV energy deposit is typically $\sim$ 1 mV; assuming a linear dependance of the signal amplitude on the energy, the r.m.s. contribution of the Johnson noise to the energy resolution of Cuoricino can be naively estimated as follows:

$$\Delta E \simeq \frac{dE}{dV} \cdot \Delta V = \frac{dE}{dV} \cdot e_R \cdot \sqrt{B} \simeq 10^9 \cdot 10^{-8} \cdot \sqrt{10}\ \text{eV} \simeq 30\ \text{eV} \tag{2.15}$$

The thermistors biasing circuit, and in particular the load resistance R_L, is usually kept at a different temperature T_L (usually at room temperature) from T_b, the operating temperature of the bolometer: the Jonhson noise due of the load resistor has therefore to be taken into account.

With reference to figure 2.3, the r.m.s. contribution of the load resistor to the detector's noise is given by:

$$e_{det} = \frac{e_L \cdot R}{R_L + R} \simeq \frac{e_L \cdot R}{R_L} \tag{2.16}$$

where e_L is the Johnson noise of the load resistors, which in turns is equal to:

$$e_L = \sqrt{4k_B R_L T_L} = \frac{\sqrt{T_L \cdot R_L}}{\sqrt{T_R \cdot R}} e_R. \tag{2.17}$$

The contribution e_{det} of the load resistor to the detector's noise can be therefore written as

$$e_{det} = \sqrt{\frac{T_L \cdot R}{T_R \cdot R_L}}. \tag{2.18}$$

Equation 2.18 shows that e_{det} can be arbitrarily reduced choosing a high load resistance R_L.

Chapter 3

Cuoricino experiment

"Torni indietro, signor Don Chisciotte, torni indietro per Dio!
Son montoni e pecore![..] La ci guardi bene: non c'è né giganti, né cavalieri
né gatti, né armature, né scudi squartati, né interi, né coppe azzurre, né diavoli!"
Miguel de Cervantes

Introduction

The use of bolometers as $0\nu\beta\beta$ detectors has been first suggested by Fiorini [86] in 1984: under his guidance $^{130}TeO_2$ bolometric detectors of increasing mass have been developed by the Milano group ever since.

Cuoricino is the last step of this process: with its total mass of 40.7 kg it is the the largest cryogenic detector operated so far.

Run in Laboratori Nazionali del Gran Sasso since 2003, it has set to $1.86 \cdot 10^{24}$ y the presently upper limit for the lifetime of $^{130}TeO_2$ against $0\nu\beta\beta$.

Its five years sensitivity (at 68 % CL) of about $9 \cdot 10^{24}$ y will allow it to test Majorana masses in the 100-700 meV range, where an evidence for $0\nu\beta\beta$ has been claimed by Klapdor-Kreingrothaus [45].

Furthermore Cuoricino has been a unique test bench for the next generation experiment CUORE: its good results and performances have demonstrated the feasibility of a large bolometric array of TeO_2 crystals in a tower-like structure, hightlighting at the same time possible problems and enabling the collaboration to face them timely.

3.1 The energy absorber: the choice of ^{130}Te

One of the main advantages of the bolometric approach over conventional semiconductor detectors is the freedom in the choice of the candidate $0\nu\beta\beta$ isotope this technique leaves: any $\beta\beta$ emitter can be used provided it can be reduced to a crystalline phase.
This fact is of fundamental importance for $0\nu\beta\beta$ decay search in general.
$\beta\beta$ experiments, in fact, usually provide little information beyond just the electron energy measurement: in case of discovery, additional information may be required to demonstrate, for instance, that an observed peak is actually due to $0\nu\beta\beta$ decay and not to some unknown radioactivity.
Although there is some uncertainty associated with the nuclear matrix elements, it is not so large that a comparison of measured rates in two different isotopes could not be used to prove the consistency with the Majorana-neutrino hypothesis.
Among the possible $0\nu\beta\beta$ emitters ^{130}Te has been chosen for Cuoricino and CUORE.
The decay searched in Cuoricino is

$$^{130}\mathrm{Te} \longrightarrow {}^{130}\mathrm{Xe} + 2e^{-} + 2\overline{\nu}_e \tag{3.1}$$

The reasons of the choice are the following:

- ^{130}Te has a high **natural isotopic abundance** equal to 33.8 %. This means that a reasonable number of ^{130}Te atoms are present in natural tellurium even without expensive enrichment procedures.
- The **transition energy Q** of $\beta\beta$ decay in tellurium, whose value is (2530.30 ± 1.99) keV, is rather high. Since the phase space for the decay is proportional to Q, an higher Q values means an higher probability for the decay. Moreover, ^{130}Te Q-value is in an energy window characterized by low natural radioactivity, being located between the full energy and the Compton edge of the 2615 photon peak of ^{208}Tl, and out of the background due to ^{248}U.
- The favourable theoretic calculation of the **nuclear matrix element** involved in the decay. Table 3.1 shows the calculated matrix elements for $0\nu\beta\beta$ of the various candidate isotopes. The values are model dependent, and the differences between results obtained with different models are large. Nevertheless it can be observed that the theoretic value for ^{130}Te is compatible with the higher ones.

In figure 3.1 the main properties of the candidate nuclei are compared. Both Cuoricino and CUORE exploit TeO_2 crystals as energy absorbers, since pure tellurium, which would have been the straightforward solution, has poor mechanical properties.
TeO_2 crystals, on the contrary, besides having excellent mechanical properties, have a higher Debye temperature with respect to pure Te: this implies a lower specific heat, hence higher pulses. Furthermore, their content in Te amounts to 80% of their mass.
Before Cuoricino, the Milano group preformed other bolometric experiments testing different sizes of TeO_2 crystals: 73 g crystals, 334 g crystals, 340 g crystals and, at last, the 790 g crystals used in Cuoricino and CUORE.
The features of the signals obtained from different size detectors were similar, and this indicates that the increase in size doesn't affect the detector's performances.

3.2 The experimental set-up

Cuoricino [87] is a tower made by 13 planes containing 62 crystals of TeO_2. 44 of them are cubes of 5 cm side while the dimension of the others is $3 \times 3 \times 6$ cm^3. Small crystals are mounted

Ref	method	$M^{0\nu}$								
		^{76}Ge	^{82}Se	^{96}Zr	^{100}Mo	^{116}Cd	^{128}Te	^{130}Te	^{136}Xe	^{150}Nd
EVZ-88	QRPA	3.0	2.3	1.9	3.5		4.0	3.5	1.6	
MBK-89	QRPA	2.84	2.65		1.69		2.91	2.36	1.08	4,17
T-91	QRPA	2.86	2.59		3.14		2.55	2.22	1.27	3.47
SKF-91	QRPA	3.37	2.72				3.17	2.94	1.71	
PSVF-99	RQRPA	4.05	3.82	2.24	4.58	2.86	3.38	2.87	1.20	5.15
SK-01	QRPA	4.45	5.60	4.16	5.37	3.99	4.84	4.73	1.69	
AS-98	QRPA	4.85	3.61	3.70		3.97		3.81	2.15	
CS-03	QRPA	3.33	3.44	3.55	2.97	3.75		3.49	4.64	

Table 3.1: Nuclear matrix elements obtained from calculations performed by different groups. All the results reported have been obtained assuming the weak axial-vector coupling g_A equal to 1. EVZ-88 = Engel, Vogel, Zirnbauer; MBK-89 = Muto, Bender, Klapdor; T-91 = Tomoda; SKF-91 = Suhonen, Khadkikar, Faessler; PSVF-91 = Pantis, Simkovic, Vergados, Faessler; AS-98 = Aunola, Suhonen; SPVF-96 = Simkovic, Pantis, Vergados, Faessler; SK-01 = Stoica, Klapdor; CS-03 = Civitarese, Suhonen

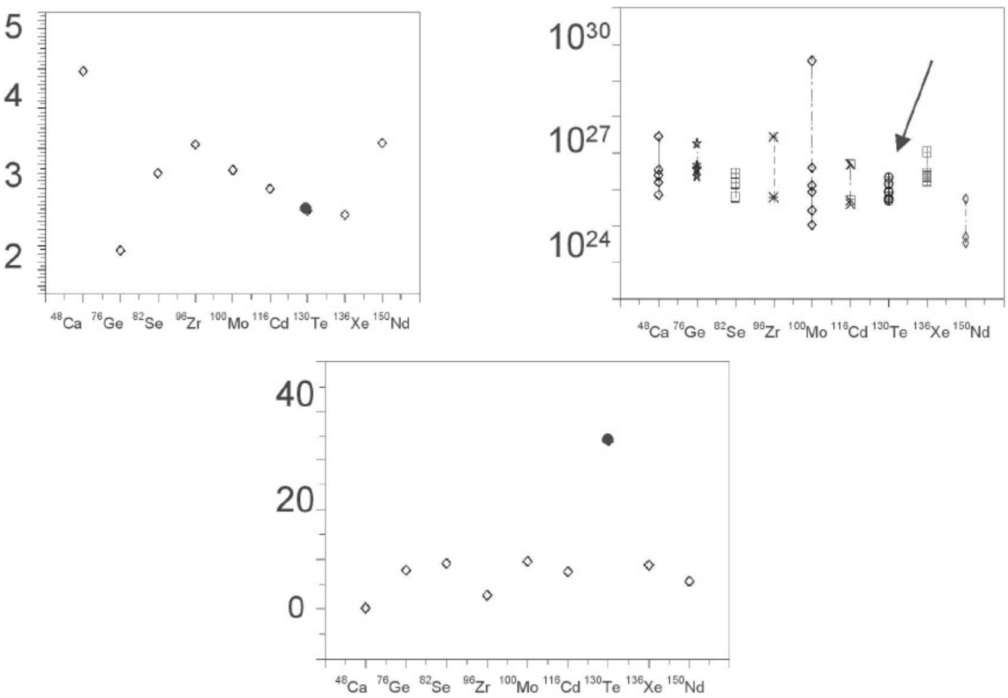

Figure 3.1: Comparison between the transition energy (a), the halflife for $0\nu\beta\beta$ (b) and the natural isotopic abundances for the $0\nu\beta\beta$ candidates

in 9 crystals modules, while the big ones are arranged in 9 crystals modules. All crystals are made with natural tellurite, apart two $3 \times 3 \times 6$ cm^3 crystals which are enriched in ^{128}Te and two others enriched in ^{130}Te with isotopic abundance of 82.3 % and 75 %, respectively.

The total mass of Cuoricino is 40.7 kg.

Great care was devoted to selection and cleaning of the materials used for the construction of the CUORICINO array.

Cuoricino crystals were grown from pre-tested low radioactivity materials by the Shangay Instituts of Ceramics in China and shipped to Italy where they were surface treated with specially selected low contamination powders.

The mechanical structure of the array was made exclusively in OFHC copper and in teflon, both previously measured to verify the extremely low radioactive content. All the copper and teflon parts of the mounting structure were separately treated with acids to remove any possible surface contamination. The array was assembled in an underground clean room in a N_2 atmosphere to avoid Rn contamination.

The tower is mounted in a diluition refregerator which maintain a temperature of about 10 mK.

In order to shield against the radioactive contaminants from the materials of the refrigerator, a 10 cm layer of Roman lead with a ^{210}Pb activity of less than 4 mBq/kg is inserted inside the cryostat immediately above the Cuoricino tower. A 1.2 cm lateral layer of the same lead is framed around the array to reduce the activity of the thermal shields.

The cryostat is externally shielded by two layers of Lead of 10 cm minimal thickness each. While the outer is made by common Lead, the inner one has a ^{210}Pb activity of (16 ± 4) Bq/kg. An additional layer of 2 cm of electrolytic Copper is provided by the cryostat thermal shields. The background due to environmental neutrons is reduced by a layer of Borated Polyethylene of 10 cm minimum thickness.

The refrigerator operates inside a Plexiglass anti-radon box flushed with clean N_2 and inside a Faraday cage to reduce electromagnetic interferences.

In order to prevent vibrations from the overall facility to reach the detectors the tower is mechanically decoupled from the cryostat through a steel spring.

Cuoricino structure is shown in figure 3.2.

3.2.1 The sensor

Thermal pulses are recorded by means of Neutron Transmutation Doped (NTD) Ge thermistors operated in the Variable Range Hopping (VRH) conduction regime.

NTD thermistors for Cuoricinoare developed and produced at the Lawrence Berkeley National Laboratory (LBNL) and UC Berkeley Department of Material Science [85].

The resistance behavior of these devices as a function of T follows the relation:

$$R = R_0 e^{(\frac{T}{T_0})^\gamma} \qquad \gamma = 1/2 \tag{3.2}$$

The VRH regime occurs in Ge when the concentration of dopants is close to the Metal to Insulator Transition, which is $6 \cdot 10^7$ atoms /cm^3.

This is achieved by exposing a Ge sample to thermal neutron radiation in a nuclear reactor. Even if other simpler Ge doping methods exist (i.e. melt doping), they usually cannot achieve the necessary uniformity and the only technique available for producing such uniform doping is NTD.

In typical applications, the neutron absorption probability for a 3 mm thick wafer of Ge is small, on the order of 3 %, leading to a very homogenous, uniform absorption process.

When a Ge sample is irradiated with neutrons, the following processes occurr

$$\begin{array}{l} ^{70}\mathrm{Ge}(21\%) + n \longrightarrow ^{71}\mathrm{Ge}\ (\sigma_T = (3.43 \pm 0.17)\,\mathrm{b}, \quad \sigma_R = (1.5 \pm 0.17)\,\mathrm{b}) \\ ^{71}\mathrm{Ge} \longrightarrow ^{71} Ga\ (t_{1/2} = 11.4\ \mathrm{day}) \qquad \mathrm{Acceptor} \end{array} \tag{3.3}$$

$$\begin{array}{l} ^{74}\mathrm{Ge}(36\%) + n \longrightarrow ^{75}\mathrm{Ge}\ (\sigma_T = (0.51 \pm 0.08)\,\mathrm{b}, \quad \sigma_R = (1.0 \pm 0.2)\,\mathrm{b}) \\ ^{75}\mathrm{Ge} \longrightarrow ^{75}\mathrm{As}\ (t_{1/2} = 83\ \mathrm{min}) \qquad \mathrm{Donor} \end{array} \tag{3.4}$$

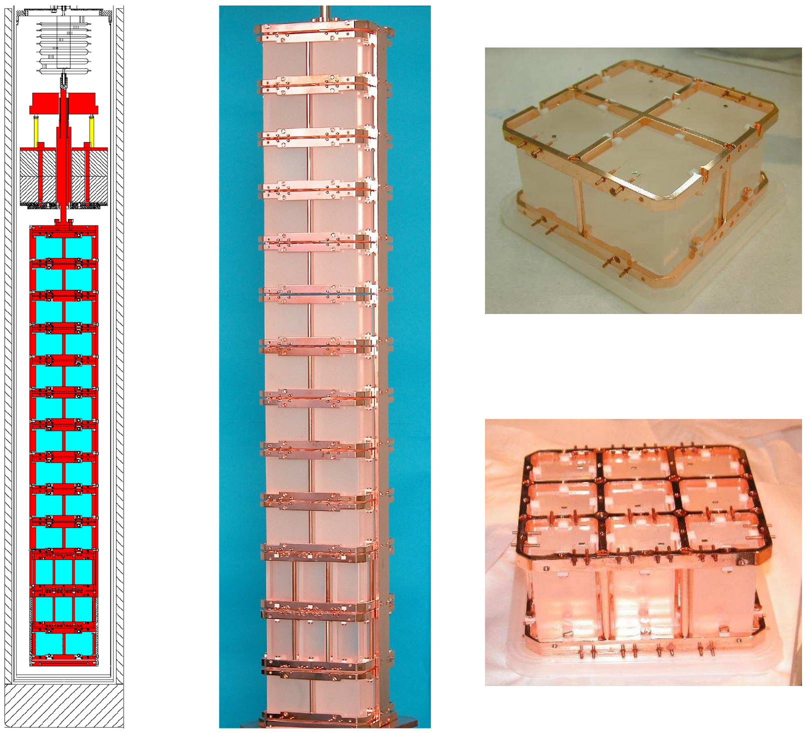

Figure 3.2: Cuoricino detector: scheme of the tower and of the internal Roman lead shield (left panel), the tower (center panel), the 4 crystals module (top right) and the 9 crystal module (bottom right).

$$\begin{array}{l} {}^{76}\mathrm{Ge}(7.4\%) + n \longrightarrow^{77} \mathrm{Ge}\ (\sigma_T = (0.16 \pm 0.014)\,\mathrm{b}, \quad \sigma_R = (2.0 \pm 0.35)\,\mathrm{b}) \\ {}^{77}\mathrm{Ge} \longrightarrow^{77} \mathrm{Se}\ (t_{1/2} = 38.8\,\mathrm{h}) \qquad \text{Double donor} \end{array} \tag{3.5}$$

where σ_T and σ_R are the thermal and epithermal neutron capture cross sections, respectively.

Placing a Ge sample in a nuclear reactor it is therefore possible to produce a significant concentration of both acceptors (Ga) and donors (As and Se).

Since the doping level of the Ge needs to be on the order of 1×10^{17} atoms/cm^3, a very high flux reactor is necessary to do the doping in a reasonable time.

Even more important is the stability of the neutron flux and the energy distribution. In addition, a minimal fast ($>$5 MeV) flux is necessary to eliminate contaminants such as ^{3}H, ^{65}Zn, and ^{68}Ge produced by fast neutrons. These radioactive contaminants degrade the detector operation because of internal radioactive decay and therefore increased background.

The significant quantity involved in thermistor performance is the net dopant concentration which is equal to the concentration of Ga atoms minus the concentration of As atoms minus twice the concentration of Se atoms.

Unfortunately, to measure the thermal performance of the thermistor, one needs to wait for the decay of the activation product ^{71}Ge (11.4 day), which requires approximately one year.

Previous measurements carried out in the Gran Sasso Laboratory [88] have shown that the residual acrtivity of the NTD thermistors becomes fully tolerable in an experiment with thermal detectors already a few months after irradiation.

Once this time has elapsed, the NTD germanium samples are heat treated to repair the crystal structure and then cut into $3 \times 3 \times 1$ mm strips. The thermistors then need to be characterized at low temperatures, following the procedure described in section 2.4.

3.2.2 The single module

The thermistors are glued to the TeO_2 crystal by 9 spots of Araldit rapid, Ciba Geigy (now Novartis) epoxy, of 0.4 to 0.7 mm deposited on the crystal surface by an array of pins: the height of each spot is 50 μm. This procedure was found to be reasonably reliable and reproducible in theMiDBD experiment [89].

The heat conductance of the epoxy spots was measured in Milan and the phenomenological relation was found to be $\sim 2.6 \times 10^{-4}$ $(T[K])^3$ watts per degree kelvin per spot.

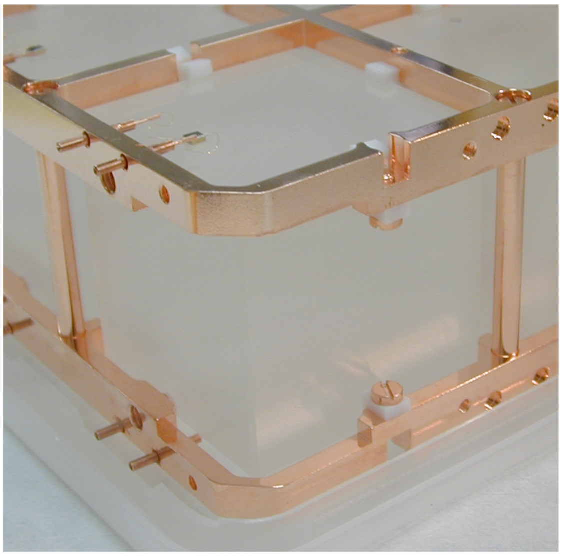

Figure 3.3: Picture of a single cuoricino detector

As explained in section 3.3, the stabilization of the response of bolometers is crucial because of the unavoidable small variations in the temperature of the heat bath that change the detector gain, and consequently deteriorates the energy resolution.

This problem is successfully addressed by means of a Joule heater glued on to each crystal. The heater is used to inject a uniform energy in the crystal and the thermal gain is monitored and corrected off-line.

The heaters are Si chips with a heavily doped meander structure with a constant resistance between 50 to 100 kΩ.

They are manufactured by the ITC - IRST company in Trento, Italy. Electrical connections are made with two 50 μm diameter gold wires, ball bonded to metalized surfaces on the thermistor. The gold wires are crimped into a copper tube, which is inserted into a larger one forming the electrical connection, and avoiding low temperature solder which contains ^{210}Pb and traces of other radioisotopes.

The larger copper tube, $\sim$ 14 mm long and 2 mm in diameter, is glued to the copper frame that supports the crystals. This tube is thermally connected to the frame but electrically insulated.

The mounting of the TeO_2 crystals is crucial to detector performance, and must fulfill a number of sometimes contradictory criteria:

1. the crystals must be rigidly secured to the frame to prevent power dissipation by friction caused by unavoidable vibrations, that can prevent the crystal from reaching the required temperature and can produce low frequency noise;

2. the thermal conductance to the heat sink (copper frame) must be low enough to delay the re-cooling of the crystal, following a heat pulse, such that the pulse decay time (re-cooling time) is much longer than the rise time;

3. however, the heat conductancemust be high enough to guarantee efficient cooling;

4. the frame must compensate for the differences in thermal expansion coefficients of the various materials used;

5. and finally, only materials selected for low radioactivity can be used.

For CUORE, only two materials will be used, copper and PTFE; they can both be obtained with very low levels of radioactivity. Copper has a thermal conductivity and specific heat high enough to be an ideal heat bath, and has excellent mechanical properties; it machines well, and has excellent tensil, tortional and compressional strengths. PTFE is used between the copper frame and the crystals.

It has low heat conductance and low heat leak [90] and it compensates for the differences between coefficients of thermal expansion of copper and of TeO_2 .

A picture of a single cuoricino detector is shown in figure 3.3.

3.2.3 The cryogenic set-up

Cuoricino tower is hosted in a cryostat installed in Hall A at LNGS. The cryogenic setup consists of a dilution refrigerator having a power of 1000 μW at 100 mK.

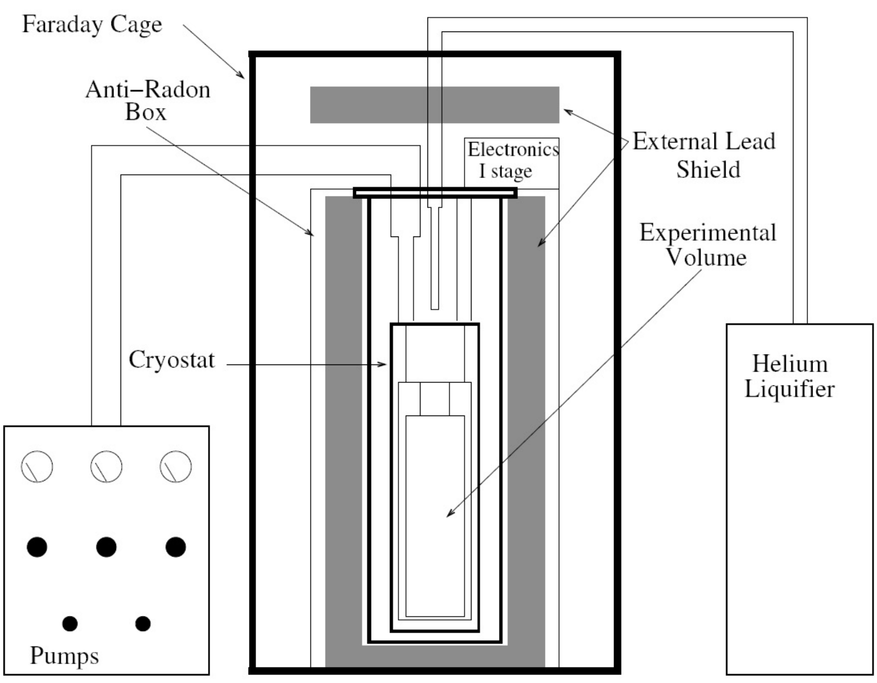

Figure 3.4: Schematic drawing of cuoricino cryostat

A second diluition refrigerator, with a cooling power of 200 μW at 100 mK, is installed in hall C and it has been dedicated to the research and development activities for Cuoricino and CUORE.

Both cryostats are housed inside Faraday cages to suppress electromagnetic interference. A much larger experimental volume is available in the Hall A cryogenic setup.

All the materials used for construction of Cuoricino were analysed to determine their radioactive contamination levels; these measurements were carried out by means of two large Ge detectors installed in the Gran Sasso underground Low Radioactivity Laboratory. The level of the radon contamination in the air of the Laboratory is continuously monitored.

Both dilution refrigerators are equipped with heavy shields against environmental radioactivity. In particular, the Hall A dilution refrigerator is shielded with two layers of lead of 10 cm minimum thickness each, a PTFE neutron shield, and is flushed with nitrogen from a dedicated evaporator to avoid radon contamination of the gas close to the cryostat, as mentioned in section 3.2.

A schematic drawing of Cuoricino cryogenic system is sketched in figure 3.4

3.2.4 The readout system: electronics and data acquisition

Electronics

Any energy release in Cuoricino bololometers can be seen as a voltage pulse across the thermistors glued on the crystals.

These pulses are rare (the background rate at the $0\nu\beta\beta$ transition is of (0.17 ± 0.02) c/keV/kg/year) and slow (the signal bandwith spans up to few tens of Hz): their typcal amplitude is $\sim 150\ \mu$V.

Therefore, great care must be taken in order to avoid every possible source of noise across each step of the electronic chain, whose main tasks are basically two: the amplification of the signal and its digitalization.

More in detail, the operations performed on the signal before its digitalization are the following:

- **thermistor biasing**
- **signal amplification**
- **triggering**
- **signal filtering**

The circuitry for the **biasing of thermistors** is located on the so called front-end main boards (MB) which also host the two amplification stages, while triggering and filtering is performed on separate dedicated boards.

the thermistor is symmetrically biased by means of 2 load resistors R_L as shown in figure 3.5: in this way a differential signal is read, thus avoiding common noise.

The value of R_L must be greater than the thermistor impedance at the working temperature in order to maintain the current bias constant even in presence of signals. The value of the dynamic resistance of the thermistors at $T \simeq 10$ mK is about 100 MΩ; the load resistors are then chosen with values of the order of GΩ.

The **amplification stage** consists of a first differential voltage sensitive preamplifier, with gain G = 218, and a programmable gain amplifier [91, 92, 93].

The gain of the whole amplification chain can be set to values in the range 440-10000 V/V, according to the settings of the programmable amplifier.

The front-end boards of all $3 \times 3 \times 6$ cm^3 detectors and of 20 of the 44 detectors of $5 \times 5 \times 5$ cm^3 are located at room temperature.

The differential configuration has been adopted to minimize signal cross talk and microphonic noise coming from the wires connecting the thermistors to the front-end board.

With this purpose a second configuration of the front-end electronics has been realized, (the so called "cold electronics") in which the first stage of amplification os operated at low temperature, closer to the thermistors.

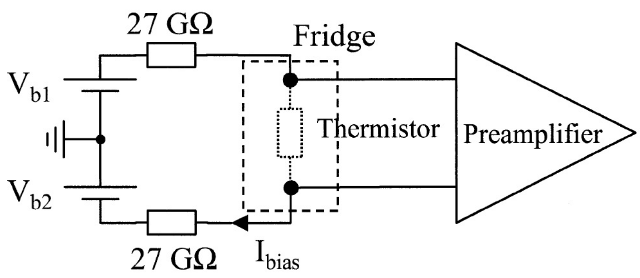

Figure 3.5: Schematic of the thermistor biasing system

In this set-up the box housing the preamplifier is in fact attached to the 4.2 K plate of the diluition refrigerator, next to the detectors.

The buffer stage is then warmed in order to reach the optimum temperature for Silicon, around 110 K.

The connection between the thermistors and the first stage of the electronics is via a twisted pair of 1 m in lenght, whereas in the standard warm preamplifier configuration this length is 5 m.

The main reason for having two different kinds of readout is to assess the effect of the microphonic noise on the connecting wires on the detector energy resolution at low energy.

The purpose is to achieve the best sensitivity at threshold, in the energy region relevant for WIMPS searches (see chapter 6).

Since other factors dominate the detector resolution at higher energies, an equivalent performance is expected there for the two set-ups.

The cold electronics has been adopted for 24 of the $5 \times 5 \times 5$ cm^3 detectors.

Regardless of the configuration considered, precautions have been taken to suppress any possible effect coming from room temperature drift [91] and main power supply instability [94].

All the necessary settings for the front-end and the biasing system are programmed remotely via computer, to allow the optimization of the overall dynamic performance separately for each detector [92].

After the second amplification stage the signal is feeded to the filter boards, which are encharged of **filtering and triggering** operations: here the signals are filtered by active 6 poles Bessel low-pass filters (roll-off of 120 dB/decade) with a programmable frequency cutoff, in order to avoid aliasing in the following digitalization of the pulse shapes.

After this stage each signal is split in two copies: the former is further filtered and amplified and it is AC coupled to the input of the trigger stage, while the latter is DC coupled to the input stage of the **digitizing boards**.

The reason for reading DC voltage levels can be understood considering equation 2.10, reported below for convenience

$$\Delta V \simeq \sqrt{P \cdot R} \cdot A \cdot \frac{E}{C \cdot T}$$

It can be seen that Cuoricino pulses height not only depends on the energy release in the absorber, but also on the base temperature of the bolometer.

Possible changes in the base temperature of the thermistor can thus influence pulses height, and must therefore be identified; this is done in Cuoricino by recording the steady state voltage drop across the thermistors (often referred to as "baseline"), which depends on the base temperature of the bolometer due to the temperature dependance of the thermistors resintance (eq. 2.8).

The details of the method used to correct CUORE pulses heights for temperature variations are given in section 3.3.1.

Noise considerations. The above described analog front-end electronics produces a noise of the order 50 nV (FWHM) referred to its inputs, over the $\sim$ 10 Hz bandwidth of the signal [95].

The 54 GΩ load resistors produce 80 nV in the same bandwidth, so that the resulting noise is $\sim$ 100 nV (FWHM), therefore considerably lower than the 1.0 μV FWHM level observed for the best performing bolometers and mostly due to vibrations induced microphonism.

Data Acquisition

Cuoricino signals are acquired by commercial digitizing boards, exploiting 16 bits ADCs.

The range of the input signals is 0 - +10 V thus meaning a resolution of 10 $V/2^{16} = 0.15\ mV$ on the amplitude of the sampled signals.

As explained above, CUORE trigger cards output one signal for each channel, explicitly shaped to be used as input for a threshold discriminator in order to generate a trigger: if the pulse amplitude is higher than the trigger threshold (that is indipendently set for each detector) the signal is digitalized and transmitted to a PC-VXI encharged of data storage.

At present, however, a software trigger is being tested in Cuoricino with good results: each signal is continuously sampled and acquired and the task to identify the pulses is demanded to a software algorythm.

The acquired signal is properly shaped by a software filter consisting of both a differentiating and an integrating stages and a trigger is generated if the signal exceeds the threshold for a time longer than a fixed amount.

After a trigger, the signal of the fired channel is retrieved in a time window of $\sim 5\ s$ around the trigger itself.

The pulses selected in this way are collected and written to disk in the form of binary files.

3.3 The analysis procedure

The purpose of the analysis procedure is to extract the relevant physical information from the raw data acquired, and this is performed in two steps:

- within the so called **first level** analysis procedure the sigle hits are identified in the the collected arrays of ADC samples, and a reliable estimate of their energy is obtained.
- within the **second level** analysis stage the pulse energies are used to extract the physical information relevant for the scientific objectives of Cuoricino detector.

  The details of this second analysis step depends on the physical process under investigation: the procedure adopted in the search for $0\nu\beta\beta$ decay is reported in chapter 4.

Cuoricino data analysis is performed completely offline: the collected data are processed after they have been wrote on disk and they are not analyzed during data acquisition.

Since the second level analysis techniques depend on the processes searched for, this section will only deal with some of the technicalities concerning Cuoricino first level analysis.

3.3.1 First level analysis

When the output voltage of one detector exceeds the trigger threshold, the acquisition system records a number of signal samples. The acquired time window (few seconds) must fully contain the pulse development in order to allow an accurate description of its waveform.

The existence of a pre-trigger interval just prior to the production of the pulse ("baseline") guarantees that a small fraction of the number of acquired samples can be used to measure the DC level of the detector (which can be directly correlated to the detector temperature).

The fact that for each trigger an entire waveform is sampled and recorded implies that off-line analysis must take care of a large body of data.

This effort is justified because of the useful information that can be extracted from the signal waveform.

The following are important goals for the (first-level or pulse) analysis (FLA):

1. maximization of the **signal to noise ratio** for the best estimate of the pulse amplitude. This is accomplished by means of the optimum filter (OF) technique [96];

2. correction of the effects of **system instabilities** that change the response function of the detectors (gain "stabilization");

3. rejection of the **spurious triggered pulses** by means of pulse shape analysis;

4. **energy calibration** of the detector

5. identification and rejection of **radioactive background pulses** by means of coincidence analysis.

The **OF technique** is frequently used with bolometers to evaluate the amplitude of a signal superimposed on stochastic noise. This algorithm has proven to provide the best estimate of the pulse amplitude under general conditions.

Relative to a simple maximum - minimum algorithm, this technique allows the evaluation of the signal amplitude with much higher efficiency resulting in an effective improvement of the detector energy resolution.

The following information is needed to implement the OF technique: the detector response function (i.e. the shape of the signal in a zero noise condition) and the noise power spectrum.

Once these are known, the OF transfer function is easily obtained and used as a digital filter for the acquired pulses.

The role of the OF transfer function is to weight the frequency components of the signal in order to suppress those frequencies that are highly influenced by noise.

The amplitude of the pulse is then evaluated using optimally filtered pulses.

Effective pulse-shape parameters can be deduced from the comparison of the filtered pulses with the filtered response function (e.g. rms difference after proper time synchronization).

In processing the data off-line, the following parameters are evaluated and recorded to disk for each digitized pulse:

1. the channel number i.e., the number of ADC channel that exceeded the trigger threshold;

2. the absolute time at which the pulse occurred with a precision of 0.1 msec;

3. the OF amplitude i.e. the amplitude of the optimally filtered signals

4. the baseline, obtained by averaging a proper number of points from the pre-trigger interval. Since the detectors are DC coupled, it provides a direct measurement of the detector temperature at the creation of the signal;

5. the signal rise and signal decay times;

6. the pulse shape parameters, obtained by comparing the acquired pulse with the expected response function of the bolometer after OF or adaptive filters. A further powerful technique is based on the use of artificial neural networks (ANN);

7. 7. the pile-up fraction. Pile-up is usually efficiently rejected by pulse-shape analysis even if this technique can't identify the rejected pile-up events. In order to improve the pile-up rejection and quantitatively evaluate its rate (e.g. for short-time coincidence analysis), the Wiener-filter algorithm is implemented [97].

The next analysis step is the **gain instability correction**. The OF amplitudes are corrected to reduce or cancel the effects of system instabilities responsible for the variation of the ratio between the energy E deposited into a given crystal and the amplitude ΔV of the corresponding electrical pulse.

According to equation 2.10, there are three instabilities that can modify the ratio $\Delta V_o/E$ (where $V_o = V \cdot G$ is the output voltage given by the product of the bolometer voltage V and the electronics gain G):

1. a variation in the electronic gain G

2. a variation in the bias V_B

3. a variation in the temperature T of the crystal.

The electronic system is designed to guarantee a stability of G and V_B within 0.1% .

It is however, much more difficult to maintain stability within 0.1% of the detector temperature on long time scales. At a temperature of 10 mK this would require maintaining the temperature of 1000 crystals to an accuracy of 10 μK for a period of several days.

To overcome this problem, and as already mentioned in section 3.2.2, a silicon resistor glued to each crystal is used as a heater to produce a reference pulse in the detector.

It is connected to a high precision programmable pulser that produces a fast voltage pulse every few minutes dissipating the same amount of energy (E_{ref}) into the crystal each time.

These voltage pulses mimic pulses produced in the crystal by particle interactions and are used to measure the value of the ratio $\Delta V/E$. Any variation of the amplitude of the reference pulse is due to variations of the $\Delta V/E$ ratio.

The OF amplitude of the reference pulse is therefore used to measure, every few minutes, the actual value of $\Delta V/E$ while the baseline of the reference pulse provides the contemporary measurement of the value of T.

A fit is then used to obtain the values of $\Delta V/E$ as a function of temperature.

Therefore, in this step of the off-line analysis, the OF amplitude of each pulse is corrected according to the given value of $\Delta V/E[T(t)]$ for the detector temperature at which the pulse has been generated.

The effectiveness of this technique has been proven in the MiDBD experiment, a previous experiment performed by the Milano group of Cuoricino collaboration, where a typical temperature fluctuation over a day ranged from a few tenths to about 100 μK .

After correction, these fluctuations were reduced to less than 1 μK [98] (fig. 3.6).

Pulse shape analysis is very useful in rejecting spurious signals produced by microphonics and electronic noise.

A confidence level is determined for each pulse shape parameter and for the rise and decay time of each pulse.

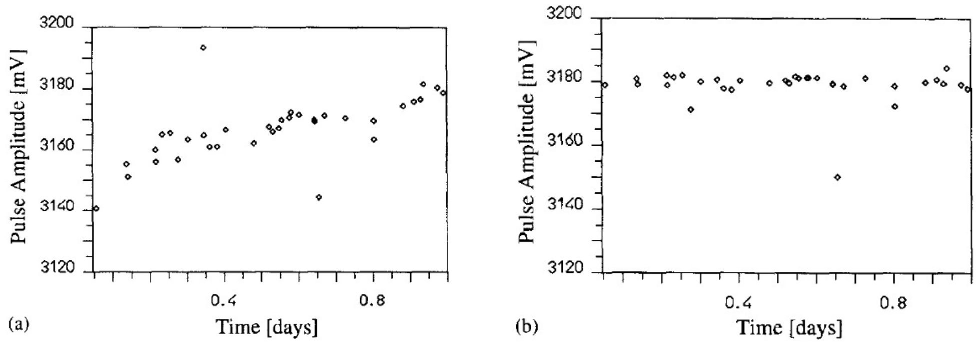

Figure 3.6: Time behaviour of the pulse amplitude before (a) and after (b) correction

Signals falling within these intervals are defined as physical pulses, while signals having one or more of their parameters outside of the relevant interval are rejected as noise.

The use of more than one pulse shape parameter results in better reliability of the rejection technique.

The linearization of the detector response is critically important for energy calibration.

The final step in data processing is the conversion of the OF amplitudes into energy values.

The naive bolometer model previously used assumes linearity; several parameters depend however on the crystal temperature, rendering the corresponding equation non-linear. Accordingly, the relation between ΔV and E are obtained periodically by the use of radioactive calibration sources.

A routine energy calibration is performed before and after each subset of runs, which lasts about two weeks, by exposing the array to two thoriated tungsten wires inserted in immediate contact with the refrigerator.

All runs where the average difference between the initial and final calibration is larger than the experimental error in the evaluation of the peak position are discarded.

The ratio $\Delta V/E$ are measured for several gamma lines, and the data will be fit to the model previously described, but taking into consideration the fact that the bolometer resistance and the crystal heat capacity are temperature dependent.

This provides the **calibration function** of E as a function of ΔV, which is then used to convert the OF amplitudes into energy values.

Finally, the close packed array of the crystals allows the **rejection of events** that left energy in more than one single crystal.

This is particularly useful in rejecting a very high energy gamma rays that enters from outside of the array. The small angle Compton scattering in a single crystal can mimic a double beta decay event, a dark matter scattering, or a solar axion, but the probability that this photon would escape the rest of the array without a second interaction is small.

In addition, background events from radioactivity within the structure of the array also have a significant probability of depositing energy in more than one crystal, and this is also true for high and intermediate energy neutrons.

In the final stage of off-line analysis these coincidence events can be identified from the data which will contain the detector number, signal time, pulse energy, and pile-up parameter.

Chapter 4

Cuoricino background and $0\nu\beta\beta$ results

"Worthy of my undying regard"
Joseph Conrad

Introduction

Cuoricino detector is running at Gran Sasso National Laboratories since the beginning of 2003.

Up to now, with its 40.7 kg of TeO_2, it collected a total statistics of 5.87 kg $^{130}Te \cdot y$: this leads to a limit for the halflife of ^{130}Te for $0\nu\beta\beta$ of $2 \cdot 10^{24}$ y.

Given the rareness of the searched decay, the reduction and control of any possible source of background is of fundamental importance for the success of the experiment: spurious counts can in fact obscure the signal counts of interest.

This requires both a great effort during the construction and assembly phase (see section 3.2), and a deep understanding of all the possible contributions to the background, essential in order to implement rejection techniques at the data analysis stage.

In this chapter Cuoricino background will be described, with particular attention to the energy region interesting for neutrinoless double beta decay, and the result obtained for the halflife of ^{130}Te against $0\nu\beta\beta$ will be discussed in detail.

In particular the so called second level analysis procedure will be presented here (see section 3.3.1 for a description of the first level analysis techniques).

The analysis of data in the energy region below 500 keV will be presented in chapter 6.

4.1 Background sources for Cuoricino experiment

The background sources dangerous for Cuoricino experiment can be schematically divided in two categories:

- **External sources**: a not negligible contribution to the background can arise from interactions due to particles originating from outside the detector set-up, such as photons and neutrons from the Gran Sasso rock or muons and muon induced particles.

  Photons originate from natural radioactivity of the rock, mainly consisting of ^{238}U , ^{232}Th and ^{40}K, while muons have mainly a cosmogenic origin.

  Neutrons can both have a cosmogenic origin or be produced by (α, n) reactions occurring in the Gran Sasso rock. The flux of cosmogenic muons and neutrons is strongly reduced by the natural shielding provided by the 1500 m of dolomitic rock (3500 mwe) of the Gran Sasso mountain.

- **Internal sources**: another important source of background arises from intrinsic radioactive contaminations of the materials used to build up the experimental setup.

  The presence of primordial radionuclides in ores and other raw materials results in a wide range of contamination in the experimental set-up. With just few exceptions, the main radioimpurities are usually ^{40}K, ^{232}Th and ^{238}U .

  The cosmogenic activation, due to the interactions of cosmic rays with the detector materials above ground (during fabrication and transportation), is also a non negligible source of internal background.

  Another unavoidable background source which can't be neglected in performing our $0\nu\beta\beta$ experiments with TeO_2 detectors is the contribution of the $2\nu\beta\beta$ decays of ^{130}Te occuring in the crystals bulk.

4.2 Cuoricino history and measured performances

Cuoricino first measurement started in March 2003.

Some detector connections broke during the cooling down procedure, so that only 32 $5\times5\times5$ cm^3 and 17 $3\times3\times6$ cm^3 crystals could be read.

Since the active mass was anyway quite large ($\sim$ 30 kg of TeO_2) and the detector performances were quite good, data taking was continued for a few months.

The average pulse height obtained with the working detectors is of (120 ± 75) μV/MeV $\cdot$ kg for the $5\times5\times5$ cm^3 crystals and (104 ± 35) μV/MeV $\cdot$ kg for the $3\times3\times6$ cm^3 crystals.

The average resolution FWHM in the $0\nu\beta\beta$ region was evaluated on the 2615 keV ^{208}Tl line measured during calibration with a ^{232}Th source: it is 7.8 ± 2.8 keV for the bigger size and of (9.1 ± 3.1) keV for the small size crystals.

At the end of October 2003 Cuoricino was stopped to undergo substantial operations of maintenance and to recover the lost electrical connections and hence increase the number of working detectors.

At the end of April 2004 the second run of Cuoricino started.

Two of the $5\times5\times5$ cm^3 crystal wire connections had broken during the cooling down procedure.

The average pulse height obtained with the working detectors is 167 ± 99 μV/MeV $\cdot$ kg for the $5\times5\times5$ cm^3 crystals and (147 ± 60) μV/MeV $\cdot$ kg for the $3\times3\times6$ cm^3 crystals.

The average resolution FWHM is (7.5 ± 2.9) keV for the bigger size and (9.6 ± 3.5) keV for the small size crystals.

This second data taking run is still ongoing. At present 42 big crystals over 44 and all the 18 small crystals are working: the total active mass of TeO_2 is about 39 kg.

4.3 Cuoricino background analysis

4.3.1 Background measurement

The background spectra obtained from the whole statisitics collected by Cuoricino are shown in fig. 4.1.

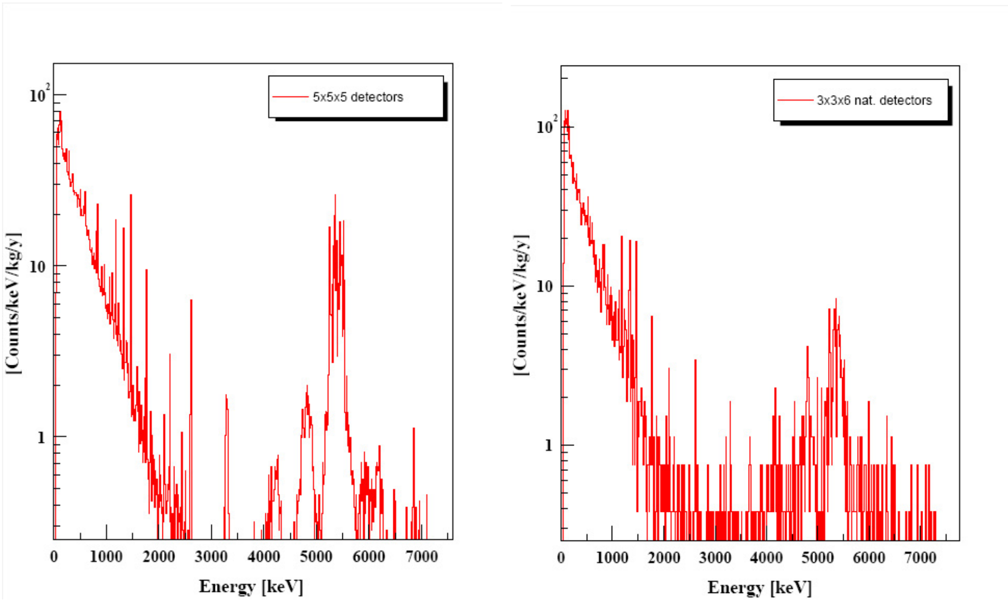

Figure 4.1: Summed background spectra from the operating $5 \times 5 \times 5$ cm^3 and $3 \times 3 \times 6$ cm^3 crystals

The gamma lines due to ^{60}Co, ^{40}K and of the ^{238}U and ^{232}Th chains are clearly visible.

These lines due to contamination of the apparatus, are not visible in the spectra of the single detectors: they appear after summing all the detectors, and are a good check of the calibration and stability of the detectors during the background measurement.

Also visible are the gamma lines due to Te activation (^{121}Te, ^{121m}Te, ^{123m}Te, ^{125m}Te and ^{127m}Te) and those due to Cu activation (^{57}Co, ^{58}Co, ^{60}Co and ^{54}Mn) by cosmic ray neutrons while above ground.

The FWHM resolution of $5 \times 5 \times 5$ cm^3 detectors at low energy, as evaluated on the 122 keV gamma line of ^{57}Co, is ~ 2.8 keV.

The ^{208}Tl gamma line at 2615 keV, clearly visible in the background sum spectrum, is used to evaluate the energy resolution in the region of double beta decay, which results equal to 8.7 keV FWHM.

The $3 \times 3 \times 6$ cm^3 and $5 \times 5 \times 5$ cm^3 crystal background spectra are compared in fig. 4.2 and fig. 4.3.

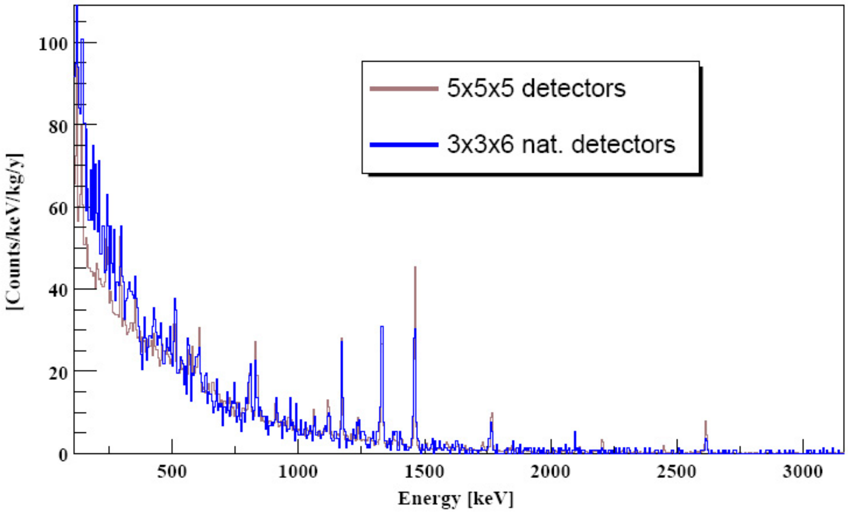

Figure 4.2: Comparison between the background of the $5 \times 5 \times 5$ cm^3 crystals and that of the natural $3 \times 3 \times 6$ cm^3 crystals in the gamma region. Only single site events have been considered

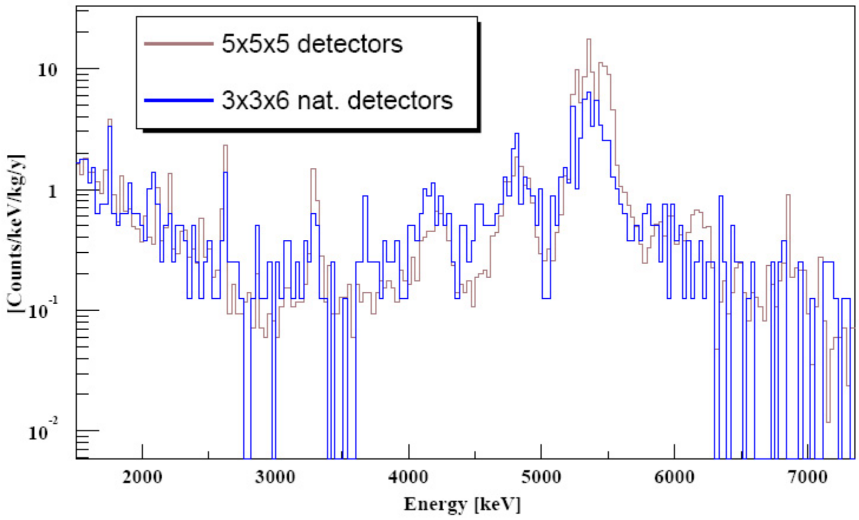

Figure 4.3: Comparison between the background of the $5 \times 5 \times 5$ cm^3 crystals and that of the natural $3 \times 3 \times 6$ cm^3 crystals in the alfa region. Only single site events have been considered

Here the statistical accuracy is much less, nevertheless the gamma lines, not visible in the single detector spectra, are clearly visible in the background sum spectrum.

The FWHM resolution at low energy, measured on the 122 keV gamma line of ^{57}Co, is ~ 1.5 keV.

The FWHM resolution on the ^{208}Tl gamma line at 2615 keV is evaluated to be of about 12 keV (this value has a large error due to the poor statistical significance of the peak).

4.3.2 Background interpretation

Any evaluation of the possible background sources necessarily has a large statistical uncertainty due to the low number of counts. Some considerations are however possible, based on the analysis of the sum spectra of the operating small and large crystals (the count rates of the single detector spectra are too low to consider them separately).

In fig. 4.2 and fig. 4.3 a comparison between the background spectra of the large and small crystals is shown.

General spectral features and counting rates (when normalised to the mass of the crystals) are quite similar.

On the other hand the intensities of the gamma lines do not show a clear behaviour: the ^{214}Bi 1764 keV (the only clearly visible one of the U chain) and the ^{208}Tl 2615 keV lines (the only clearly visible one of the Th chain) seem to scale with the efficiency of the detectors (according to the results of a Monte Carlo analysis, the ratio of the detection efficiency of $5 \times 5 \times 5$ cm^3 and $3 \times 3 \times 6$ cm^3 crystals is ~ 3).

The ^{40}K line at 1460 keV has the same intensity per unit mass on the two kind of detectors. The ^{60}Co lines at 1173 and 1332 keV, on the contrary, show a higher intensity per unit mass in small crystals.

Moreover they undergo a larger reduction with respect to other γ lines when the requirement that the signal is present on one channel only (single site events) is made.

In order to disentangle the different sources of background it is convenient to consider the counting rates in smaller regions as that between the two gamma peaks at 2448 and 2615 keV (^{238}U and ^{232}Th chains respectively), where contributions by both degraded α's from surface contaminations and ^{208}Tl γ's from bulk contaminations are expected, and the region just above the ^{208}Tl 2615 keV line where background sources should be limited to surface contaminations.

Moreover, it should be stressed that the effect of disconnected detectors in reducing the efficiency of the anticoincidence cut (a fundamental tool to study and localize background sources) is not negligible.

Because of the poor statistical significance of the data so far collected, the analysis has to be considered as preliminary (it was in particular limited to the $5 \times 5 \times 5$ cm^3 detectors for which the statistical accuracy is better) even if its results already tend to identify the most important sources of the Cuoricino background besides giving a first quantitative guess of their relevance.

The percentage result of the measured background in the $0\nu\beta\beta$ region, is summarized in table 4.1.

Source	^{208}Tl	$0\nu\beta\beta$ region	3-4 MeV region
TeO_2 ^{238}U and ^{232}Th surface contamination	-	$10 \pm 5\%$	$20 \pm 10\%$
Cu ^{238}U and ^{232}Th surface contamination	$\sim 15\%$	$50 \pm 20\%$	$80 \pm 10\%$
^{232}Th contamination of cryostat Cu shields	$\sim 85\%$	$30 \pm 10\%$	-

Table 4.1: Estimate of the relative contributions of the different sources responsible for the background measured in Cuoricino

A better determination of the actual depth and density profile of this contamination will be available when a better statistical accuracy will allow a more significant analysis of the multiple events.

Analysis of the background above 3 MeV

The following analysis tries to identify the background sources responsible of the Cuoricino counting rate in the region above 3 MeV.

The analisys is based on both the spectra obtained from multiple sites events (not used in the previous analyses) and from single sites events collected with $5 \times 5 \times 5$ cm^3 detectors during the first run of Cuoricino.

The single spectra have been calibrated and linearized in energy as follows: both the gamma lines of the ^{232}Th source measurements and the alpha line of ^{210}Po, clearly visible in the background spectra, are used, assuming a power law dependence for the relashionship between pulse amplitude and particle energy.

The sum spectrum of the single site events from the $5 \times 5 \times 5$ cm^3 detectors calibrated in this way is shown in fig 4.4.

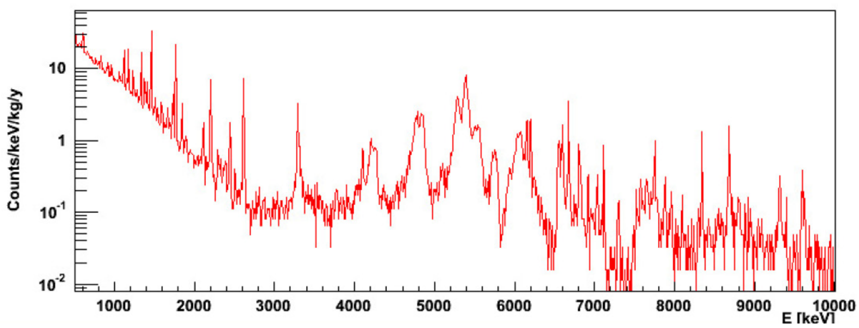

Figure 4.4: Cuoricino energy spectrum in the high energy region

As already mentioned in previous discussions, alpha and beta particles produced by environmental radioactivity can give important contributions to background above 3 MeV.

Because of their low range these particles can only be located either in the crystals or on the surfaces of the materials directly facing the crystals: the copper holder or, less likely, small components placed near the crystals or on the crystal surface such as the NTD thermistor, the Si heater, their gold wires, the glue and other smaller parts.

Monte Carlo simulations of the single and multiple sites event sum spectra of $5 \times 5 \times 5$ cm^3 detectors produced by radioactive contaminations of the above mentioned elements have been obtained using a GEANT4 based code.

These spectra have been compared with the measured spectra in order to identify the actual contaminations responsible of the measured background.

As a first step, bulk and surface contaminations of the crystals have been considered.

Both these contaminations give rise to peaks (centered at the transition energy of the decay) in the single site events spectrum, but in the case of bulk contaminations these peaks are gaussian and symmetric while in the case of surface contaminations the peaks show a low energy tail.

On the contrary, the only possible sources contributing to the multiple sites events spectrum are the surface contaminations of the crystals. The general shape and the structures appearing in both background spectra strongly depend on the depth and density profile assumed for the contamination (an exponentially decreasing function characterized by a depth $\lambda : \rho(x) = Ae^{-\lambda x}$ yielded the best results).

The results of the comparison between Monte Carlo simulations and measured spectra allows to prove that the alpha peaks of the anticoincidence spectrum of Cuoricino are due to a surface (and not bulk) ^{232}Th and ^{238}U contamination of the crystals with the only exception of the ^{210}Po line which has to be attributed to a bulk contamination of the crystals.

The shape of the peaks in the multiple sites events spectrum and the shape of the single sites events spectrum are fully accounted for when a surface contamination depth of the order of 1 μm or less is assumed.

As shown in fig. 4.5 the identified crystal contaminations yield a satisfactory explanation of the coincidence spectrum.

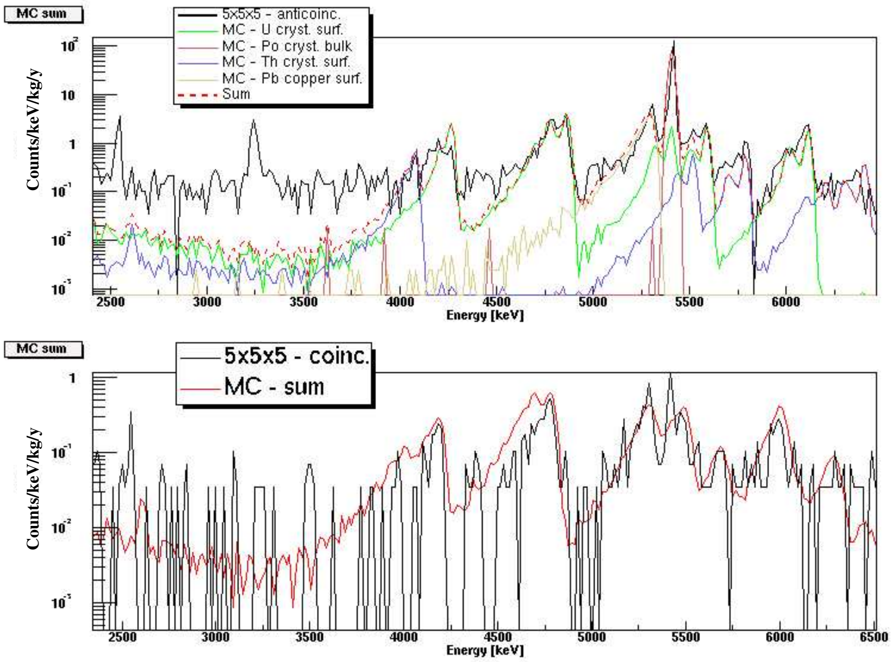

Figure 4.5: Comparison between Monte Carlo and Cuoricino single site event (top) and multiple site event (bottom) spectra in the case of the $\mathrm{TeO_2}$ crystal surface contaminations ($\lambda \sim 1\ \mu m$) specified in the figure

Some contribution to the continuous part of the anticoincidence spectrum seems however still missing.

In order to explain this continuum, a further source, not contributing to the coincidence spectrum, has to be considered.

Such a source can be a ^{232}Th or ^{238}U contamination on the copper surface, as shown in fig. 4.6.

The depth of the contamination should be of the order of ~ 5 μm (a deeper contamination would produce too high gamma peaks while a thinner contamination would give rise to structure in the anticoincidence spectrum) with a total activity in the first 1.5 μm of the order of 10^{-9} g/g either in ^{238}U or ^{232}Th or both.

This analysis shows the importance of continuing the Cuoricino background measurement in order to improve the statistical accuracy of the above described results.

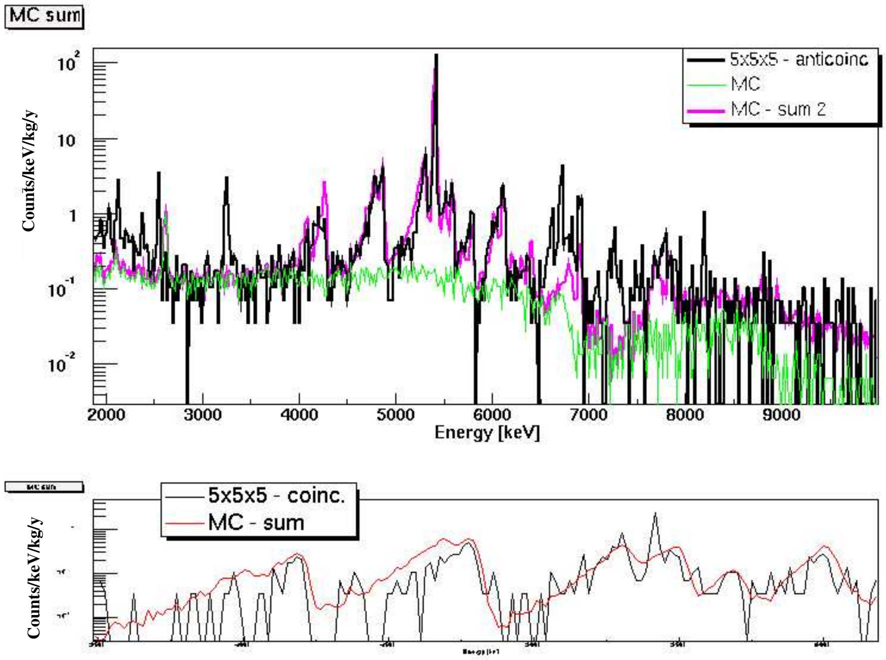

Figure 4.6: Comparison between Monte Carlo and Cuoricino single site events (top) and multiple site events (bottom) spectra when a Th surface contamination of the detector copper holder (green line) is added (pink line) to the crystal conatminations considered in fig. 4.5

These results, on the other hand, show that with a substantial reduction of the copper and TeO_2 crystal surface contamination levels the sensitivity goal for CUORE (i.e. a background counting rate of the order of 0.01 c/keV/kg/y or better) can be reached.

4.4 Cuoricino $0\nu\beta\beta$ results

The results presented here refer to the data acquired with the working TeO_2 crystals up to July 2005, with a total statistics of 5.87 kg ^{130}Te $\cdot$ y. The sum of the spectra of the $5 \times 5 \times 5$ cm^3 and $3 \times 3 \times 6$ cm^3 crystals in the $0\nu\beta\beta$ region is shown in fig. 4.7, where the peaks at 2447, 2505 keV and 2615 keV due to ^{238}U , ^{60}Co and ^{232}Th contaminations respectively are clearly visible. The background value measured in this region is of (0.18 ± 0.01) c/keV/kg/y.

No evidence is found for a peak at 2530.3 keV, the energy of the $0\nu\beta\beta$ of the isotope ^{130}Te .

By applying a maximum likelihood procedure [99] [100] to search for the maximum signal compatible with the measured background, the 90% C.L. lower limit of 2×10^{24} y on the ^{130}Te lifetime is obtained for this decay.

This limit leads to a constraint on the electron neutrino effective mass ranging from 0.19 to 1.04 eV, depending on the nuclear matrix elements considered in the computation [101]. By using the same nuclear matrix element value used by H.V. Klapdor-Kleingrothaus et al. [102] a value for $\langle m_{\beta\beta} \rangle$ of 0.500 eV is obtained.

The reported data show that Cuoricino is a competitive experiment in the field of Neutrinoless Double Beta Decay.

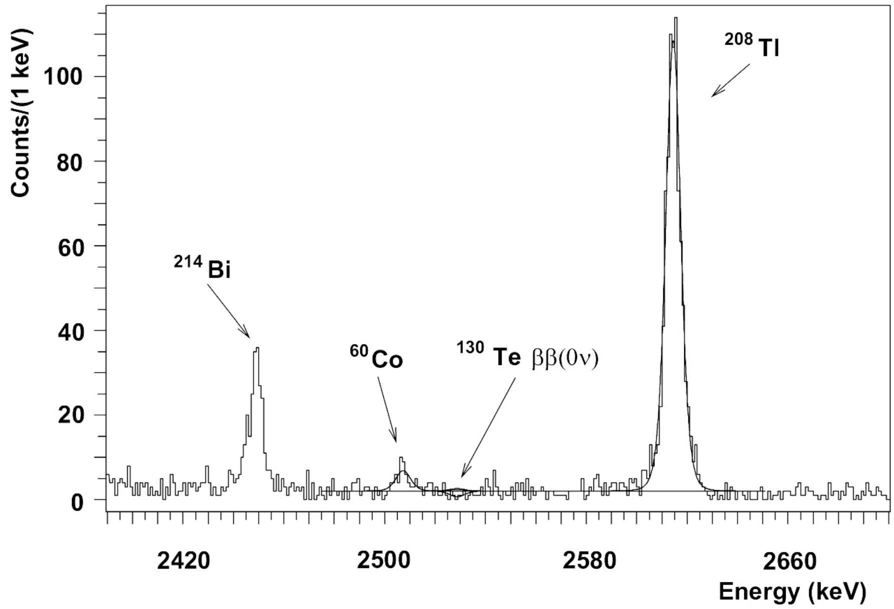

Figure 4.7: Spectrum of the sum of the two electron energies in the region of neutrinoless $0\nu\beta\beta$

It has a 5 year sensitivity (at 68% C.L.) of about 9×10^{24} year for the $0\nu\beta\beta$ of ^{130}Te : this means that Cuoricino will be able to test the Majorana mass in the 100-700 meV range.

Chapter 5

CUORE experiment

"The finest emotion of which we are capable is the mystic emotion.
Herein lies the germ of all art and all true science.
who is no longer capable of wonderment
and lives in a state of fear,
is a dead man"
Albert Einstein

Introduction

As discussed in chapter 1, a number of recent theoretical interpretations of atmospheric, solar and accelerator neutrino experiments imply that the effective Majorana mass of the electron neutrino, $\langle m_{\beta\beta} \rangle$, could be in the range 0.01 eV to the present bounds.

The CUORE project originates as a natural extension of the Cuoricino ^{130}Te experiments, described before, where large arrays of bolometers were used to search for $0\nu\beta\beta$ decay.

The CUORE detector will consist of an array of 988 TeO_2 bolometers arranged in a cylindrical configuration of 19 towers of 52 crystals each and operated at a temperature of $\sim$ 10 mK.

Its total mass, of 741 kg, will be $\sim$ 18 times that of Cuoricino: this will allow CUORE to achieve the sensitivity required for the next generation $0\nu\beta\beta$ experiments.

The detector will be installed in hall A of Gran Sasso National Laboratories and it will start taking data in 2010.

Thanks to the high natural isotopic abundance of TeO_2 , it can be launched without isotopic enrichment.

Moreover, the experience earned with Cuoricino makes an extensive Research and Development (R & D) not necessary for CUORE.

The good results obtained so far prove that the bolometric technique, although novel, is competitive and alternative to the traditional calorimetric Ge technique.

In this chapter the pertinent details of the detector, as well as the background issues, electronics, DAQ and data-analysis are described.

Some of these topics are common to CUORE and Cuoricino, and therefore they have already been discussed in chapters 2 and 3: when this is the case, references to the dedicated sections will be included in the text.

5.1 The experimental set-up

The CUORE detector will consist of an array of TeO_2 bolometers, assembled in Cuoricino-like towers: a picture of CUORE structure is shown in figure 5.1

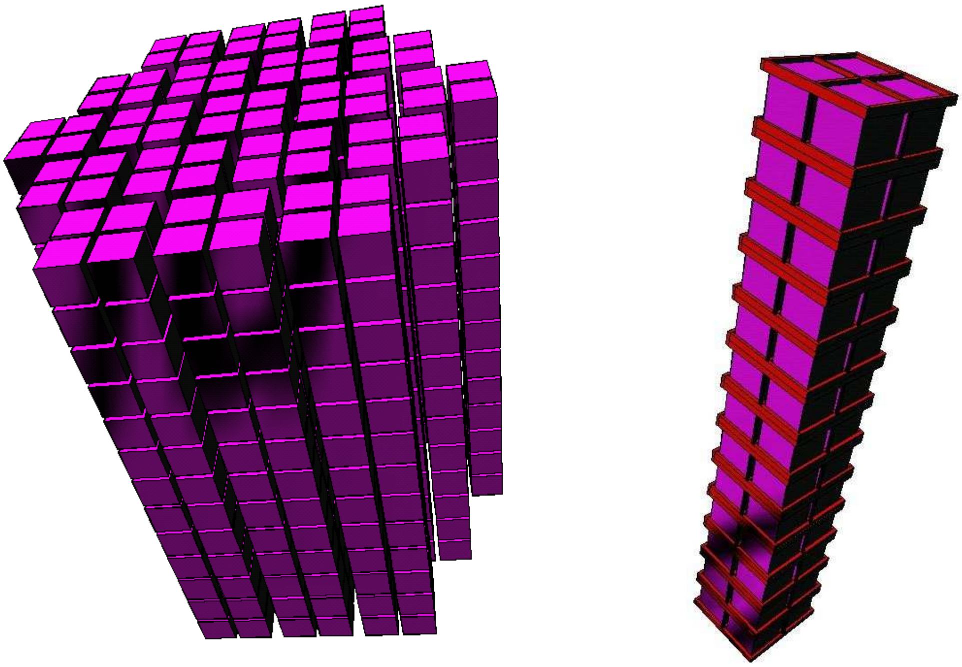

Figure 5.1: The CUORE detector (left), one of the 19 towers (right)

The principles of operation of TeO_2 bolometers has been described in detail in chapter 2.

As in the case of Cuoricino, the raise in temperature generated by the particles impinging on CUORE crystals is measured by Neutron Transmutation Doped (NTD) germanium thermistors.

NTD thermistors for CUORE are developed and produced at the Lawrence Berkeley National Laboratory (LBNL) and UC Berkeley Department of Material Science [85], as those used for Cuoricino.

They have been made uniquely uniform in their response and sensitivity by neutron exposure control with neutron absorbing foils accompanying the germanium in the reactor.

The TeO_2 crystals will be produced by the Shanghai Institute for Ceramics (SICCAS), which already provided Cuoricino TeO_2 crystals.

A single CUORE detector consists of a $5 \times 5 \times 5\ cm^3$ single crystal of TeO_2 that acts both as a detector and source.

The detectors will be held by a copper frame in the 19 tower configuration shown in fig. 5.1 (left panel).

The frame, and dilution refrigerator mixing chamber to which it is thermally connected, forms the heat sink, while the PTFE (Polytetrafluoroethylene or TEFLON) stand-offs provide the thermal impedance which delays the re-cooling of the bolometers which will be operated at ~ 10 mK.

As described above (cap. 3), the good performance of the $5 \times 5 \times 5\ cm^3$ crystals to be used in

CUORE has been already proved by Cuoricino, whose structure corresponds to a tower of length and number of floors slightly larger than in CUORE.

5.1.1 The single module

A single CUORE detector is a $5 \times 5 \times 5\ cm^3$ single crystal of TeO_2 grown with ultrapure TeO_2 powders and polished on the surfaces.

Crystals of TeO_2 have a tetragonal structure, and are grown along the (001) axis.

The two axes normal to this axis are crystallographically equivalent, a fact relevant to their use in the search for solar axions discussed in chapter 6.

The surface hardness is not the same for all sides, which complicates the crystal polishing. It has been shown that repeated thermal cycling does not damage the crystals, as in the cases of crystals of other tellurium compounds, or those of tellurium metal.

The Debye temperature of the TeO_2 crystals was specially measured for the CUORE project as 232 K [103].

The specific heat of the TeO_2 crystals was found to follow the Debye law down to 60 mK, and the heat capacity of the 750 g crystals is 2.3×10^{-9} J/K extrapolated down to 10 mK.

The NTD thermistors are glued by epoxy to the crystal and are operated in the Variable Range Hopping (VRH) conduction regime with a Coulomb gap (see sec. 2.3).

The structure of CUORE single module will be identical to Cuoricino: the reader is therefore invited to refer to section 3.2.2 for furhter details on this topic.

5.1.2 The sensor

The principles of operation of NTD thermistors have already been discussed in section 2.3.

In particular, CUORE thermistors will be of the same kind used for Cuoricino and described in section 3.2.1.

The key to the success of CUORE is the production of large numbers of nearly identical neutron-transmutation-doped (NTD) Ge thermistors.

It is very important to optimize the neutron irradiation exposure and to make the exposures as uniform as possible.

It is not possible to evaluate the thermistor material directly from the reactor because of the long half life of ^{71}Ge (11.43 days).

A delay of several months is required to see if the Ge needs more exposure. To circumvent this difficulty, the Ge material is accompanied by foils of metal with long-lived (n, γ) radioactive product nuclides.

Accordingly, the neutron exposure of the Ge can be determined accurately, and uniformity of exposure is achieved.

This technique was developed recently by the Lawrence Berkeley National Laboratory group of the CUORE Collaboration.

Samples of the NTD thermistors produced for CUORE were cooled to 30 mK and resistance vs. temperature measurements were made over approximately the 300-30 mK range.

It was demonstrated [104] that the variation of the temperature performances of detectors irradiated twice were smaller than those measured for the same detectors after a single irradiation, and that their properties were closer to those of NTD-31, currently being used in CUORICINO.

The problem of producing large numbers of identical thermistors is quite complicated.

These thermistors, nearly identical to NTD-31, were made with an iterative process whereby the second doping was calculated following a measurement of the first.

This is a very inefficient process for producing large numbers of thermistors.

Fortunately, the same method used to make the thermistors can be used to analyze the results: short-lived gamma-emitting isotopes of Ge and As are in fact produced during the irradiation, and their measurement allows to make precise measurements of both Ga and As doping level.

Two, or even three, irradiations will be required to produce thermistors with properties close enough to be used in the large array of CUORE.

These techniques will be further refined in order to allow faster and more uniform production of the thousands of thermistors required for CUORE.

The plan to make these irradiations more predictable is to use the NTD facility at the MIT reactor with multiple irradiations on a single large batch of Ge wafers.

Each wafer will have its own monitor, and each will be separately analyzed to determine the appropriate subsequent irradiation to bring them to the right temperature characteristics.

5.1.3 The cryogenic setup

The CUORE bolometers will operate at temperatures between 7 and 10 mK. This will require an extremely powerful dilution refrigerator (DR), since at these temperatures, the cooling power of a DR varies approximately as T^2.

Estimates were made of the parasitic power the detector and DR would receive from: heat transfer of the residual helium gas in the inner vacuum chamber (IVC), power radiated from the 50 mK shield facing the detector, and from vibrational energy (microphonic noise).

The estimated value is $\sim 1\ \mu W$ at 7 mK, using reasonable values for the residual gas pressure and achievable surface quality for radiation transfer.

The resulting estimate for the radiation contribution was negligible.

The CUORE detector will be cooled by a ^{3}He/^{4}He refrigerator with a cooling power of 3 mW at 120 mK.

A shematic drawing of CUORE cryostat is shown in figure 5.2.

Refrigerators with the required characteristics are technically feasible: one example is the DRS-3000 DR model constructed by the Kamerling Onnes Laboratory in Leiden.

One important design feature is the 50 mm diameter clear access to the mixing chamber to allow a rod, suspended from an external structure, to suspend the detector array to minimize vibrations from direct connection to the mixing chamber.

The temperature of the rod will be controlled in stages along its length by flexible thermal contacts to avoid vibrations.

The dewar housing the diluition refrigerator will have a jacket of liquid nitrogen (LN) to avoid the need of superinsulation which is not free of radioactivity. The system is designed with several tubes passing through the LN bath, the liquid He bath, and the IVC, to allow refilling with cryogenic liquids, and for sufficient feed through for electrical connections.

Liquefiers will provide constant liquid levels for the two baths over long periods of operation.

The He that evaporates from the main bath and from the 1K-pot will be recovered in a buffer tank and re-liquefied with a helium liquefier with a capacity of several tens of l/day.

The gas will be cooled to $\sim$ 70 K, then to 10 K, by a two stage Gifford-MacMahon cycle.

This will be followed by a Joule-Thompson cycle that liquefies it and injects it back into the main bath.

The nitrogen liquefier, on the other hand, will require only a single stage Gifford-MacMahon cycle to cool a cold finger above the liquid nitrogen bath.

It will condense the evaporated N_2 and let it fall back into the bath.

This complex cryogenic system will require a constant monitoring system, capable of surveying the operating conditions to allow prompt intervention to correct malfunctions rapidly.

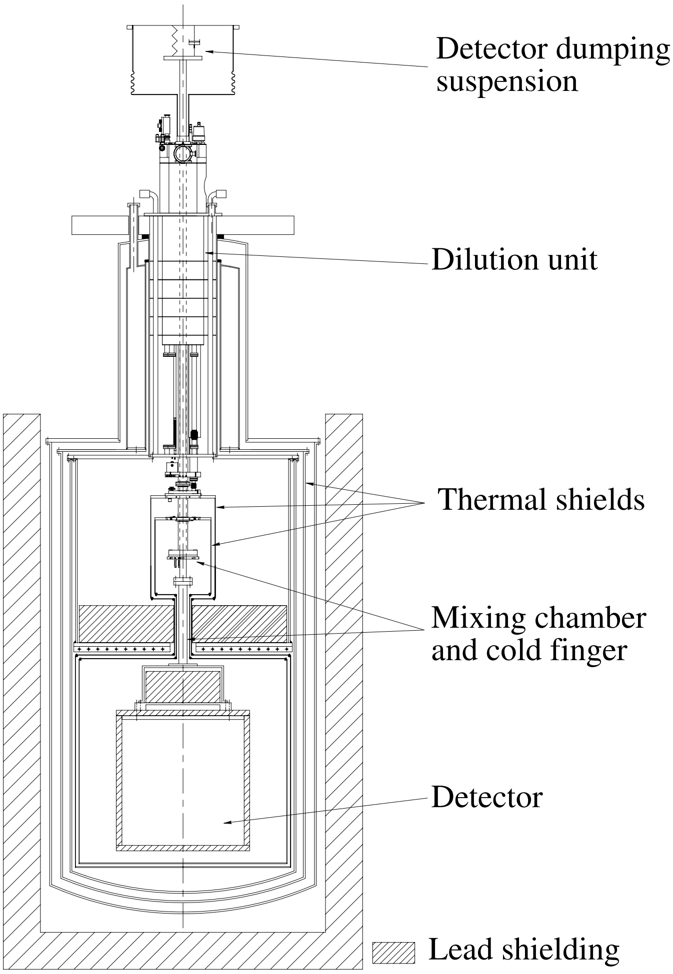

Figure 5.2: Schematic drawing of CUORE cryostat

In addition, the operating conditions of the entire cryogenic system must be recorded for future correlation with instabilities in the experimental data (see sections 3.3.1 and 7.1.3).

Besides housing the CUORE detector, the dewar will be able to support an effective system of roman lead shields maintained at the low temperature close to the detectors.

The experience collected by the proponents in running Cuoricino, shows that a constant (or very slowing varying, of the order of 1 %/day) level of liquid helium in the main bath of the cryostat helps in achieving a steady response of the detectors.

Any variation of the main bath level translates into small changes of the mixture flow and therefore of the refrigerator cooling power.

These changes are harmful for the stability of the bolometer output and could spoil the effectiveness of the correction procedure (see section 3.3).

A fundamental point is that the stabilization procedure is effective only if the detector operation point (and therefore its steady state voltage level, often referred to as "baseline") is kept inside a narrow range around of the initial value.

This cannot be achieved in presence of relatively large or fast changes of the liquid helium level.

The basic design described above for CUORE, is based on the successful operation of Cuoricino, in which the helium level was kept almost steady by means of a helium re-liquefier.

This system is however based on a twenty-year-old technology and has exhibited many weak points during the multi-annual operation of the bolometric arrays, such as unpredictable variations of the liquefaction efficiency and microphonic noise introduced by the cryogenic heads of the GM cycle.

These problems could be even more serious in the CUORE cryogenic system, due to the much larger boil-off of the CUORE cryostat.

For this reason an alternative cryogenic configuration will be considered, which could allow to keep the 4 K stage temperature constant for the whole duration of the experiment.

This solution is based on a new commercial device provided by the modern cryogenic technology: a Pulse Tube (PT) cooler.

PT coolers consist of a compressor, a rotary valve and a cold head. Their advantages are:

- low maintenance, due to the absence of moving displacers and cold seals
- low noise, due to the lack of moving parts in the cold head, which assures a very quiet system
- low cost, due to its simplicity, which allows the PT to be manufactured at less cost than common cryo-refrigeration systems

Commercial two stage PT's provide two cold points, typically at 80 K and 4 K, with a cooling power of the order of 0.5 W at 4 K. In this framework, a liquid-heliumfree medium-power dilution refrigerator was installed in September 2003 at the Insubria University: it will be a precious test-bench for this new technique, in terms of reliability and noise level.

In the event of convincing performance of this system, a refrigerator for CUORE endowed with an array of PT's will be designed with the aim to stop or reduce the main bath boil-off or, as an extreme solution, to get rid completely of cryogenic fluids.

Shielding requirements

Double-beta decay experiments, as well as dark matter searches and searches for rare events in general, require deep underground locations and ultra low radioactive environments.

This latter requirement is usually accomplished by placing severe constraints on the selection of the materials used and by the realization of proper shielding surrounding the detectors.

Since in Cuoricino a non negligible contribution to the background rate in the $0\nu\beta\beta$ region was recognized as originating from environmental radioactivity, and radioactive contaminations of the cryostat structure (chapter 4), the design of effective shields (specially those directly surrounding the detector) is crucial to reach the sensitivity goal of CUORE.

Figure 5.3 shows a schematic drawing of Cuoricino cryostat and shielding: part of the bulk lead shielding will be placed inside of the cryostat, and part outside, in order to shield the detector from environmental radioactivity and from radioactive contaminations of the dewar structure.

A 4π layer of ultra-low background lead will constitute 3 cm thick walls of the structure of the array. This layer will be Roman lead whose ^{210}Pb is less than 4 mBq/kg.

Even if the dilution refrigerator will be constructed from materials specially selected for low levels of radioactivity, these levels might be higher than can be tolerated by the sensitivity requirements: the main goal of the inner lead shield will be therefore of cancelling their dangerous contributions to the CUORE background level.

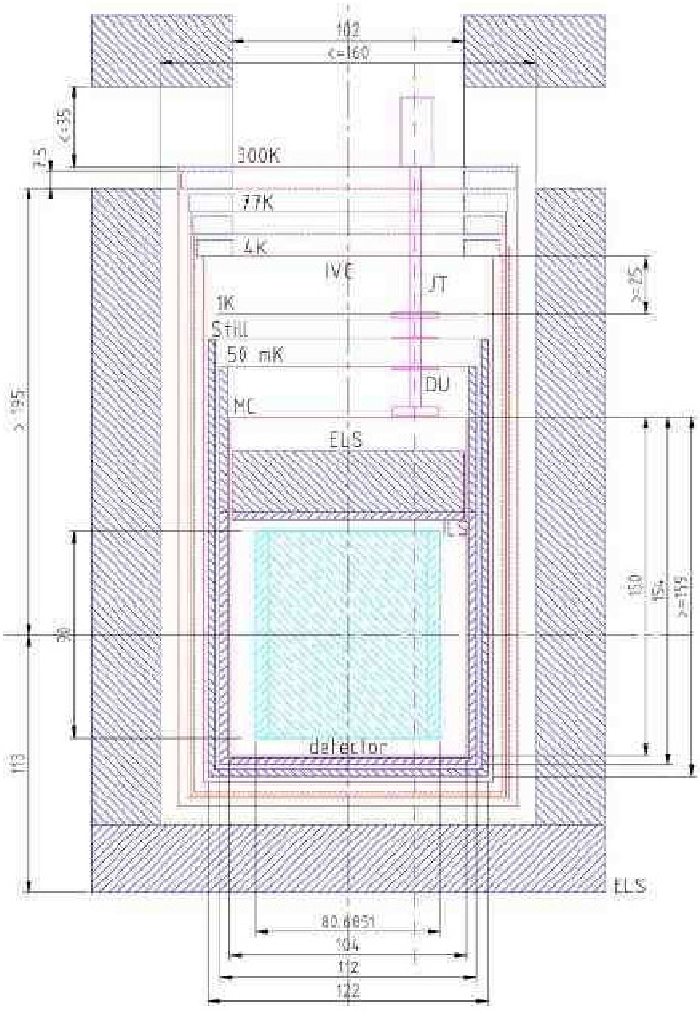

Figure 5.3: CUORE cryostat and shielding.

The top of the detector array will be protected by two Pb layers of ~ 1 m diameter and 10 cm thickness each.

The layer close to the detector will be made of high quality lead with an activity of 16 Bq/kg of ^{210}Pb, whereas the upper layer will be made of modern lead with an activity of ^{210}Pb of 150 Bq/kg.

Another layer of lead (16 Bq/kg of ^{210}Pb), 17 cm thick, and with a diameter of ~ 40 cm will be placed directly on the top face of the detector.

Finally, outside the dewar, there will be two 10 cm thicknesses of lead, 16 Bq/kg of ^{210}Pb for the inner layer, and 200 Bq/kg for the outer layer.

The lead shield will be surrounded with a 10 cm thick box of borated polyethylene that will also function as an hermetically sealed enclosure to exclude radon, and will be flushed constantly with dry nitrogen.

The entire dewar, detector, and shield will be enclosed in a Faraday cage to exclude electromagnetic disturbances that also constitute a source of background, albeit at low energies, important to dark matter and solar axion searches.

The addition of a muon veto surrounding the entire structure will be also considered.

5.1.4 The location

CUORE will be located in the underground hall A of Laboratori Nazionali del Gran Sasso (LNGS, L'Aquila - Italy) at a depth of 3400 m.w.e. where the muon flux is reduced to $\sim 3 \times 10^{-8}$ μ/cm^{-2}/s and the neutron flux to $\sim 10^{-6}$ n/cm^{-2}/s.

After the approval of CUORE by the Gran Sasso Scientific Committee its final location just near the CRESST installation has been decided.

The entire CUORE setup will be installed inside a proper building which will have to guarantee room for all the setup parts (e.g. cryogenics, electronics, shieldings), for a controlled area to be used during assembling procedures and for all normal monitoring activities.

The hut in which the CUORE experiment will be housed will have therefore to satisfy the following main requirements:

- the cryostat and the detector have to be sustained by means of two independent structures, in order to avoid any possible transmission of mechanical vibrations to the bolometers from the cryogenic facility
- the dilution refrigerator has to be kept at a suitable height from the floor to give the possibility of an easy dismounting of the thermal and radioactivity shields when necessary
- the area where the cryostat and the front-end electronics are located has to be shielded from electromagnetic interferences by means of a Faraday cage
- the area where the detector will be assembled must be a clean room in order to avoid radioactive contamination of the array in the mounting phase

Following these requirements a schematic design of the hut has been made.

It will be divided in three levels as shown in fig. 5.4.

At the ground floor a platform of reinforced concrete, with a central aperture of about 3 m diameter, will be placed. In this aperture a lifting platform, able to raise at least 50 tons, will be realized with four couples screw-nut, driven by four motors simultaneously controlled. The radioactivity shielding will be placed on the lifting platform; in this way it will be easy to pull down the shieldings whenever is necessary to open the cryostat. On the ground level, the pumps of the cryostat and the compressors for the liquefiers (or for the pulse tubes) will also be placed. The dilution refrigerator will be suspended at about 3.5 m from the ground in order to guarantee an easy dismounting of the thermal shields (fig. 5.4).

The concrete platform at the ground floor will be the base for two sets of three pillars each: the first set will go up to the floor of the second level and will support a plate to which the cryostat top flange will be anchored; the second set will go up to the ceiling of the second level and will bear the support structure of the detector.

An appropriate design for the mechanical suspension for the CUORE array is under study.

The first level will consist of two separated sections: a clean room (at least class 100), where all the CUORE detector parts will be assembled and stored, and a control room for the cryostat.

The second level will also be separated in two sections.

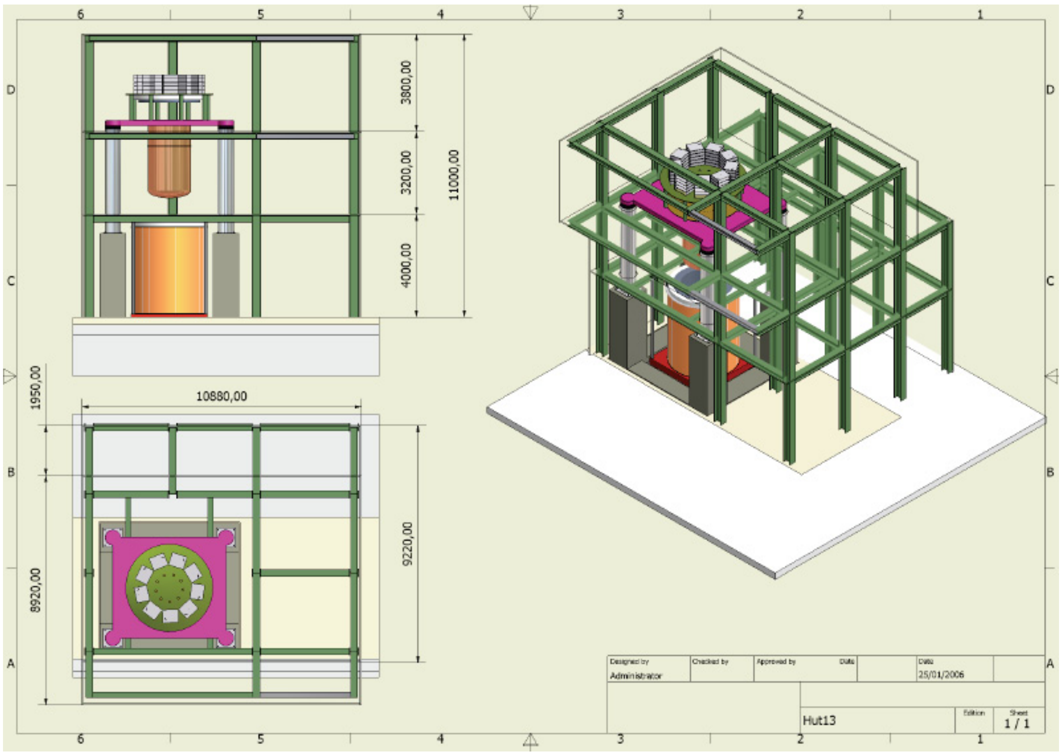

Figure 5.4: Scheme of the CUORE set-up installation

The first one, containing the top of the cryostat, the support structure and the front-end electronics, will be surrounded by a Faraday cage.

The second will be used for the data acquisition system.

5.1.5 Electronics

The design of CUORE electronics has been developed with the aim of satisfying the requirements (electrical specifications, space occupation, cost, etc.) of CUORE.

CUORE electronics will therefore the same as Cuoricino one (see section 3.2.4), the only significant difference being in the number of read channel: 62 in the case of Cuoricino and 988 in the case of CUORE .

Only minor technical modifications will be required in order to accomodate the increased number of channels, and they will not be discussed in this work.

5.1.6 Data acquisition

The Data Acquisition System for CUORE will be described in detail in chapter 8.

5.2 Data analysis

CUORE data analysis system is currently being developed.

The experience of Cuoricino allowed to identify the best analysis techniques for the data collected with this kind of detector, and to fully test and tune them.

CUORE system will largely exploit this knowledge: from a conceptual point of view it will in fact closely follow the structure outlined in section 3.3.

A special effort will be dedicated to automating some of the necessary algorithms, such as, for instance, the calculation of the detectors' response functions necessary for the implementation of the Optimum Filter algorythm.

Possible improvements to the currently adopted techniques are also investigated, such as Artificial Neural Networks: their efficiency in selecting pulse shapes is currently being evaluated.

From a technical point of view, CUORE analysis system will be written under Linux OS: its code will have an Object Oriented structure, will be written in C++, and will heavily exploit the functionalities of the Root[1] package.

It will provide a user friendly interface with both CUORE data base and Data Acquisition System: in particular, a simplified version of CUORE analysis system will run during data taking and will allow to monitor the collected data and to assess their quality online.

5.3 Predicted performances

The goal of CUORE is to achieve a background rate in the range 0.001 to 0.01 c/keV/kg/y at the $0\nu\beta\beta$ transition energy of ^{130}Te (2528.8 keV).

A low counting rate near threshold (that will be of the order of $\sim 5-10$ keV) is also foreseen and will allow CUORE to produce results for Dark Matter and Axions searches.

In this section an evaluation of the background attainable with CUORE will be presented, based on the state of the art of detector design and of radioactive contaminations.

CUORE construction will however require about four years, during which an R&D dedicated to background reduction will be carried on.

Radioactive contamination of individual construction materials, as well as the laboratory environment, were measured and the impact on detector performance determined by Monte Carlo computations.

The code is based on the GEANT-4 package; it models the shields, the cryostat, the detector structure and the detector array.

Even smallest details of the detector apparatus (copper frames, screws, signal wires, NTD thermistors, etc.) and of the cryogenic setup were taken into account.

It includes the propagation of photons, electrons, alpha particles and heavy ions (nuclear recoils from alpha emission) as well as neutrons and muons.

For chains or radioactive isotopes, alpha, beta and gamma/X rays emissions are considered according to their branching ratios.

The time structure of the decay chains is taken into account and the transport of nuclear recoils from alpha emissions is included. The considered background sources are:

- bulk and surface contamination of the construction materials from the ^{238}U, ^{232}Th chains and ^{40}K and ^{210}Pb isotopes;
- bulk contamination of construction materials due to cosmogenic activation;
- neutron and muon flux in the Gran Sasso Laboratory;
- gamma ray flux from natural radioactivity in the Gran Sasso Laboratory;

[1] Root is a C++ package for Physical Analysis developed at CERN (http://root.cern.ch)

Contaminant	^{232}Th	^{238}U	^{40}K	^{210}Pb	^{60}Co
TeO_2	0.5	0.1	1	10 μBq/kg	0.2 μBq/kg
copper	4	2	1	0	10 μBq/kg
Roman lead	2	1	1	4 mBq/kg	0
16 Bq/kg lead	2	1	1	16 Bq/kg	0

Table 5.1: Bulk contamination levels (in picograms per gram, unless otherwise indicated) used in the simulation for TeO_2, copper and lead.

Contaminant	method	^{232}Th	^{238}U	^{40}K	^{210}Pb	^{60}Co
TeO_2	bolometric	0.7	0.1	1	100 μBq/kg	1 μBq/kg
Copper [105]	Ge diodes	5.6	2	0.3	-	10 μBq/kg
Roman lead	Ge diodes	50	30	2	4 mBq/kg	-
Low act. lead [106]	Ge diodes	3.4	2.7	1.7 ± 0.3	23.4 ± 2.4 Bq/kg	$18 \pm 1\mu$Bq/kg

Table 5.2: Available 90% C.L. upper limits for bulk contaminations of TeO_2, copper and lead (levels in picograms per gram if not differently indicated).

- background from the $2\nu\beta\beta$ decay.

In the next sections these background sources and their contribution to CUORE background are discussed.

It will be shown that, in a very conservative approach where the CUORE-tower mechanical structure is assumed identical to the structure used in Cuoricino, considering the worst possible condition for bulk contaminations (i.e. all the contamination equal to the present 90% C.L. measured upper limits 5.1) and assuming for surface contamination a reduction of about a factor ten with respect to Cuoricino, the CUORE background will be ~ 0.007 c/keV/kg/y at the $0\nu\beta\beta$ transition and ~ 0.05 c/keV/kg/d near threshold.

5.3.1 Contamination of the construction materials

The main contribution to CUORE background is expected to come both from bulk and surface contaminations in the construction materials.

Bulk contaminants are present in the cryostat structure (cryostat radiation shields), in the heavy structures close to the detectors (the copper mounting structure of the array, the Roman lead box and the two lead disks on the top of the array) and in the detectors themselves (the TeO_2 crystals).

Surface contaminations contribute to the background when they are localized on the crystals or on the copper mounting structure directly facing them.

In particular, the estimate of the relative contributions to Cuoricino background from different sources, summarized in table 4.1, shows the leading role of surface copper contaminations in producing events in the $0\nu\beta\beta$ energy region.

The radioactivity levels used in the estimate of the contribution of bulk contaminants are given in table 5.1.

These levels are nearly equal to the best upper limits obtained for the radioactive content of these same materials as shown in table 5.2 during Cuoricino first run with $5 \times 5 \times 5$ cm^3 crystals.

The results of the Monte Carlo simulations using the contamination levels discussed here are given in table 5.3 for the $0\nu\beta\beta$ decay and the low energy (10-50 keV) regions.

The assumed threshold is 10 keV and only values obtained after requiring an anti-coincidence between detectors are indicated.

Simulated element	TeO_2 crystals	Cu structure	Pb shields	TOTAL
$0\nu\beta\beta$ decay region c/keV/kg/y	1.6×10^{-3}	1.5×10^{-3}	7.0×10^{-4}	3.8×10^{-3}
dark matter region c/keV/kg/d	2.3×10^{-2}	9.6×10^{-4}	5.0×10^{-5}	2.4×10^{-2}

Table 5.3: Computed background in the $0\nu\beta\beta$ decay and in the low energy regions for bulk contaminations in the different elements, the Cu structure accounts for the detector mounting structure and the 50 mK shield.

Element	Contamination Bq/cm^2	Contribution to the $0\nu\beta\beta$ region c/keV/kg/y
TeO_2	$1.9 \cdot 10^{-8} \pm 9.8 \cdot 10^{-9}$	$1.6 \cdot 10^{-2} \pm 8.4 \cdot 10^{-3}$
Copper	$4.9 \cdot 10^{-8} \pm 1.9 \cdot 10^{-8}$	$5.8 \cdot 10^{-2} \pm 6.6 \cdot 10^{-3}$
Total	$3.4 \cdot 10^{-8} \pm 1.3 \cdot 10^{-8}$	$7.4 \cdot 10^{-2} \pm 1.1 \cdot 10^{-2}$

Table 5.4: Estimated upper contribution to the CUORE $0\nu\beta\beta$ region from surface contaminations obtained by using the surface contamination levels evaluated for Cuoricino and assuming an exponential density profile with $\lambda = 1\ \mu m$ for TeO_2 crystals (^{238}U) and $\lambda = 5\ \mu$m for Copper (^{238}U and ^{232}Th).

These values have to be considered as upper limits on the possible contribution of bulk contaminations to the CUORE background.

Concerning surface contamination, no direct measurements of the typical impurity levels present on TeO_2 and copper surfaces are available, therefore the results obtained in Cuoricino are used as input for the Monte Carlo simulations.

These indicate that both a surface contamination of the crystals and of the copper surface of the mounting structure is present.

In the case of TeO_2, the contamination is mainly ^{238}U and its presence is strictly connected to the kind of surface treatment undergone by the crystals.

In the Cuoricino $5 \times 5 \times 5$ cm^3 crystals, this contamination produces a background counting rate in the $0\nu\beta\beta$ region of about $(4 \pm 3) \times 10^{-2}$ c/keV/kg/y (table 4.1).

Concerning the copper surface contamination, a clear indication of its origin and identity is still missing, but an evaluation of the $0\nu\beta\beta$ background counting that can be ascribed to them (whatever they are, ^{238}U or ^{232}Th) is available: $\sim 0.1 \pm 0.05$ c/keV/kg/y.

According to a Monte Carlo simulation of the CUORE detector, based on the Cuoricino contamination levels, the background counting rates in the $0\nu\beta\beta$ region (after the anticoincidence cut) of about 1.6×10^{-2} c/keV/kg/y and 5.8×10^{-2} c/keV/kg/y were obtained for the TeO_2 crystals and the copper structure respectively, as shown in table 5.4.

The goal of CUORE is to reduce the surface contribution by a factor at least 20 with respect to this evaluation, obtaining a background coming from surfaces of about 3×10^{-3} c/keV/kg/y.

Improvements of a factor of $\sim 1.5 - 2$ are expected simply by possible reductions of the copper mounting structure dimensions (the Monte Carlo simulation used so far refers to an identical mechanical structure for the CUORE and Cuoricino single detector modules).

A reduction by a factor of at least ten of the copper (TeO_2) surface contamination is therefore necessary for CUORE.

Recent bolometric measurements performed in Hall-C, as part of the program of surface cleaning of the detector materials, provided good results in this direction.

A setup composed of a 2-planes array (RAD) made of 8 $5 \times 5 \times 5$ cm^3 TeO_2 crystals was operated to test the efficacy of new techniques for crystals surface cleaning: the crystals were etched with nitric acid (removing about 10 micron on the surfaces) and then polished with a SiO_2 powder, whereas the copper mounting structure was etched, treated through electroerosion (removing from 10 to 30 microns on the surfaces), and, finally, the copper faced to the crystals was covered with a polyethylene film.

This treatment allowed to reduce Cuoricino TeO_2 surface contamination in U anf Th by a factor 5: from this result an upper limit of 3 10^{-3} c/keV/kg/y can be estimated for CUORE.

The major fraction of the flat continuous background, due to degraded alpha particles, that extends down to the $0\nu\beta\beta$ region, however, has been reduced by only $(38+/-7)\%$.

Indirect evidences suggest to attribute the origin of these counts to copper surface contaminations: extrapolating, under this assumption, the results of the measurements to Cuoricino, the background in the $0\nu\beta\beta$ region would be lower than 5 10^{-2}c/keV/kg/y.

A further reduction of the background level is expected from the use of Surface Sensitive Bolometers (SSB) [107]: these are elements constituted by a main TeO_2 crystal surrounded by six 0.3 mm thicks slabs operated as bolometers, and constituting an active veto.

Figure 5.5 outlines the main feature of such a detector: any particle depositing its energy only in the Main, as a $0\nu\beta\beta$ decay event, produces a large particle-induced signal on the Main and a small slow thermally induced signal in the SSB (due to temperature rise of the Main).

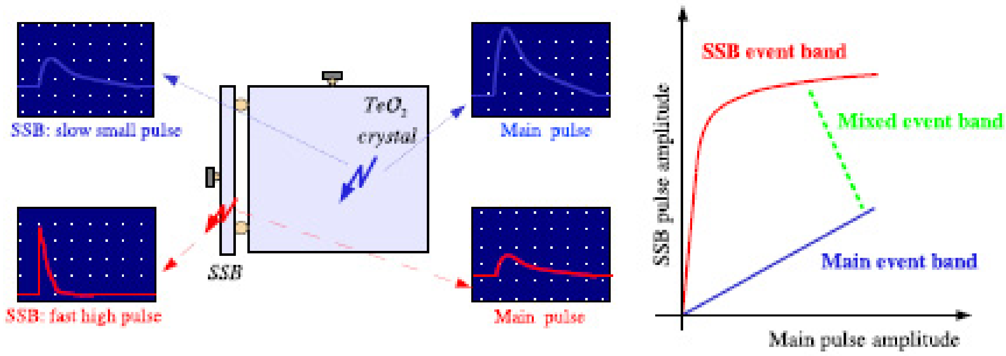

Figure 5.5: The behaviour of composite bolometers with respect to a signal produced by interaction in the slab or in the TeO_2 crystal. The scatter plot shows the different shapes of the curves drawn by pure SSB events and pure Main ones. The curve originated by a monochromatic alpha sharing its energy between SSB and Main (a surface contamination) is also shown.

A similar pattern is obtained for alpha particle interactions due the bulk contamination of the Main, and for gamma rays.

Indeed the probability that a gamma ray interacts also in the SSB is negligible due its small mass.

On the contrary any particle interacting just in the SSB, as an alpha particle due to a bulk contamination of the SSB or an alha coming from the copper mounting surface facing the SSB, yields a fast high particle induced signal in the SSB and a small thermally induced signal in the Main.

A degraded alpha (those that contribute to the $0\nu\beta\beta$ decay region) is, in this detector, a particle that shares its energy between the Main and the SSB.

This is an intermediate case between the two described above: for both Main and SSB a "particle" and a "thermal" contribution to pulse formation are present. The scatter plot of signal amplitudes as measured by the Main and by the SSB allows to clearly distinguish these different event tipologies (see figure 5.5 right panel).

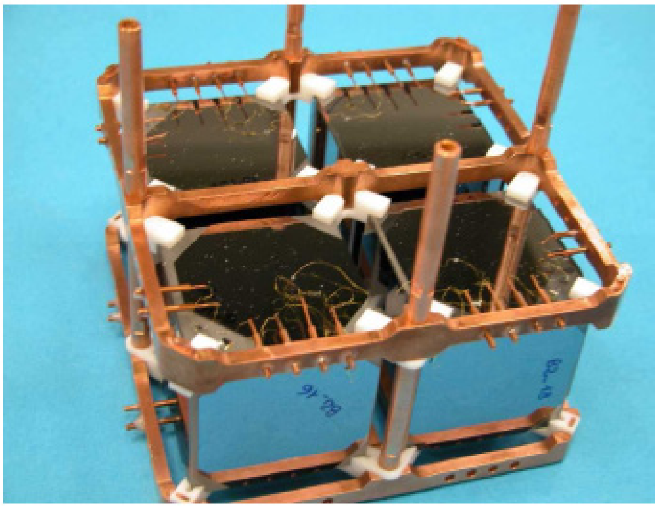

Figure 5.6: The SSB plane.

Figure 5.6 shows a an array of 4 detectors coupled to Si SSB.

A new array of 3 Cuoricino-like planes has been prepared and will start data taking in April 2006.

The crystals have undergone a surface treatment identical to the one used for RAD crystals.

The copper of the mounting structure has been treated as the RAD one and will be completely covered with the same polyethylene film used the previous tests.

Finally one of the three planes will mount SSB detectors covering each crystal face.

On one side this run will test the reproducibility of the surface treating techniques (both for TeO_2 and for copper) and therefore should yield results similar to the last achievements of RAD.

On the other side the four SSB coupled detectors will give the final answer concerning the origin and location of the 3-4 MeV background and in the meantime will tell us if a TeO_2 crystals coupled with SSB will be suffcient to fulfil the background requirements for CUORE.

5.3.2 Cosmogenic Contribution

Cosmogenic activation is produced by cosmic rays when the crystals are above ground during fabrication and shipping of the crystals from the factory to the underground laboratory.

In order to determine the type and amount of radionuclei produced by cosmic rays on TeO_2 the COSMO [108] code was used, based on computed cross sections.

The radionuclei produced by the activation of tellurium are mostly tellurium isotopes (A=121,123,125,127) as well as ^{124}Sb, ^{125}Sb, ^{60}Co and tritium, these last three being of more concern because of their long half-life (^{125}Sb: beta decay of 2.7 years, end-point energy of 767 keV, ^{60}Co: beta decay of 5.27 years end-point energy 2823 keV and ^{3}H: beta decay of 12.3 years, end-point energy of 18 keV).

On the basis of the present knowledge of the cosmic rays production rates, a possible time schedule for the crystal growth and shipping to Gran Sasso has been studied that can guarantee the required low level of ^{60}Co.

The total induced activities remaining after 2 years underground have been estimated and the consequent contribution to the detector counting rate was deduced by aMC simulation.

The radionuclei that contribute to background throught their β^- decay are:

- the long living ^{60}Co isotope in the $0\nu\beta\beta$ region, with an activity of ~ 0.2 μBq/kg, while a minor contribution is due to the isotopes ^{110m}Ag and ^{124}Sb whose activity is 4 times lower and fast decreasing with time;

- in the dark matter regions the long lived nuclei of ^3H and ^{125}Sb with an activity of $\sim$ 7 μBq/kg for the former and of $\sim 15\mu$Bq/kg for the latter.

The influence of ^{60}Co in CUORE background was already considered in the evaluation of the contributions due to bulk contaminations of the crystals, while the contribution of ^{3}H and ^{125}Sb to the dark matter region is completely negligible if compared to the intrinsic background from all other sources.

5.3.3 Underground neutron, μ and γ interactions

The contribution from cosmic muons has not been taken into account in detail in the estimation of the background.

However, the following simplified arguments will serve to have an approximate idea of their contribution.

The depth of the LNGS (3500 m.w.e) reduces the muon flux down to $\sim 2 \times 10^{-8}$ cm$^{-2}s^{-1}$, but a further effective reduction could be obtained with the use of an efficient (99.9%) active veto for muons traversing the CUORE setup in order to tag possible events associated with them.

The muon-induced contribution to the background is therefore expected to be negligible.

On the other hand, the heavy shieldings surrounding the CUORE detector will substantially reduce the event rate due to environmental radiation of various origin (neutrons and photons), environmental radioactivity (natural decay chains U/Th, ^{210}Pb, ^{40}K,...), as well as muon interactions in the surroundings rock or in the shielding itself.

Neutrons may constitute a worrisome background for the dark matter experiment because for appropriate neutron energies (few MeV) they can produce nuclear recoils ($\lesssim$ 100 keV) in the detector target nuclei which would mimic WIMP interactions.

Their contribution to CUORE background has been evaluated by means of Monte Carlo simulations, taking into account both neutrons originated from radioactivity in the surroundings, and muon-induced ones.

The environmental neutron flux adopted was in agreement with the highest reported in literature ([109], [110]), and neutron flux produced by muons interacting in the rocks and in the CUORE 20 cm external lead shield was included as well.

The results demonstrated that neutrons contribution in the $0\nu\beta\beta$ region amounts to $\sim 4 \cdot 10^{-4}$ c/keV/kg/y.

$\sim 2 \cdot 10^{-4}$ c/keV/kg/y are due to neutrons produced in the rocks surrounding CUORE detector: this contribution is negligible if compared with the background level due to the radioactive contaminations in the detector's materials, and can be reduced by a neutron shield (a borated polyethylene shield, not included in the simulated setup).

$\sim 2 \cdot 10^{-4}$ c/keV/kg/y are due to muons interacting in the lead shield: this contribution, also negligible, will be reduced by a muon veto.

A preliminary evaluation of the influence of the environmental γ background in Gran Sasso resulted in a negligible contribution for the $0\nu\beta\beta$ region and a contribution similar to that of bulk contaminations for the dark matter region.

A more complete and detailed study of the background rates from external sources for CUORE is underway and will be used for the optimization of shieldings and muon veto.

5.3.4 Two neutrinos double beta decay background

Using the present upper limits for the ^{130}Te $2\nu\beta\beta$ half-life, the unavoidable background produced by the $2\nu\beta\beta$ decay in the dark matter region is lower than 10^{-4} c/keV/kg/y and is completely negligible in the $0\nu\beta\beta$ region.

This is true because of the relatively good energy resolution of the TeO_2 bolometers.

Chapter 6

CUORE and Cuoricino in the low energy range

"There are three kinds of lies: lies, damned lies, and statistics."
Benjamin Disraeli

Introduction

Even if neutrinoless double beta decay is the main scientific aim of CUORE, other interesting searches can be addressed with such a massive detector.

Dark matter detection experiments have largely benefitted in the past from the techniques developed for double beta decay searches and such a symbiosis is expected also in the case of CUORE.

A number of other searches for rare processes (rare nuclear α and β decays, electron and nucleon stability, etc.) could also take advantage of the large mass and low background of CUORE.

Solar axions could be searched in principle, detecting the photons produced after their conversion via Primakoff mechanism in CUORE crystals.

Most of the searches listed above imply the detection of very low energy events, namely events which would deposit in detectors like CUORE and Cuoricino less than ~ 50 keV.

This energy range is troublesome for CUORE, because the background level in this region is generally much higher than at the $0\nu\beta\beta$ Q value, and the origin of background events at such low energies is often nonphysical: since the signal to noise discrimination is harder for low amplitude signals, dealing with events in this range can be problematic.

In this respect Cuoricino turns out to be a precious tool for understanding how to deal with signals near threshold: the analysis of low energy events in Cuoricino is fundamental for the optimization of CUORE set-up in view of this kind of Physics.

In some cases, in particular, Cuoricino is already a competitive experiment: this is the case of some rare nuclear decays such as the ^{123}Te K-electron capture, for which significant results can be obtained from the data collected up to the present.

In this chapter the potential of CUORE and Cuoricino for Physics other than $0\nu\beta\beta$ will be presented.

The first sections will be devoted to an introduction to the physical problems which can in principle be addressed by CUORE and Cuoricino , and to the detection approach exploited.

Section 6.2 will deal with a study performed on Cuoricino background near threshold, both in view of the search for ^{123}Te K-electron capture, and as a feasibility study for other Physics at low energy with CUORE.

Afterwards, in section 6.2 the results of preliminary analysis performed on Cuoricino data in search of ^{123}Te K-electron capture will be described, and the results will be shown.

Finally, the implications for Cuoricino and CUORE Physics at low energies will be discussed.

6.1 The Physics of CUORE and Cuoricino at low energies

6.1.1 WIMP detection

Recent cosmological observations [111] provide compelling evidence for the existence of an important component of non-baryonic cold dark matter in the Universe.

The Dark Matter candidate particles are usually classified in *hot* Dark Matter (particles relativistic at decoupling time with masses $\leq 30\ eV$) and in *cold* Dark matter (particles non relativistic at temperatures greater than $10^4\ K$ with masses from few GeV to the TeV region or axions generated by symmetry breaking during promordial Universe).

The observed amount of small-scale structures [112, 113] rules out the hypothesis of a pure *hot* Dark Matter scenario; a pure *hot* Dark Matter scenario also disagrees with the measurements of the CMB radiation, which does not show sufficiently large inhomogeneities.

Oppositely, a pure *cold* dark matter scenario seems to be not favoured by the observed power spectrum of the density perturbations.

A mixed Dark Matter scenario in which *cold* Dark Matter candidates are present in large amount is generally favourably consedered.

Under the hypothesis that WIMPS are the main component of the dark matter, these particles should fill the galactic halos and explain the flat rotation curves which are observed in spiral galaxies.

The detection of such particles could be attempted both by means of direct and indirect methods.

The direct detection approach, which can be pursued with bolometric detectors, will be introduced in the next section.

A review of the most experienced detection techniques can be found, for instance, in [114, 115].

Generalities on the WIMP direct detection approach

The direct detection of WIMPs relies on the measurement of their elastic scattering off the target nuclei of a suitable detector [116].

The non relativistic and heavy (GeV - TeV) WIMPs could hit a detector nucleus producing a nuclear recoil of a few keV.

Because of the small WIMP-matter interaction cross sections the rate is extremely low.

In the case of SUSY WIMPs, most of the cross section predictions [117, 118, 119] (derived using MSSM as the basic frame implemented with different unification hypothesis) encompass a range of values several orders of magnitude (the so-called scatter plots) providing rates ranging from 1 $c/kg/day$ down to 10^{-5} $c/kg/day$ according to the particular SUSY model.

The predicted nuclear recoils rate (cpd/keV/kg) for the WIMP elastic scattering is given [115] by

$$\frac{dR}{dQ} = \frac{\sigma_0 \rho_0}{\sqrt{\pi} v_0 m_\chi m_r^2} F^2(Q) T(Q) \tag{6.1}$$

where σ_0 is the total WIMP-nucleon cross section at zero momentum transfer

$$\sigma_0 = \int_0^{4m_r^2 v^2} \frac{d\sigma(q=0)}{d|\mathbf{q}|^2} d|\mathbf{q}|^2. \tag{6.2}$$

ρ_0 is the local WIMP density, m_χ is the WIMP mass, $m_r^2 = m_\chi m_N/(m_\chi + m_N)$ is the nucleus-WIMP reduced mass, $v_0 \approx 220\ km \cdot s^{-1}$ is the circular speed of the Sum around the Galactic center.

$F(Q)$ is the nuclear form factor and $T(Q)$ is given by

$$T(Q) = \frac{\sqrt{\pi}}{2} v_0 \int_{v_{min}}^{\infty} \frac{f_1(v)}{v} dv \tag{6.3}$$

where $f_1(v)$ is the distribution of WIMPs speeds relative to the detector, found by integrating the three dimensional velocity distribution over angles (it is normalized to $\int f_1(v)dv = 1$), and v_{min} is given by

$$v_{min} = \sqrt{\frac{Q m_N}{2 m_r^2}} \tag{6.4}$$

For detectors with multiple elements, the differential rate is given by

$$\frac{dR}{dQ} = \sum_i f_i \frac{dR_i}{dQ} \tag{6.5}$$

where f_i is the mass fraction and $\frac{dR_i}{dQ}$ is the differential rate for element i.

Figure 6.1 shows the theoretical differential event rate versus deposited energy for several different nuclear form factors.

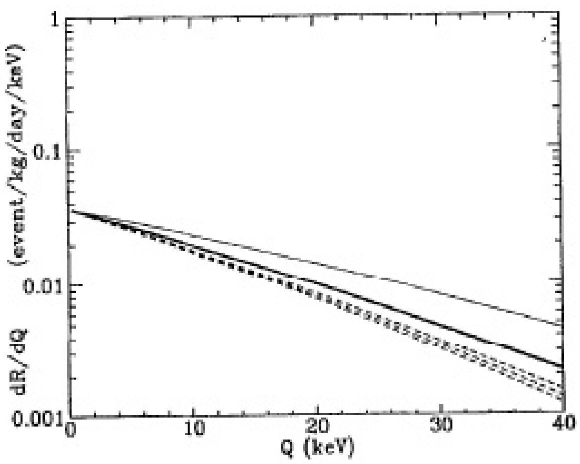

Figure 6.1: Theoretical differential event rate versus deposited energy for several different nuclear form factors. An arbitrary cross section if $\sigma = 4 \times 10^{-36}$ was chosen, with $m_\chi = 40\ GeV$ and $m_N = 68\ GeV$, and standard values of the other parameters. The light solid line shows $F(Q) = 1$ (no form factor) whereas the remaining lines are obtained adopting different estimates of form factors both for scalar and for spin dependent interactions. A Maxwellian distribution for the WIMPs speed has been chosen for the purpose of illustration.

It can be seen that the predicted signal for the WIMP elastic scattering has an exponentially decaying energy dependence, hardly distinguishable from the background recorded in the detector.

Two general approaches are followed when looking for WIMPS.

In case the statistics collected by direct experiments is poor, the simple comparison of the measured energy distribution with an expectation from a given model framework is carried out.

This approach, the only which can be pursued by either small scale of very poor duty cycle experiments, allows only to calculate model dependent limits on WIMP-nucleus cross section at a given C.L: it implies in fact some hypothesis to be done, on the WIMPs local density and distribution, on the mechanism dominating their interaction with the nuclei, and on the dependence of the WIMP-nucleus cross section on the WIMP-nucleon cross section.

A distinctive signature for WIMPs can instead be obtained from the correlation between the distribution of the events with the galactic motion of the Earth.

Three possibilities exist in principle.

According to the first one the recoil direction can be correlated with the Earth velocity [120, 121]: this approach is however practically discarded because of the technical difficulties in reliably detecting the short recoil tracks.

The second approach correlates the time of occurrence of each event with the diurnal rotation of the Earth [122]: a diurnal variation of the low energy WIMP rate is in fact expected since the Earth shields a given detector with a thickness variable during the sidereal day.

This effect is however expected to be appreciable only for relatively high cross section candidates.

The third possibility implies the search for an annual modulation signature, induced by the Earth revolution around the Sun: as a result, the detector is crossed by a WIMP flux whose intensity is expected to change during the year.

For the purpose of illustration, the differential recoil rate expected taking into account the motion of the Sun and the Earth in a Maxwellian halo is

$$\frac{dR}{dQ} = \frac{\sigma_0 \rho_0}{4 v_e m_\chi m_r^2} F^2(Q) \left[erf\left(\frac{v_{min} + v_e}{v_0}\right) - erf\left(\frac{v_{min} - v_e}{v_0}\right)\right] \tag{6.6}$$

where v_e id the Earth velocity

$$v_e = v_0 \left[1.05 + 0.07 \cos\left(\frac{2\pi(t - t_p)}{1\mathrm{y}}\right)\right] \tag{6.7}$$

$t_p =$ June $2^{nd} \pm 1.3$ days and v_{min} is given in equation 6.4.

The amount of the observable effect depends on different factors, such as the sensitivity of the experiment, the coupling of the WIMP candidate, its particle physics features, the target-nucleus used and the quality of the running conditions.

The relative annual variation of the signal is however small (a few percent) so in order to detect it one needs large detector masses to increase statistics and several periods of exposures to minimize systematics (it is worth to note that the detector's mass is instead not crucial for the "time-integrated" approach described above).

This approach has been pursued by several experiments [123, 124, 110] and since 1997 the DAMA group has reported a positive signal which stands now at 6.3 σ level.

Some of the main parameters typically contributing to determine the experimental sensitivity of a detector searching for WIMPs can be extracted from equation 6.1:

- *background counting rate*. Radioactivity and cosmic rays are the most important sources of spurious events. To reduce their contribution, WIMP searching experiments must be performed with heavily shielded detectors in underground laboratories

- *energy threshold.* The maximum sensitivity for WIMP-nucleus interactions is obtained for low recoiling energies thus the energy threshold of the detector must be kept as low as possible

- *nuclear recoil quenching factor*, i.e. sensitivity of the employed device to nuclear recoils

- total *detection efficiency*, which must take into account any kind of signal loss that could be produced during both data acquisition and data analysis

Although not included in this list, the *energy resolution* of the detector plays an important role in determining the value of the experimental sensitivity. This in fact provides a precious help for background identification and rejection.

Another very important feature is the ability to *reject ionizing events*: this is accomplished, for instance, scintillating bolometers.

Cuore prospects

As pointed out in the previous section, two approaches can be adopted to analyze the data collected by a dark-matter experiment: either the data can be integrated in time and used to set upper limit on the dark matter candidates masses and cross section, or an annual signal modulation in the signal rate can be searched as a distinctive signature of the presence of WIMPs.

In the former case the experimental signal rate has to be compared with the theorical WIMPs recoil rate.

As can be seen from equations 6.1 and 6.6, to calculate the theoretical WIMP rate, several hypothesis have to be made.

In particular, a specific form for the distribution of WIMPs speeds must be chosen and, in order to compare results of different experiments the cross sections mist be normalized per nucleon, and this requires to make an hypothesis on the kind of interaction contributing to the scattering process.

An important semplification occurs because the elastic scattering of dark-matter WIMPS takes place in the extreme nonrelativistic limit.

In particular, the axial-vector current becomes an interaction between the quark spin and the WIMP spin, while the vector and tensor currents assume the same form as the scalar interaction.

For a general WIMP, the rates from both spin and scalar interactions must be added together to get the total event rate (it is worth to remark, hovewer, that only nuclei with spin different from zero are sensitive to WIMPs with both spin independent (SI) and (SD) couplings).

The procedure is to calculate $\sigma_{0scalar}$ and σ_{0spin}, pick a form factor for each, and plug into equation 6.6: the comparison between the predicted time-integrated differential rate and the observed one allows to set upper limits on the pairs (m_χ,σ) at a given C.L.

As an example, figure 6.2 shows the exclusion plot obtained from the data collected by several experiments in the simple hypothesis of spin-independent WIMP-nucleus interaction

$$\sigma_{N\chi} = \sigma_{n\chi} A^2 \frac{m_r^2}{\mu_{W,n}^2} \tag{6.8}$$

where A is the target mass number, m_r^2 is the WIMP-nucleus reduced mass and $\mu_{W,n}^2$ is the WIMP-nucleon reduced mass.

Figure 6.3 shows the exclusion plots for spin-independent WIMP-matter interaction expected for two possible values of the background of CUORE: 0.05 and 0.01 c/keV/kg/day.

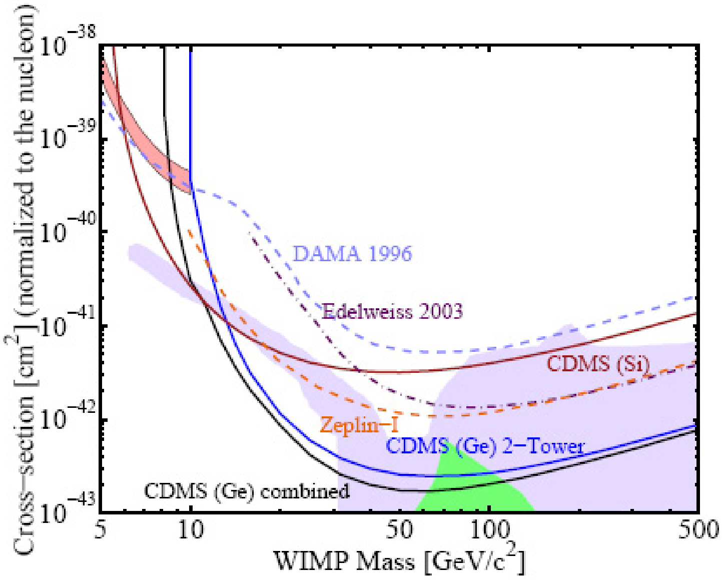

Figure 6.2: WIMP-nucleon cross section upper limits (90% C.L.) versus WIMP mass. The upper CDMS Ge curve also uses data from the current run, while the lower Ge curve includes the previous run [125]. Supersymmetric models allow the largest shaded (light-blue) region [126], and the smaller shaded (green) region [127]. The shaded region in the upper left (see text) is from DAMA [128], and experimental limits are from DAMA [129], EDELWEISS [130], and ZEPLIN [131].

The (m_W,σ) exclusion plot is derived by requiring the theoretically predicted signal for each mm_W and σ in each energy bin to be less than or equal to the (90% C.L.) Poisson upper limit of the recorded counts. The bin width is assumed to be equal to the detector resolution.

The plot has been obtained in the hypothesis that the WIMPs form an isotropic, isothermal, non-rotating halo (the isothermal sphere model) of density ρ = 0.3 GeV/cm^3, which has a Maxwellian velocity distribution and a the assumed relative Earth-halo velocity is v_0 = 220 km/s.

As previously mentioned, a modulation in time of the recoil rate could be also searched for in the data: due to the Earth's rotation around the Sun, the expected count rate of WIMP's scatterings off the target's nucleus changes periodically in time according to

$$S = S_o + S_m \cos\omega(t_i - t_0) \tag{6.9}$$

where S_0 and S_m are the constant and the modulated amplitude of the signal respectively.

The oscillating frequency is $\omega = 2\pi/T$ and the i index indicates the day.

The theoretical inputs introduced in the evaluation of the WIMP-nucleus elastic scattering (cross sections, nuclear form factors, scalar or spin dependent nature of the coupling) and all the parameters entering in the halo velocity distribution make the evaluation of the functions S_0 and S_m model dependent.

The amplitudes S_0 and S_m are expressed in terms of the WIMP mass m_W and of the WIMP-nucleus cross section σ.

Given a set of experimental count rates N_{ik} representing the number of events collected in

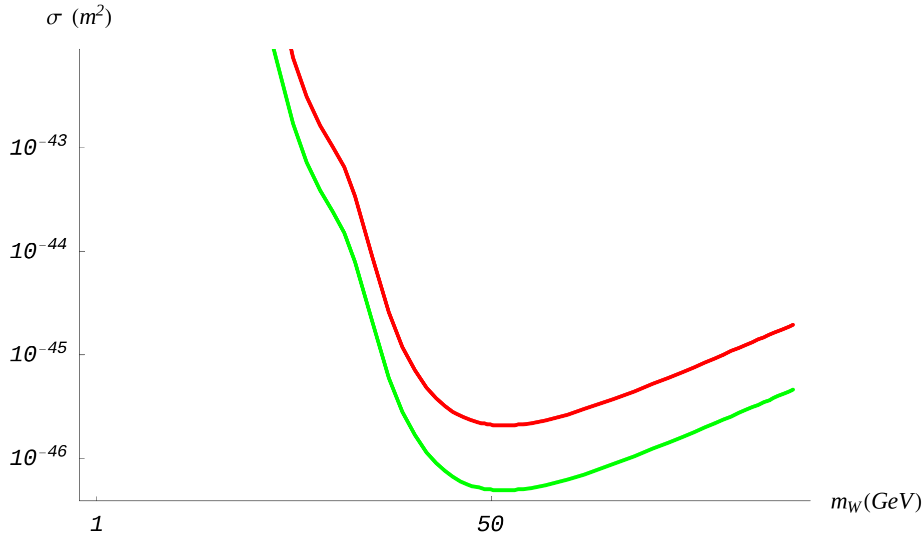

Figure 6.3: Exclusion plot projected for 2 year of CUORE assuming a threshold of 10 keV, a low energy resolution of 1 keV, and low energy background levels of 0.05 (red) and 0.01 (green) c/keV/kg/day respectively.

the i^{th} day and k^{th} energy bin, the mean value of N_{ik} is

$$\langle N_{ik} \rangle = [b_k + S_{0,k} + S_{m,k} \cos \omega (t_i - t_0)] \cdot W_{ik} \tag{6.10}$$

where the b_k and the $S_{ik} = S_{0,k} + S_{m,k} \cos \omega (t_i - t_0)$ represent the average background and the signal respectively, in number of counts per unit of detector mass, time and interval of collected energy E (which is related to the recoil energy Q by the relation $E = \alpha Q$ where α is the quenching factor of the detector).

$W_{ik} = M \Delta T_i \Delta E_k \epsilon_k$ are the corresponding exposures, where M is the mass of the detector, ΔE_k is the amplitude of the k^{th} energy bin, while ΔT_i represents the i^{th} time bin.

The ϵ_k are efficiencies that have to be taken into account whenever some subtraction method is used with the data.

Assuming that the average background rates b_k and the efficiencies ϵ_k are constant in time, a possible WIMP oscillating solution can be searched for in the data.

This implies that the time dependent fluctuations of background and efficiencies should stand well below the size of the searched modulation effect: if this condition is verified, a WIMP analysis is justified.

The sensitivity of CUORE to the annual modulation signal has been estimated in [132] assuming that all these fluctuations are controlled well below the levels needed: as discussed in [132], the sensitivity of a given experimental device to the annual modulation signal can be precisely quantified by means of the δ parameter, defined from the likelihood function L or, equivalently, from the χ^2 function of the cosine projections of the data

$$\delta^2 = -2 \log L(\sigma = 0) + 2 \log L_{min} \simeq \chi^2(\sigma = 0) - \chi^2_{min} \tag{6.11}$$

This parameter measures the statistical significance of the modulation signal detected in an experimental set of data.

Following a standard procedure a region of n standard deviations around the minimum in the plane (m_W,σ) can be found by imposing the condition $-2 \log L(m_W, \sigma) + 2 \log L_{min} \leq n^2$: δ^2 therefore assesses the goodness of the null hypothesis.

However, for a given (m_W,σ) and a given experiment, the expected value $\langle\delta^2\rangle$ can be estimated using the expression [132]

$$\langle\delta^2\rangle = \frac{1}{2}\sum_k \frac{S_{m,k}(\sigma, m_W)^2 \Delta E_k}{b_k + S_{0,k}} MT\beta + 2 \tag{6.12}$$

being β a coefficient accounting for the temporal distribution of the exposure time around modulation maxima and minima ($\beta = 1/n\sum_{i=1}^{n}\cos^2\omega(t_i - t_0)$ for n temporal bins).

Using this equation the region that could be within reach for CUORE, with the above mentioned assumptions on the background levels, has been extimated and the results are shown in figure 6.4.

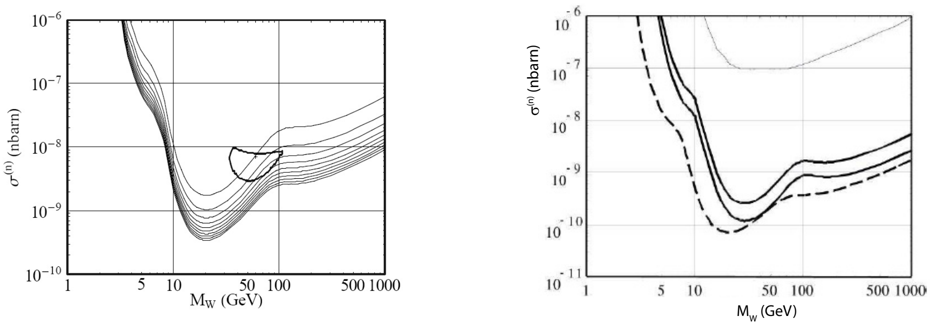

Figure 6.4: Left panel: sensitivity plots in the ($\sigma^{(n)} - m_W$) plane for a TeO_2 detector with threshold energy E_{th} = 5 keV, flat background b = 0.01 cpd/kg/keV and calculated for $\langle\delta^2\rangle = 5.6$. The set of curves correspond to different values of the exposure, $MT\beta$ = 10 to 100 kg $\cdot$ y in steps of 10 from top to bottom. The closed contour represents the 2σ C.L. region singled out by the modulation analysis performed by the DAMA experiment [133] and the cross indicates the minimum of the likelihood found by the same authors. Right panel: the solid lines represent the same sensitivity plot assuming a threshold of 10 keV, two years of exposure (1500 kg $\cdot$ y), flat backgrounds of 0.05 and 0.01 c/keV/kg/day and the same value for $\langle\delta^2\rangle$ The sensitivity curve has been compared with that obtained for a threshold of 5 keV with a background of 0.01 c/keV/kg/day (dashed line).

In conclusion, CUORE will be able to explore (and/or exclude) WIMPs lying in large regions of their parameter space.

The capability of CUORE to investigate the DAMA region through the exclusion plot (time integrated method) relies on getting a background of 0.1 c/keV/kg/day from 10 keV onwards, independently of more elaborated time modulation methods which require an exhaustive control of the stability of the experiment.

However, CUORE could also attempt to look for annual modulation of WIMP signals provided that the stability of the experiment is sufficient.

6.1.2 Solar axion detection

Axions are light pseudoscalar particles which arise in theories in which the Peccei- Quinn U(1) symmetry has been introduced to solve the strong CP problem [134]. They could have been produced in early stages of the Universe being attractive candidates for the cold dark matter (and in some particular scenarios for the hot dark matter) responsible to 1/3 of the ingredients of a flat universe.

Dark matter axions can exist in the mass window $10^{-6}\ eV < m_a \leq 10^{-2(3)}\ eV$, but hadronic axions could exist with masses around the eV.

Axions could also be copiously produced in the core of the stars by means of the Primakoff conversion of the plasma photons.

In particular, a nearby and powerful source of stellar axions would be the Sun.

The solar axion flux can be estimated [135, 136] within the standard solar model, resulting in an axion flux of an average energy of about 4 keV that can produce detectable X-rays when converted in an electromagnetic field.

Figure 6.5 shows the expected solar axion flux in proximity of the Earth.

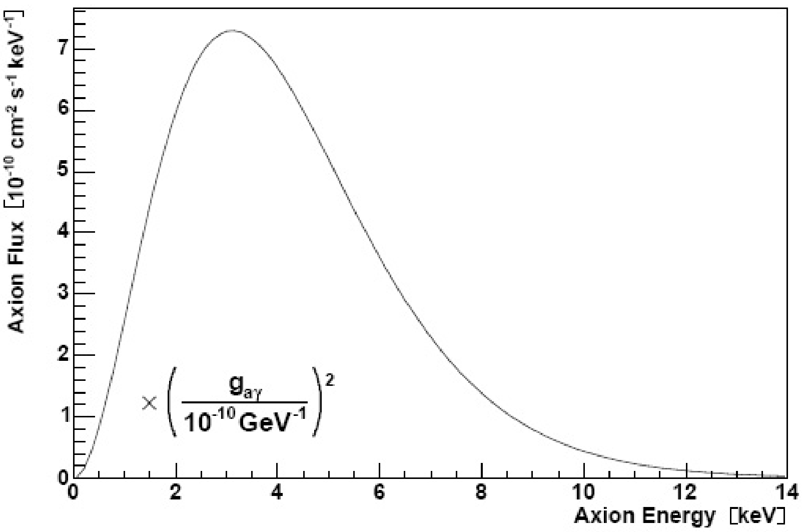

Figure 6.5: Axion flux spectrum at the Earth.

Single crystal detectors provide a simple mechanism for solar axion detection [136, 137].

Axions can pass in the proximity of the atomic nuclei of the crystal where the intense electric field can trigger their conversion into photons.

The detection rate is enhanced if axions from the Sun coherently convert into photons when their incident angle with a given crystalline plane fulfills the Bragg condition.

This induces a correlation of the signal with the position of the Sun which can be searched for in the data and allows for background subtraction. The potentiality of Primakoff conversion in crystals relies in the fact that it can explore a range of axion masses ($m_a \gtrsim 0.1$ keV) not accessible to other direct searches.

Moreover it is a relatively simple technique that can be directly applied to detectors searching for WIMPs.

Primakoff conversion using a crystal lattice has already been employed in two germanium experiments: SOLAX [138] and COSME-II [139] with the ensuing limits for axion-photon coupling $g_{a\gamma\gamma} \lesssim 2.8 \times 10^{-9}\ GeV^{-1}$ and $g_{a\gamma\gamma} \lesssim 2.7 \times 10^{-9}\ GeV^{-1}$ respectively.

Mass (kg)	Resolution (keV)	Treshold (keV)	Background (c/kg/keV/day)	$g_{a\gamma\gamma}^{lim}$ (2y) (GeV^{-1})
750	1	5	0.01	6.5×10^{-10}
750	1	5	0.05	8.0×10^{-10}
750	2	3	0.1	8.42×10^{-10}
750	2	5	0.1	9.0×10^{-10}
750	2	3	1	1.1×10^{-9}
750	2	5	1	1.2×10^{-9}

Table 6.1: Expected limits on the photon-axion coupling for 2 years of exposure of CUORE assuming the quoted values for the experimental parameters

Also the DAMA collaboration has analyzed 53437 $kg \cdot day$ of data of their NaI set up [140], in a search for solar axions, following the techniques developed in [141], where a calculation of the perspectives of various crystals detectors (including NaI) for solar axion searches has been made.

The DAMA result $g_{a\gamma\gamma} \lesssim 1.7 \times 10^{-9}\ GeV^{-1}$ improves slightly the limits obtained with other crystal detectors [138, 139] and agrees with the result predicted in [141, 142].

The use of CUORE to search for solar axions via Bragg scattering should have some advantages with respect to germanium detectors, because of the higher Z, larger mass and known orientation of the crystals.

Since the cross-section for Primakoff conversion depends on the square of the atomic number, TeO_2 will be a better candidate than Germanium.

A low energy threshold is mandatory because the expected signal lies in the energy region $2\ \text{keV} \lesssim E \lesssim 10\ \text{keV}$ and is peaked at $E \simeq 4$ keV.

As for dark matter searches, this requires of course specific R&D directed to a better performance in the low energy region.

A detailed analysis has been performed [141, 142] for a TeO_2 crystal (which has a tetragonal structure [143]) assuming different values for the experimental parameters.

As it is shown in ref. [141, 142], the bound on axion-photon coupling which a given experiment can achieve can be estimated through the expression

$$g_{a\gamma\gamma} < g_{a\gamma\gamma}^{lim} \simeq k \left(\frac{b}{\text{c/keV/kg/day}} \frac{kg}{M} \frac{y}{T} \right)^{1/8} \times 10^{-9}\text{GeV}^{-1} \tag{6.13}$$

where k depends on the crystal structure and material, as well as on the experimental threshold and resolution.

For the case of TeO_2 and a threshold of 5 keV, k has been calculated to be k = 2.9 assuming an energy resolution of 1 keV.

Cuore Prospects

The computation of expression 6.13 for some assumed values of the experimental parameters is shown in table 6.1 for CUORE.

Flat backgrounds and 2 years of exposure are assumed.

It is worth noticing the faible dependence of the ultimate achievable axion-photon coupling bound on the experimental parameters, background and exposure MT: the 1/8 power dependence of $g_{a\gamma\gamma}$ on such parameters softens their impact in the final result.

The best limit shown in table 6.1 is in fact only one order of magnitude better than the present limits of SOLAX and COSME-II.

The $g_{a\gamma\gamma}$ bound that CUORE could provide is depicted comparatively to other limits in figure 6.6.

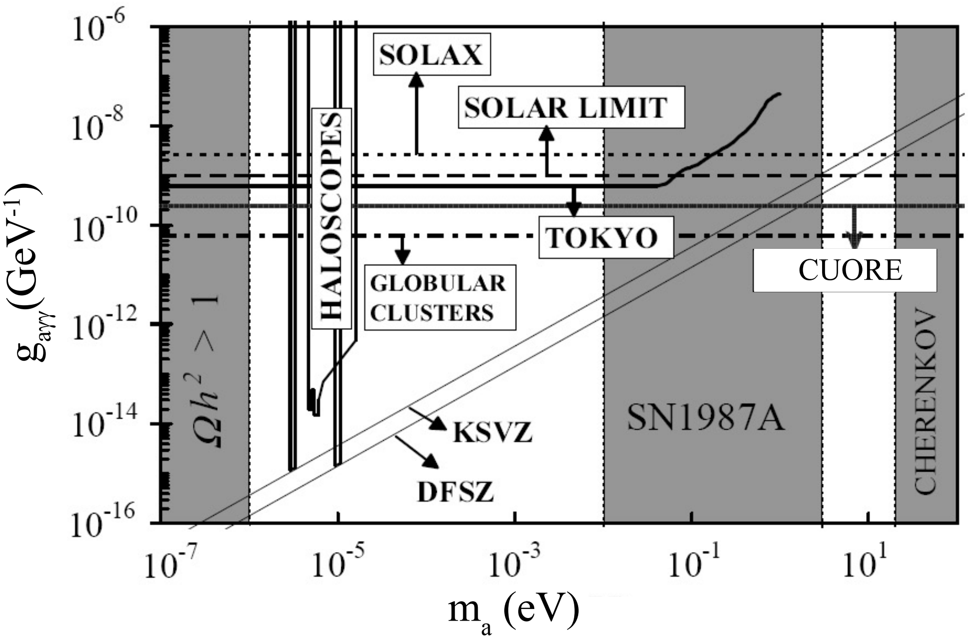

Figure 6.6: Best bound attainable with CUORE (straight line labelled "CUORE") compared with others limits.

It can be seen that the limit which can be expected from CUORE is better than the helio-seismological bound mentioned before (see figure 6.6 and table 6.1).

Notice however that an energy threshold $E_{tr} \leq 5$ keV (and resolution ≤ 2 keV) has been assumed.

As was described at length in [141, 142], the crucial parameters for estimating the perspectives on solar axion detectors with crystals rely on the energy threshold and resolution (appearing in k), and the level of background achieved (although the influence of this parameter is damped by a factor 1/8).

In particular, a threshold of 5-8 keV would loose most of the axion signal.

Other crystal detectors with, say, Ge or NaI (GENIUS, MAJORANA, GEDEON, DAMA, LIBRA, ANAIS,...) could surpass CUORE as axion detectors because the energy thresholds of these projects are supposed to be significantly lower. Also the background is expected to be better.

Summarizing, the requirements CUORE must satisfy in order to be competitive in the search for axions are the following:

- the energy threshold must be solid at or below 4 keV
- the background must be reduced at low energy to about 1-10 counts per day per kg per keV

- the crystal orientation must be known (see e.g. [136])
- a clever data analysis scheme must be developed to fully exploit the signal modulation of the Bragg coherent conversion of axions to photons to reduce background (see again [136])
- the energy resolution near threshold should be $E_{res} \leq 2$ keV

6.1.3 Other rare processes

The technique of massive thermal detectors is particularly suitable to search for many rare atomic or nuclear events.

Among the others, rare beta processes and apha decays can be investigated: the β decay of ^{113}Cd [144, 145], and the α decays of ^{209}Bi [146] and ^{180}W [147], are just some of the possible candidates.

The subject of section 6.3 will be the results obtained by Cuoricino in the search for ^{123}Te K-electron capture, a process theoretically predicted but never observed.

For a detailed review of the rare processes wich could be investigated with a bolometric detector see [107].

‘

6.2 Study of the background at low energy in Cuoricino

A feature common to many of the searches described in the previous sections is that they imply the analysis of events whose energy is less than ~ 50 keV.

In this section the main issues related to this energy range will be dealt with, and the results of a dedicated analysis performed on Cuoricino data near treshold will be discussed.

This work must be considered as a feasibility test for Cuoricino detector, but its results cannot trivially be extended to CUORE : as explained in the next section, the background at low energy is largely affected by the detector's features.

The thickness of the shielding, for instance, which in Cuoricino has been reduced to fit the preexistent cryostat[1], will be doubled for CUORE (see sections 3.2.3 and 5.1.3).

Other important differences between Cuoricino and CUORE will be in the cryostats themselves, and in the mechanical structure of the detectors: these are two major factors influencing the background at low energy, as will be shown below.

Although CUORE design will grant a proper background level at the $0\nu\beta\beta$ energy (see section 5.3), a reliable prediction on CUORE behaviour at low energy is instead very hard, being largely determined by details of the detector's behaviour.

6.2.1 Problematics

The main problem when considering low energy data collected by bolometric detectors is that, due to the need to lower the trigger treshold, even low amplitude fluctuations in the signal baseline can exceed the threshold and be sampled as physical pulses.

[1] The cryostat used for Cuoricino is the same previously used for the smaller MiBeta detector. As a consequence, the thickness of the lead shield surrounding the array has been reduced to 10 cm. The minimum thickness of the lead shield surrounding CUORE will be twice as much: 20 cm.

These fluctuations are caused by low frequency components in the microphonic noise, induced by vibrations or by particular conditions of the cryogenic apparatus[2], and appear as low amplitude pulses whose equivelent energy is $E \lesssim 50$ keV and whose shape is often variable.

Due to this effect the trigger rate at low energy is by far higher than at higher energies: for the purpose of illustration, the count rate measured by the best Cuoricino crystals is 1.69 ± 0.56 c/keV/kg/d at 15 keV, whereas the value measured at $0\nu\beta\beta$ is 0.18 ± 0.01 c/keV/kg/y.

As explained in section 3.3, fake pulses are rejected in Cuoricino by pulse shape analysis: before performing any kind of analysis, it is necessary to estimate the efficiency of the signal to noise discrimination methods exploited, thus assessing the reliability of the collected data.

Concerning the rejection of nonphysical events, different parameters are evalued for each acquired pulse, comparing its shape with the expected response function of the bolometer after Optimum Filter.

A confidence level is determined for each pulse shape parameter and for the rise and decay time of each pulse: signals falling within these intervals are defined as physical pulses, while signals having one or more of their parameters outside of the relevant interval are rejected as noise.

The larger is the separation of signal and noise pulses in the space of the shape parameters the better the strength and the reliability of this method are.

It turns out, however, that at low the two populations mix and when this happen it is no more possible to distinguish physical pulses from the noise; as a consequence, a "software" threshold is set at the energy value at which this happens, which is in general different for each bolometer.

Figure 6.7 shows this effect in Cuoricino data.

The efficiency of the method has to be evalued against two criteria: both the effectiveness in rejecting false pulses must be estimated, and the ability to recognize physical pulses without mistaking them for noise.

Then, if the data turn out to be reliable, they can be further analized.

Another major issue concerns the stability of the energy treshold.

The noise conditions of Cuoricino have proved to be very variable in time, both in the rate and in the shape of the observed spurious pulses, mainly because of their correlation with the status of the cryogenic system (see sections 3.2 and 3.3).

The overall response of each bolometer is moreover different, resulting in different pulse shape parameters distribution both for physical and for fake pulses.

Therefore, the effectiveness of the signal to noise discrimination method is in general different from channel to channel, and it often changes in time even for the same channel, because of the mentioned variability of the noise conditions.

As a result the (software) energy threshold is in general different for each bolometer and its value changes in time, being different, fon instance, from one data set[3] to another.

The available statistics at low energy depends on the number of channels having a threshold low enough for the kind of analysis to be performed: in this respect the stability of the energy threshold is crucial in view of anly kind of low energy analysis with CUORE detector.

6.2.2 Data Analysis

The results of the analysis performed on the data collected with Cuoricino till the end of July 2005 will be presented in the following.

[2]Fake pulses are due, in Cuoricino , to microphonism induced by vibrations of the detector caused by pumps, or by the evaporation of the helium bath. Spurious events are generated also by the occasional presence of helium in the Inner Vacuum Chamber, or by oscillations of the hanging tower of crystals.

[3]A data set comprises all the measurements taken in between two subsequent calibrations, see section 3.3.1

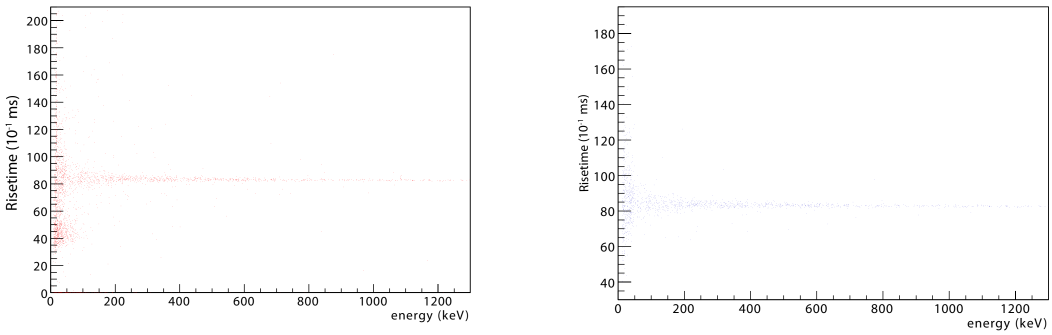

Figure 6.7: Left panel: Rise time versus energy of some pulses acquired by Cuoricino detector before any selection is made: two separate populations of pulses appear im the plot, the lower one being composed of fake (noise) pulses. Right panel: the plot shows the same events after a selection on the basis of their pulse shape parameters. The mixing of the two classes of pulses at low energies can be observed in the first plot, whereas the selection operated on the grounds of shape parameters is appearent from the difference between the two.

This section will focus on a general study dedicated to Cuoricino background at low energy, with reference to the issues just raised, whereas section 6.3 will deal in particular with the results obtained concerning the search for ^{123}Te K-electron capture.

Cuoricino data taking started in April 2003: after six months, in October 2003, the detector was warmed up for maintenance and cooled down again in May 2004; since then data taking is proceeding uninterrupted.

The run performed during the first cool down is termed *run 1*, the current one is termed *run 2*.

The total statistics collected by Cuoricino detector up to the 27^{th} of July 2005 is 152488 $kg \cdot h$; table 6.2 shows the details for each data set.

As explained in section 3.3, during each measurement a reference pulse was generated by means the Si heater that is glued on each crystal, with the purpose to correct gain instabilities that would otherwise spoil the energy resolution of the detectors in time.

The reference pulse is generated with a frequency of about 1 every 300 seconds and corresponds to an energy position of $\sim$ 1500 keV.

Since the 8^{th} data set of run 2 two more reference pulses were added, the former at an energy of $\sim$ 70 keV, the latter at an energy of $\sim 5-10$ MeV (depending on the detector): the first one, in particular, had the purpose of assessing the stability of the energy treshold.

Unfortunately, during most of the measurements listed in table 6.2 the noise conditions were such that the energy treshold could not be kept low ($\lesssim$ 30 keV) for any detector: the only data sets in which some channels had a low enough treshold were the $1^{st}, 2^{nd}, 9^{th}$ and 10^{th} of run 2.

Among these, the 1^{st} and 2^{nd} data sets showed the presence of a Rn contamination, observed

Data set	measurement start	measurement stop	time (h)	Working detectors $5\times5\times5$	Working detectors $3\times3\times6$	Statistics ($kg\cdot h$) $5\times5\times5$	Statistics ($kg\cdot h$) $3\times3\times6$	Statistics ($kg\cdot h$) ^{130}Te	Statistics ($kg\cdot h$) ^{128}Te
Run 1									
2	Apr 22, 2003	May 13, 2003	458	29	11	10430	-	-	-
3	May 26, 2003	Jun 13, 2003	424	28	11	9376	1539	280	280
4	Jul 11, 2003	Jul 19, 2003	210	29	11	4816	763	139	139
5	Oct 13, 2003	Oct 27, 2003	230	29	9	5253	681	759	151
Run 2									
1	May 11, 2004	May 17, 2004	131	35	13	3608	560	86	86
2	May 25, 2004	June 10, 2004	260	38	13	7890	1115	172	172
3	Aug 24, 2004	Oct 9, 2004	654	39	13	19376	2805	432	432
4	Oct 21, 2004	Nov 10, 2004	380	40	13	11742	1629	250	250
5	Nov 14, 2004	Dec 6, 2004	375	40	13	11782	1605	247	247
6	Dec 15, 2004	Jan 5, 2005	434	26	12	8930	1709	285	285
7	Jan 18, 2005	Feb 14, 2005	571	39	6	17541	1127	376	376
8	Feb 17, 2005	Mar 27, 2005	856	39	9	26020	2505	555	551
9	Apr 6, 2005	May 13, 2005	308.6	40	13	9752	1324	204	204
10	Jun 29, 2005	Jul 27, 2005	485	36	12	13975	1736	315	312

Table 6.2: Cuoricino statistics collected up to the end of July 2005. The labels "^{130}Te" and "^{128}Te" indicate the two ^{130}Te enriched crystals and the two ^{128}Te enriched crystals respectively. $5\times5\times5$ and $3\times3\times6$ indicate the $5\times5\times5$ cm^3 and the $3\times3\times6$ cm^3 crystals respectively.

as an increase in the background counting rate on both continuum and the ^{214}Bi peaks[4], hence they were discarded in the following analysis, which was therefore limited to the 9^{th} and 10^{th} data sets.

The ultimate goal of this analysis was the search for ^{123}Te K-electron capture, whose signature, as will be explained in section 6.3, is a monochromatic line at 30 keV; the only detectors whose energy treshold was low enough for this kind of analysis were six, and they corresponded to channels 15, 16, 17, 56, 64, 67.

The crystals of all these channels were all $5\times5\times5\times$ cm^3 in size.

The first study performed on the data was aimed to estabilish if any physical pulse was erroneously rejected by the selection method adopted to discriminate between signal and noise.

The pulses generated by the Si heaters have been used for this purpose: as already mentioned, one of the heat pulses periodically generated by the heater glued on each crystal has an equivalent energy of ~ 70 keV.

Since the time of occurrence and amplitude of these pulses are known (the data acquired within a time window of 1 s are flagged), they can easily be found and recognized among the other: a comparison of the number of heater pulses retrieved from the data with the expected one, exactly known, allows to determine the amount of physical pulses erroneously rejected by the signal to noise discrimination method.

The results obtained for channels 15, 17, 56 and 64 are shown in figure 6.9: channels 16 and 67 could not be used for this analysis because of some problems with the system controlling the generation of the heat pulses.

The figure shows, for each of the four detectors, the fraction of heater pulses which passed the noise rejection cuts, calculated as

$$\varepsilon = \frac{N_{expected} - N_{found}}{N_{expected}}. \tag{6.14}$$

[4]Radon is an intermediate mamber of the radioactive decay chains of ^{238}U, ^{235}U and ^{232}Th. It may escape from the rock and diffuse in the interstitial air or in the underground water. Its longer living progeny ^{210}Pb is readily attached to aerosols and naturally deposited on the surface by washout and by dry deposition. ^{222}Rn, in particular, belongs to the ^{238}U decay chain; its presence is observed as a raise in the background counting rate on both the continuum and the ^{214}Bi gamma lines. Figure 6.8 shows the most intense ^{214}Bi gamma line, at ~ 609 keV, as measured during four different data sets.

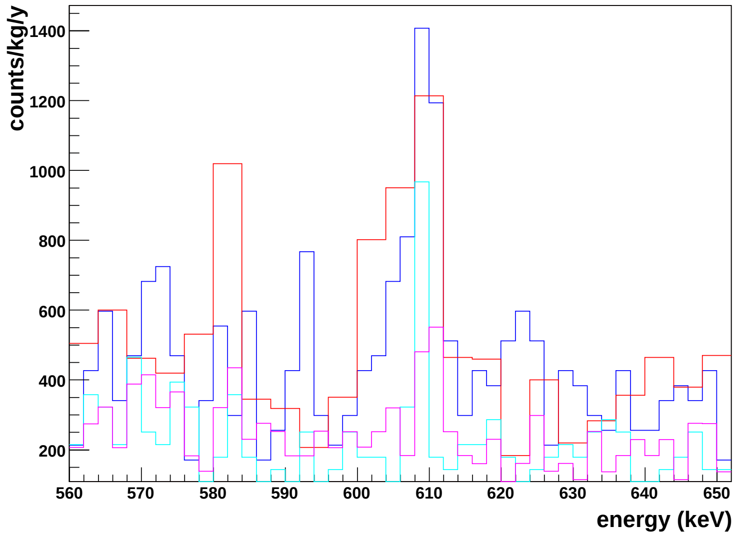

Figure 6.8: ^{214}Bi gamma line measured during data sets 1(red), 2(blue), 9(azure) and 10(violet). The higher counting rate observed in the first two sets demonstrates a radon contamination.

The found values are very close to 1, the slight differeces being due to chance overlaps of physical pulses with the heat ones[5], which can be easily calculated from the known average event rate per channel ($\sim 2\ mHz$) and from the time duration of each recorded pulse ($\sim 3\ s$) as

$$P(k \geqslant 1, \mu = 2 \cdot 10^{-3}\ Hz \times 5\ s) = 1 - P(k = 0, \mu) = 1 - \frac{\mu^0 \cdot e^{-\mu}}{0!} \simeq 0.006. \tag{6.15}$$

This proves that, with some caveats, the fraction of physical pulses mistaken for noise is negligible.

The caveats are the following:

1. the heat pulse used had an equivalent energy of $\sim$ 70 keV. The efficiency of the noise rejection method at lower energies is probably worse.

2. the shape of the heat pulse is slightly different from that of the physical ones: the efficiency of a pulse shape discrimination method might be different for heat and from physical pulses.

Concerning the former, some measurements with reference pulses at lower energies are scheduled for the next future.

In order to accurately determine the efficiency of the signal to noise discrimination method on physical pulses, a mechanism capable of generating pulses and noise is required: this can be done, for instances, exploiting artificial neural networks.

[5]in case of pile up, both pulses are discarded, since the consequent changes in the pulses' shapes makes them useless.

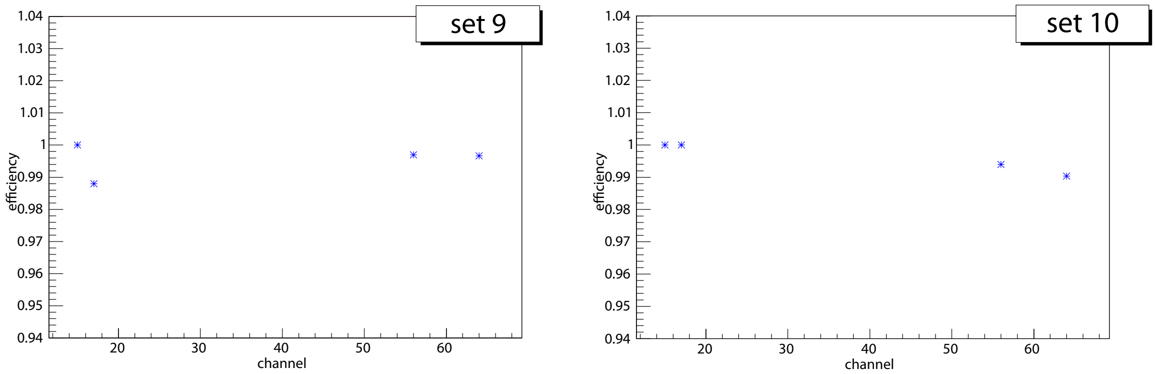

Figure 6.9: The fraction of heater pulses which passed the noise rejection cuts is shown for channels 15, 17, 56 and 64: in the left panel the results obtained for set 9 are shown, while in the right panel those corresponding to the set 10 can be seen. All the values found are very close to 1.

This procedure is currently being studied and will be applied in the next future.

A second study was made to check wether some noise did pass the cuts aimed to reject it.

Since the noise is not known a priori, both in the shape and in the time of occurrence, there is not a method to determine exactly the amount of noise left; however, some consistence checks can be made.

Cuoricino physical pulses are generated by radioactive decays, which are typical random events: the distribution of the time intervals between adjacent ones is therefore exponential [80], and in particular is given by

$$I(t) = re^{-rt} \tag{6.16}$$

where r is the average event rate. If some non-random noise contaminates the data, the measured I(t) should not agree with the equation 6.16.

The distribution of the time intervals between the events occurred in the same detector have been obtained for the data sets 9 and 10; each of the six channels (as before: 15, 16, 17, 56, 63, 67) analyzed has been considered independently, and the time intervals between events with energy in the interval 20 keV $< E <$ 30 keV have been gathered in the same histogram.

Figure 6.10 shows the distributions obtained for the events from the 10^{th} data set: the events filling the histogram in the left panel are all those acquired, whereas in the right panel only those events which passed the signal-to-noise selection are shown. Both histograms have been fitted with an exponential function and the parameters have been left free in the fit.

An eccess of events at low values of t can be seen in left hand side plot: this indicates the presence of pulses whose time distribution is not random and whose typical repetition interval is less than 500 s.

Those pulses, most likely originated from noise, are missing in the right hand side plot, and have therefore been correctly rejected by the signal-to-noise discrimination algorythm: their time distribution is easily understood considering that spurious events often appear in bursts, being due to transitory conditions of the system or to fortuitous external interferences.

It can be shown that the presence of these fast, time correlated pulses modifies the fitting distribution function so that its slope, which in case of random events should be equal to the event rate (see equation 6.16), is no more compatible with it.

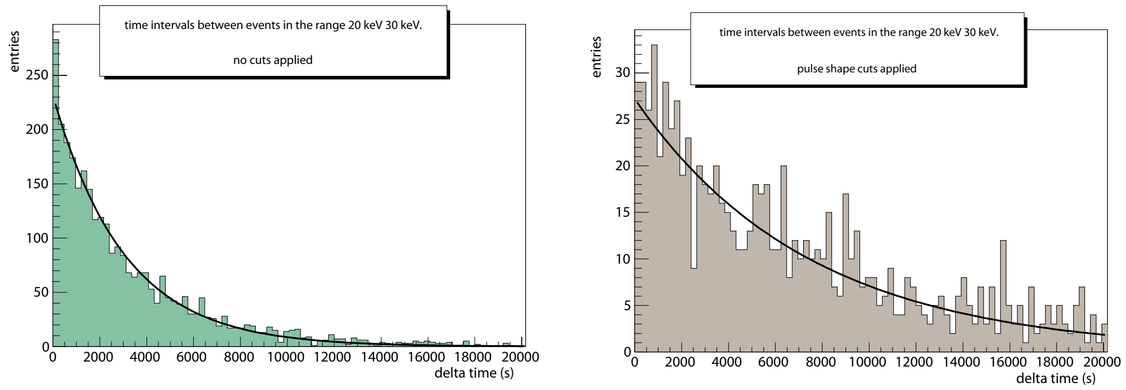

Figure 6.10: Distribution of the time intervals between pulses occurred in the same detector in the energy interval $20\ \mathrm{keV} < E < 30\ \mathrm{keV}$. The data shown correspond to set 10, channels 15, 16, 17, 56, 63, 67. Left panel: distribution obtained for all the pulses collected by the DAQ system. Right panel: distribution of the pulses selected by the signal-to-noise discrimination algorythm. Both histograms have been fitted with an exponential function and the parameters have been left free in the fit.

Figure 6.11 shows both the measured and the expected event rate in different energy intervals, for the data of the 10^{th} set.

The measured event rate has been obtained as the slope of the exponential function fitting the distribution of the time intervals with energies in the considered range (its value was left free in the fit), whereas the expected event rate has been calculated as the ratio of the number of events in that energy interval and the time duration of the measurement.

The values shown on the horizontal axis are the middle point of the energy interval considered during the time distribution fit.

It can be seen that before the event selection the measured rate is not compatible (error bars are 3σ wide) with the expected one for the lower energy pulses: this means that their time interval distribution is not accounted for by equation 6.16 if the expected value for the rate r is used.

The agreement is found after the noise pulses are rejected from the data by pulse shape analysis (right panel), and this suggest that the selection cuts applied are effective in eliminating most of the non-random noise.

This is also supported by the fact that the results obtained performing the same kind of analysis on the 9^{th} set of data are basically the same.

However this kind of analysis does not provide any quantitative result, and it has a great limit: if any random noise contaminates the data its presence would be completely unobservable by the method just described.

A cross check of the correctness of the previously evalued efficiencies is obtained verifying that the the background level is stable in time: whatever fluctuation in time is found at low energy, its origin should be ascribable to radon contaminations (or to lead, its longer lived daughter), and it must therefore be correlated with higher energy events, namely with the ^{214}Bi γ lines, as previously explained.

The *anticoincidence*[6] events energy spectra of each detector was obtained for the 4 data

[6]the term *anticoincidence* indicates those events occurring on a single detector only

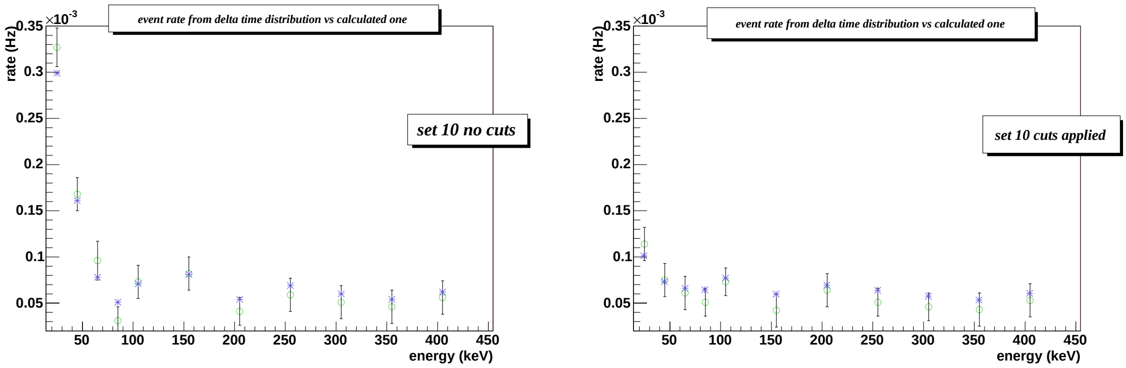

Figure 6.11: The plots show the measured (green circles) and expected (blue stars) event rates in different energy intervals. On the horizontal axis the middle value of the considered energy interval is reported. The error bars on the expected values are too small to be seen. The measured event rate has been obtained as the slope of the exponential function fitting the distribution of the time intervals with energies in the considered range, whereas the expected event rate has been calculated as the ratio of the number of events in that energy interval and the measurement time. The plot on the left panel has been obtained considering all the data collected during set 10, while the right hans side plot has been obtained considering only those events selected by the signal-to-noise discrimination algorythm.

sets considered in this study (only the events selected on the basis of their pulse shapes were included), and the check that the event rate in each energy bin was statistically compatible from set to set was made; in particular, the width of each energy bin was chosen approximately equal to the measured energy resolution ($\simeq$ 1.4 keV FWHM measured from the 46 keV γ line of ^{210}Bi).

The only statistically significant fluctuations in the event rate were found in the 1^{st} and 2^{nd} data sets and were attributed to a radon contamination, as already discussed; after this control the two sets were in fact excluded from the next analysis.

A similar check was performed comparing the data collected by different detectors: this control has the purpose to find out possible anomalies in single channels, under the assumption of an uniform contamination for all of them.

As in the previous case, the event rate in each energy bin was required to be statistically compatible from channel to channel, and the requirement was found to be satisfied.

The study described in this section produced results in support of the reliability of Cuoricino data near treshold; in particular the signal to noise discrimination method exploited for Cuoricino data analysis has been proved to reduce the number of noise pulses under appreciable levels (the noise pulses have been identified here on the grounds of their different shape or time distribution).

6.3 The search for ^{123}Te K-electron capture with Cuoricino

6.3.1 Introduction

The process this section deals with is the capture of a K-shell atomic electron by its nucleus, described by the reaction

$$(A, Z) + e^-(K - shell) \longrightarrow (A, Z - 1) + \nu_e. \tag{6.17}$$

In particular the decay considered here is the following:

$$^{123}\mathrm{Te}(1/2^+, g.s.) + e^-(K - shell) \longrightarrow ^{123}\mathrm{Sb}(7/2^+, g.s.) + \nu_e \tag{6.18}$$

where $g.s.$ stands for *ground state*.

This process is a second-forbidden[7] transition with a Q value $Q_{EC} = 53.3 \pm 0.2$ keV.

The interest in this decay lays in the fact that the most stringent tests on the predictive power of the adopted models of nuclear structure are nowadays provided by the experimental measurements of very rare electroweak decays such as the nuclear double beta decay [148], the nuclear (μ^-, e^-) conversion, and highly forbidden β-decay and electron-capture (EC) processes [149].

Because of this reason, the measurement of ^{123}Te K-EC lifetime is interesting also in view of CUORE , where nuclear matrix elements enter in the determination of $\langle m_{\beta\beta} \rangle$ from the ^{130}Te $0\nu\beta\beta$ halflife.

After an electron capture (EC) occurs, a vacancy is left in an atomic shell of the daughter nucleus, and is immediately filled by outer electrons: EC processes are in fact observable through the atomic deexcitation cascade (X-rays and/or Auger electrons) following the decay.

In principle the captured electrons can emit photons with a continuous energy spectrum: this decay, named Internal Bremmstrahlung Electron Capture (IBEC) is however a second order process and it is by far less probable than the non radiative transition: the number of photons per capture emitted is approximately 10^{-4}.

The favourite way to observe this decay is therefore through the detection of the subsequent atomic deexcitation, and this can be pursued exploiting either of the two following approaches.

Individual atomic transitions (single X-rays or Auger electrons) can be observed using a detector in direct contact, but external to the decay source.

A single line corresponding to the binding energy of the captured electron (sum of all atomic transition energies) is on the contrary expected for a pure calorimetric approach, in which the source is also the detector (as is the case for a low temperature thermal detector.

Unfortunately, atomic deexcitation cascades can be induced also by the interaction between the environmental radiation and the source (e.g. photoelectric or Compton effect).

In this case, however, the involved atomic levels are those of the parent atom, while in a genuine EC decay they correspond to those of the daughter one.

Considering in particular the search for ^{123}Te K-electron capture with a calorimetric detector, discussed here, a single line at 30.5 keV is expected as decay signature.

[7] An *allowed* transition occurs between states with the same parity ($\pi_i \cdot \pi_f = +1$) and with a spin difference of $J_i - J_f = \Delta J = 0$ or ± 1.
Forbidden transitions are non-allowed transitions and are further subdivided into their order of forbiddenness, the transitions becoming slower as the order increases.
A general definition for an n-times forbidden beta transition is:

$$\Delta\pi = \pi_i \cdot \pi_f = (-1)^n, \quad \Delta J = n,\ n+1 \quad \text{(except first-forbidden which may have } \Delta J = 0\text{)}$$

$$\Delta J = n + 1 \quad \text{transitions are called } n^{th} \text{ forbidden-unique beta transitions}$$

6.3.2 A brief history

Evidence for the K EC decay of ^{123}Te was obtained by Watt and Glover [150] with a lifetime $t^K_{1/2} = (1.24 \pm 0.10) \times 10^{13}$ y, using a proportional counter.

Such a value is still reported in the Nuclear Tables [151].

Only the X-rays escaping from the Te source (anode wires) could be recorded in such an experiment.

Furthermore, due to the insufficient energy resolution of the proportional counter, there was no possibility to discriminate between the Sb X-ray line at 26.1 keV, distinctive of Te EC decay, and the 27.3 Te X-ray line due to the excitation of the tellurium source by cosmic rays and radioactivity.

The inclusion of a non negligible background contribution (the experiment was carried out at sea level) could explain therefore why the authors obtained a so large rate for this process.

This result was contradicted by a a previous cryogenic experiment carried out underground by Fiorini's group using a low activity setup consisting of four thermal 340 g TeO_2 detectors.

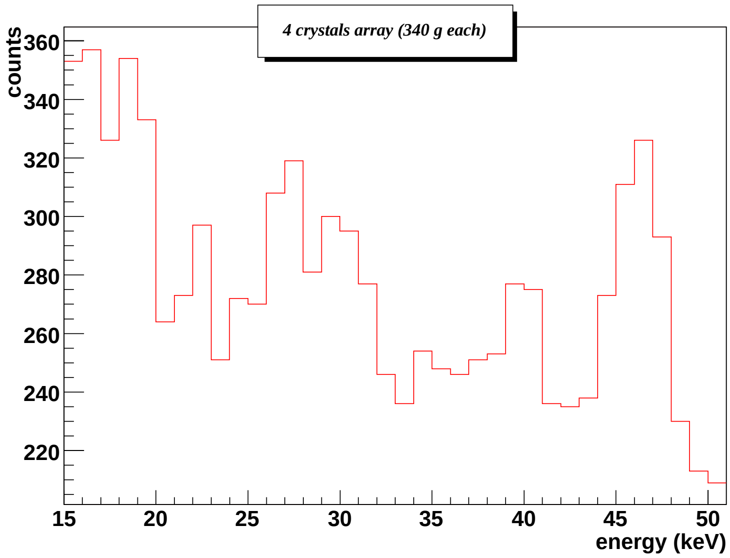

Figure 6.12: Energy spectrum obtained by Fiorini's group operating an array of four TeO_2 crystals of 340 g each. Two peaks are clearly visible in the spectrum: a peak at 27.3 keV corresponding to the energy of Te K_α X-rays and a peak at 30.5 keV, corresponding to the total energy released by Te K EC to Sb.

In addition to the almost complete elimination of the external background due to cosmic rays, special care was devoted to the reduction of background from environmenthal radioactivity.

Thanks to the good energy resolution of the detectors, two peaks could be distinguished in the spectrum recorded at low energy: a peak at 27.3 keV corresponding to the energy of Te K_α X-rays (produced by the interaction of radiation with nearby Te detectors), and a peak at 30.5 keV, corresponding to the total energy released by Te K EC to Sb.

The energy spectrum obtained is shown in figure 6.12.

The different origin of the two peaks was demonstrated by the comparison of the spectra collected requiring or not an anticoincidence between the four TeO_2 detectors [152]: the 27.3 keV line in fact disappeared in the anticoincidence spectra.

By attributing the 30.5 keV peak to K EC of ^{130}Te an evidence for this process was obtained and a lifetime $t^K_{1/2} = (2.4 \pm 0.9) \times 10^{19}$ y was quoted, six orders of magnitude higher than in the experiment by Watt and Glover.

The next experiment performed by the same group showed that the 30.5 keV line, previously attributed to ^{123}Te K-electron capture, was instead due to ^{121}Te and ^{121m}Te: these short lived ($\tau_{1/2}(^{121}\text{Te}) = 16.8\ d$, $\tau_{1/2}(^{121m}\text{Te}) = 154\ d$) isomers are produced by neutron activation of ^{120}Te and yeld the same signal as the one expected for the EC decay of ^{123}Te.

Although the expected neutron activation in the underground laboratory is negligible (thermal neutrons are suppressed by a factor of 10^4 with respect to sea level), ^{121}Te and ^{121m}Te nuclei could have been produced when the detectors were outside the laboratory.

A larger cryogenic setup consisting of an array of twenty 340 g crystals of natural TeO_2 [152] was realized (fig. 6.13), and two separate data taking runs performed.

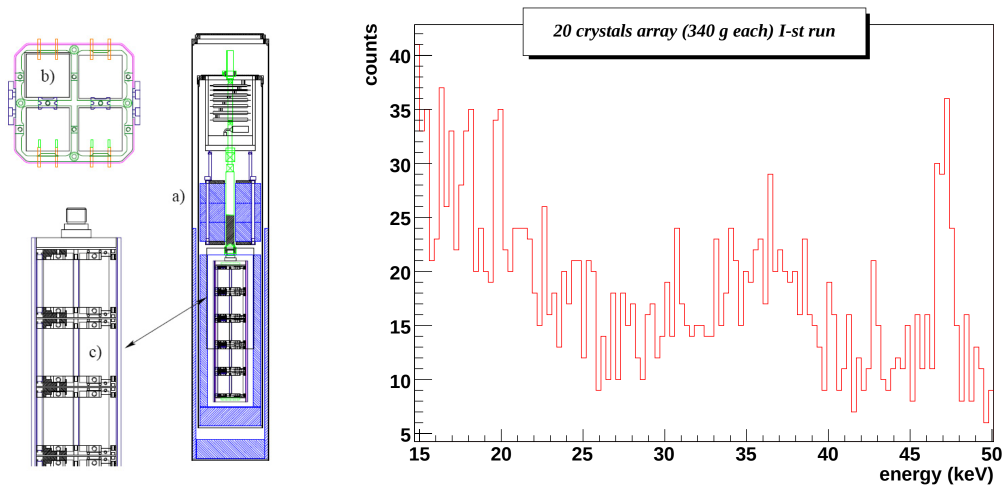

Figure 6.13: Left panel: cryogenic setup used in the second measurement performed by Fiorini's group (a). Details of the inner Roman lead shield are apparent. Top (b) and side (c) view of the 20 TeO_2 crystal array are also shown. Right panel: single site events energy spectrum obtained: no evidence of the 30.5 keV peak can be seen.

The former (Run 1) started two years after the crystals were stored underground, in order to allow a substantial decay of the ^{121}Te and ^{121m}Te nuclei produced during their preparation.

The spectrum corresponding to 724.88 h $\times$ kg of effective running time is shown in fig. 6.13.

The disappearance of the 27 keV X-ray peak due to background excitation of Tellurium can be explained by the reduced level of the background (about one order of magnitude).

The peak at 46.5 keV is due to surface activity of ^{210}Pb; the same contamination is also responsible of the bump at ~ 35 keV[8].

In this first run no evidence was found of the peak at 30.5 keV, where the observed counts are 17 ± 12.

[8] As confirmed by Monte Carlo simulations this bump is the consequence of the ensemble of processes (γ absorbtion and atomic rearrangement) following the β decay of ^{210}Pb to the 46.5 keV excited state of ^{210}Bi

In order to assess the origin of the disagreement with the previous result, a second run was performed after all crystals were brought outside the underground laboratory for a surface treatment.

They remained in fact exposed to environmental neutrons for a period of about two months, and they were again installed underground afterwards.

During this second run, totalling 259.59 h $\times$ kg, a peak at 30.5 keV was found, and was therefore attributed to the K EC of ^{121}Te isomers produced by cosmic ray neutrons outside the tunnel and not to K EC of ^{123}Te.

By applying a maximum likelihood analysis to the data collected during the first run, a 90 % C.L. lower limit $t^K_{1/2} > 5 \times 10^{19}$ y on the half lifetime for K EC of ^{123}Te was set.

6.3.3 Data analysis and the result of Cuoricino

The statistics collected by Cuoricino at low energy is 156.61 kg $\times$ d: as discussed in section 6.2 the corresponding data have been collected by six of the 64 crystals composing the array.

The spectrum obtained collecting all the single site events is shown in figure 6.14.

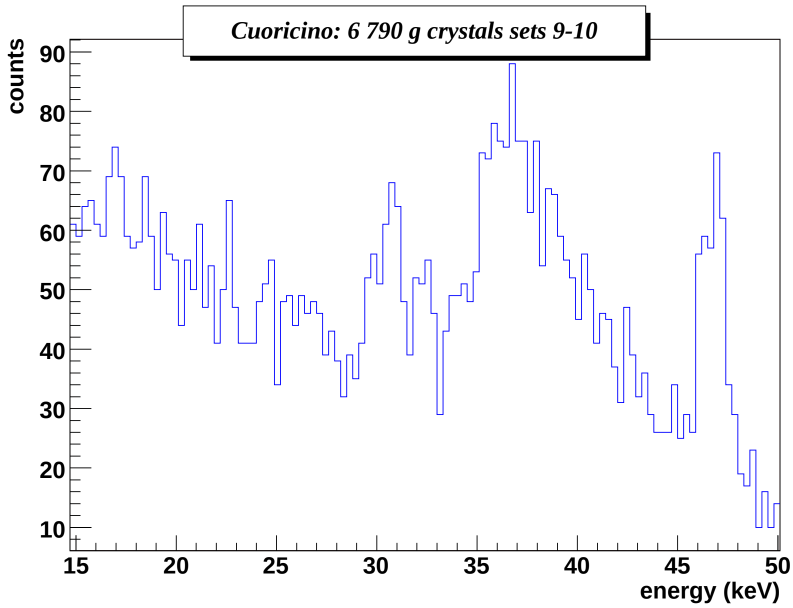

Figure 6.14: Energy spectrum obtained from six crystals of Cuoricino detector. Only single site events have been considered. A peak at 30.5 keV is clearly visible.

The background in this energy region has both a continuous component, due to β decays and γs, and a discrete one: monoenergetic lines are observable originated by nuclear and atomic decays.

Among the nuclear γ lines the most evident is at 46.5 keV and it is due to ^{210}Bi deexcitation following ^{210}Pb β decay.

The most important atomic lines contributing to the background in this region are those, already mentioned, due to ^{121}Te and ^{121m}Te K-electron capture.

A peak at 30.7 keV is clearly visible in Cuoricino spectrum, but before attributing it to ^{123}Te K EC other possible contributions to it must be excluded.

Energy Interval (eV)		**neutron flux (10^{-6} n/cm^2/s)**	
Low	High	Belli [154]	Arneodo [109]
0.00E+000	5.00E-002	1	-
5.00E-002	1.00E+003	1.8	-
1.00E+003	2.50E+006	0.54	-
1.00E+006	2.50E+006	-	0.14
2.50E+006	5.00E+006	0.27	0.13
5.00E+006	1.00E+007	0.05	0.15
1.00E+007	1.50E+007	6.00E-004	4.00E-004
1.50E+007	2.50E+007	5.00E-007	-

Table 6.3: Measured neutron flux at LNGS.

According to [153], the only contribution to a 30.7 keV γ line could come from ^{121}Te and ^{121m}Te K-electron capture.

Both isomers are produced by neutron activation of ^{120}Te, present in TeO_2 with a 0.908% abundance.

^{120}Te could in principle have been activated by environmental neutrons in the underground laboratories, or the line could have been due to a residual activity of ^{121}Te induced by cosmic rays activation.

Although unlikely (the flux of thermal neutrons is strongly suppressed in the underground laboratories, see table 6.3, and Cuoricino crystals have been stored underground, shielded from cosmic rays, for a long time), both these hypothesis have been probed.

Direct measurements of the neutron flux at LNGS were performed up to 25 MeV: the results are summarized in table 6.3.

The ^{121}Te production rate due to (n, γ) interactions on ^{120}Te is then easily calculated as

$$\frac{dN}{dt} = N_{^{120}\mathrm{Te}} \cdot \sigma(n, \gamma) \cdot \Phi_n \tag{6.19}$$

where $\sigma(n, \gamma)$ is the cross section for ^{121}Te production from (n, γ) interactions on ^{120}Te, and $= N_{^{120}\mathrm{Te}}$ is the number of ^{120}Te nuclei present in the detector, given by

$$N_{^{120}\mathrm{Te}} = \varepsilon \cdot \frac{N_{Av} \cdot M}{m_{TeO_2}} \tag{6.20}$$

where $\varepsilon = 0.096\%$ is ^{120}Te isotopic abundance, M is the sensitive mass N_{Av} is Avogadro's number, and m_{TeO_2} is the molar mass of TeO_2 .

In the reasonable hypothesis of equilibrium between ^{121}Te production and decay, the following value for the decay rate of ^{121}Te can be obtained

$$\frac{dN^{dec}_{^{121}\mathrm{Te}}}{dt} = 10.9 \cdot 10^{-10} \text{ c/h/crystal} \tag{6.21}$$

Since this value is independent on the ^{121}Te decay process, it represents an upper limit for the ^{121}Te K-electron capture and in particular for the contribution of ^{121}Te to the 30.5 keV line considered here.

From the durations of the data sets exploited for this analysis
the following upper limits to the counts due to ^{121}Te in the 30.7 keV line are obtained

$$N^{set9}_{counts} < 3.3 \cdot 10^{-7} \text{ c/channel} \tag{6.22}$$
$$N^{set10}_{counts} < 5.2 \cdot 10^{-7} \text{ c/channel.} \tag{6.23}$$

data set	duration (h)
9	309.6
10	485.21

Table 6.4: Duration in hours of the two data sets considered fot the search for ^{123}Te K-electron capture.

Since the number of channels (crystals) considered is 6, the contribution of ^{121}Te to the 30.7 keV is completely negligible.

Concerning the possible contribution of cosmic rays to the production of ^{121}Te, the following considerations can be made.

An activation line is present in the spectra of both ^{121}Te and ^{121m}Te at 603 keV, besides the 30.5 keV one.

For each isomer, the ratio between the intensities of the two lines can be estimated by a Monte Carlo simulation.

Cuoricino Monte Carlo simulation software was used to reproduce 10^6 decays of both isomers: from a fit to the lines observed in the single site events spectra the following results have been obtained

$$^{121}\mathrm{Te}: \qquad \frac{I(30\ \mathrm{keV})}{I(603\ \mathrm{keV})} \simeq 0.836 \tag{6.24}$$

$$^{121m}\mathrm{Te}: \qquad \frac{I(30\ \mathrm{keV})}{I(603\ \mathrm{keV})} \simeq 0.839 \tag{6.25}$$

The intensity of the 603 keV line allows therefore to estimate the contribution of the ^{121}Te isomers to the 30.5 keV line.

Since the 603 keV line was not visible in the energy spectra obtained from the data of both sets 9 and 10 (Cuoricino detectors had remained underground since the start of data taking, hence for ~ 2 y at least, allowing ^{121}Te nuclei to decay), its intensity was calculated from that obtained during Cuoricino first run, found equal to $\sim 2.73 \cdot 10^{-3} \pm 7.0 \cdot 10^{-4}$ counts/h/crystal.

Assuming an exponential decay rate with a time constant equal to the longer lifetime of the two isotopes ($\tau_{^{121m}\mathrm{Te}} = 154\ d$) the following upper limits to the intensities of the line in the recent data have been obtined

$$I^{603\ \mathrm{keV}}_{set\ 9} < 1.40 \cdot 10^{-4}\ \mathrm{c/h/crystal} \tag{6.26}$$
$$I^{603\ \mathrm{keV}}_{set\ 10} < 9.58 \cdot 10^{-5}\ \mathrm{c/h/crystal} \tag{6.27}$$

From the durations of data sets 9 and 10, and from the ratios in equations 6.24 and 6.25, the following upper limits to the 30.5 keV line contribution by cosmogenic ^{121}Te and ^{121m}Te in the recent data were obtained:

$$I^{30.5\ \mathrm{keV}}_{set\ 9} < 3.59 \cdot 10^{-2}\ \mathrm{c/crystal} \tag{6.28}$$
$$I^{30.5\ \mathrm{keV}}_{set\ 10} < 3.86 \cdot 10^{-2}\ \mathrm{c/crystal.} \tag{6.29}$$

Also cosmic ray activation gives therefore a negligible contribution to the 30.5 keV line observed in Cuoricino spectrum (see figure 6.14).

From the results shown in this and in the past sections it turns out that the energy spectrum shown in figure 6.14 can be trusted, both because its features are the same from channel to channel and from set to set, as discussed in section 6.2.2, and because the preliminary tests on the signal to noise discrimination method have provided results in support of its good performances.

However, the shape of the observed spectrum is not fully understood at present: the bump visible at ~ 37 keV, for instance, is still unexplained, and no certain statement about the nature of the 30.5 keV line can be made until all the features in the spectral shape will be exhaustively accounted for.

Keeping this in mind, some preliminary results will be shown for the lifetime of ^{123}Te against K-EC, in two different scenarios: a lower limit for the halflife will be obtained in the hypothesis that the observed peak is not due to the investigated decay, and the value for the lifetime, estimated assuming ^{123}Te K-EC as the responsible for the 30.5 keV line, will be shown.

In the following both the efficiency and the quenching factor of Cuoricino detector have been assumed equal to one: the quenching factor of TeO_2 bolometers was in fact measured by the members of Fiorini's group [155] and was found compatible with 1.

Concerning the detection efficiency, although the analysis presented in section 6.2.2 found it very close to 1 at ~ 70 keV, its value is expected to be slightly worse at lower energies: a set of measurements dedicated to its determination is scheduled in the short term.

The 30, 5 keV line in figure 6.14 has been fitted with a gaussian function whose width has been set equal to the detector's energy resolution ($\sigma_{r.m.s.} \simeq 0.5$ keV), obtained from a fit to the 46, 5 keV ^{210}Bi line.

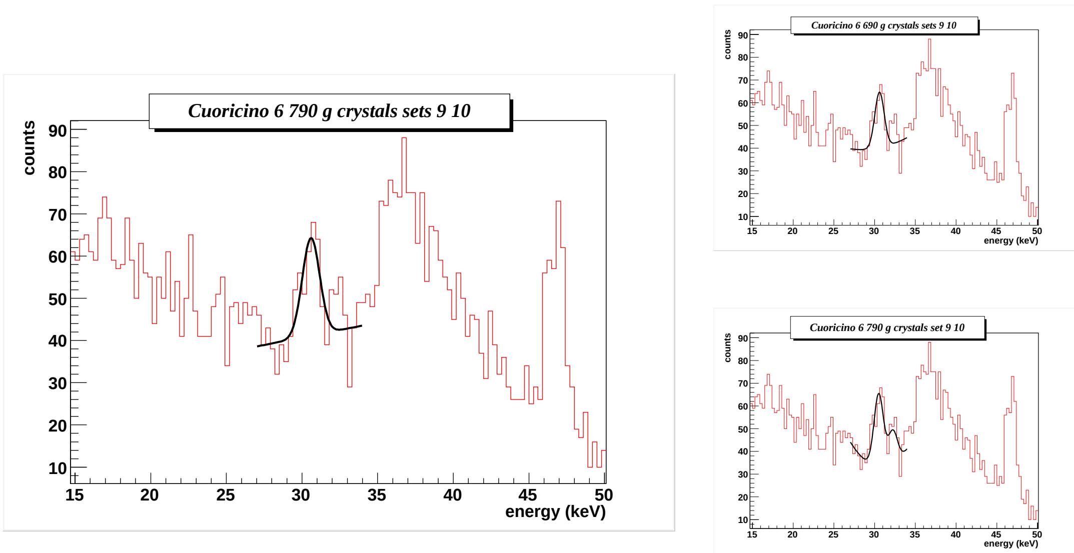

Figure 6.15: Different models assumed for the fit to the background arounf the 30, 5 keV peak (fitted with a gaussian function). Left panel: linear function. Top right: 2^{nd} degree polynomial. Bottom right: 2^{nd} degree polynomial plus gaussian peak.

In order to estimate the background contribution in the energy region of interest, different hypothesis for its shape have been probed: as shown in figure 6.15, the background has been fitted both with a linear function and with a polynomial of 2^{nd} degree, and in this last case a gaussian peak has also been added (besides the main one at 30, 5 keV) in order to better match the observed background shape.

The fit has been performed in the energy range [26 keV, 35 keV]: no significant changes have been observed when changing such interval, provided the inclusion of structures in it is avoided.

Both the upper limit on $\tau_{1/2}$ and its best fit value have been computed following the standard procedure described in [156].

The values obtained are summarized in table 6.5, together with the corresponding confidence intervals provided by Feldman's and Cousins's method [157].

Background model	Lower Limit (90 % C.L.)	Best Fit $\tau_{1/2}$	Confidence Interval (90% C.L.) Feldman & Cousins
Linear background	$7.07 \cdot 10^{19}$ y	$(9.18 \pm 1.65) \cdot 10^{19}$ y	$6.66 \cdot 10^{19}$ y $< \tau_{1/2} < 1.39 \cdot 10^{20}$ y
2^{nd} degree polynomial	$6.79 \cdot 10^{19}$ y	$8.71 \pm 1.71 \cdot 10^{19}$ y	$6.41 \cdot 10^{19}$ y $< \tau_{1/2} < 1.29 \cdot 10^{20}$ y
2^{nd} degree polynomial + gaussian peak	$5.48 \cdot 10^{19}$ y	$6.61 \pm 1.07 \cdot 10^{19}$ y	$5.25 \cdot 10^{19}$ y $< \tau_{1/2} < 8.71 \cdot 10^{19}$ y

Table 6.5: Results for the halflife of ^{123}Te against K-electron capture obtained from the fit of Cuoricino energy spectrum under different hypothesis on the origin on the $30,5$ keV peak and of the shape of the background. See text.

These values can be compared with the current lower on limit ^{123}Te halflife against K-electron capture, quoted in section 6.3.2: $\tau^{K}_{1/2} > 5 \times 10^{19}$ y.

In the hypothesis of ascribing the $30,5$ keV peak observed in Cuoricino spectrum to ^{123}Te K-EC, the best fit values (and confidence intervals) reported in table 6.5 are compatible by the previous result of Fiorini's group.

If, otherwise, the choice is made to ignore it, attributing its origin to something else, the lower limit which can be set is better than the previous one.

A decision on the approach to follow will be taken when an exhaustive comprehension of all the spectral features observed is reached: the analysis of Monte Carlo simulations is currently being performed with this purpose.

6.4 Considerations

The results shown in section 6.3 demonstrate the good potentials of Cuoricino for the search of rare decays in general and of ^{123}Te K-EC in particular.

However, if a peak at 30, 5 keV is undoubtedly visible in Cuoricino energy spectrum, its intensity strongly depends on the model assumed for the background: a better undestanding of the backgroung is required, and it will pursued, as mentioned, through the analysis of the Monte Carlo spectra.

Besides the peculiar problem of ^{123}Te, the study of Cuoricino background discussed in section 6.2 strongly supports the reliability of Cuoricino data at low energy.

It makes sense, then, to wonder if Cuoricino could address any of the other topics discussed in section 6.1, namely the searches for WIMPS and for solar axions.

Concerning the latter, the main requirements for their search exploiting Primakoff conversion in crystal lattice is the knowledge of the crystals' orientation: this is not the case for Cuoricino, which is therefore ruled out for this kind of search.

When the direct search for WIMPs is considered, the main problem turns out to be the instability of the energy threshold: as explained in section 6.2.1, Cuoricino energy threshold is different for each detector and depends on the noise conditions, wich, due to the features of the adopted experimental setup, strongly depend on factors outside the experimenter's control[9].

As a simple exercise, it is however interesting to determine the minimum requirements for a Cuoricino like detector in otder to be sensitive to a WIMP signal such as that claimed by the DAMA collaboration.

Since most of the modulation signal would be in this case expected at ~ 4 keV, the energy threshold should be kept low enough.

A simple analysis shows that, if this could be done, the number of channels needed should be greater than ~ 15 (considering 790 g crystals), otherwise the background level would be so high that its statistical fluctuations would completely overwhelm the modulation signal searched for.

Going into details, the count rate of WIMP's scatterings off the target's nucleus is expected to change periodically in time according to equation 6.9

$$S = S_o + S_m \cos\omega(t_i - t_0).$$

The average experimental count rates N_{ik} will therefore be given by equation 6.10

$$\langle N_{ik}\rangle = [b_k + S_{0,k} + S_{m,k}\cos\omega(t_i - t_0)] \cdot W_{ik}$$

(see section 6.1.1 for the meaning of the symbols adopted).

A basic requirement for any experiment aiming to look for a WIMP induced modulation signal is that the time and statistical fluctuations of the background should stand well below the size of the searched modulation effect.

Considering the statistical fluctiations only, this means

$$N_k^{max} \geqslant \Delta N_k^{signal+background} \tag{6.30}$$

where N_k^{max} is the maximum expected modulation in the number of counts and $N_k^{signal+background}$ is the statistical error associated with the counts collected, including both signal and background.

[9]Most of the noise has microphonic origin and is induced by vibrations in the cryogenic set-up. Its amount and its features are largely influenced by the current conditions of the cryostat (pressures, levels. flows and so on...). See alse section 6.2.1

N_k^{max} will in general be given by the number of counts collected in the k^{th} energy bin around the $t_0 = 2^{nd}$ of June:

$$N_k^{max} = M \int_{t_0-\frac{\Delta t}{2}}^{t_0+\frac{\Delta t}{2}} S_{m_k} \cos[\omega(t_i - t_0)]dt = \frac{2MS_{m_k}}{\omega} \sin\frac{\Delta t}{2}\omega \tag{6.31}$$

where Δt is the duration chosen for the time bins.

$\Delta N_k^{signal+background}$ will have the contributions of both signal and background: defining

$$S_c = S_0 + b \tag{6.32}$$

it will be given by

$$\Delta N_k^{signal+background} = \sqrt{MS_{c_k}\Delta t + N_k^{max}} = \sqrt{MS_{c_k}\Delta t + \frac{2MS_{m_k}}{\omega}\sin\frac{\Delta t}{2}\omega} \tag{6.33}$$

Using equations 6.31 and 6.33, eq. 6.30 can be written as

$$4M\left(\frac{S_{m_k}}{\omega}\right)^2 \sin^2\left(\frac{\Delta t}{2}\omega\right)^2 \geqslant S_{c_k}\Delta t + 2\frac{S_{m_k}}{\omega}\sin\left(\frac{\Delta t}{2}\omega\right). \tag{6.34}$$

According to the DAMA collaboration [158], the WIMPs induced modulation signal has a modulated cosine-like behaviour in agreement with equation 6.9, with a period $T = \frac{2\pi}{\omega} = (1.00 \pm 0.01)$ y.

Its best fitted modulation amplitude is given by (0.0233 ± 0.0047) cpd/kg/keV for the (2-4) keV energy interval, (0.0210 ± 0.0038) cpd/kg/keV for the (2-5) keV energy interval, (0.0192 ± 0.0031) cpd/kg/keV for the (2-6) keV energy interval, respectively.

The corresponding residual rates expected for Cuoricino and CUORE can be obtained formulating an hypothesis about the kind of interaction between WIMPs and nuclei and then using equations 6.1 and 6.5.

Supposing a spin independent interaction the nuclear recoil rate expected for TeO_2 is 1.0011 times that observed for NaI.

In the (very optimistic) hypothesis of having 6 Cuoricino 790 g detectors running for more than one year, with an energy treshold $E_{tr} \leqslant 2$ keV, and with a background rate equal to the one currently achieved at 15 keV (1.28 ± 0.23 cpd/kg/keV), equation 6.34 would never be satisfied independently on the time bin width adopted.

For the purpose of illustration, figure 6.16 shows the first and the second members of the inequality 6.34, obtained integrating the expected count rate over the (2-6) keV energy interval, and plotted against the time bin width chosen: it can be observed that 6.34 is not satisfied unless at least 14 Cuoricino detectors are successfully operated with a 1.28 ± 0.23 cpd/kg/keV background rate at an energy treshold $E_{tr} \sim 2$ keV.

The experience of Cuoricino shows however that an energy treshold lower than $\sim$ 15 keV is hardly obtained for a limited set of detectors, and is very unstable with the time: for the analysis shown in the previous section, only for 6 detectors out of the 64 available, could the thresholds be kept as low as 15 keV for a total time of ~ 800 h.

The only information Cuoricino can provide about WIMPs is therefore a (m_W,σ) exclusion plot: in this case, in fact, the stability of the energy threshold is not crucial, the most important parameter being the background level.

The results obtained from Cuoricino data in the simplest hypothesis of a spin independent WIMP-nucleus interaction are shown in figure 6.17.

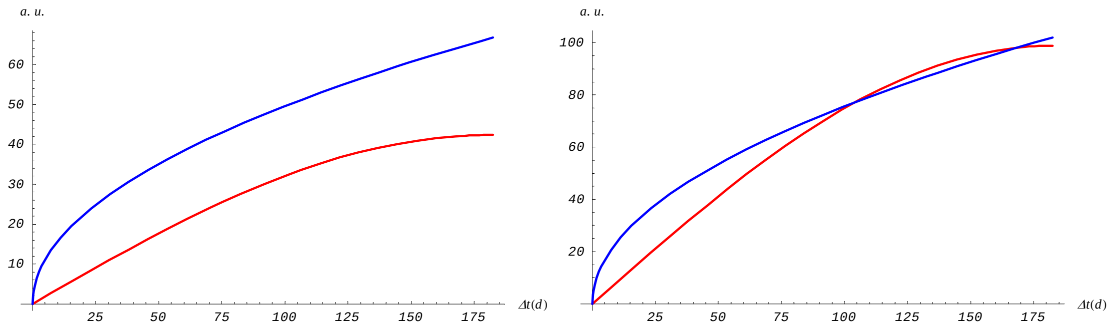

Figure 6.16: Left panel: the two graphs represent the first (red) and second (blue) member of the inequality 6.34 in the hypothesis of having 6 Cuoricino 790 g detectors running for more than one year, with an energy treshold $E_{tr} \leqslant 2$ keV. Whatever width is chosen for the time bins, the equation is never satisfied. Right panel: in the hypothesis discussed in the text, the minimum sensitive mass required to appreciate a modulation effect would be $\sim 11\ kg$, equivalent to 14 790 kg Cuoricino crystals. The two graphs represent the first (red) and second (blue) member of the inequality 6.34 in this hypothesis.

The plot is derived by requiring the theoretically predicted signal for each m_W and σ in each energy bin to be less than or equal to the (90% C.L.) Poisson upper limit of the recorded counts. The bin width is assumed to be equal to the detector resolution.

The same hypothesis previously used for CUORE have been assumed here concerning the WIMPs distribution, namely: that they form an isotropic, isothermal, non-rotating halo (the isothermal sphere model) of density $\rho = 0.3$ GeV/cm^3, which has a Maxwellian velocity distribution and that the relative Earth-halo velocity is $v_0 = 220$ km/s.

This result, however, cannot compete with those obtained by dedicated experiments shown in figure 6.2.

Concluding, the only kind of low energy Physics which can realistically be addressed by Cuoricino is the search for rare nuclear decays: the good results obtained for the study of ^{123}Te K-electron capture have been discussed in the previous section.

CUORE potentials to address WIMPs or solar axions searches relies on the performances that will be reached in terms of background, energy threshold and stability, and have been discussed in section 6.1.

A strong reduction in the physical background rate, with respect to Cuoricino, is expected from the choice of highly radiopure materials and from the use of a heavier shielding: as discussed in section 5.3, Monte Carlo simulations [107] shows that background levels lower than $\sim 3 \times 10^{-2}$ c/keV/kg/d in the low energy (10-50 keV) region can be obtained with the already available materials, exploiting the increased effectiveness of the anti-coincidence method CUORE will get by virtue of its larger number of channels.

The value of the energy treshold and its stability is strongly dependent on the rate of spurious events, mostly due to vibration induced microphonism, and on its fluctuations: a further improvement in this direction is expected from the innovations forseen both for the cryogenic apparatus, and for the whole CUORE structure.

Concerning the former, the use of a Pulse Tube cooler will strongly reduce the amount of

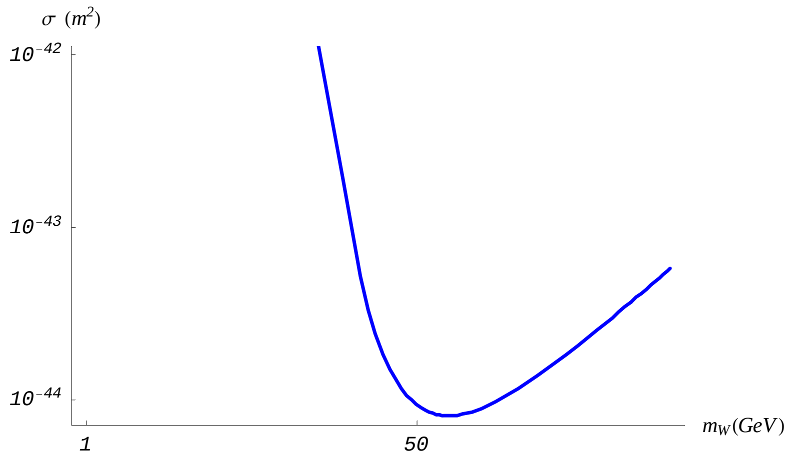

Figure 6.17: Exclusion obtained with Cuoricino . The data analyzed were those of run II, sets 9 and 10. The total measurement time was ~ 25 d, the energy threshold was 15 keV, and the background rate near threshold was 1.28 ± 0.23 c/keV/kg/day.

vibrations on the cold head of the cryostat, as mentioned in section 5.1.3.

The whole structure of CUORE hut, described in section 5.1.4, has moreover been designed in order to prevent vibrations to reach the sensitive part of the detector: this will be accomplished both keeping possible source of vibrations (e.g. pumps) far from the tower, and sustaining the tower itself in such a way to mechanically decoupling it from the cryostat and from the surrounding building.

Chapter 7

CUORE Data Acquisition and Control System

"Reason's last step is the recognition
that there are an infinite number of things which are beyond it."
Blaise Pascal

Introduction

A large part of my activity has been dedicated to the project and realization of the data acquisition and control system for CUORE experiment.

Although CUORE detector is small when compared to the typical high energy accelerator experiments, its size and complexity are large enough to require a dedicated system capable of handling the various components of the experimental apparatus.

Data acquisition and storage is not the only capability required: the different subsystems and plants contributing to the detector's running must be controlled or monitored, and their status must be correlated with the acquired data.

When possible, all this must be automatic, and the user should only take care of those operations for which a manual intervention is necessary.

It is worth to note here that such a system is absent in Cuoricino: the different parts of the experimental apparatus (e.g. data acquisition system, cryogenic plant monitor, electronics control system ...) are run independently, and often manually.

Besides being time consuming this approach has the further disvantage of complicating the offline data analysis procedures, since it inevitably implies a lack of correlation between the data acquired and the corresponding experimental condition, correlation which can only be reconstructed *a posteriori* with unnecessary efforts and sometimes incompletely.

The increase in size when going from Cuoricino to CUORE, and the consequent further complexity of the experimental apparatus, makes however this approach unfeasible, and requires a completely new system to be realized for CUORE.

The Genova group of the CUORE collaboration has thus been incharged of projecting and realizing a dedicated data acquisition and control system for CUORE.

Its core will be the data acquisition (DAQ) system.

This will also the more delicate subsystem: the requirements to CUORE DAQ, both in terms of energy resolution and accuracy, are very compelling, as will be shown in the following sections.

This chapter will give an overview of the ideas driving the design of CUORE DAQ and control system.

Starting from a review of its requirements and of their motivation, the functionalities of the system will be explained in section 7.1.

Being the system project at an early stage of development, many details will not be given here: only those technical requirements imposed by the features and size of the subsystems handled will be provided in section 7.2.

7.1 Requirements and general features

CUORE experimental set-up has been described in chapter 5.

In orded to better understand the requirements for the DAQ and control system, it is worth schematically reviewing its structure, outlining its main components.

Once assembled, the set-up will basically consist of the following subsystems:

- the array of TeO_2 crystals
- the cryogenic system, with its ancillary plants (pumps, power supplies...)
- the analog electronic system
- the data acquisition system

The DAQ and control system for CUORE is required to provide the functionalities needed to:

- digitize the analogue pulses provided by the front end cards
- control the data taking operations
- interface with the slow control system
- monitor the operations online

In the following sections these items will be separately described.

7.1.1 Data acquisition system

The main task of the system will be to convert the analogue output of the warm front end boards into digital data on computer disk.

The signals to be acquired are the voltage pulses produced by the bolometers after amplification by the front end electronics: their number will be therefore 988.

The whole shape of the physical pulses has to be acquired at a sampling rate high enough to allow an accurate reconstruction of the signal amplitude and, thereby, energy.

This requires, in turn, a trigger system: CUORE data acquisition system will make use of both an hardware and a software trigger system: the former will basically consist of a threshold discriminator whose output will enable/disable data acquisition, the latter will require data to be continuously acquired.

In this second option, a set of software algorythms will find physical pulses identifying their shapes in the acquired signals, and will store the data on disk accordingly.

The details of the data acquisition and trigger system will be provided in chapter 8.

7.1.2 Control system for data acquisition

The DAQ system will be controlled by a logic capable of handling the various operations required during data taking.

This system will provide a friendly interface between the user and the DAQ software processes.

It will moreover handle all those operations which require the data acquisition system to be operated together with other sybsystems, such as, for example, the routine characterization of the NTD thermistors (see section 7.1.3), during which DAQ ans Slow Control system must be operated contemporarily.

At last, it will handle the exchange of data between the DAQ system and the data base when this is necessary.

7.1.3 Slow Control System

The Slow Control System will allow the user to monitor many parts of the experimental apparatus, and to control the electronics system, both the front end and the filter cards.

The former task has a twofold purpose: besides checking the correct behaviour of the detector during its operation, it will allow, at a later time, the correlation of data with the experimental conditions during their acquisition.

The experience gained with Cuoricino detector has in fact shown the fundamental role played by the temperature instabilities and by the vibrations sometimes induced by the cryostat and the liquefier.

In order to identify these frequently occurring situations and to analyze the data accordingly, it is very important to continuously check the main parameters of the cryogenic system (e.g. pressures, mixture flows, cryogenic liquid levels and others).

The cryogenic apparatus must be equipped with transducers able to measure these quantities providing as output a voltage value which will be acquired by the DAQ during the detector's run.

This environmental data monitor can be implemented directly in the DAQ or be designed independently and correlated off-line with the experimental data after a synchronization between the two systems.

The choice of the best approach can definitely be taken later on; the control system and DAQ designs have in fact little intereference and can evolve independently.

As previously mentioned, the Slow Control System will not only be dedicated to the monitoring of the cryogenic system: it will provide control and/or monitor of the following sub-systems:

- Front end cards
- Filter cards
- Heater pulser
- Power supplies
- Cryogenic system
- Environment sensors

While most of the features of the front-end and filter cards and of the heater pulser are already well defined, the details of the cryogenic system and power supplies, as well as those of the environment sensors, are not yet known, being these systems themselves under development at present.

The Slow Control System will be however only required to monitor (and not to control) these last subsystems, and possibly to detect anomalous conditions generating alarm signals accordingly.

It will provide a user friendly interface to parameter settings, will store these parameters in a data base and will be interfaced to the data flow system, in order to make some routine procedures (setting of cards parameters, determination of thermistors load curves) automatic.

The procedure adopted to charterize CUORE NTD thermistors, in particular, has been described in section 2.4.

Given the large number of thermistors forseen for CUORE, it is absolutely necessary that it is performed automatically: a system for the determination of the thermistors load curves will be therefore included in CUORE DAQ and control system.

7.1.4 Online monitor

CUORE data acquisition system will be capable of performing a first low level online data analysis, mainly with the purpose of verifying the quality of the data while they are collected.

Besides some trivial checks, such as the control that the input signals are in the correct voltage range (temperature fluctuations can cause variations in the voltage drop across the thermistors, which can therefore exceed the input range of the DAQ system), further tests can be executed.

The signal rate, for instance, can be monitored: anomalous behaviours of the electronic/cryogenic system may in fact result in exceedingly high event rates.

The noise power spectrum is another significant quantity, since it can highlight possible problems providing at the same time an indication about their origin.

The basic functionalities provided by the system and their relationships are sketched in figure 7.1.

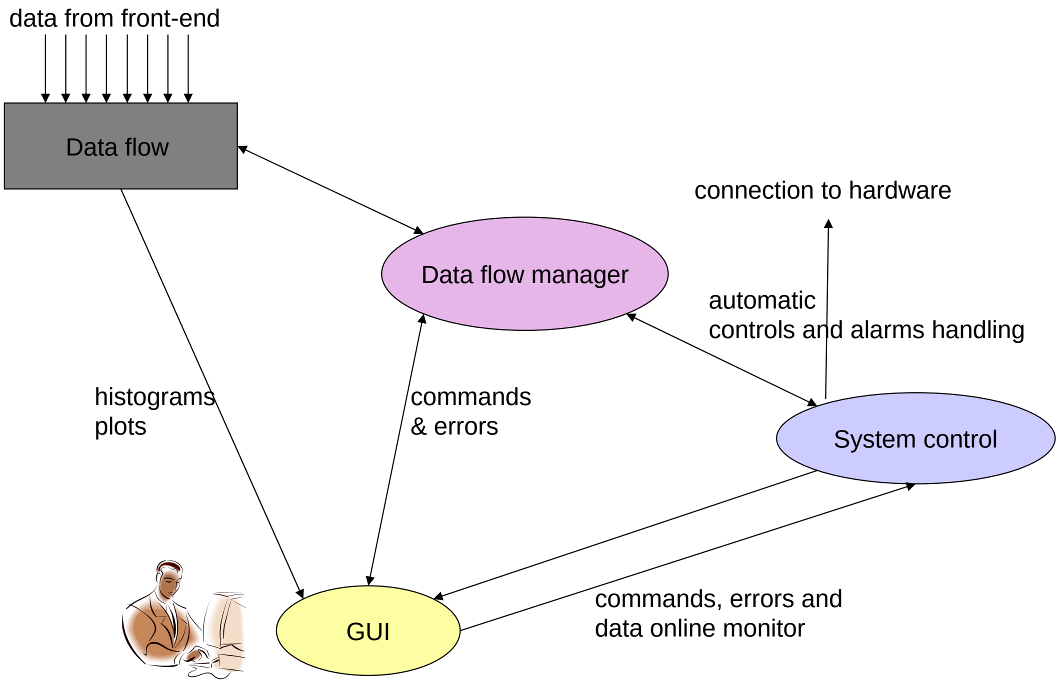

Figure 7.1: Conceptual diagram of the Acquisition and Control System

7.2 Technical requirements

In this section the thechnical requirements for the slow control system will be described; the details of the data acquisition system will be dealt with in chapter 8.

As stated above, the slow control system will handle the interface with CUORE electronics and cryogenic system.

While the design of CUORE electronic system is already well estabilished (CUORE front-end and filter cards will be the same as those used for Cuoricino), the cryogenic system is still at an early stage of development, therefore only some general requirements for the part of the slow control system dedicated to its handling have been collected so far.

The design of power supply system for CUORE set-up is also not well estabilished at present, therefore it will not be described in this document.

7.2.1 Interface with electronics

CUORE electronics system will be made of 576 two channels front-end boards, arranged in 8 towers of 6 crates each, and 353 three channels trigger/filter boards housed in 22 crates (see section 3.2.4 for an overview of their design and operation).

The electronics system will be controlled via I^2C or another serial protocol, and the link will possibly optical. The protocols will be master-slave, with the Slow Control PCs being always the transaction master.

7.2.2 Interface with the cryogenic sytem

Concerning the cryogenic system, only a preliminary estimate of the kind and number of parameters to be monitered has been compiled so far and it is reported below.

- Estimated number of monitor parameters
  1. 5 flow meters
  2. 20 warm termometers
  3. 60 special channels (NTD used as termometers for detector)
  4. 25 pressure gauges
  5. 5 level meters
- Actuators
  1. 4 compressors
  2. Chiller
  3. 8 pumps
- Valves
  1. 40 valves (most of them ON/OFF)
- Monitor of Cuore chiller
  1. about 10 parameters

The communication protocol with the monitored devices has not been estabilished yet; however, the knowledge of the approximate number of devices to to monitor already allows to dimension the slow control system, and in particular to estimate the resources necessary to handle the required operations.

The typical times over which the devices listed are expected to change are different from one kind of device to another. However all the response times will be longer than $\sim 1m$, and this will be therefore the maximum sampling rate expected.

Chapter 8

CUORE Data Acquisition System

"Questions are never indiscreet, answers sometimes are"
Oscar Wilde

Introduction

In this chapter the architecture of the DAQ system for CUORE will be described.

The system is being projected and realized by the Genova group of the CUORE collaboration; according to the officially proposed time schedule for the CUORE project a complete working set-up should be ready by the end of 2009, just before the start of the first run.

Although CUORE detector can be considered in some respects an enlarged version of Cuoricino, CUORE DAQ cannot be realized just scaling Cuoricino DAQ to the increased number of channels.

Some features needed by CUORE DAQ system are in fact absent in Cuoricino: one of the requirements (see section 8.1) for CUORE DAQ is to have auto-triggering boards, capable of handling the dedicated output signals produced by the electronic system (see section 3.2.4).

Cuoricino digitizing boards have not this capability, and this makes them unusable for CUORE in the hypothesis of relying on a hardware trigger method.

Moreover, the way some tasks are handled in Cuoricino is not suited to be extended to a larger set-up, and some tasks which are desirable for CUORE are missing in Cuoricino.

The data acquired by different channels, for instance, are not correlated in space and time during Cuoricino data taking: CUORE data acquisitione system will perform such correlations online, together with a first rough analysis on the collected data.

Cuoricino data acquisition system, moreover, doesn'have a data base: this is already very inconvenient for Cuoricino, because, as a consequence, the correlation of informations related to different subsystem is often difficult, but is certainly to be avoided for CUORE where, due to the increased size of the detector, the event rate will be higher and the amount of useful informations larger.

Besides the data base, all the necessary tools for handling the communications with it, for automatically keeping it up to date and for retrieving data from it have to be realized for CUORE and integrated in the remainder of the data acquisition and control system.

For these and for similar reasons, a completely new system, expressely thought for CUORE, is being developed, and this implies the realization of both the hardware set-up and the software necessary to operate it.

In the following the main requirements that have driven the system design will be reported, and the general architecture of the system will be described.

8.1 Requirements

The DAQ system has been designed to sample and read out the signals of about 1000 channels with virtually zero dead time.

The input stage must match the features of the analog signals, which are reported in the following paragraph.

Features of the input signals. The features reported refer to the signals as they come out from the last stage of the electronics set-up, neglecting the previous stages of the acquisition chain in which they are generated, amplified and shaped (see section 3.2.4).

The typical shape of the signal due to an event is shown in figure 8.1

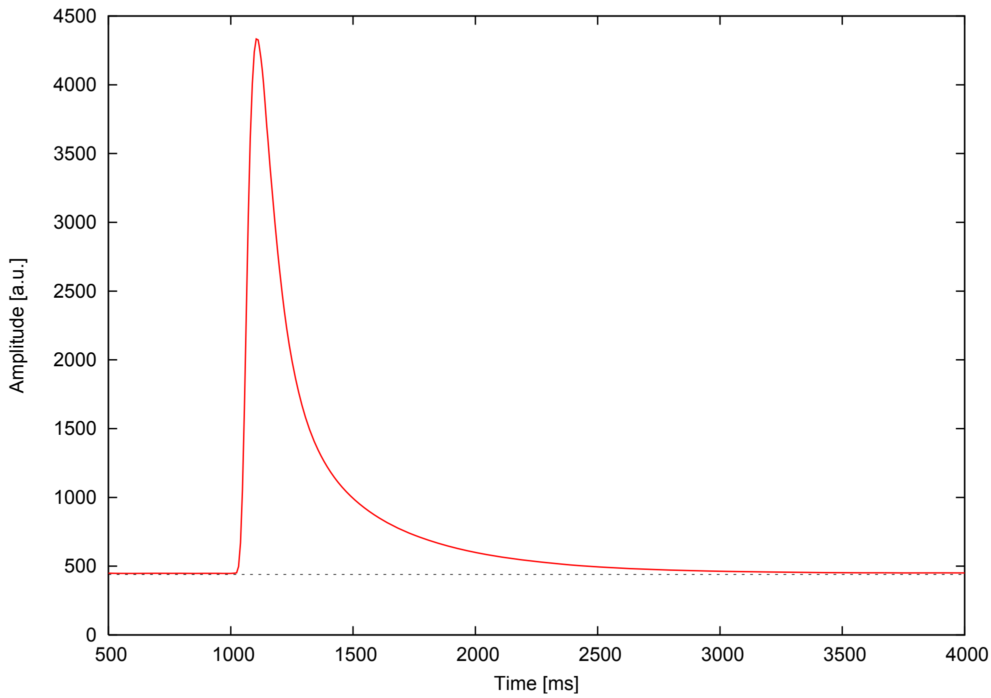

Figure 8.1: Typical shape of a signal due to an event

The input signal will be differential for a better rejection of the common mode noise, and will be characterized by the features summarized below:

- Amplitude V of the differential signal from the front-end ranging from -10 V to +10 V
- Differential signal simmetric with respect to the ground: $V_+ = -V_-$
- Typical rise time (10% $\rightarrow$ 90%) of $\sim$ 30 ms
- Fall time (90% $\rightarrow$ 10%) variable from $\sim$ 50 ms to several hundreds of ms
- Total duration of each pulse around 5 s

It should be stressed that, being the input signal differential, V designates the quantity:

$$V = V_+ - V_- \tag{8.1}$$

where V_+ and V_- are the two individual voltage levels of the differential pairs measured with respect to ground.

During regular data taking V must be a positive value in the range:

$$0 < V < +10\ V \tag{8.2}$$

During the thermistors characterization procedure the polarity of the input range must be sometimes reversed in order to measure and subtract possible effects due to tiny assimmetries in the first stage of the front-end electronics [95].

As a consequence, during this operation, the DAQ system must be able to accept input signals in the range [-10 V, +10 V].

Since many of CUORE events are expected to involve only one bolometer, the readout must be independent for each channel: in particular all the channels must be **auto triggering**, with **programmable threshold** on the incoming signal; this last feature is required by the known large spread in the thermistors performances, experienced in Cuoricino and expected for CUORE.

During the past bolometric experiments performed by the Milano group a hardware trigger was exploited (see section 3.2.4); recently, however, a software trigger algorythms has been developed and is currently being tested with good results in Cuoricino.

CUORE digitizing boards, however, are required to support a hardware trigger: only after exhaustive tests will demonstrate the good performances of a software algorythm in CUORE the hardware trigger will be possibly abandoned in favour of the software one.

In order not to spoil the energy resolution over the whole range (up to 20 MeV), real 16 bit sampling is required, as explained by the following considerations.

Energy resolution. The full scale energy range is usually set around 20 MeV.

The energy resolution measured for the best Cuoricino detectors is $\sim$ 4 keV around 2.5 MeV, and it is limited by non linearities in the E(V) dependence and by gain instabilities induced by drifts of the detector temperature (see section 3.3.1).

For the best detectors at low energy, around few hundreds of keV, the measured resolution is better than 1 keV FWHM.

This values corresponds to a r.m.s. value of (1/2.355) keV$\sim$ 425 eV.

The enegy resolution obtained with a 16 bits sampling and the aforementioned full scale range is (20 MeV)/$2^{16} \simeq$ 300 eV, therefore hardly sufficient for the best detectors but adequate for most of them.

The greater part of the remaining detectors have in fact an energy resolution worst by a factor 1.5-2.

In addition to what already said, each pulse must be sampled for $\sim$ 5 s, in order to get a good measurement of the tail and of the background level.

As mentioned in sections 3.2.4 and 3.3.1 this is crucial for correcting the pulse height for effects of temperature variations.

A typical **sampling rate** of 1 kHz seems adequate, but it is highly recommended to allow for a programmable sampling speed around this value.

With the values mentioned above, the typical **event size** for one channel is

$$1000\ Hz \times 5\ s \times 16\ bits = 10\ kbytes \tag{8.3}$$

8.2 Architecture of of the system

In order to minimize the cost and allow for a maximum flexibility in the on-line analysis and triggering, the projected system is mostly based on the large and cheap computing resources that are now commercially available, reducing the complexity, and therefore the cost, of the readout boards as much as possible.

The general structure of the system is shown in fig. 8.2.

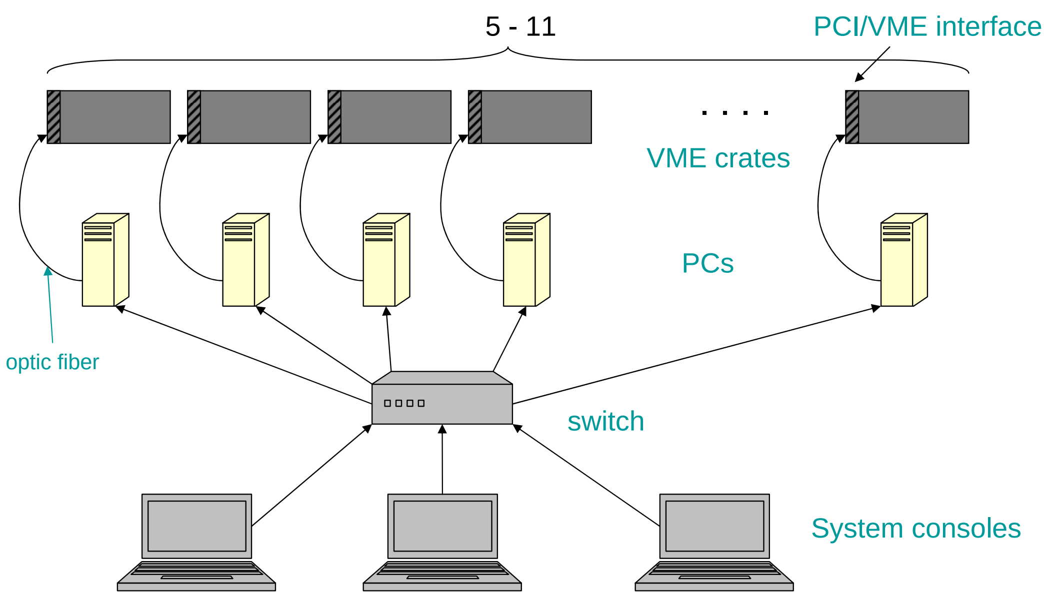

Figure 8.2: Block diagram of the proposed DAQ system. The digitizing boards are housed in VME crates (whose number can range from 5 to 11, see text), each controlled and read by a dedicated Linux PC that uses a VME-PCI interface to access the VME bus. All computers are connected via a network (normal 100 Mbit ethernet or fast optical link if required) to a set of consoles that provide graphical user interface and event display. A custom designed software runs on all computers.

It is composed of a set of personal computers, a network infrastructure, a PCI based interface and some crates housing the digitizing boards.

Two options are forseen for the data acquisition boards: either they will be VME custom made boards, or commercial PXI devices.

When the original project of CUORE DAQ was made, a commercial option didn't exist: none of the aquisition boards available on the market were suited for CUORE purposes.

The digitizing boards already used for CUORE , for instance, were not capable of handling trigger signals; other commercial boards didn't have the required energy resolution.

A simple digitizing VME board with 18 bit dynamic range was therefore designed and build and the architecture of CUORE DAQ system was developed accordingly.

The VME standard (see appendix A) has all the features needed to satisfy the requirements listed in section 8.1, and it is well known by the members of Genova electronic workshop: it was therefore chosen for CUORE digitizing boards.

At the end of 2005 a new series of digitizing boards were produced by National Instrument Company: although they still don't have those triggering capabilities Cuoricino DAQ boards were lacking of, their low cost makes them an attractive alternative to the custom ones.

The choice between the two possibilities will be made after a deep compared test of their performances, which will be carried on in Gran Sasso Laboratories before the end of next summer.

In any case, the decision will imply only minor technical modifications to the general infrastructure of the system.

In this and in the next chapters the original DAQ system will be discussed, because its development and testing has been a consistent part of this Ph. D. work; the implications of a possible decision in favour of the commercial set-up will be briefly described in section 8.4.

As already stated the choice to demand most of the complexity to the software part of the system has been made. In the next two sections the architecture of the data acquisition hardware and software will be described.

8.2.1 The data acquisition hardware

In the original project for CUORE DAQ, it was proposed to design and build a simple digitizing VME board with 18 bit dynamic range, large internal circular buffers, optional self-triggering capability, programmable threshold and digitizing speed.

A prototype of the board has actually been realized: its details and performances will be described in the next chapter.

Each board can handle 12 channels: in the hypotesis of housing 20 boards in each crate 5 VME crates would be required for 1000 channels.

Most likely the digitizing boards will be distributed in more than 5 crates (up to 11 VME crates are forseen) in order to increase their mutual distance thus reducing possible electromagnetic interferences between them.

The conceptual structure of the system is depicted in fig. 8.2.

Each VME crate is controlled and read by a dedicated PC connected with a PCI-VME interface. The connection is optical and guarantees electrical decoupling.

The software running on each PC collects the data, performs the first level trigger (if this is required, see section 8.2.1) and transfers the data to the system consoles, where event building and data storage occurs.

The output data format is described in section 8.3.

The system consoles (whose number is not critical and will be defined in the future) will also provide the user interface.

One of the computers will also control the I^2C or serial bus that will allow communication with the power supplies and with the front end cards, as discussed in section 7.1.3.

The details of the communication protocol with the front end electronics and with the power supplies will be defined in the future.

All computers are connected with each other via a standard network switch.

Although a simple 100 Mbit would be adequate for Cuore needs, it would be easy to implement this structure using 1 Gbit optical link without any architectural modifications, were it necessary.

In this framework the digital boards are just pure digitizers, that continuously convert the input analogue signal into a stream of digital words; when a trigger occurs the words stored in the internal buffers are copied to another memory that can be accessed by the main DAQ software via the VME bus.

The system is designed to perform triggering in three possible ways, which are described in the next section.

The triggering philosopy

The goal of the triggering system is to identify the useful pulses in the random background.

CUORE DAQ system is designed to perform this operation in three possible ways reffered here as "modes": hardware trigger mode (HTM), hardware flag mode (HFM) and the software trigger mode (STM).

- **HTM**: In this mode the trigger is generated exploiting a hardware analogue circuit on the front end cards.

  When a trigger occurs, a large anmplitude (>100 mV) pulse is in fact generated by the mentioned circuit and delivered to the digitizing board, which is equipped with additional inputs for these signals and with programmable treshold discriminators (there are therefore two inputs for each channel: one for the real signal and one for this "trigger" signal).

  The digitized data contained in a given time window around the trigger are then transferred to the DAQ PCs (the typical window width will be several seconds, starting well before the trigger signal) and written on disk. No other data are acquired in this mode.

- **HFM**: In this mode the data around a hardware trigger is only flagged by the digitizing board, but it is transferred to the DAQ computers anyway.

  Only a software algorithm, possibly but not necessarily using the hardware flag, will take the final decision to store the data or not.

- **STM**: In this case all data are read continuously and the triggering algorithms is done only with software.

The system will support all these 3 modes.

HFM and STM can be run at the same time to allow cross checks.

It will also be possible to have HTM with very low threshold refined by the STM.

The large and cheap computing power available nowadays yields a large flexibility in the possible on-line filtering and processing of the data.

Full on-line analysis is possible with this structure, allowing a fast and efficient monitoring of the experimental conditions.

Linux based PCs will be used for all computers and Root as a software environment.

In partucular, the software running on each computer will be custom designed while the consoles and the graphical interfaces will be Root based.

A possible WEB interface to the system is foreseen, though network security problem will probably limit its use.

8.2.2 The data acquisition software

The data acquisition software will be completely custom made, written in C++ and based on the Root package.

The user interface will be deveroped exploiting Perl-GTK.

It will have a multiprocess architecture and will run under Linux operative system.
It will basically provide the following features:

- User Interface with the Slow Control System.
- Data Acquisition and Storage
- Online data monitor and analysis system

Interface with the Slow Control System As already stated, the Slow Control System will allow the user to monitor many parts of the experimental apparatus (see section 7.1.3), and to control both front end cards and filter cards.

It will provide a user friendly interface to parameter settings, will store these parameters in a data base and will be interfaced to the data flow system, in order to make some routine procedures (setting of cards parameters, determination of thermistors load curves) automatic.

Data Acquisition, storage and online analysis system The structure of the dedicated software is sketched in figure 8.3.

Its task is, at each trigger, to retrieve over the network the data coming from the fired channel plus the data collected by a subset of channels whose correlations with the triggering one are considered interesting.

These additional channels could be the nearest neighbours of the fired one, but they could also be chosen according to different criteria: the pulses coming from them are defined as "side-pulses" in the following.

The system will consist of a few processes, presumably running on separate hosts and exchanging commands and data between them.

Each process will carry out a different task (a description of these tasks will be given below) under the control of Apollo Server, the main process, devoted to make the system work as a body.

Communications between processes on separate hosts will be handled via network using TCP sockets.

Data will be finally stored as Root Files, in the format described in section 8.3. Figure 8.3 also shows the data flow from the VME crates to the storage disks.

In the following a definition of each process task is provided.

- **Apollo Server** This is the master process. It creates other processes and controls their running status.

  Moreover, it is the only process capable of handling incoming messages (debug messages, warnings etc.) sent by other processes.

- **Crate Receiver** This is the first process in the data handling chain: each physical crate has its associated Crate Receiver process.

  Before each run starts it performs a check of the valid boards and channels in the crate and allocates a buffer (CRBuffer in figure) of the proper size in the host pc's memory.

  Once the run has started it continuously reads data from the digitizing boards and writes them on the buffer.

- 1^{st} **level trigger** This process continuously reads data from the Crate Receiver Buffers, applies various (selectable) triggering algorithms on them and, in case an event is found, sends a Trigger Record to the Data Finder Process.

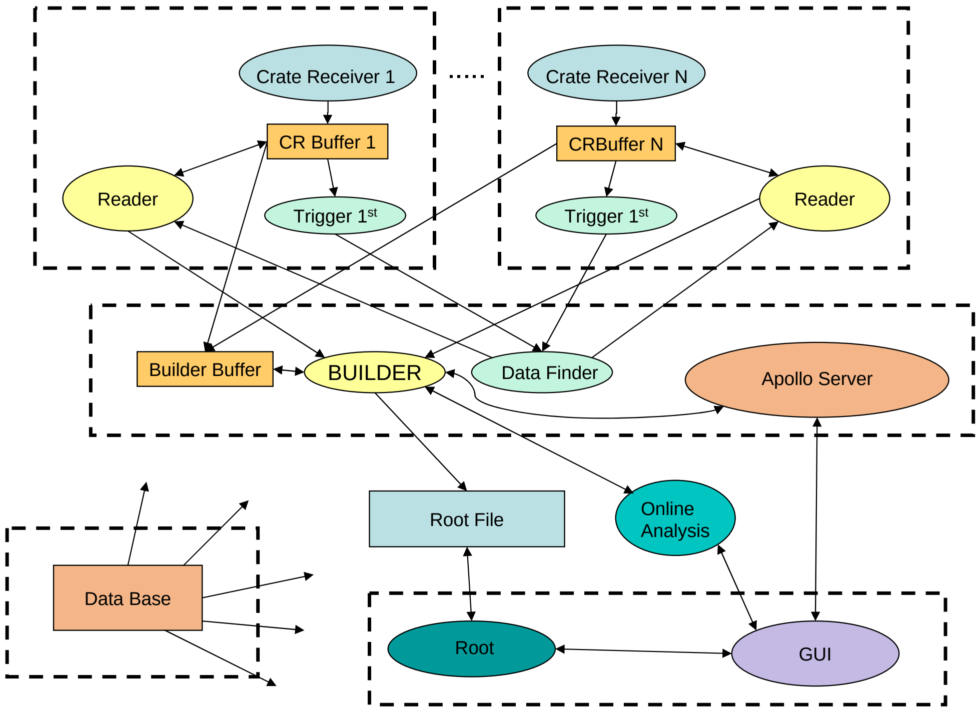

Figure 8.3: Architecture of the DAQ software. Dashed lines: architectural constraints (host PCs). Ovals: processes. Squares: buffers or data bases. Root: the Root package

A Trigger Record is a bunch of data containing the identity of the fired channel and the absolute time of the event found: this is the minimum amount of data needed for the event to be retrieved.

- **Data Finder** This process drives the Reader process according to the Trigger Records received by the First Level Trigger Process.

  It basically chooses which data will be actually stored on disk: according to the mapping between crystals and DAQ channels and to the criteria selected to define "side pulses" (see section 8.3), this process replicates the received Trigger Record and sends the copies to the proper Reader processes (i.e. to each of the Reader processes handling the channels defined as "neighbours" to the fired one) via network, after adding an event identifier to them.

- **Builder**

  This process builds the events: it performs every kind of second level online analysis on the read data, and at last it writes the processed data in the form of Root files (see section 8.3).

- **Reader**

This is the process which retrieves the data recognized as belonging to a pulse (or a side-pulse, see section 8.3) and writes them in a temporary buffer (Builder Buffer), where they can be accessed by the Builder process for further analysis.

Each reading operation is driven by the Data Finder process, and causes valid data to be transferred from one buffer (Crate receiver Buffer) to another (Builder Buffer) via network (the Builder buffer and the Crate Receiver Buffer are on separate hosts).

- **GUI**

  This process provides the user interface for the Data Acquisition system. It will enable the user to control acquisition runs, to choose between different run options and parameters, and to view online the output from the current run in the form of graphs, histograms, data streams etc.

  Remote control of the Data Acquisition system will also be possible. Visualization tools, graphics and data storage (Root Files) will be realized exploiting the Root package.

Most of the described infrastructure has already been realized: a part for the Builder process, the data base, and the Online Analysis System, all the software implementing the tasks just described has been written and tested on simulated data.

In its present configuration the DAQ software is capable to find pulses in streams of simulated data by a simple threshold discrimination algorythm, to identify the "nearest neighbours" of the fired channels, to retrieve the data they collected in a proper time window around the trigger, and to copy them in a dedicated buffer where they can be accessed by the Builder process.

8.3 CUORE event format

As previously mentioned the data collected by the Cuore Data Acquisition System will be stored in a Root file: this is the most convenient format in view of the successive data analysis, which will heavily exploit the Root package (see (http://root.cern.ch for details about the ROOT system and about the ROOT files features).

A preliminary format for this ROOT file has been defined and will be described in this section.

The data collected by Cuore will be organized in pulses, side-pulses, events and runs.

A **pulse** is a collection of ADC samples that is identified and accepted by the triggering system, i.e. a voltage pulse at the digitizer input that either exceeded the hardware threshold or was positively identified by the first level software trigger.

A **side-pulse** is a collection of ADC samples that did not trigger, but that are correlated in space and time with a valid pulse.

Each time a valid pulse is identified, the system also collects and keeps the ADC samples of the nearest neighbor crystals.

Therefore, for each pulse, up to 9 side-pulses are also read and stored. The time duration of the side-pulses will be a programmable parameter, though it will probably be about the same of the triggering pulse.

The concept of side-pulse can be used unchanged even if we decide to collect the data from a different topology, i.e. not simply from the nearest neighbors but from a different list of crystals that might be suggested by MonteCarlo simulations.

An **event** is a single pulse together its side-pulses: a one to one correspondence between triggers and events will be kept.

Note that because of this feature the same physical pulse could appear within different events: e.g. the second of two consecutive pulses generated on the same bolometer will be included in (at least) two events.

Name	Description	Type	Bytes
Run Number	Unique identifier for this run	Int32	4
Num Events	Number of events collected in this run	Int32	4
Profile	Identifier for Hardware Profile Used in This Run	Int32	4
Start Time	Date and Time at Which Run Was Started	time_t	4
Stop Time	Date and Time at Which Run Was Finished	time_t	4
Trigger Word	Word describing which trigger were enabled	Int32	4
Trigger Word	Word describing which trigger were enabled	Int32	4
To be defined	Other parameters describing detector status	To be defined	To be defined
To be defined	Other parameters describing trigger settings	To be defined	To be defined
To be defined	Parameters describing general noise conditions (mean values, rms and such) for each channel at the beginning of the run and at the end	To be defined	To be defined

Table 8.1: List of the parameters stored for every run

Besides the data representing the pulses and the side-pulses, the event will contain all other ancillary informations that might be relevant for data analysis.

For detector monitoring, noise events will be continuosly acquired at a programmable rate.

A noise event is a collection of side-pulses taken from a set of crystals randomly chosen (possibly for all crystals).

A **run** is a collection of events.

There will be one Root file for each run, containing the collection of events plus possibly a set of histograms that were produced during the online monitoring activity and that might be useful for future use.

8.3.1 Root file format

The files produced by the DAQ system should contain all the information needed for the successive offline analysis.

A tentative format for such data files has been defined and is schematically presented in the following.

The information which doesn't change during a run will be stored in the top of the Root file[1] and is summarized in table 8.1.

Besides this general run information, the TTree will contain a list of QEvent objects, each of them containing the information of a single event.

The structure of this QEvent object is sketched in table 8.2.

Some technicalities

- **QTree**

  A QTree is a TTree class for CUORE.

  A TTree is basically a collection of events in a ROOT file format. It is the best approximation of a ñtupleïn Root language.

- **QHeader**

  Each QTree will contain one QHeader object.

[1] Technically, this run information will be variables of the TTree class

Name	Description	Type	Bytes
Event Number	Unique identifier for this event	Int32	4
Heater Flag	Heater pulse identifier	bool	2
Trigger Word	Identifier of the triggering machine(s)	char	1
Event time	Date and Time for this event	Int32	4
Num Side Pulses	Number of side pulses in this event	Int16	2
Channel	Fired channel number	Int16	2
Channel[k]	Side pulses channels	Int16 Vector	2 $\times$ NumSidePulses
Pulse Time	Start time of the pulse as reconstructed online	Float	4
PulseHeight	Pulse height as reconstructed online	Float	4
Baseline	Baseline below the pulse as reconstructed online	Float	4 4
Baseline RMS	RMS of the baseline as reconstructed online	Float	4
ADC Samples[i]	List of ADC samples of the pulse	Float Vector	4 $\times$ PulseLength
ADCSideSamples[k][i]	List of ADC samples of the k^{th} side-pulse	Float Vector of Vectors	4 $\times$ Num Side Pulses $\times$ PulseLength

Table 8.2: List of the parameters stored for every event

This object contains all information that do not change during the run.

It will store a subset of the information contained in the data base, typically the most used for analysis.

See table 8.1 for the list implemented at present.

- **QEvent**

  This class contains the information peculiar of an event (see table 8.2).

- **QRawPulse**

  This class contains the informations about a record of pulses, not necessarily a triggering one.

  It contains, as data members:

  1. A channel identifier
  2. A vector of samples

- **QRawTriggerPulse** This class contains the same set of information of a QRawPulse.

  It is filled with the data coming from a triggering channel, hence it stores also the information about the position of the trigger from the beginning of the record.

  It contains, as data members:

  1. A channel identifier
  2. A vector of samples
  3. An identifier of the trigger position

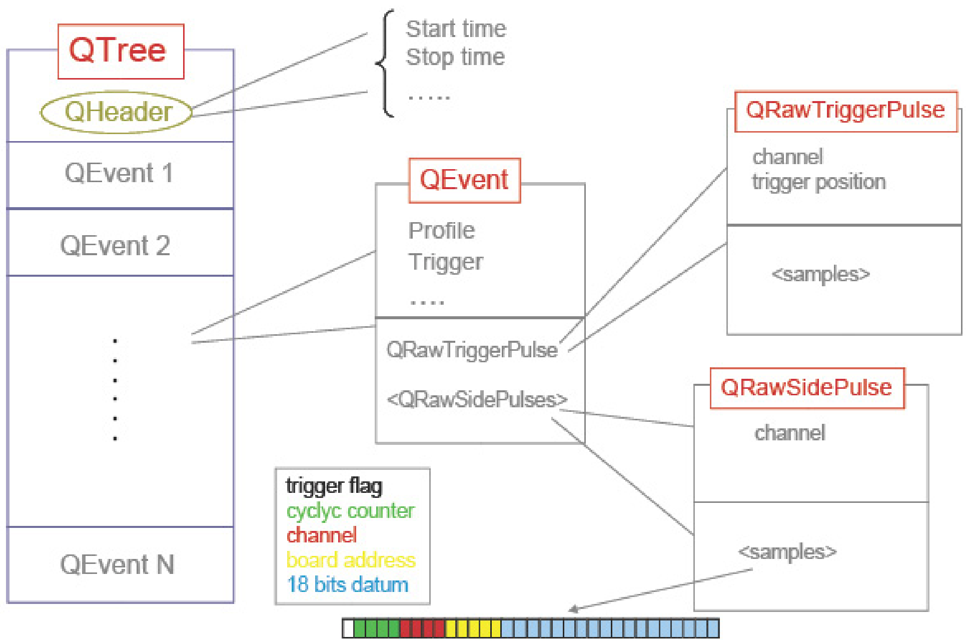

Figure 8.4: Schematic representation of the class structure realized for CUORE event. The ownerships relating the different classes and their content are sketcked. For details about the format of the raw data word see chapter 9

The structure just described is schematically represented in figure 8.4.

A program which converts Cuoricino raw data files into the format just described has been written.

Since, with possible minor modifications, this will be CUORE raw data file format, such programs allows to test on Cuoricino data CUORE analysis system, which is currently being developed.

8.3.2 CUORE data storage requirements

As will be discussed in the next chapter, CUORE sampling rate will be programmable up to 10 kHz.

The higher the sampling rate will be, the better quality will be obtained for the reconstructed pulse shapes; as a drawback, the disk space required for data storage will also increase.

In this section it will be shown that storage requirements are not a problem for CUORE .

A rough estimate of CUORE typical data throughput can be obtained assuming a sampling rate of 1 kHz, twice as much the value currently adopted for Cuoricino.

The size on disk of a CUORE event can be computed from the event format just described.

Most of the space will be occupied by the raw ADC samples (vectors of 4 Bytes words): in the hypotesis of collecting data for 5 s at every trigger (as currently done in Cuoricino), the space required for a single pulse shape will be:

$$5\ s \times 1000\ Hz \times 4\ B = 20\ kB \tag{8.4}$$

Considering the Cuoricino typical trigger rate of 2 mHz/channel, the amount of data written on disk for the whole CUORE detector (988 channels) in the unit time will therefore be:

$$20\ kB \times 2 \times 10^{-3}\ Hz \times 988\ \simeq 40\ kB/s \simeq 3.4\ GB/d \tag{8.5}$$

In the hypotesis of collecting N side-pulses (see section 8.3) per event, the space needed on disk will be N times as much.

This rough estimate proofs that CUORE disk storage needs can be easily satisfied even by standard personal PCs.

An upper limit to the overall data throughput can be obtained in the hypotesis of countinuously acquiring the signals sampled by all the 988 channels at 1 kHz sampling rate:

$$1000\ Hz \times 988 \times 4\ B \simeq 4\ MB/s \simeq 350\ GB/d \tag{8.6}$$

Again, this amount of disk space is commercially available and nowadays cheap enough; however the choice of writing all data on disk without any kind of selection should be avoided, because it would cause an useless overhead of the following offline analysis procedure.

8.4 The commercial digitizing board option

Recently the National Instruments company has produced a series of 18 bits, 500 kS/s data acquisition boards (NI6280, NI6281, NI6284 and NI6289 [159]), featuring up to 16 differential (or 32 unipolar) analog inputs.

According to their data sheets, these cards satisfy all the requirements listed in section 8.1, except the one concerning the auto-triggering capabilities, and are cheap.

A NI6281 card is currently being tested in Genova: if its performances are good, and in the hypothesis to definitively adopt a "software" trigger, they will possibly be adopted as digitizing boards for CUORE DAQ system, because of their low cost and reduced size.

Even in this scenario the overall structure of CUORE data acquisition and control system won't be modified: the replacement of the custom cards with the commercial ones will inply only minor changes in the low level data acquisition software.

Chapter 9

The prototype of CUORE digitizing board

"If you look for truth, you may find comfort in the end;
if you look for comfort you will not get either comfort or truth
only soft soap and wishful thinking to begin,
and in the end, despair."
C.S. Lewis

Introduction

The digitizing board is probably the most delicate part of the whole CUORE data acquisition system.

The energy resolution required to pursue the objectives of CUORE science is $\sim$ 300 eV r.m.s. (see section 8.1); as explained in this chapter, this means for CUORE digitizing board an indetermination on the sampled values lower than $\sim$ 150 μV.

The immediate implication of such constraint is that the influence in the sampling operations of any element potentially contributing to spoil the energy resolution (such as noise, drifts induced by environmental factors) must be lower than the $\sim$ 150 μV quoted above.

Understandably, this is a major challenge for this kind of devices, where fast, digital signals must unavoidably coexist with the analog signals to be sampled: great care must in fact be taken in order to prevent the formers from polluting the latters.

Since the late 2004, the Genova group of the CUORE collaboration is working at the realization of CUORE digitizing board.

The first prototype has been realized and characterized: it has a 6U VME format (233 x 280 mm), 12 independent inputs, buffering capabilities and is fully programmable via VME interface.

In this chapter the requirements for CUORE acquisition board will be discussed, and the board itself described: some sections will be in particular dedicated to the description of an evaluation board previously realized in order to determine the preformances expected for the final prototype.

The results of the tests on the latter will be discussed, together with the current perspectives and future plans for possible improvements of the device.

9.1 Requirements

The design of CUORE data acquisition board was driven by the same general requirements discussed in section 8.1, plus some technical constraints specifically related to the electrical specifications of the input signals and to the mechanical and electrical specifications of the VME standard (see appendix A).

A list of these requirements and of their motivations is reported here for convenience.

- CUORE digitizing board must accept input signals as they come out from the last stage of the electronic system.

  Their features have been described in section 8.1.

  The voltage range of the input signals, in particular, will vary in the range [0 V,+10 V] during normal data taking, but during thermistors characterization it will also be negative: during this operation the input signals will vary in the range [-10 V, +10 V].

- All the channels must be auto triggering, since typical Cuoricino signals will involve only one bolometer, and will therefore be seen as pulses on one channel.

- The threshold of each channel must be programmable: because of the large spread expecter for the performances of CUORE bolometers, different thresholds will be required for different channels.

- The sampling speed must be high enough to allow the correct reconstruction of pulse shapes: the experience of Cuoricino showed that a sampling rate around 500 Hz fulfils this requirement.

- The board must have buffering capabilities to allow the DAQ system to completely retrieve the pulse shapes in case of a trigger, whithout introducing dead times.

  At every trigger the signal of the fired channels must be sampled for $\sim$ 5 s, in a time window including the instant during which the trigger occurred and large enough to allow a good measurement of both the tail and of the voltage level before the pulse (baseline).

  In order to achieve this, each signal must be continuously sampled, and the samples must be temporarily stored in a memory buffer, waiting for the acquisition software to retrieve them: the buffer must therefore be large enough to allow the complete retrieving of "old" samples without interrupting sampling operation.

  Typically, data readout is performed by a software process handling several digitizing boards: the size of the buffer must be large enough to allow a single board to continuously acquire data while the other boards are being read.

  When estimating the depth of the buffers, the delays introduced by the system processes [1] running on the DAQ PCs must be additionally taken into account.

- The precision on the acquired samples must be higher than 1 LSB[2] out of 16, namely $\sim$ 15 ppm of the full scale range.

  Since during data acquisition the input signals will vary in the range [0 V,+10 V], this means that the acquired voltage levels must be known with an error lower than 150 μV.

[1] The normal operation of any operating system requires a set of processes to continuously run in background. The CPU resources and time are therefore shared between these essential processes and the processes responsible for DAQ operation.

The need to switch between different tasks can cause delays of the order of tents of ms in the case of Linux OS

[2] Least Significant Bit

This requirement is driven by the need of obtaining an energy resolution better than ~ 300 eV r.m.s., as discussed in section 8.1.

Besides the mentioned requirements, consequence of the kind of measure to be performed and of the features of the front-end system, other more technical constraints imposed by the VME standard must be satisfied, namely:

- The board must fit the size of a VME crate (see A).
- The power supply for all the active devices used must be generated from the three standard voltage values provided by a VME standard power supply, namely ± 12 V and $+5$ V.

  Care must be taken to keep the supply of the analog devices (and of the ADCs in particular) as clean as possible avoiding to degrade their performance thus spoiling the board resolution.
- Being a VME slave device (see A), the board must be capable of handling the communications with the VME master, namely the PC connected to the crate.

  The logic on board must handle the communications with the crate controller according to the VME data transfer protocol.
- The logic on board must also handle the sampling operation allowing some parameters to be remotely proggrammable: one of these parameters is, for instance, the trigger threshold of the the various channels.

9.2 The design of CUORE Digitizing Board

The first prototype of CUORE digitizing card has been built in May 2005 and tested during the following months.

Its development, however, started in the late 2003, when the first project for CUORE acquisition board was conceived.

According to this original design, CUORE digitizing card should have had a modular structure, each one being composed by a mother board housing three piggy backs[3]: the analog circuitry on the board should have been kept confined on the piggy backs, physically separated from the digital signals responsible of the communications on the VME bus.

Even if this early idea was successively modified and finally evolved in the currently adopted design, it is worth dwelling upon it: one of the three piggy backs forseen was in fact realized and tested, and the results obtained have been of great help during the following development of the next prototype.

9.3 The first project and the 4 channels evaluation board

In the original design CUORE board was conceived as a mother-board with attached 3 piggy-backs handling 4 channels each.

The choice to handle 12 channels per board was the result of a compromise between the effort to maximize the number of channels per board, in order to reduce the overall number of boards needed, and the constraint imposed by the limited space available on each card.

[3] A piggy back is a little board attached to a bigger mothed-board through a connector.
Its purpose is both to enlarge the surface usable for ICs, and to keep the circuitry on the piggy-back as far as possible from that on the main board, in order to prevent the signals on the two cards from influencing each other

The choice was also modivated by the attempt to simplify the connection of the DAQ system with the front-end electronics: since the last stage of the electronic system is made by the trigger/filter cards (described in section 3.2.4), which handle 3 channels each, a DAQ board with a number of channel multiple of 3 would noticeably simplify the cabling operations.

The reason to adopt for the digitizing boards the structure just described was, as mentioned, to decouple the analog circuitry from the digital one: according to the proposed design each piggy-back should have accomodated the signals input stages, the ADCs, the circuitry responsible for the generation of the triggers and one programmable logic whose task should have been to control the ADCs and the trigger logic.

The main-board should have instead hosted the logic needed for the data transfer on the VME bus, the memories for data buffering, and the circuitry responsible of deriving, from the power supplies provided by the VME bus (±12 V and +5 V), the voltage levels required by the variuous ICs on the board.

A schematic drawing of the architecture just described is shown in figure 9.1.

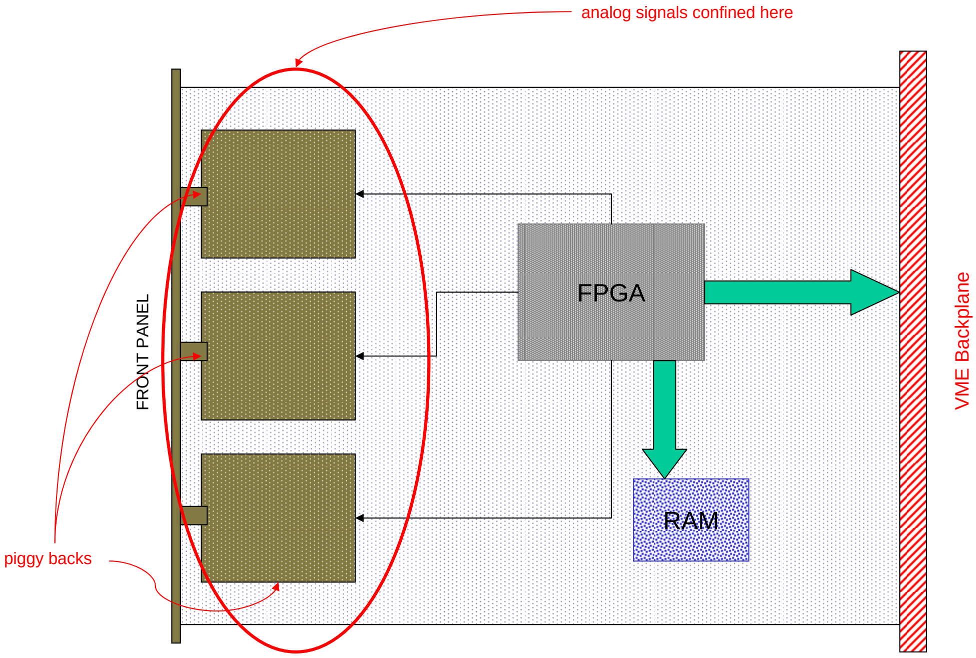

Figure 9.1: Schematic representation of the structure of CUORE digitizing board in the first project.

The functional blocks a piggy-back is made of are shown in figure 9.2.

Each one has 8 input connectors, 4 for to the normal analog signals, and 4 for the "trigger signals", generated from the front-end electronic expressely for triggering purposes (see section 3.2.4).

Four ADCs are mounted on each piggy-back, one per channel, with a buffer (an operational amplifier in the voltage follower configuration) at each of their inputs.

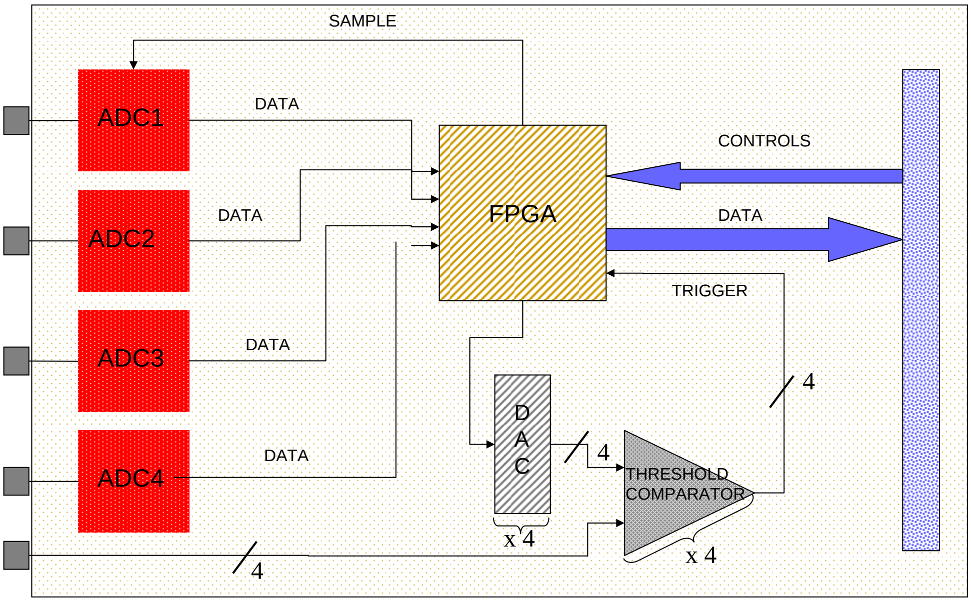

Figure 9.2: Schematic representation of the structure of a piggy-back

A threshold comparator is responsible to generate a trigger signal when a signal from the trigger inputs exceeds the voltage level set by the corrsponding DAC.

Four DACs and four threshold comparators are mounted on each piggy-back, one per channel.

The logic necessary to control the sampling operations and to handle the data and commands flow towards the mother-board is provided by a FPGA[4], which is also encharged of controlling each channel's threshold by setting the DACs outputs according to the instructions received from the main board.

Inorder to minimize the board's intrinsic noise, some precautions have been adopted during its design and in the definition of its layout.

The starting point has been the choice of the ADCs: the AD7678 [160] (Analog Devices) SAR[5] ADC has been adopted.

Among its outstanding features it is worth mentioning its great precision (INL[6] $= \pm 2.5$ LSBmax $= \pm 9.5$ ppm of the full scale), accompanied by a high sampling speed (up to 100kSPS[7]).

The PCB tracks of the analog signals have been kept as short as possible and far from digital signals, the analog grounds have been connected to each other in a star-like way, thus avoiding possible ground

[4] Field Programmable Gate Array. It is a kind of IC which can programmed so that it can perform even complicated logic operations.

[5] Successive Approssimation Register. SAR ADCs determine the digital value of the sampled signals by successive approximations, thus achieving a high precision.

[6] Integral Non Linearity error is described as the deviation, in LSBor percent of full-scale range (FSR), of the actual transfer function from a straight line.

[7] Kilo Samples Per Second

loops.

A picture of the first piggy back realized is shown in figure 9.3.

9.3.1 Measured performances

The measures performed on the piggy-back had the purpose to estimate the contribution of the card to DC noise.

Further test would have been made once the main board had been realized, and the complete board could therefore be inserted in a VME crate and controlled by a PC.

The results of this first tests were encouraging: it was in fact proved that the only contributions to the noise induced by the board were due to the power supply.

A very simple logic was written and loaded on the FPGA mounted on the piggy-back, which included only a reduced set of functionalities strictly necessary for the measures performed.

A Pattern Generator was used (a Tektronix TLA7PG2) in order to run this logic, and the sampled data were read exploiting a Logic State Analyzer (a Tektronix TLA715 equipped with a TLA7AA2 unit for logic analysis).

A dedicated test board was realized with the twofold purpose of generating the power supplies needed by the piggy-back starting from the levels provided by a bench generator, and providing a set of connectors to interface the piggy-back with the two devices just mentioned.

The test set-up is shown in figure 9.3.

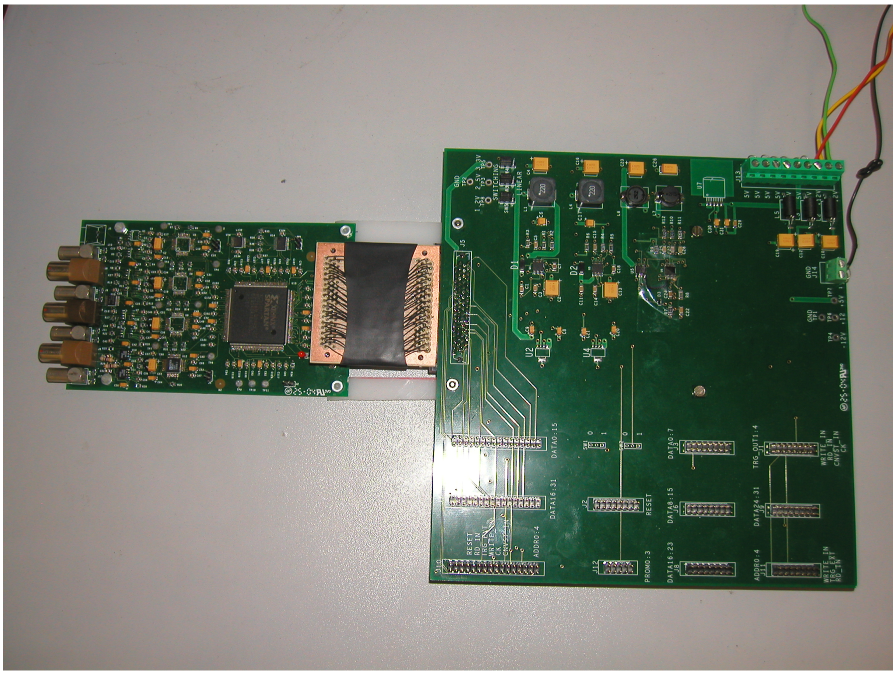

Figure 9.3: The piggy-back (left) connected to the test board (right)

A first measurement was made powering set-up with a linear bench power supply, and using a bench generator to provide an input DC signal.

The values of the samples taken have been collected in the histogram shown in figure 9.4.

The electronic noise (r.m.s.) affecting the measurement has been estimated fitting the histogram and it is given by

$$\sigma = (14.0 \pm 0.3)\ LSB = 534\ \mu\text{V} \tag{9.1}$$

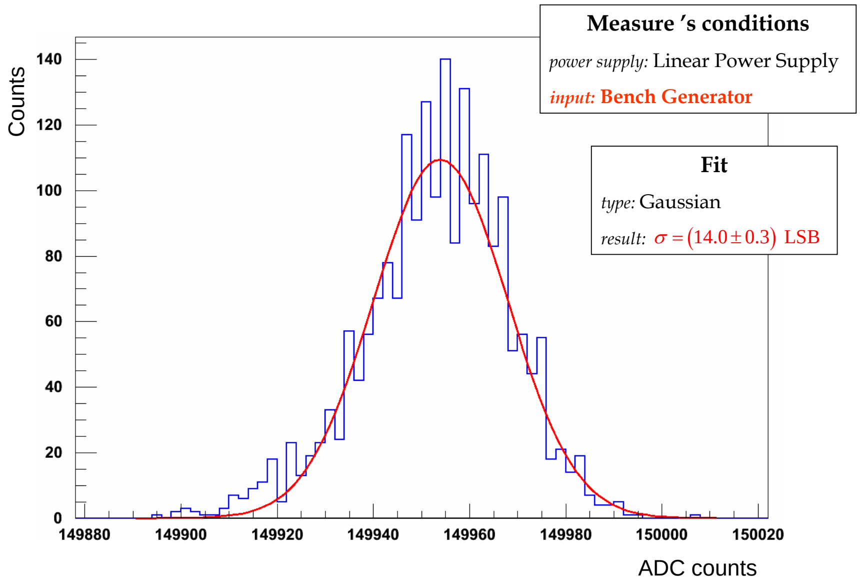

Figure 9.4: Histogram of the data taken with the piggy-back powered by a linear power supply. The input DC signal were provided by a bench generator

This value is by far outside the specifications discussed in sections 8.1 and 9.1, but the next measure performed proved that the main contribution to the noise came from the inputs: a commercial 1.5 V AA battery was connected to the inputs instead of the previously used bench generator, and a new set of measurements was taken.

The results are shown in figure 9.5.

The measured noise level was, in this case:

$$\sigma = (0.942 \pm 0.012)\ LSB = 35.8\ \mu\text{V} \tag{9.2}$$

A last set of measurements was taken replacing the linear power supply generator with a switching one: the results obtained are shown in figure 9.6.

The goal of this last measure was to estimated the possible noise contribution of a switching power supply: VME crates come in fact with a switching gerenerator, which although slightly more noisy than a linear one, has better efficiency.

The measured value was, in this case:

$$\sigma = 1.069 \pm 0.017\ LSB = 40.6\ \mu V \tag{9.3}$$

slightly worse than those obtained with a linear supply but still in accordance with the requirements.

The results obtained by this preliminary test showed that the precision of the board on the single sample was satisfactory, therefore proving the correctess of the choices made during its design.

They also demonstrated that a switching power supply is suited for CUORE digizizing board since its noise contribution is negligible.

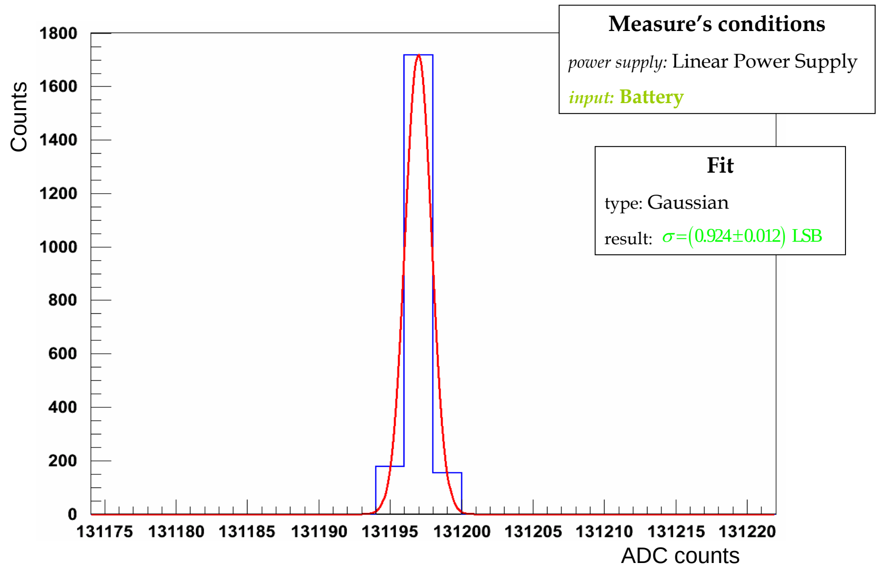

Figure 9.5: Histogram of the data taken with the piggy-back powered by a linear power supply. The input DC signal were provided by a commercial AA battery

9.4 The 12 channels prototype

After the encouraging results obtained during the tests of the piggy back, the first prototype of CUORE digitizing board was designed.

The main functional blocks the board is made of are the same forseen in the original project and described in section 9.3.

The structure of the board, however, has been modified: in the new design the idea of the piggy-backs has been abandoned.

This choice was motivated by the effort to reduce the number of the input connectors, thus simplifying the cabling operations: according to the new design, only two input connectors are mounted on each board instead of the 24 forseen by the previous option.

The compact layout of the board allows in fact all the signals and all the "trigger signals" to be grouped and to enter the board through two connectors only; this would have been impossible within the previous modular structure.

The physical separation between analog and digital signals, which motivated the previous modular design, is now achieved by carefully confining the two kinds of signals on separate areas of the card.

Another modification with respect to the original design concerns the digital part of the board: the number of FPGAs on each board has been reduced from four (one for each piggy-back and one on the main board) to two.

During the tests described in the previous section, it turned out that the FPGA (a Xilinx Spartan XC3S50 [161]) used to control the four ADCs on the piggy-back could be sufficient to control all the 12 ADCs of the board[8]: it was therefore decided to use one FPGA (a Spartan XC3S50) to control the

[8]The resources (system gates and RAM) of the FPGA actually exploited during the tests, were much less than those available.

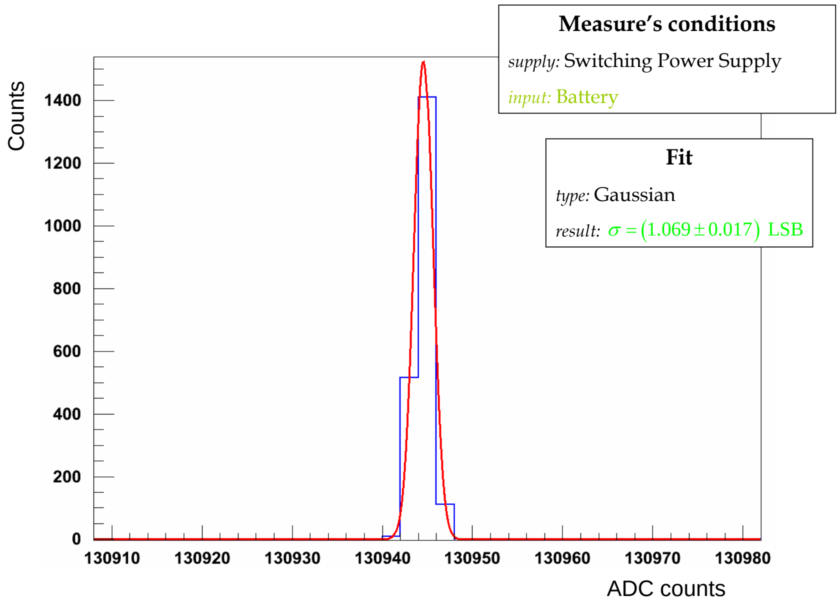

Figure 9.6: Histogram of the data taken with the piggy-back powered by a switching power supply. The input DC signal were provided by a commercial AA battery

sampling operations, and another one (a Spartan XC3S400[9]) to handle both data buffering and the VME protocol.

The last modification in the new design is on the analog input stage: the simple buffers mounted on the piggy back (Analog Devices AD8021 operational amplifiers [162] in the voltage follower configuration) have been replaced by a slightly more complicated network in order to match the voltage levels of the input signals to the input range of the ADCs [160].

The main functional blocks of CUORE DAQ board are sketched in figures 9.7 and 9.8.

All the "data" signals enter the board through a single connector (CONNs in figure 9.7); afterwards they are matched to the ADC input ranges by an analog input stage consisting of two operational amplifiers per channel, a resistive network and a DAC (DAC2 in figure 9.7): the principles of operation of the input stage will be described in section 9.4.1.

Each signal is sampled by a dedicated ADC controlled by a FPGA (FPGA1 in figure 9.7) which also reads the 18 bits digital data, adds to them other useful information (see section 9.4.2) and temporarily stores them in a circular buffer, waiting for a second FPGA (FPGA2 in figure 9.7) to copy them on a 4Mbyte SRAM (SRAM in figure 9.7) towards the VME.

The "trigger" signals used by the trigger system enter the board through a second connector (CONNt in figure 9.7).

Each of their voltage levels is compared with the output of a DAC (DAC1 in figure 9.7) controlled by FPGA2: the voltage value provided by each DAC, and therefore the threshold of each channel, is remotely programmable via the VME bus.

FPGA2 handles all the communications with the crate controller: its main task is to read the data from FPGA1, to copy them in the SRAM, and to allow them to be retrieved under VME control.

[9] the choice of a different, more powerful, model was motivated by the need to have more I/O pins, and more logic/memory resources available for the trasmission of the data on the VME bus

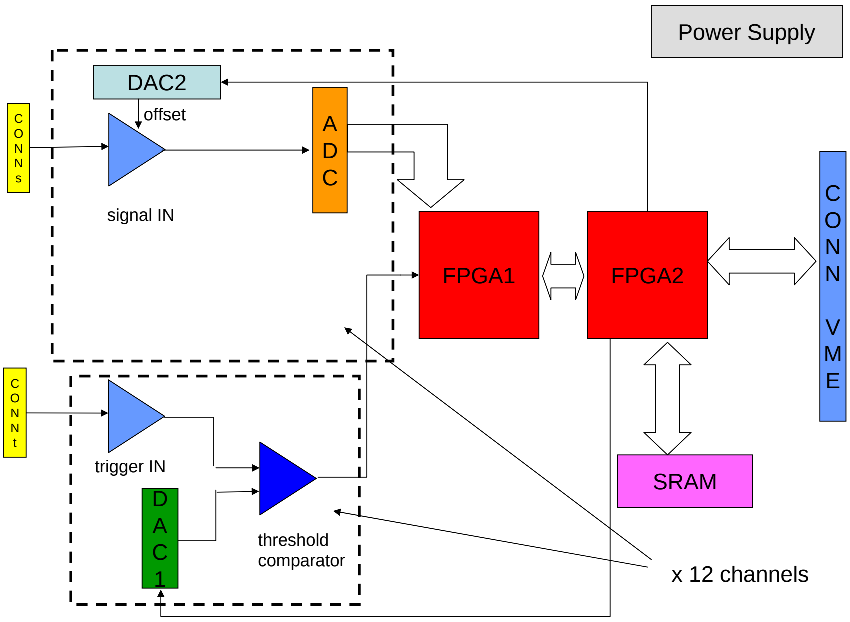

Figure 9.7: Schematic representation of the DAQ board: the main functional blocks are highlighted.

It allows the values of all the programmable parameters (sampling frequency, thresholds, etc.) to be written in dedicated registers on the board and it executes commands (see section 9.4.6).

The power supply for all the ICs mounted on the boards is provided by a set of voltage regulators (Power supply in figure 9.7) capable of obtaining the needed voltage levels from the voltage values provided by the VME bus (±12 V, ±5 V).

In the following sections each of the functional blocks previously mentioned will be described in detail.

9.4.1 The analog input stage

The purpose of the analog input stage is to match the voltage level of the input signals with the input range of the ADCs.

As stated in sections 8.1 and 9.1, each signal will be differential and its value will be in the range [0 V, +10 V] during data taking. During the procedure for thermistors characterization, negative voltage values need to be measured: the input signal, in this case, will assume values in the interval [-10 V, +10 V].

In both cases the two individual votages of each differential pair will be simmetrical with respect to the ground.

Such signals must be matched with the specifications of the chosen ADCs (AD7678) [160]: according to the data sheets, each ADC must be provided with a couple of signals whose values must be in the range [0 V, +5 V] (referred to ground).

The solution adopted for this purpose is shown in figure 9.9.

The voltage at pin 6 of the INA117 is given by:

$$V_6 = V_3 - V_2 + 19 \cdot V_5 - 18 \cdot V_1 \tag{9.4}$$

where V_x is the voltage at pin x.

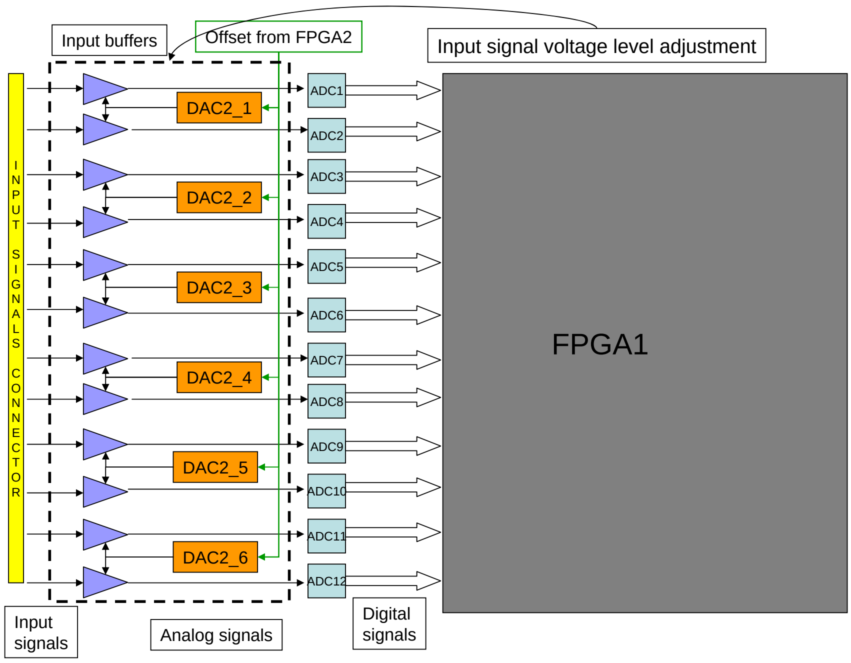

Figure 9.8: Schematic representation of the input and sampling stages of the DAQ board: the main functional blocks are highlighted.

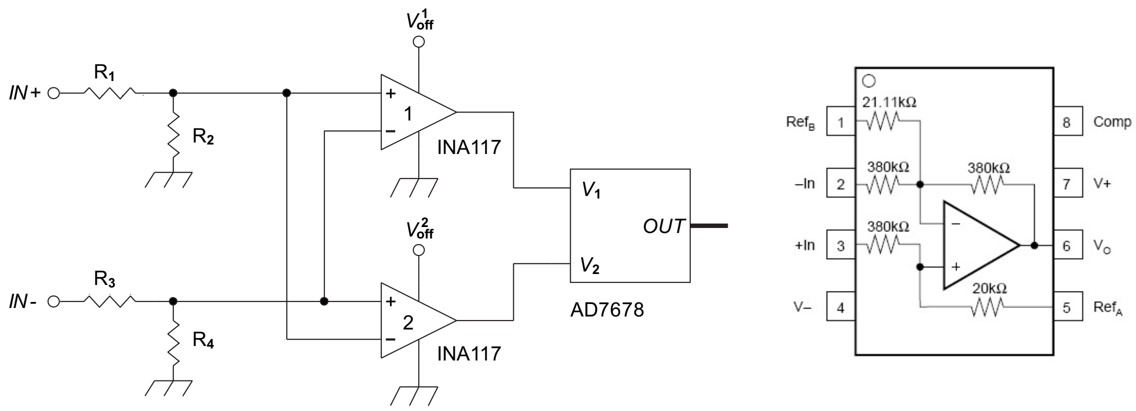

Figure 9.9: Left panel: the input stage of one channel. IN+ and IN- are the differential signal provided by the electronic system. V_1 and V_2 are the ADC input. Right panel: internal diagram of an INA117 [163]: each device is an operational amplifier connected to the precision resistors network shown

If pin 5 and pin 1 are electrically connected equation 9.4 becomes:

$$V_6 = V_3 - V_2 + (V_5 - V_1) = V_3 - V_2 + V_{off} \tag{9.5}$$

an arbitrary offset can therefore be added to the difference $V_3 - V_2$ by simply being applied to pins 5 and 1.

This was done on CUORE digitizing board: if the two wires of each input signal are connected as shown in the left panel of figure 9.9, then the voltages seen by each ADC are given by:

$$\begin{aligned} V_1 &= \frac{R_2}{R_1+R_2}\,IN_+ - \frac{R_4}{R_3+R_4}\,IN_- + V^1_{off} \\ V_2 &= \frac{R_4}{R_3+R_4}\,IN_- - \frac{R_2}{R_1+R_2}\,IN_+ + V^2_{off} \end{aligned} \tag{9.6}$$

With the choices

$$\begin{aligned} R_1 = R_2 \qquad R_3 = R_4 \\ V^1_{off} = 0 \quad V^2_{off} = +5V \end{aligned} \tag{9.7}$$

the voltages V_1 and V_2 satisfy the requirements shown above when $IN_+ - IN_-$ range in the interval [0 V, +10 V].

If the values of V^1_{off} and V^2_{off} are exchanged, the valid range of the input signals becomes

$$-10\ V < IN_+ - IN_- < +10\ \mathrm{V} \tag{9.8}$$

and the digitizing board becomes capable of accepting negative signals.

In general, with a suitable choice of the voltages V^1_{off} and V^2_{off}, the input range of the digitizing board can be set to any 10 V wide interval whose midpoint ranges in between -5 V and + 5 V.

In order to achieve such flexibility the voltages V^1_{off} and V^2_{off} are provided by two DACs on CUORE digitizing board (DAC2 in figures 9.7 and 9.8): their values are set by FPGA2 and are programmable via VME bus.

9.4.2 Sampling logic

The control of the sampling operations is demanded to FPGA1.

Figure 9.10 shows a simplified scheme of the digital logic on CUORE digitizing board: all the logic is handled by the two FPGAs mounted on the board (FPGA1 and FPGA2).

The logic implemented on each of them has been obtained from the synthesis of a custom verilog code whose details won't be discussed in this document.

FPGA1 controls data conversion driving the 12 ADCs through their digital interface.

The data of all the 12 channels are sampled simultaneously and read sequentially: the first datum read is acquired by the first channel, and the last belongs to the twelfth channel; the sampling speed is programmable in the range [0.8 Hz, 100 kHz] (the maximum sampling frequency is limited by the ADCs conversion time, which is 10 μs = 1/100 kHz).

The 18 bits data words are read by FPGA1 and copied in an internal FIFO memory.

At this point further informations are added to each data sample, namely:

- 4 bits identifying the **channel**
- 1 bit identifying the samples above the **trigger** threshold: the output of the threshold comparators responsible of generating the trigger signals are connected to FPGA1 which can therefore flag the data accordingly.
- 5 bits identifying the **board**. These bits are actually set to 0 by FPGA1: their value is set later on by FPGA2 according to the position of 5 dedicated jumpers on the digitizing board.
- 4 **time stamp** bits. A 4 bits counter is incremented every time the data from all the 12 channels are read and its value becomes part of each datum. When the counter reaches its maximum value it is reset to zero.

In this way 32 bits words are obtained out of the original 18 bits data, and FPGA2 must read them fast enough to prevent the FIFO from filling up: the FIFO can store up to 256 32 bits words.

If enabled, FPGA1 can average the data from each channel over 16[10] consecutive samples; this feature can be enabled and disabled by a dedicated VME command.

[10]the number of samples mediated over will soon be made programmable

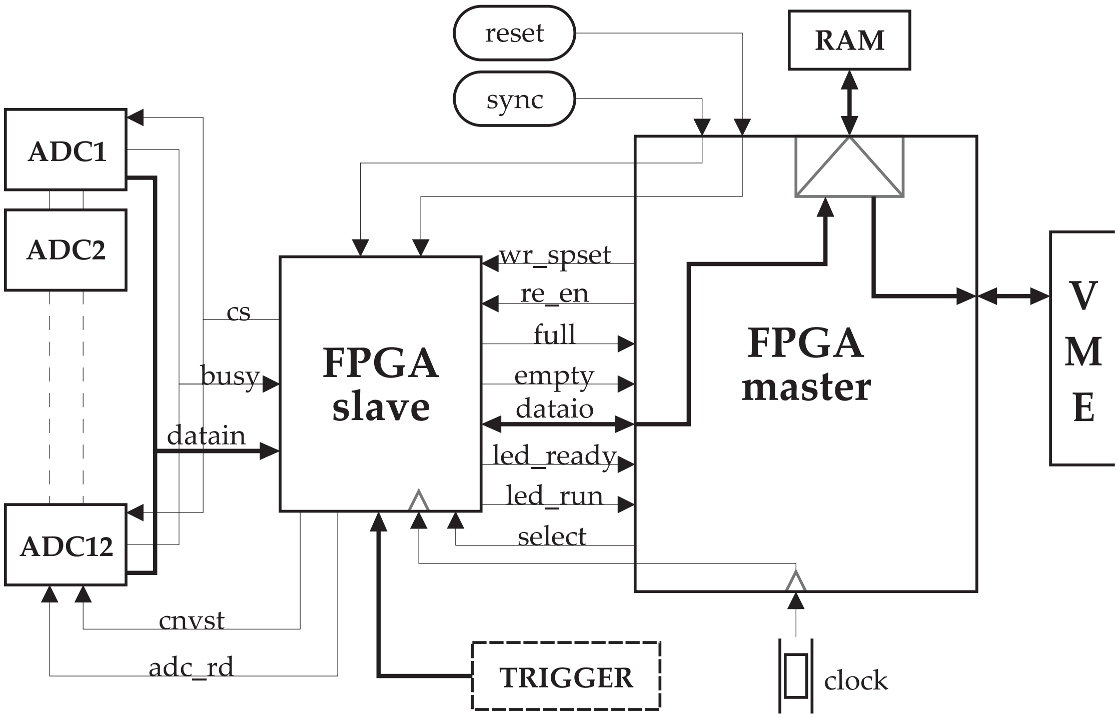

Figure 9.10: Schematic representation of the digital logic on CUORE DAQ board: rectangles are ICs, thin lines are digital signals, thick lines are data buses and ovals are front panel buttons

9.4.3 Trigger handling

The analog signals provided by the front-end electronics for triggering purposes (see 3.2.4) feed the digitizing board through a dedicated connector.

The output of a threshold comparator (one per channel, see figures 9.7 and 9.8) is raised when the relevant signal overcomes its threshold, and the corresponding digital data are flagged as explained in section 9.4.2.

In this way all the data are read by the DAQ PCs during data taking, and the pulses are found afterwards, by looking at the trigger bit in the data word during off-line analysis.

9.4.4 Data buffering and the VME interface

The words stored within the FIFO inside FPGA1 are copied by FPGA2 on a 4MB SRAM[11] on the digitizing board through a bidirectional data bus: this memory can store 1 million (4 MB/4B) words before filling up, and is therefore capable to store data for 17.5 s at 5 kHz sampling rate.

When requested by the DAQ controller, FPGA2 must retrieve the older data and make them available on the VME bus.

During this operation the data read by FPGA1 cannot be copied on the SRAM, because the necessary data bus is busy, therefore some precautions must be taken in order to prevent these data from being lost.

Data buses arbitration is done by FPGA2 according to the following criteria:

[11] Static Random Access Memory. 6 512 kB SRAM chips are actually mounted on the board.

- If the 256 words FIFO inside FPGA1 is not empty priority is given to data transfer from FPGA1 to the SRAM and any request from the VME bus is temporarily delayed.
- When the FIFO is empty, possible requests from the VME bus are accepted and the data written on the SRAM are made available to the DAQ PCs, which read them by 64 words block transfers.
- If, during a block transfer, any word is written on FPGA1's FIFO, the current transfer is normally finished but the next one is delayed until the whole content of the FIFO has been copied on the SRAM.

Since the FIFO on FPGA1 has a smaller capacity than the SRAM, it needs to be read much often, and this motivates the criteria above.

Besides data transfers, FPGA2 also handles all the programmable parameters:

- sampling frequency[12]
- trigger thresholds
- offset values for the analog input stage

Every time their values is changed by a software command, the content of a dedicated register on FPGA2 is modified and the necessary operations performed.

At last, FPGA2 is responsible of resetting the board and syncronizing it with the other ones as described in section 9.4.6.

9.4.5 The power supply

The various voltage supplies needed by the ICs on the digitizing board are obtained from the three standard voltages provided by the VME crate (± 12 V and $+5$ V) exploiting DC/DC converters.

Switching converters have been used to generate the supplies for the digital components: although they are slightly more noisy[13] than linear ones, they have much higher power conversion efficiencies.

The voltage levels needed by the analog components and by the ADCs have been generated both by linear and switching regulators: the preferred supply source can be chosen by changing the position of a dedicated jumper.

Bypass capacitors[14] have been placed across the power supply network in order to filter away possible ripples.

9.4.6 Syncronization and Reset functions

CUORE digitizing board can be reset in three ways:

1. pressing a dedicated button located on the front panel (see figure 9.11)
2. sending a proper signal to the right pins of the dedicated connector on the front panel (see figure 9.11)
3. issuing a software command

The RESET command is handled by FPGA2, which, after receiving it, deletes the data on the board and sets all the programmable parameters to their default values (in this way the sampling frequency is set to zero and sampling is therefore interrupted).

The effect of a SYNC command is to delete the data on the board without changing the configuration.

[12] The default value of the sampling speed is zero: sampling operations are started when a non zero sampling frequency is set. When, during data acquisition, the sampling speed is set to zero, data sampling is stopped again.

[13] The operation of a switching regulator requires a current within the regulator itself to be continuously inverted with a frequency of some tenths of kHz: this can cause a ripple with the same frequency in the output voltage level.

[14] A bypass (or decoupling) capacitor is placed in between the signal to be filtered and the ground. Its capacitance, together with its parasitic inductance and the inductance from the PCB current paths, form a LC circuit which behaves as a low pass filter.

After a SYNC, however, the sampling operations are restarted: the cyclic control counter mentioned in section 9.4.2 is set to zero and the next data acquired belongs to the first channel of the board.

In this way different boards can be syncronized by a simultaneous SYNC command sent ot all of them.

A SYNC signal can be given to a board in the same ways a RESET signal does: in order to feed a SYNC signal simultaneously to different boards, however, the SYNC connector must be used (neither the button nor a software command can be used for this purpose).

The opportunity to syncronize different boards allows to achieve a precision equal to $1/f_s$ (where f_s is the programmable sampling frequency) in the determination of the time each sample is acquired: after the digitizing boards have been syncronized at time t_0, the instant each sample has been acquired is given by

$$t = \frac{N}{f_c} + t_0 \tag{9.9}$$

where N is the number of samples acquired so far by the considered channel.

A picture of the board is shown in figure 9.11, where the functional blocks described are highligted.

Some attention must be deserved to the physical layout of the board: the PCB[15] is 1.6 mm thick, and it is made of 8 different stacked layers.

Both the placement of the various components and the routing[16] have been performed with the purpose of minimizing any kind of noise.

Analog signals have been confined on the left area of the card, close to the input connectors and far away from the digital signals circulating around the two FPGAs: in order to do this, the components have been placed accordingly.

Figure 9.12 shows, in the left panel, the silk-screen printed on the card: the main analog and digital components have been highlighted.

The 3 ground and power supply layers have been placed in between the signals layers in order to screen possible electromagnetic interferences between them.

Analog and digital return paths have been realized as separate metallic areas on the ground plane, as shown in the right panel of figure 9.12.

Each analog return path has been joined with the digital ground in one place only, located underneath the corresponding ADC, as suggested by data sheets [160].

Power supply paths have been made as large as possible, in order to reduce their parasitic resistances and inductances.

[15] Printed Circuit Board

[16] The routing is the procedure by which the electrical connections between the various ICs are physically defined.

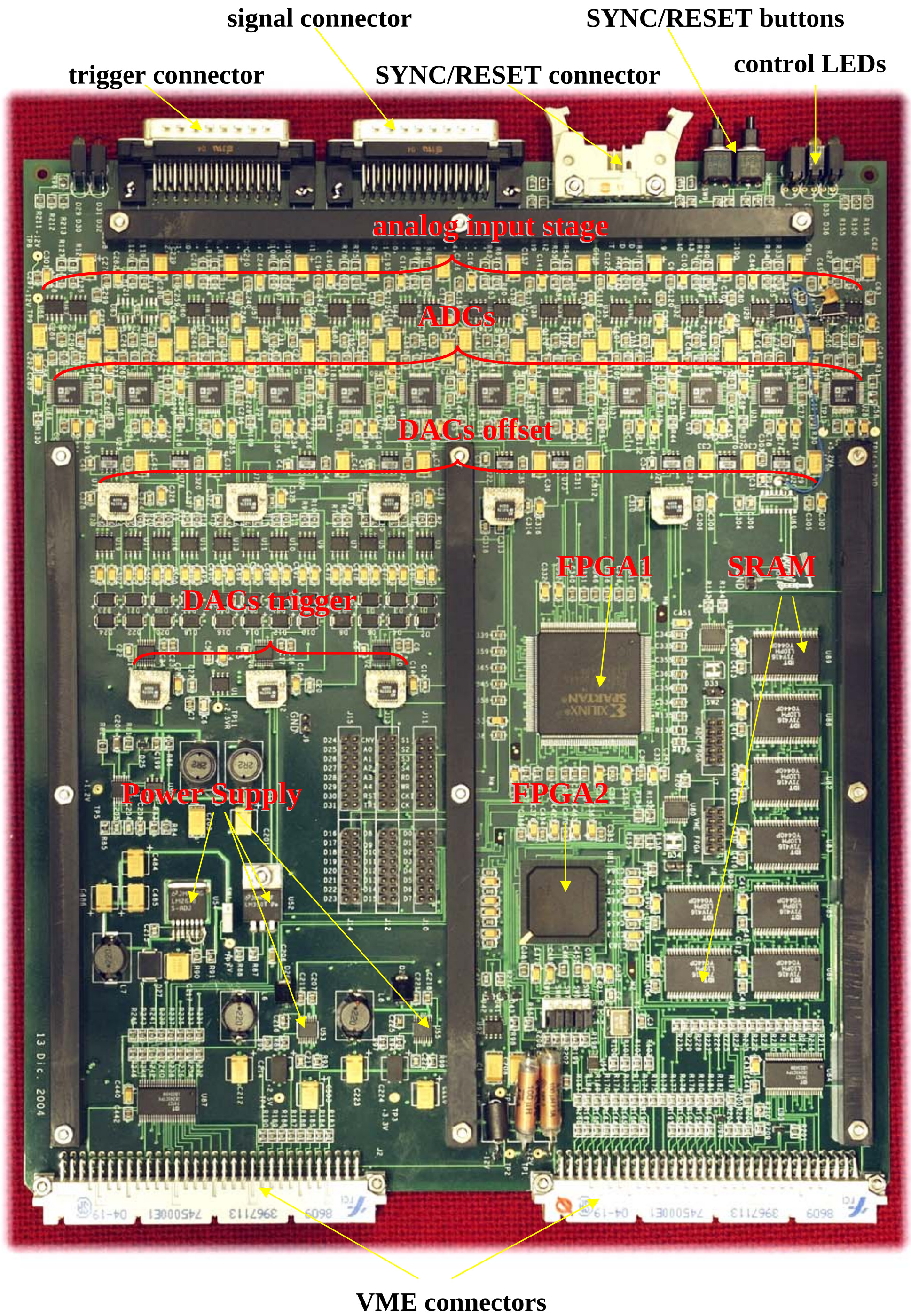

Figure 9.11: Picture of the prototype of CUORE digitizing board: the main components and functional blocks are highlighted.

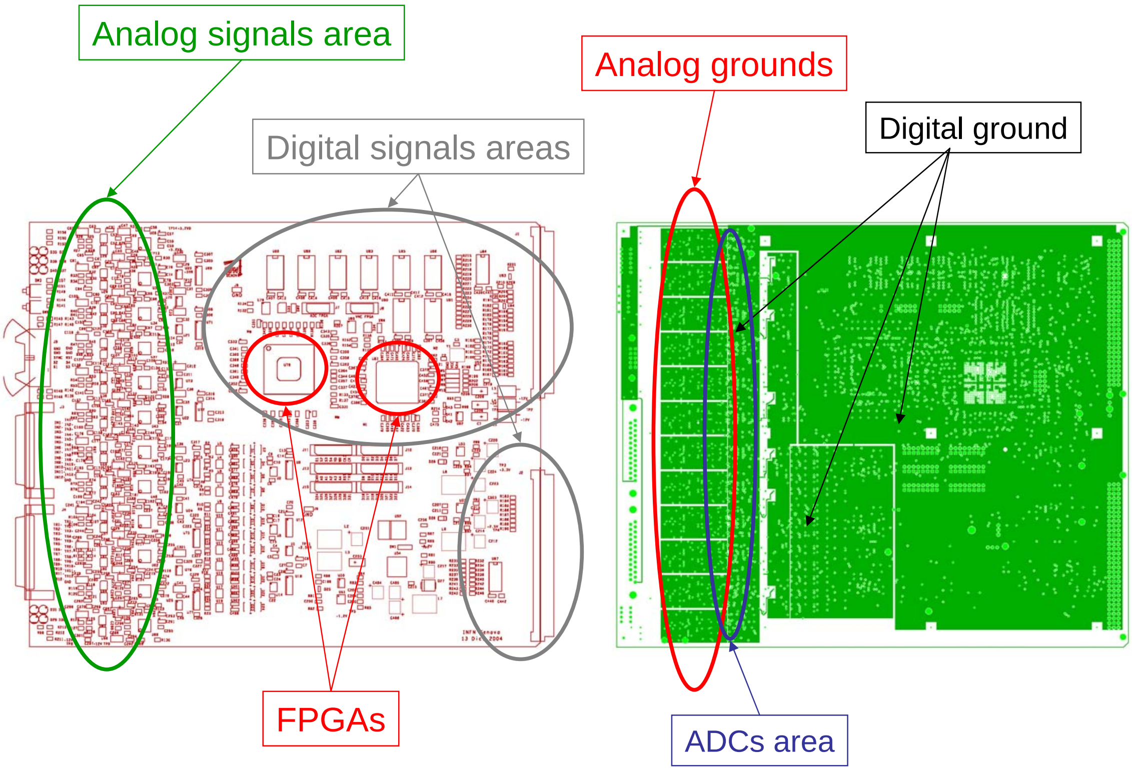

Figure 9.12: Left panel: silk-screen printing of CUORE digitizing board: the distribution of the analog and digital components is highlighted. Right panel: the ground layer. The 12 analog grounds under the analog input signals are cleary visible on the left hand side of the board, close to the input connectors. Each of them is connected with the digital ground in only one point located underneath the corresponding ADC.

9.5 Tests on the 12 channels prototype and measured performances

CUORE digitizing board has been characterized and tested in a set-up very close to the one in wich it will actually be used: the card was placed in a VME crate and the dedicated firmware was loaded on the two FPGAs[17].

During the tests the board was controlled by a Linux based PC, exploiting a commercial PCI/VME interface (Struck SIS1100/3100 [164]): the connection between the PC and the VME crate was realized by means of an optical fiber in order to electrically decouple the two systems.

For future convenience, a C library has been realized exploiting the basic functions provided with the drivers of the crate controller [164]: their purpose is to ease the setting of the programmable parameters.

A C program has also been written which contonuously reads the data sampled by the board, and writes them in ASCII files.

It actually consists of two separate asynchronous processes: the former is encharged of copying the data from the SRAM on the digitizing board onto a memory allocated on the PC for the purpose, the latter has the task to read the data from the memory and to write them on disk in the form of ASCII files.

Being the processes independent, the slower operation of writing data on disk doesn't delay the reading of the SRAM on the board, thus preventing it from filling up.

Three series of tests have been performed on the prototype so far: a first set of measurement has been made in Genova, with the main purpose of characterizing the board.

During a second test in Gran Sasso National Laboratories, the digitizing board was used to acquire the signals produced by CUORE like bolometers; this test confirmed the good performances of the card.

These tests and their results are described in the next sections.

9.5.1 Tests in Genova

The purpose of the first tests performed in Genova was to characterize the new board; its behaviour has been determined measuring the following quantities:

- **gain** and **offset** of the single channels
- **nonlinearity** in the gain possibly caused by asimmetries of the input signal
- intrinsic **noise** contribution of the board
- **stability** of the characteristic parameters with respect to temperature fluctuations

The set-up adopted is shown in figure 9.13: the digitizing board was inserted in the VME crate together with a VME adapting board.

The latter was realized with the purpose of converting unipolar signals into differential pairs symmetrical with respect to the ground; in this way the input signals for the DAQ board could be suorced either by a standard unipolar signal generator or voltage supply.

The crate was powered by its standard supply generator and connected to a PC by means of the Struck SIS100/3100 PCI/VME interface: the physical connection between the VME crate controller (SIS3100) and the PCI card (SIS1100) was provided by an optical fiber.

The measurements performed are separately shown and discussed in the following sections.

[17] Configuration data are actually stored in two PROMs, externally to the FPGAs: after applying power, the data are written to the FPGAs. PROMs are programmed individually once, connecting a dedicated PC to the board and exploiting the standard 4-pins JTAG protocol.

Figure 9.13: Picture of the set-up used during the tests performed in Genova. In the lower area of the picture the VME crate is visible. Three cards are inserted into the crate: the first on the left is the crate controller, the second one is the prototype of CUORE DAQ board, and the last one is the card used to adapt the input signals for the DAQ board. On the scaffold above the VME crate are placed the multimeter and the signal generator. The orange fiber optics connecting the crate controller to the DAQ PC is also visible.

Channels response

If a signal $V_{IN} = V_{IN+} - V_{IN-}$ is given as input to the digitizing board, the voltage level of the acquired signal is

$$V_S = GV_{IN} + V^{OFF} \tag{9.10}$$

where G is the gain of the board and V^{OFF} is its offset.

The parameters G and V^{OFF} will in general be different from channel to channel: in the first measurement performed on the 12 channels prototype all of them have been determined.

The linearity characteristics of the variour channels have been studied performing DC measurements of different input signals: the same voltage level has been applied to all channels and its value increased from 0 V to +5 V at 0.5 V steps.

Every voltage value has been measured both with the board and with a digital high precision multimeter (Agilent 34401A [165]) in order to obtain an accurate estimate of its absolute value.

The table in figure 9.14 shows the results obtained for a single channel (channel 6): the remaining channels had similar behaviours.

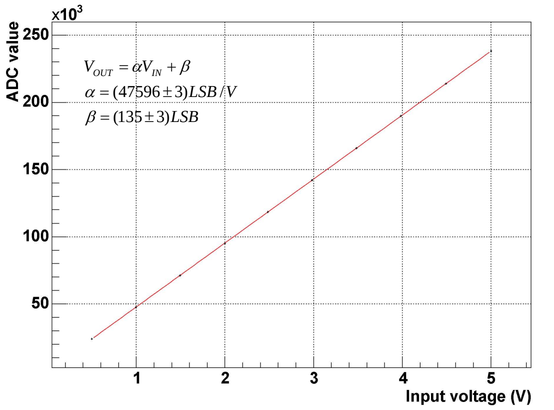

V_{IN} (V)	ADC out (LSB)
0.49910 ± 0.000011	23890.9 ± 0.1
0.99632 ± 0.000019	47556.2 ± 0.1
1.4925 ± 0.00006	71173.7 ± 0.1
1.9886 ± 0.00007	94784.1 ± 0.1
2.4851 ± 0.00008	118415.0 ± 0.1
2.9830 ± 0.00008	142113.0 ± 0.1
3.4826 ± 0.00009	165893.0 ± 0.1
3.9851 ± 0.00010	189813.0 ± 0.1
4.4914 ± 0.00011	213911.0 ± 0.1
5.0013 ± 0.00012	238179.0 ± 0.1

Figure 9.14: The table shows the values of the voltage levels measured with the digitizing board (channel 6) as a function of the input voltage level. The tabulated values are plotted in the left panel. The points, whose error bars are too small to be seen, have been fitted with a straigth line: the fit parameters are shown on the plot.

The plot in figure 9.14 has also been fitted with a straight line: the gain of each channel can be obtained as the slope of the line, whereas the offset is provided by its intercept with the y axis.

The gains of the 12 channels resulted very similar: their spread was found smaller than 0.2%, as shown in figure 9.15.

The spread in offset of the 12 channel was instead found smaller than 1200 LSB, as shown in figure 9.15.

The inhomogeinities between channels don't represent a problem for data taking since they can be accounted for by a calibration procedure: this requires however the characteristics of the board to remain stable in time.

A preliminary study of the board's stability has been made and its results are discussed in section 9.5.1.

Nonlinearity

A more detailed analysis of the data discussed in the previous section showed a tiny nonlinearity in the transfer function of the input analog stage of CUORE digitizing board: the difference between

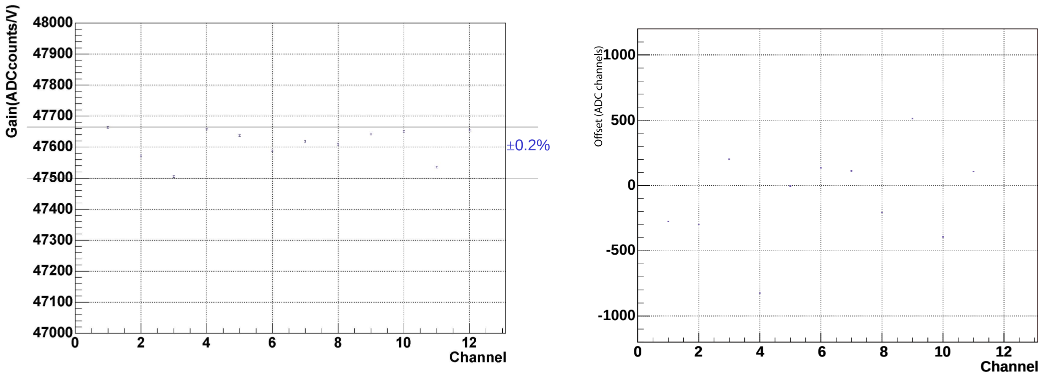

Figure 9.15: Left panel: the values of the gain is shown for the variuos channels: the difference between the channels is smaller than 0.2%. Right panel: the offset values fot the 12 channels is shown: their inhomogeneity is less than 1200 LSB.

the measured voltage levels and their values as determined from the best fit line (see figure 9.14) was determined and found always smaller than 4 LSB, as shown in figure 9.16.

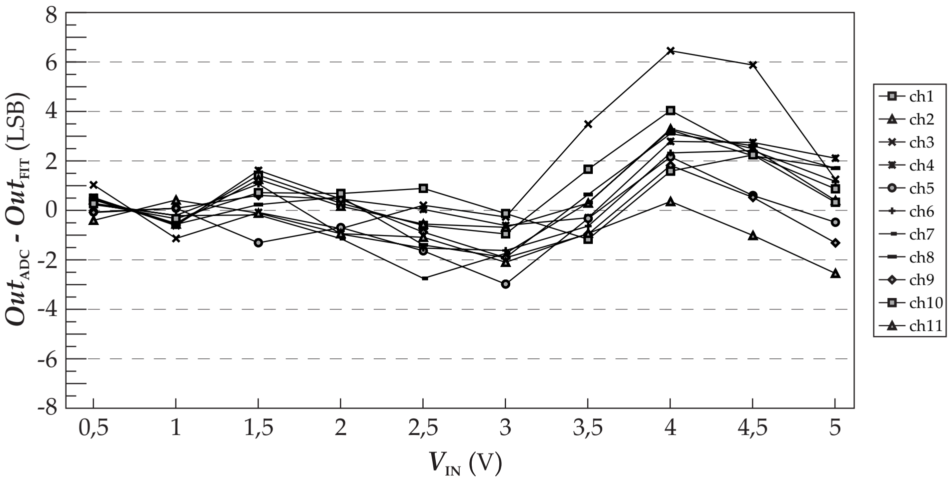

Figure 9.16: Difference between the measured voltage levels and the theoretical ones, determined from the best fit line (see figure 9.14), as a function of the input voltages applied. Channel 3 shows an anomalous behaviour, probably caused by interventions (manual solderings) during the initial set-up of the board.

In order to explain this value, the input analog stage of the board must be considered in detail.

With reference to figure 9.9, every acquisition channel is provided with an ADC whose inputs V_1 and V_2 are driven by two differential amplifier with unitary gain ($G = 1 \pm 0.05\%$ [163]).

These devices, together with the input resistive voltage dividers, can contribute to the nonlinearity of the channel's response.

The INL of the ADCs, quoted by their data sheets, is 9.5 ppm (2.5 LSB) [160], whereas the value reported for the differential amplifier [163] is 10 ppm of the full scale range.

The transfer function of the whole input analog stage is given by

$$V_1 - V_2 = G_1^+ \alpha IN_+ - G_1^- \beta IN_- + V_1^{\mathrm{off}} - G_2^- \beta IN_- + G_2^+ \alpha IN_+ - V_2^{\mathrm{off}} \tag{9.11}$$

where $G_1^+ \cong G_1^- \cong G_2^+ \cong G_2^- \cong 1$ are the gains of the differential amplifiers (the gain of each amplifier has been splitted into the two contributions corresponding to each of the two differential inputs) and $\alpha = \frac{R_2}{R_1+R_2} \cong \frac{1}{2}$ and $\beta = \frac{R_4}{R_3+R_4} \cong \frac{1}{2}$ are the gains of the resistive voltage dividers.

Equation 9.11 can be rewritten as

$$V_1 - V_2 = (G_1^+ \alpha + G_2^- \beta)(IN_+ - IN_-) + (G_2^+ \alpha - G_2^- \beta) IN_+ + (G_1^+ \alpha - G_1^- \beta) IN_- + V_1^{\mathrm{off}} - V_2^{\mathrm{off}} \tag{9.12}$$

The first term is responsible for the linear contribution to the board's response (GV_{IN} in eq. 9.10), while the second and third terms contribute with nonlinear effects to the board's gain.

In the ideal case in which the two amplifiers are exacly identical ($G_1^\pm = G_2^\pm = G^\pm$) these latter terms become:

$$(G^+ \alpha - G^- \beta)(IN_+ + IN_-) \tag{9.13}$$

therefore the nonlinear contribution vanishes if the input signals are perfectly symmetrical with respect to the ground.

In order to determine the maximum nonlinearity of the board, this contribution has to be estimated and added to the intrinsic contributions of the ADCs (9.5 ppm) and of the amplifiers (10 ppm).

The differential signals acquired during the measurements were generated by an adapting card (seee section 9.5.1) mounting the same amplifiers (INA117) as the digitizing board.

The assymmetry in the produced signals may only be due to the inhomogeneity in gain of these devices ($< 0,05\%$), which, multiplied for the difference in gain between the two voltage dividers in the input stage of the board ($< 1\%$, due to the tolerance in the nominal values of the component resistors) gives a contribution of 5 ppm.

The overall maximum value expected for the INL of each channel can be therefore obtained as $\sqrt{9,5^2 + 2 \cdot 10^2 + 5^2} \simeq 18$ ppm, corresponding to about 5 LSB.

This value perfectly accounts for the observed INL, which, as previously mentioned, was found to be smaller than 4 LSB.

A precise determination of the nonlinearity due to the asymmetry of the input signals has been obtained by a further set of measurements.

In order to maximize the nonlinear contribution in the board's response (equation 9.13), the same signal $IN_+ = IN-$ was applied to both the differential inputs of each channel, and DC measurements were taken increasing its value from -3.5 V to +4 V at 0.5 V steps.

In this way the linear contribution vanished ($IN_+ - IN- = 0$) and the nonlinear contribution could be therefore appreciated.

The results obtained for channel 1 are shown in figure 9.17.

The data agree with the linear law predicted by equation 9.13, which can therefore be used to account for a possible unbalance of the input signal.

If the symmetry $IN_+ = -IN_-$ is respected, the response of the board is however linear, as shown in section 9.5.1.

Noise measurements

In order to estimate the intrinsic noise contribution of the digitizing board a set of DC meaurements has been performed: during the most significant one the input signal connector was grounded, therefore the only contribution to the noise was due to the board itself.

The result obtained for channel 6 is shown in figure 9.18: the remaining channels presented very similar behaviours.

The distribution of the acquired samples was found gaussian, with a FWHM of about 30 LSB.

After several unsuccessful attempts to understand the origin of the observed noise, a measurement was made bypassing the input differential amplifiers and feeding the ADCs directly with an external signal: the result is shown in figure 9.19.

$IN_+ + IN-$ (V)	ADC out (LSB)
0.20000 ± 0.00006	345.556 ± 0.011
1.00012 ± 0.00004	355.617 ± 0.011
2.00000 ± 0.00006	372.292 ± 0.011
3.00200 ± 0.00020	386.354 ± 0.011
4.00100 ± 0.00020	400.875 ± 0.011
5.00020 ± 0.00020	416.533 ± 0.011
6.00320 ± 0.00020	431.720 ± 0.011
7.00120 ± 0.00020	446.562 ± 0.011
8.00080 ± 0.00030	463.214 ± 0.011
-1.00080 ± 0.00004	326.480 ± 0.011
-2.00010 ± 0.00006	310.882 ± 0.011
-2.99860 ± 0.00020	295.496 ± 0.011
-4.00760 ± 0.00020	280.645 ± 0.011
-5.00080 ± 0.00020	266.460 ± 0.011
-6.00000 ± 0.00020	252.287 ± 0.011
-7.00280 ± 0.00020	237.078 ± 0.011

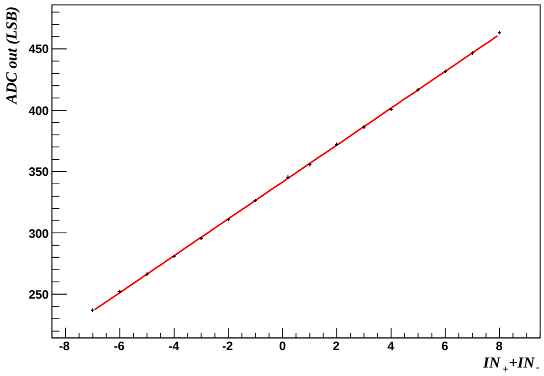

Figure 9.17: Left panel: values of the voltage levels measured with the digitizing board as a function of the sum of the voltage levels applied to the two differential inputs. Both inputs of channel 1 have been feeded with the same voltage level $IN_+ = IN-$: the asimmetry of the input signal with respect to the ground level causes a nonzero value to be measured even in the absence of a differential signal $IN_+ - IN- = 0$. The tabulated values are plotted in the right panel.

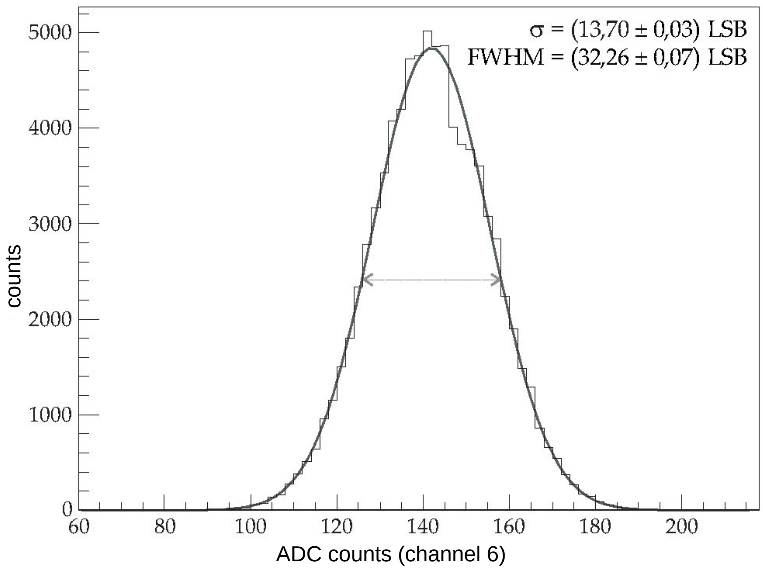

Figure 9.18: Histogram of the values acquired by channel 6: during the measurement the input signals were connected to ground.

The width (FWHM) of the distribution obtained in this configuration was $2,65$ LSB, and this proved

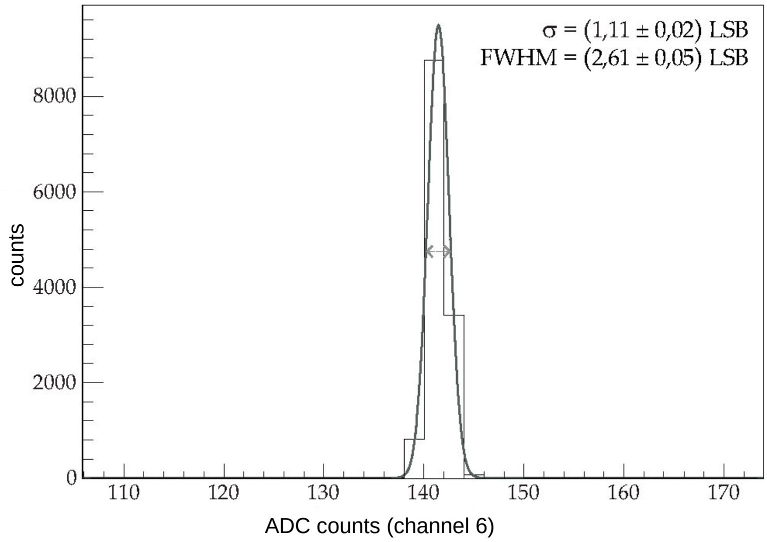

Figure 9.19: Histogram of the values acquired by channel 6: during the measurement the input amplifiers have been bypassed.

that the main contribution to the previously observed noise was due to these components[18].

As a consequence of this check it was decided to replace, in the next version of CUORE DAQ board, the adopted differential amplifiers (INA117 [163]) with the same operational amplifiers (AD8021 [162]) already used on the piggy-back (see section 9.3.1) with very good noise performances.

In spite of this problem, noise can be reduced exploiting the wide margin in the sampling frequency: the board has in fact a maximum sampling speed of 100 kHz (determined by the adopted ADCs), against the 5 kHz required to the DAQ system.

If the acquired data are averaged over, the noise can therefore be reduced at the expense of the acquisition speed.

The averaging procedure can be either demanded to the DAQ PC or to the logic on the board: this last option has the advantage of reducing the data flow through the VME bus, and has therefore been adopted enabling FPGA1 to average over 16 consecutive samples (see section 9.4.2).

The plot of figure 9.20 shows the effect of averaging over 16 and 64 consecutive samples: the gaussian distribution of the acquired values shrinks from an initial width (FWHM) of 32 LSB to about 8 and 4 LSB respectively.

A summary of the results obtained in the three cases is provided in table 9.1.

As a further check, the power spectrum was obtained for all the channels: each one was fed by a 1.5 V AA battery, and the the signals were acquired at a 781.25 Hz sampling frequency, averaging over 16 consecutive samples.

Figure 9.5.1 shows a sample signal and its power spectrum: this last was calculated from the FFT[19]

[18]The measured noise contribution of the INA117 amplifiers was found to agree with the specifications reported by the data sheets [163] and underestimated during the design phase of the board. In particular, the contribution of the amplifiers' noise spectral density, integrated over the ADCs' sampling time accounted for most ($\sim$ 30 LSB FWHM) of the observed noise; the remaining contribution ($\sim$ 9 LSB FWHM) was found to be due to the DACs in the analog input stage. The data shown in figure 9.19 have actually been obtained removing both the amplifiers and the DACs from the digitizing board.

[19]the FFT was calculeted with Matlab using a "sliding window" technique

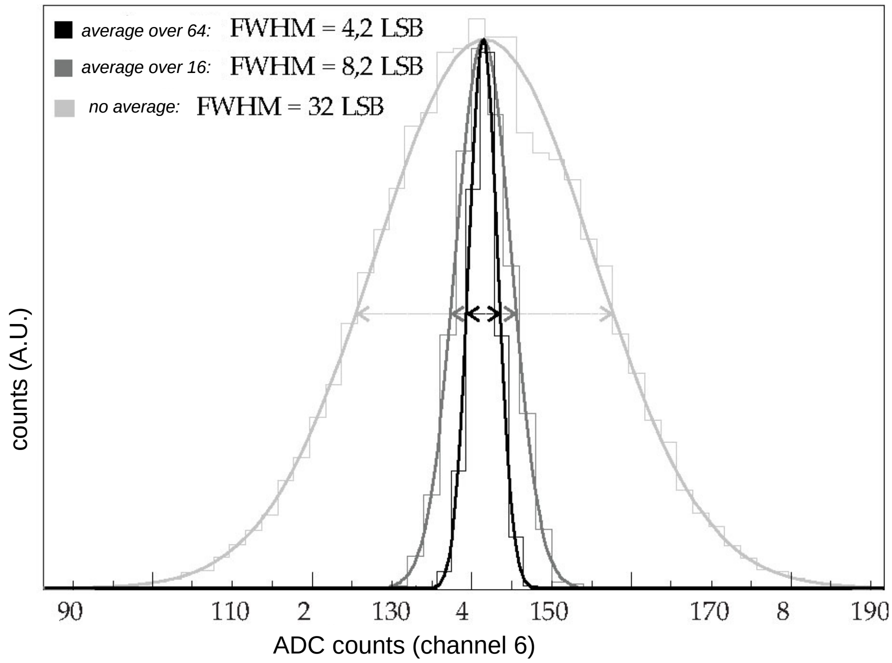

Figure 9.20: Distribution of the samples obtained without any average over the acquired data, compared with those obained averaging over 16 and 64 consecutive samples.

averaged samples	*sampling frequency*	*noise FWHM*
1	100 kHz	~32 LSB
16	6,25 kHz	~8 LSB
64	1,56 kHz	~4 LSB

Table 9.1: Sampling speed and noise level as a function of the number of consecutive samples averaged over.

of the signal over a period of about 3 minutes.

The noise spectrum was found "white" for all the channels (the behaviour of the remaining channels was similar to that of channel 5), and this proves the immunity of the digitizing board from possible environmental disturbances.

Stability

An obvious requirement for CUORE DAQ board is its long term stability: being CUORE DAQ system destinated to acquire data for a long time, the response of each channel must remain constant during data taking.

A first rough analysis of this issue was made comparing the characteristic parameters of the board measured at a distance of ~ 2 weeks.

Figure 9.22 and table 9.2 show the values of gain and offset (these quantities have been defined in section 9.5.1) measured for the various channels at a distance of 12 days.

The relative change in gain from one measurement to the other was found to be $0.876 \cdot 10^{-4}$, almost constant for all the channels, as can be observed from figure 9.22: this suggests a possible dependance

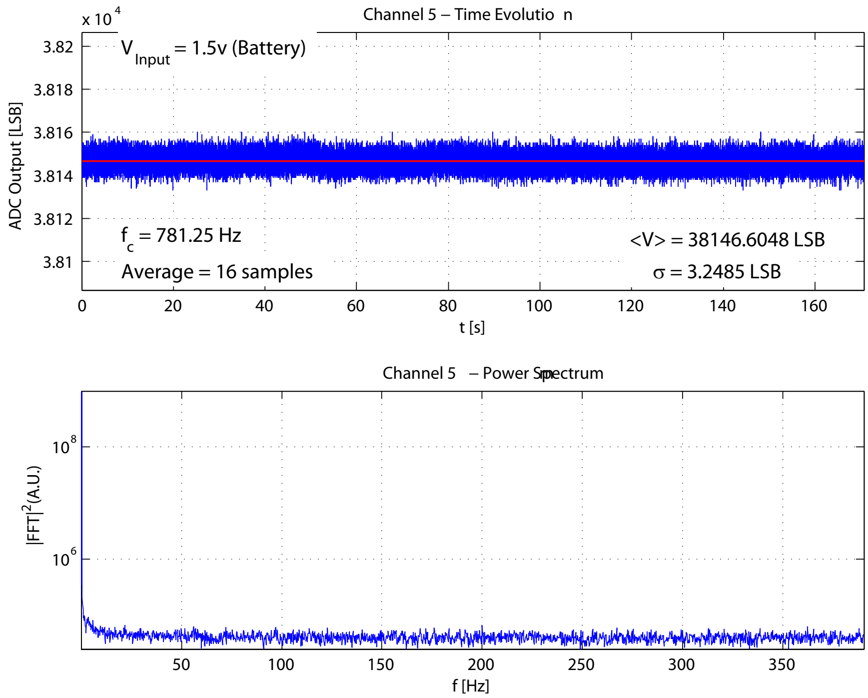

Figure 9.21: Time evolution and power spectrum of the signal acquired by channel 5 of the digitizing board. The signal was acquired at a 781.25 Hz sampling frequency, and each sample was obtained averaging over 16 data. the absence of peaks in the noise power spectrum shows, in particular, the good decoupling between the digitizing board and its environment.

on the environmental temperature.

The maximum change in offset resulted to be ~ 20 LSB (~ 10 %).

In order to investigate the effects of the temperature on the aforementioned parameters a further set of DC measurements has been taken in which the linearity parameters (gain and offset) of the digitizing

	5 May 2005		17 May 2005	
channel	*gain*	*offset*	*gain*	*offset*
1	47671 ± 3	-276 ± 3	47630 ± 3	-278 ± 3
2	47580 ± 3	-298 ± 3	47539 ± 3	-298 ± 3
3	47513 ± 3	200 ± 3	47473 ± 3	216 ± 3
4	47666 ± 3	-825 ± 3	47624 ± 3	-813 ± 3
5	47645 ± 3	-3 ± 3	47603 ± 3	14 ± 3
6	47596 ± 3	135 ± 3	47556 ± 3	149 ± 3
7	47626 ± 3	111 ± 3	47587 ± 3	125 ± 3
8	47617 ± 3	-207 ± 3	47576 ± 3	-187 ± 3
9	47650 ± 3	513 ± 3	47609 ± 3	529 ± 3
10	47658 ± 3	-393 ± 3	47617 ± 3	-379 ± 3
11	47544 ± 3	108 ± 3		

Table 9.2: Values of gain and offset determined from measurements taken at some days distance.

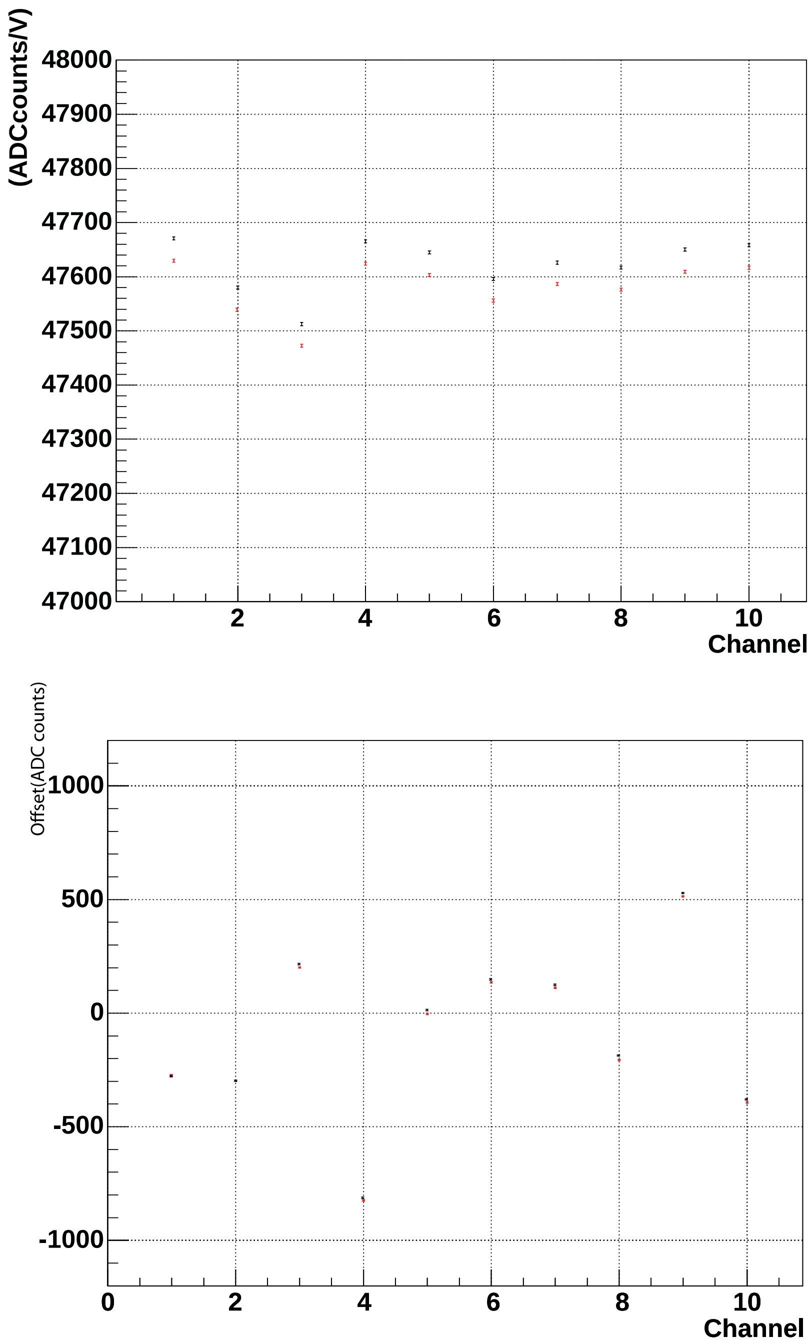

Figure 9.22: Values of gain and offset measured for the 12 channels of the digitizing board at 12 days distance: the blue dots mark the first set of measurements, acquired on the 5^{th} of May 2005, the red dots mark the second set, acquired on the 17^{th} of May 2005.

board have been measured as a function of the environmental temperature.

The wavefunction generator Agilent 34410A [166] was programmed to cyclically generate constant voltage levels of increasing value: at every increase the multimeter Agilent 33250A [165] should acquire its value while the temperature close to the VME crate was measured by a termometer provided with a data logger.

In this way the value for both the linearity parameters could be obtained from the acquired data with the same procedure described in section 9.5.1 and their fluctuations compared with the changes in temperature: the results obtained for the gain are shown in figure 9.23.

A clear dependance of the gain on the temperature appeared, whereas the offset didn't show an obvious behaviour: a likely explanation of this fact can come from the analysis of the analog input stage of the single channel.

With reference to figure 9.9 and equation 9.12, the transfer function of each channel's input stage is given by:

$$V_1 - V_2 = (G_1^+\alpha + G_2^-\beta)(IN_+ - IN_-) + V_1^{\mathrm{off}} - V_2^{\mathrm{off}} \tag{9.14}$$

where V_1^{off} and V_2^{off} anre the positive voltage levels outputted by the dedicated DACs (see figure 9.9), and where the contribution of a possible asymmetry of the input signal, discussed in section 9.5.1, has been neglected for convenience (the contributions of the remaining terms is by far dominant, see section 9.5.1).

In the reasonable hypotesis that a change in temperature has a similar influence on both $G_1^+\alpha$ and $G_2^-\beta$, equation 9.14 shows that a dependance of the gain $(G_1^+\alpha + G_2^-\beta)$ on the temperature is expected.

On the contrary, since V_1^{off} and $-V_2^{\mathrm{off}}$ have opposite signs, a possible influence of the temperature on their values is not expected to give a predictable contribution to the overall channel's response.

The dependance of the linearity parameters on the temperature, unambiguously shown by this preliminary analysis, will be studied in detail in the next future.

Two different approaches can be adopted during data acuisition with respect to this issue: if a clear, stable, dependance of the characteristic parameters on the environmental temperature is found, data will be corrected for the effects of temperature fluctuations; otherwhise the cooling system will be required to mantain the environmental temperature stable within the necessary precision.

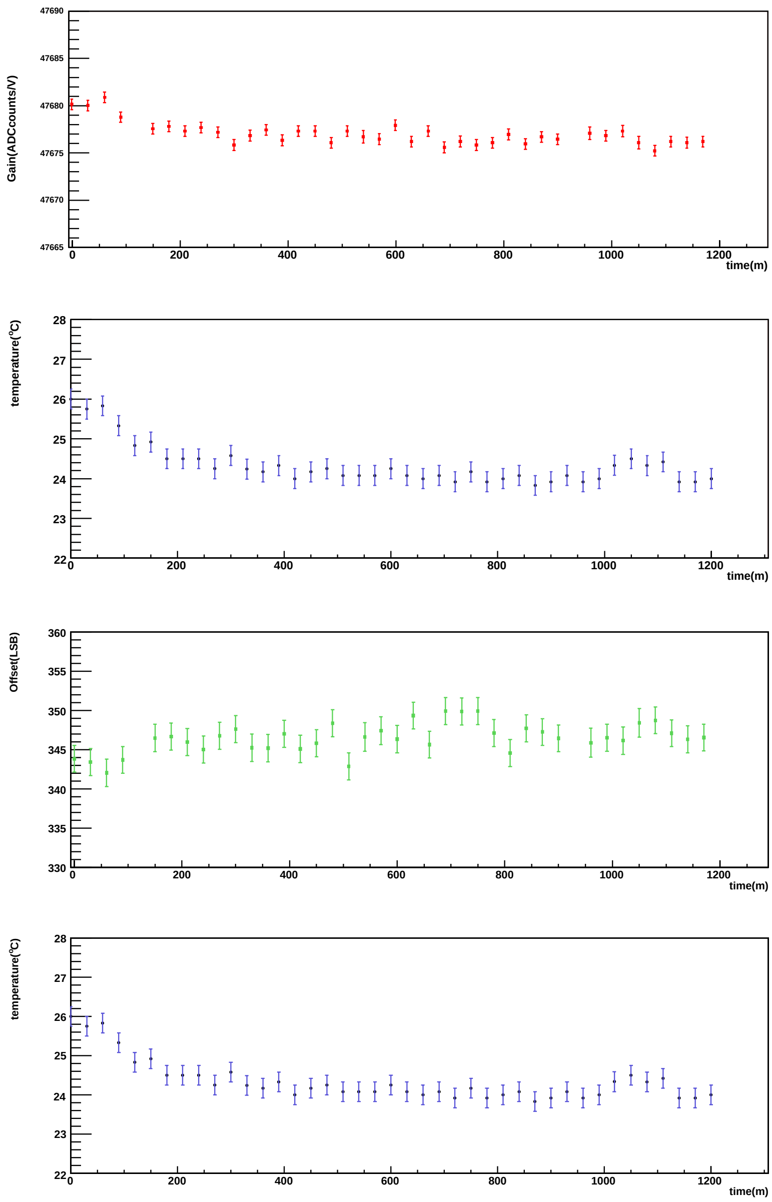

Figure 9.23: First and second panels: values of gain and temperature measured for channel 1 as a function of time, over a period of about 1 day. The fluctuations in gain are clearly related to the temperature changes. Lower panels: values of offset and temperature measured for channel 1 as a function of time, over the same time period. An obvious dependance is not visible in this case. The behaviour of all other channels were similar.

9.5.2 Test at LNGS

After the prototype of CUORE DAQ board was characterized in Genova, and its performances were found to satisfy the requirements discussed in section 9.1, a set of measurements was performed in Gran Sasso Underground Laboratories: the digitizing board was used to acquire real signals from the front-end stage of the experimental set-up located in Hall C and devoted to CUORE R&D[20]: the signal read-out system of the Hall-C set-up is analogous to Cuoricino apparatus, the main difference being in the reduced number of channels of the former.

It is worth remembering that CUORE electronic system will be realized as an extension of Cuoricino and Hall-C ones, which could therefore be used as a test bench for determining the performances of the data acquisition system in a realistic configuration.

The test in Hall C had in fact the purpose to confirm the results obtained in Genova and to check that the new data acquisition system didn't significantly interfere with the whole electronic system.

Only three channels out of the 24 available were acquired - other measurements were in progress on the remaining ones - corresponding to the following crystals: B675 and B705, located on the 3^{rd} floor of the crystal tower, and CTI-26, located close to the mixing chamber.

The cable previously connecting the front-end system with the DAQ system in use in Hall C was replaced by a filtered[21] one, which was splitted at one end: in this way three signals were connected to the new DAQ system (referred to as "Genova DAQ system" in the following), while the remaining signals were still acquired by the preexisting system (referred to as "Hall C DAQ system" hereafter).

Before being acquired, the latter signals passed across an analog selector which allowed one of them to be connected to an oscilloscope.

A schematic representation of the adopted configuration is shown in figure 9.24.

The prototype of CUORE digitizing board was inserted in the VME crate already used during the tests in Genova, which was placed on the Faraday cage containing the last stage of the front-end electronics.

The VME crate was connected to the DAQ PC through an optic fiber.

The set-up adopted for data reading was the same described in section 9.5.1.

During the measurements performed the characteristics of Genova DAQ were determined and compared with the pre-exixtent system: the results obtained are discussed in the following section.

Measurements and results

The configuration adopted during the measurements performed in hall C has been described above: the purpose of this test was to evaluate the performances of Genova DAQ system: in particular the noise contribution of the system and its pulse shape capability reconstruction were compared with those of the pre-existent Hall-C DAQ set-up.

Once data acquisition was started, the signals were continuously acquired by the digitizing board and stored in its 4MB SRAM.

The data were read from the board by two asyncronous processes, the former encharged to copy them in a local buffer, the latter to write them on disk: this frame was adopted to avoid that the time consuming operation of writing data on disk could interfere with their retrieving from the VME board, thus causing the SRAM to fill up.

No data selection was made at this stage.

Data were acquired at a sampling frequency of 781.25 Hz, enabling the feature of averaging over 16 consecutive samples see section 9.4.2; the sampling frequency adopted by the Hall-C system was about 500 Hz.

The r.m.s. value of the noise was calculated over 2 s time windows chosen on order to avoid any pulse was included in them: figure 9.25 shows the typical shape of the noise observable in the bolometers signals.

[20] CUORE Hall C facility is an array of 24 TeO_2 crystals operated in a dilution refrigerator, basically a reduced version of Cuoricino detector

[21] The analog signals were fed to the DAQ board by means of high inductance input cables, in order to suppress possible high frequency noise.

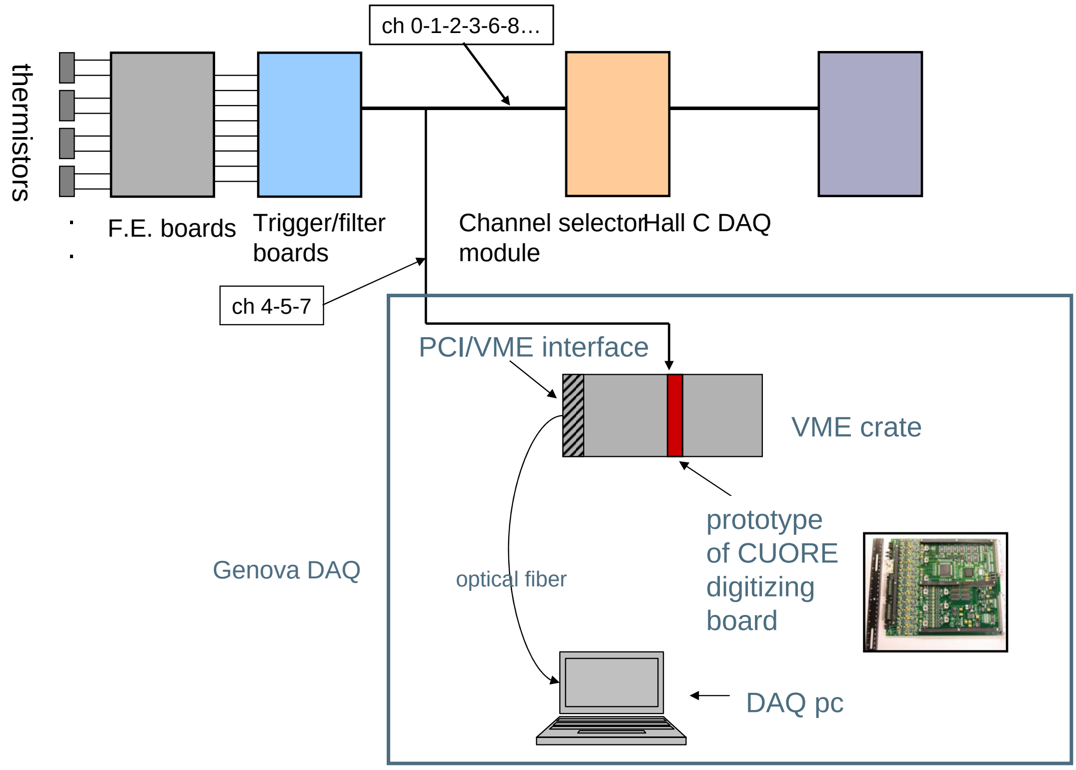

Figure 9.24: Experimental set-up adopted during the tests in Gran Sasso Underground Laboratories: the cable carrying the signals coming from the front-end system was split: three channels were acquired using the prototype of CUORE DAQ system, the remaining channels were acquired by the pre-existent system.

Hall-C DAQ system exploited 16 bits ADCs, whereas the nominal resolution of Genova system is 18 bits: in order to compare the values measured with the two systems a factor 4 must therefore be multiplied for the values measured with the former set-up.

If the r.m.s. values of the baselines are compared, the samples acquired with Genova system present a narrower distribution.

The observation of figure 9.25 shows however that the main contributions to its width is not due either to the electronic or to the DAQ system: the slow fluctuations clearly observable in figure 9.25 are in fact primarily due to microphonic noise caused by vibrations of the cryogenic apparatus.

The difference between the two measurements, which had been performed at different times[22], is therefore likely due to changed conditions of the cryogenic set-up.

High frequency fluctuations have a typical amplitude of 3 LSB of 18 bits $\simeq 110\ \mu$V (r.m.s.) and 1 LSB of 16 bits $\simeq 150\ \mu$V (r.m.s.) when extracted from the data taken with either systems respectively.

This preliminary measurements showed that the intrinsic noise level of the prototype of CUORE digitizing board is well within the specifications discussed in section 9.1, and lower than the characteristic level featured by the pre-exixting DAQ system.

[22] The same signal couldn't be acquired simultaneously by the two DAQ system because of crosstalks between them.

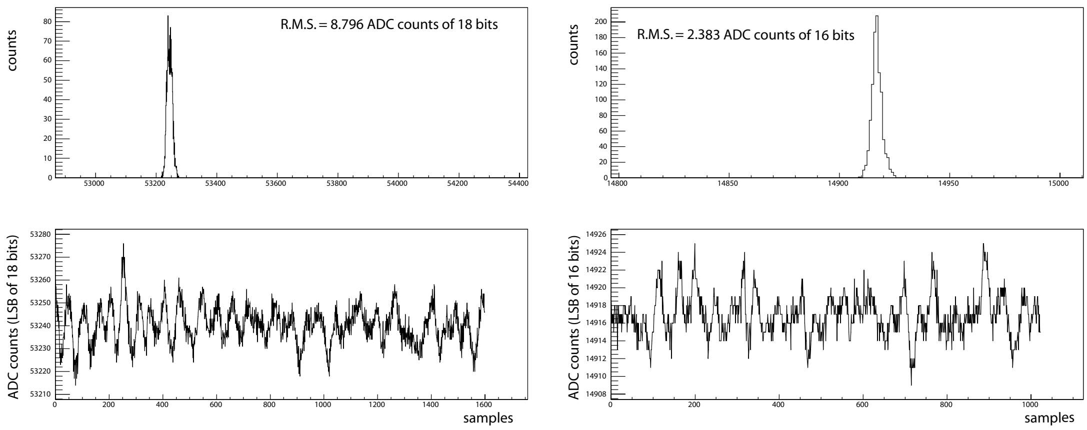

Figure 9.25: Left panel: sample of signal baseline acquired with Genova DAQ system: the low frequency (~ 10 Hz) fluctuations producing the main contribution to the measured r.m.s. noise, are not due to electronics. Right panel: sample of the same signal baseline acquired with the Hall-C DAQ system one day later: the higher r.m.s. noise observed ($2.383 \cdot 4 = 9.532 \gtrsim 8.796$ is probably due to different conditions of the cryogenic system.

A further analysis was dedicated to check that the pulse shapes acquired by Genova system were correctly reconstructed offline, and this was done comparing them with those obtained by the Hall-C one.

Several (~ 50) pulses of exactly the same height[23] have been averaged over, and the resulting pulse shapes, properly scaled, compared: figure 9.26 shows the resulting pulses superimposed.

The first effect investigated was the reduction of fast components in the signal spectrum, possibly caused by the filtered cables used for the analog signals: this would have resulted in longer risetimes for the acquired signals.

A negligible difference was instead found between risetimes obtained with Genova DAQ and those obtained with the Hall-C DAQ: the formers were found, on the average, 5% faster than the latter.

This error, equal to about twice the time difference of two consecutibe samples, is compatible with the jitter of the pulse shape due to the finite sampling frequency, and this demonstrates that the effect on the pulse shape of the filtered cables on the signals is negligible.

The signals sampled by the new system could be moreover reconstructed with better accuracy due to the higher sampling frequency exploited.

Other features of the sampled heater pulses, measured with the two systems, were compared, and their values were found compatible within the observed resolutions: a qualitative result is shown in figure 9.27 where the peak heights of the heater pulses, determined with the tho systems, are compared.

In summary, the tests performed in Hall-C demonstrated that the prototype of CUORE digitizing board can reconstruct pulse shapes as well as the pre-existing DAQ and with higher resolution (18 bit and ~ 800 Hz sampling frequency), and is less noisy during "normal" operation.

[23] A heater is glued on each crystal of the array in Hall-C and connected to a pulse generator programmed to periodically generate reference pulses. These are exploited for correcting possible variations of the baseline levels caused by temperature fluctuations, according to the procedure described in section 3.3.1. These thermal pulses have been selected and exploited for the analysis described in this section.

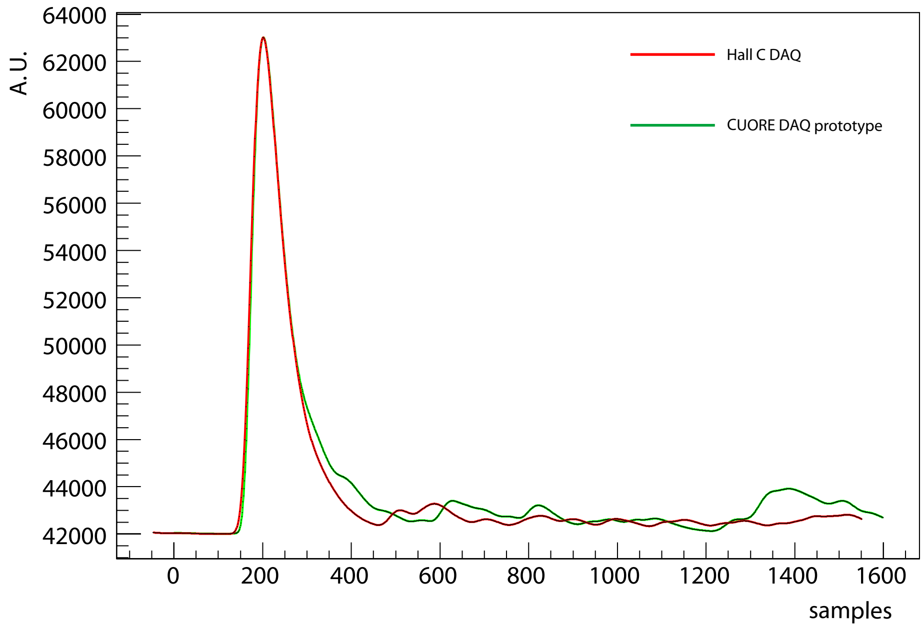

Figure 9.26: The pulse shapes obtained averaging over ~ 50 thermal pulses of the same height are shown: the green shape was obtained from the data acquired by Genova DAQ system, the red pulse was acquired by the Hall-C set-up. The fluctuations vosoble after the peak are due to particle induced pulses occurred after the main thermal pulse: their height has been only partially reduced by the average procedure. The time duration of the window displayed is about 2 s.

9.6 Summary

The tests on the prototype of CUORE digitizing board, performed both in Genova and in LNGS, have demonstrated that the board fulfils the requirements discussed in section 9.1: in particular it is capable of sampling and reconstructing input signals with the needed resolution and accuracy, and without introducing any dead time.

Its interface with the data acquisition system allows to correctly acquire data at sampling rates up to 50 kHz[24], exploiting its buffering capacity of 4MB.

A new campaign of tests will be performed in the next future with the goal of comparing the preformances of this custom board with those of the commercial NI digitizing board described in section 8.4.

[24] The maximum sampling rate tolerated by the digitizing board is actually 100 kHz: at this sampling frequency the time taken by the 4MB SRAM on the board to fill up is 1 s: it is a task of the software running on the DAQ PCs to prevent any loss of data, reading them fast enough.

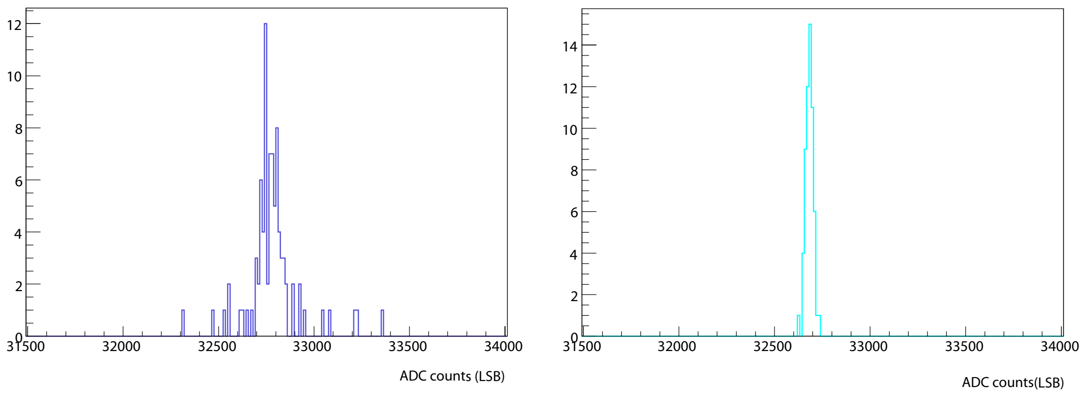

Figure 9.27: Left panel: distribution of the peak height as obtained from the data sampled with the Hall-C DAQ system. The values on the horizontal axis have been multiplied by a factor 4 in order to compare them with those shown in the right panel. Right panel: distribution of the peak height as obtained from the data sampled with Genova system. The difference in the width of the two observed distributions (138 L.S.B. r.m.s. for the former, 20 L.S.B. r.m.s. for the latter) is mostly due to different noise conditions during the measurements compared, as previously discussed: only in minimal part can it be attributed to the better resolution of the new system.

Appendix A

The VME standard

VME bus [167] (Versa Module Europa) is a flexible bus system which makes use of the Eurocard standard.

It was introduced by Motorola, Phillips, Thompson, and Mostek in 1981.

VME bus was intended to be a flexible environment supporting a variety of computing intensive tasks, and has become a very popular protocol in the computer industry.

It is defined by the IEEE 1014-1987 standard [168].

The bus usage was developed from a computing point of view, which leads to a completely memory mapped scheme: every device can be viewed as an address, or block of addresses.

Under VME, addresses and data are not multiplexed.

A block transfer, however, is possible for DMA[1] style applications.

The bus allows multiple masters, and contains a powerful interrupt scheme.

A resource manager is required to handle the interrupts.

The VME bus is a TTL based backplane which, although the system is asynchronous, sets the maximum data transfer speed to approximately 20 Mbytes per second.

Being however data transfer asynchronous, modules with a broad variety of response times are supported.

A typical transfer consists of an arbitration cycle (to gain bus control), an address cycle (to select the register) and the actual data cycle.

Read, write, modify and block transfers are supported.

Three main types of cards reside on the bus. The Controller, which supervises bus activity. A Master which Reads/Writes data to a Slave board, and a Slave interface which simply allows data to be accessed via a Read or Write from a Master.

- **Controller.** The VMEbus Controller "controls" access to the bus.

  Upon receiving a "Bus Request" signal from a bus Master, the Controller will "Bus Grant" that Master access to the bus.

  The Controller also handles Interrupts on the bus.

  When an Interrupt is received on one of the IRQ[2] lines the Controller will process that Interrupt by accessing the Interrupting card, and acknowledge the Interrupt.

  Only one Controller may reside on the VME bus.

- **Master.** The VMEbus Master Reads and Writes data to or from a Slave board.

  The Master "Bus Requests" access to the VME bus from the Controller.

  Once the Controller "Bus Grants" the Master access, the Master drives the Address and Data bus to perform a data transfer to a Slave board.

[1] Direct Memory Access

[2] Interrupt Request

Any number of bus Masters may reside on the VME bus, but only one may have control of the bus at any one time.

- **Slave.** A VMEbus Slave interface simply monitors the Address and Data bus for Reads or Writes sent to it.

  Once a correctly decoded address is received the Slave will either receive information for a Write, or output information onto the Data bus in the case of a Read.

  The bus Master continues to control the Data bus during either interface. A Slave may also generate Interrupts over any of 7 IRQ lines.

  The Interrupts are acknowledged by the bus Controller.

  Any number of Slave boards may reside on the VME bus.

The VME bus system consists of 4 sub-buses: the Data Transfer Bus, the Arbitration Bus, the Priority Interrupt Bus and the Utility Bus.

- **Arbitration Bus**

  The bus controller will drive the bus busy line (BBSY) low to show that it is in use.

  When this line is not low the arbiter module will sample the bus request lines (BR0-BR3) looking for a pending action.

  Requests on BR3 have the highest priority.

  Requests of equal priority are handled by a daisy chain using the bus grant in lines (BG0IN-BG3IN) and the bus grant out lines (BG0OUT-BG3OUT).

  The arbiter module which sits in slot 1 generates the first grant signal and this is passed to modules of increasing slot number.

- **Data Transfer Bus** The data transfer bus is used for reading and writing data between modules.

  The data bus (D00-D31) holds the actual data during a transfer.

  The address of the register being accessed is presented on the address bus (A01-A31).

  The address modifier lines (AM00-AM05) indicate the length of the address, the kind of data cycle and the master identifier.

  The address strobe (AS) is used to signal the presence of a valid address.

  The data strobes (DS0,DS1) are used by the module controlling the transfer (master) to signal the presence and acceptance of valid data on the bus along with information on the size of the word to be transferred (together with the long word select, LWORD).

  The WRITE line is used to distinguish between read and write operations.

  The data transfer acknowledge (DTACK) is used by the module being accessed (slave) to signal the completion of a transfer.

  Errors in this transfer are signaled using the bus error line (BERR).

  The timing of a data transfer is shown in figures A.1 and A.2.

  The data charts above relate to rev. 'C' and 'D' of the VME specifications (which was replaced by VME64). The newer versions of the spec added two new enhancements, termed 2eVME and 2eSST.

  2eVME which means "2 Edges", increased transfer speed by reducing data transfers from 4 edges to 2. Instead of the source taking DAV low (data valid), the slave taking DTACK low (data accepted), than the source bringing DAV high, and waiting for the slave to take DTACK high which would allow a new cycle to begin.

  The new process transfers data on each edge of DAV, effectively doubling the data transfer rate. So DAV going low would allow one data transfer, waiting for a low on DTACK, than DAV going high would allow another data transfer.

  2eSST which means "2 Edges, Source Synchronous Transfer"; adds to 2eVME, 2eSST does not wait for an acknowledgment (during data phases).

  This means that the VME hand-shake does not exist.

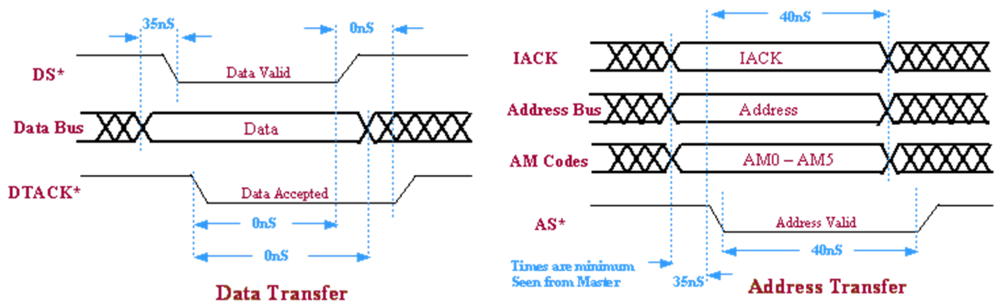

Figure A.1: Left panel: VME data bus Transfer timing. The Master places data on the Data Transfer Bus (DTB). The Master then waits a minimum of 35 ns before bringing one or both of the Data Strobe(s) (DS) low. The Data Strobe(s) going low indicate to the Slave that the Master has placed valid data on the bus. There is no defined time for the Slave to acquire the data and acknowledge the transfer. However, once the Slave has latched the data it will bring DTACK low. The Master will then release the Data Strobe(s). Once both of the data strobes are taken high the slave will release DTACK completing the data transfer cycle. The level of the data strobes during transfer indicate which bytes are accessed. Right panel: Address Transfer timing. The VMEbus Master takes IACK high and places the address and AM (0-5) codes on the bus. Once the lines have been valid for 35 ns the Master takes the Address Strobe (AS) low to indicate a valid address on the bus. For Interrupt cycles the IACK lines are driven low.

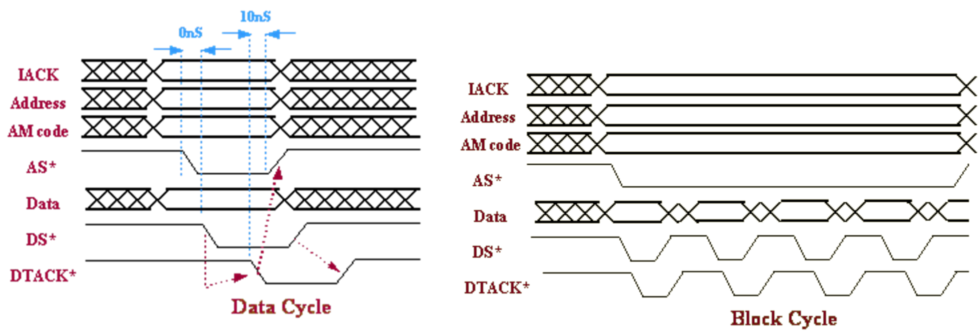

Figure A.2: Left panel: Single data transfer cycle. Right panel: Block transfer cycle. A VMEbus BLock Transfer (BLT) consists of a single Address cycle followed by up to a 256 Byte Data transfer (in ether 8, 16, or 32 bit segments). VME64 added the Multiplexed BLock Transfer (MBLT). MBLT uses all 32 data bits and all 32 address bits to transfer 64 data bits at once over the bus.

2eSST transfers data at the Masters rate and is not slowed by the slaves ability to accept data. DS1 is used as the clock when transferring data, and DTACK is used as the clock when reading data.

- **Priority Interrupt Bus** Normally only one processor is dedicated to handling interrupts by monitoring the interrupt request lines (IRQ1-IRQ7).
  IRQ7 has the highest priority.

In response to an interrupt, an address cycle is generated where the address indicates the request being acknowledged.

The interrupt acknowledge (IACK) is changed in the arbiter to a signal which is daisy chained down the bus using the interrupt acknowledge in pin (IACKIN) and interrupt acknowledge out pin (IACKOUT).

A data cycle follows where the module requesting the interrupt asserts its status and ID.

- **Utility Bus** Power is supplied to modules via pins at +5 V, -12 V and +12 V.

  An optional battery backup of the +5 V supply (+5STDBY) can also be present.

  The utility bus supports an independent 16 MHz system clock (SYSCLK).

  The system failure line (SYSFAIL) and AC failure line (ACFAIL) are bussed lines used to indicate global problems. The system reset line (SYSRESET) is used for initialization.

  Additional data transfers can take place along the serial data line (SERDAT) and are synchronized with the serial clock line (SERCLK).

A schematic representation of the communications between Controller, master and Slave is provided in figure A.3.

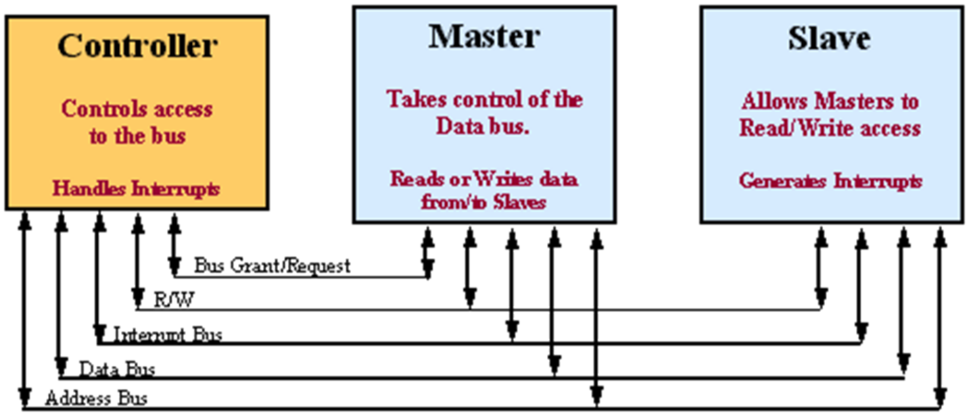

Figure A.3: VME card types and communications between them

Crates and modules mechanics The system is modular and follows the Eurocard standard.

VME card cages contain 21 slots, the first of which must be used as a crate manager.

The usual card sizes are 160 x 216 mm and 160 x 100 mm.

Cards of both sizes can be mixed in the same crate. The smaller cards are capable of 8 or 16 bit transfers.

The larger cards can perform 8, 16 or 32 bit transfers and also can support a larger address range (4 Gbytes vs. 16 Mbytes).

All VME boards have a P1 connector.

Larger cards may be equipped with the optional P2 connector.

Crates may support both connectors or (in less expensive systems) only P1.

The three standard VME card sizes are shown in figure A.4.

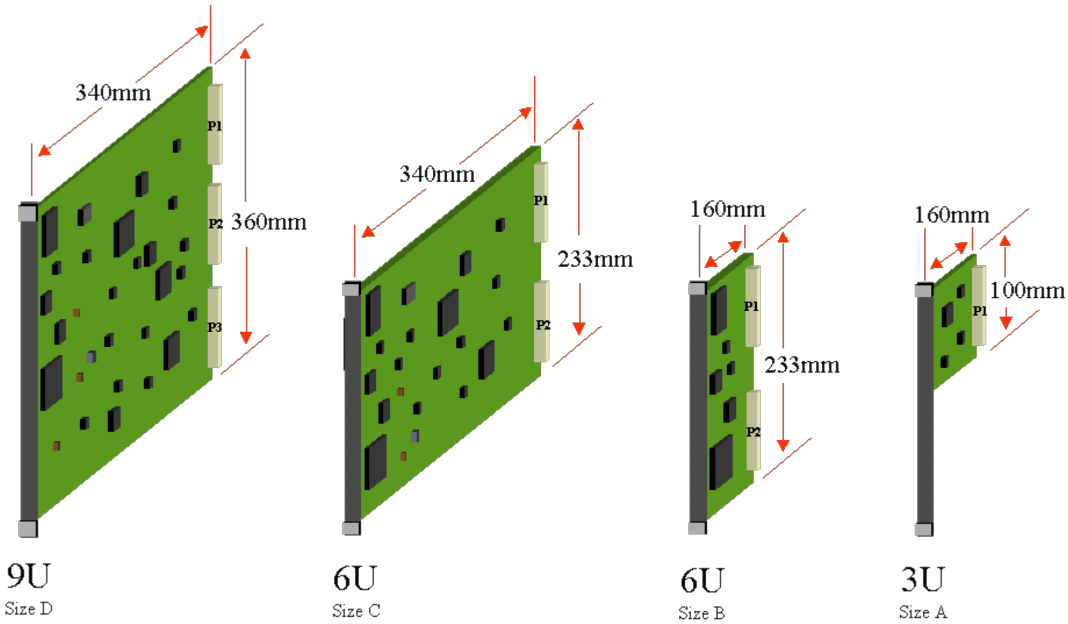

Figure A.4: Three basic VMEbus card sizes are shown above, which include 9U, 6U, and 3U. Two 6U card sizes are depicted. The VME64 spec added the P0 connector between P1 and P2 on the 6U size card (not shown)

List of Figures

List of Tables

Bibliography

[1] C. Weinheimer. Direct neutrino mass experiments: Present and future. *Nucl. Phys. Proc. Suppl.*, 118:279–286, 2003. 5, 20

[2] V. M. Lobashev et al. Direct search for neutrino mass and anomaly in the tritium beta-spectrum: Status of 'troitsk neutrino mass' experiment. *Nucl. Phys. Proc. Suppl.*, 91:280–286, 2001. 5, 20

[3] Steen Hannestad and Georg Raffelt. Cosmological mass limits on neutrinos, axions, and other light particles. *JCAP*, 0404:008, 2004. 5

[4] R. Bertlmann and H. Pietschmann. The decay of the neutral intermediate boson. *Phys. Rev.*, D15:683, 1977. 6

[5] John R. Ellis, Mary K. Gaillard, Georges Girardi, and Paul Sorba. Physics of intermediate vector bosons. *Ann. Rev. Nucl. Part. Sci.*, 32:443–497, 1982. 6

[6] T. Kajita. 1998. Talk presented at Neutrino'98 conference. 9, 15

[7] Y. Fukuda et al. Evidence for oscillation of atmospheric neutrinos. *Phys. Rev. Lett.*, 81:1562–1567, 1998. 9, 13, 15

[8] Samoil M. Bilenky and C. Giunti. Seesaw type mixing and muon-neutrino → tau-neutrino oscillations. *Phys. Lett.*, B300:137–140, 1993. 9

[9] Ling-Lie Chau and Wai-Yee Keung. Comments on the parametrization of the kobayashi-maskawa matrix. *Phys. Rev. Lett.*, 53:1802, 1984. 9

[10] Samoil M. Bilenky, C. Giunti, and W. Grimus. Phenomenology of neutrino oscillations. *Prog. Part. Nucl. Phys.*, 43:1–86, 1999. 9

[11] J. N. Bahall. *Neutrino Physics and Astrophysics.* Cambridge University Press, 1989. 12

[12] John N. Bahcall, Sarbani Basu, and M. H. Pinsonneault. How uncertain are solar neutrino predictions? *Phys. Lett.*, B433:1–8, 1998. 12

[13] Jr. Davis, Raymond, Don S. Harmer, and Kenneth C. Hoffman. Search for neutrinos from the sun. *Phys. Rev. Lett.*, 20:1205–1209, 1968. 12

[14] M. Altmann et al. Complete results for five years of gno solar neutrino observations. *Phys. Lett.*, B616:174–190, 2005. 12

[15] V. M. Vermul. Results from sage. *Nucl. Phys. Proc. Suppl.*, 110:315–319, 2002. 12

[16] Q. R. Ahmad et al. Measurement of the charged current interactions produced by b-8 solar neutrinos at the sudbury neutrino observatory. *Phys. Rev. Lett.*, 87:071301, 2001. 12

[17] T. J. Haines et al. Calculation of atmospheric neutrino induced backgrounds in a nucleon decay search. *Phys. Rev. Lett.*, 57:1986–1989, 1986. 13

[18] D. Casper et al. Measurement of atmospheric neutrino composition with imb- 3. *Phys. Rev. Lett.*, 66:2561–2564, 1991. 13

[19] K. S. Hirata et al. Experimental study of the atmospheric neutrino flux. *Phys. Lett.*, B205:416, 1988. 13

[20] L. Borodovsky et al. Search for muon-neutrino oscillations muon-neutrino → electron-neutrino (anti-muon-neutrino → anti-electron-neutrino) in a wide band neutrino beam. *Phys. Rev. Lett.*, 68:274–277, 1992. 14

[21] B. Zeitnitz. Karmen: Neutrino physics at isis. *Prog. Part. Nucl. Phys.*, 32:351–373, 1994. 14

[22] C. Athanassopoulos et al. Evidence for anti-nu/mu –> anti-nu/e oscillation from the lsnd experiment at the los alamos meson physics facility. *Phys. Rev. Lett.*, 77:3082–3085, 1996. 14

[23] G. Zacek et al. Neutrino oscillation experiments at the gosgen nuclear power reactor. *Phys. Rev.*, D34:2621–2636, 1986. 14

[24] G. S. Vidyakin et al. Limitations on the characteristics of neutrino oscillations. *JETP Lett.*, 59:390–393, 1994. 14

[25] M. Abbes et al. The bugey-3 neutrino detector. *Nucl. Instrum. Meth.*, A374:164–187, 1996. 14

[26] M. Apollonio et al. Limits on neutrino oscillations from the chooz experiment. *Phys. Lett.*, B466:415–430, 1999. 14, 16

[27] K. Eguchi et al. First results from kamland: Evidence for reactor anti- neutrino disappearance. *Phys. Rev. Lett.*, 90:021802, 2003. 14

[28] M. H. Ahn et al. Indications of neutrino oscillation in a 250-km long- baseline experiment. *Phys. Rev. Lett.*, 90:041801, 2003. 14, 16

[29] S. M. Bilenky. Neutrino masses, mixing and oscillations, 2000. Lectures given at the 1999 European school of High Energy Physics, Casta Papiernicka,Slovakia. 14, 15

[30] Abhijit Bandyopadhyay, Sandhya Choubey, Srubabati Goswami, S. T. Petcov, and D. P. Roy. Update of the solar neutrino oscillation analysis with the 766-ty kamland spectrum. *Phys. Lett.*, B608:115–129, 2005. 16, 173

[31] "international conference on neutrino physics and astrophysics "neutrino '98", 2004. `http://neutrino2004.in2p3.fr`. 17, 173

[32] F. Boehm et al. Results from the palo verde neutrino oscillation experiment. *Phys. Rev.*, D62:072002, 2000. 16

[33] Riccardo Barbieri, D. V. Nanopoulos, G. Morchio, and F. Strocchi. Neutrino masses in grand unified theories. *Phys. Lett.*, B90:91, 1980. 17

[34] Tsutomu Yanagida. Horizontal gauge symmetry and masses of neutrinos. *Prog. Theor. Phys.*, 64:1103, 1980. 17

[35] Rabindra N. Mohapatra and R. E. Marshak. Local b-l symmetry of electroweak interactions, majorana neutrinos and neutron oscillations. *Phys. Rev. Lett.*, 44:1316–1319, 1980. 17

[36] A. Zee. A theory of lepton number violation, neutrino majorana mass, and oscillation. *Phys. Lett.*, B93:389, 1980. 17

[37] T. J. Loredo and D. Q. Lamb. Implications of the sn 1987a neutrinos for supernova theory and the mass of nu/e. In *Santa Cruz 1989, Supernovae* 405-407. 19

[38] John F. Beacom, R. N. Boyd, and A. Mezzacappa. Technique for direct-ev scale measurements of the mu and tau neutrino masses using supernova neutrinos. *Phys. Rev. Lett.*, 85:3568–3571, 2000. 19

[39] D. E. Groom et al. Review of particle physics. *Eur. Phys. J.*, C15:1–878, 2000. 19

[40] R. Barate et al. An upper limit on the tau neutrino mass from three- and five-prong tau decays. *Eur. Phys. J.*, C2:395–406, 1998. 19

[41] A. Osipowicz et al. Katrin: A next generation tritium beta decay experiment with sub-ev sensitivity for the electron neutrino mass. 2001. 20

[42] A. Balysh et al. Subev limit for the neutrino mass from ge-76 double beta decay by the heidelberg - moscow experiment. *Phys. Lett.*, B356:450–455, 1995. 21

[43] V. Vasilev et al. Limits on different majoron decay modes of mo-100, cd-116, se-82, and zr-96 for neutrinoless double beta decays in the nemo-2 experiment. *Part. Nucl. Lett.*, 108:68–79, 2001. 21

[44] R. L. Avignone, F. T. Brodzinski. *Prog. Part. Nucl. Phys.*, 21:99, 1988. 21

[45] H. V. Klapdor-Kleingrothaus, I. V. Krivosheina, A. Dietz, and O. Chkvorets. Search for neutrinoless double beta decay with enriched ge- 76 in gran sasso 1990-2003. *Phys. Lett.*, B586:198–212, 2004. 21, 26, 41

[46] C. E. Aalseth et al. The igex ge-76 neutrinoless double-beta decay experiment: Prospects for next generation experiments. *Phys. Rev.*, D65:092007, 2002. 21, 26

[47] I. Ogawa et al. Search for neutrino-less double beta decay of ca-48 by caf- 2 scintillator. *Nucl. Phys.*, A730:215–223, 2004. 21

[48] H. Klapdor-Kleingrothaus, H. V. Pas and A. Yu Smirnov. *Phys. Rev. D.*, 63:073005, 1991. 21, 26

[49] S. R. Elliott, A. A. Hahn, M. K. Moe, M. A. Nelson, and M. A. Vient. Double beta decay of se-82. *Phys. Rev.*, C46:1535–1537, 1992. 21

[50] H. Ejiri et al. Limits on the majorana neutrino mass and right-handed weak currents by neutrinoless double beta decay of mo-100. *Phys. Rev.*, C63:065501, 2001. 21

[51] Fedor A. Danevich et al. Search for 2 beta decay of cadmium and tungsten isotopes: Final results of the solotvina experiment. *Phys. Rev.*, C68:035501, 2003. 21

[52] T. Bernatowicz et al. *Phys. Rev. C*, 47:806, 1993. 21

[53] C. Arnaboldi et al. *Phys. Lett. B*, 584. 21

[54] R. Luescher et al. *Phys. Lett. B*, 434:407, 1998. 21

[55] A. De Silva et al. *Phys. Rev. C*, 56:2451, 1997. 21

[56] R. N. Mohapatra and P. B. Pal. *Massive Neutrinos in Physics and Astrophysics.* World Scientific, October 2003. 21, 22

[57] Amand Faessler, Sergei Kovalenko, Fedor Simkovic, and Joerg Schwieger. Dominance of pion-exchange in r-parity violating supersymmetric contributions to neutrinoless double beta decay. *Phys. Rev. Lett.*, 78:183–186, 1997. 21, 22

[58] J. Schechter and J. W. F. Valle. Neutrinoless double-beta decay in su(2) x u(1) theories. *Phys. Rev.*, D25:2951, 1982. 21

[59] A. Vissani F. Feruglio, F. Strumia. *Nucl. Phys.*, B659:359, 2003. 22

[60] V. Cirigliano, A. Kurylov, M. J. Ramsey-Musolf, and P. Vogel. Neutrinoless double-beta decay and lepton flavor violation. *Phys. Rev. Lett.*, 93:231802, 2004. 23

[61] F. T. Avignone. Strategy for future double beta decay experiments. invited paper to Neutrino 2004. 24

[62] G.F. Dell'Antonio and E. Fiorini. *Suppl. Nuovo Cimento*, 17:132, 1960. 24

[63] E. Fiorini, A. Pullia, G. Bertolini, F. Cappellani, and G. Restelli. A search for lepton nonconservation in double beta decay with a germanium detector. *Phys. Lett.*, B25:602–603, 1967. 26

[64] C. E. Aalseth et al. Neutrinoless double-beta decay of ge-76: First results from the international germanium experiment (igex) with six isotopically enriched detectors. *Phys. Rev.*, C59:2108–2113, 1999. 26

[65] M. Gunther et al. Heidelberg - moscow beta beta experiment with ge-76: Full setup with five detectors. *Phys. Rev.*, D55:54–67, 1997. 26

[66] Steven R. Elliott and Petr Vogel. Double beta decay. *Ann. Rev. Nucl. Part. Sci.*, 52:115–151, 2002. 26

[67] H. V. Klapdor-Kleingrothaus, A. Dietz, H. L. Harney, and I. V. Krivosheina. Evidence for neutrinoless double beta decay. *Mod. Phys. Lett.*, A16:2409–2420, 2001. 26

[68] Yu. G. Zdesenko, Fedor A. Danevich, and V. I. Tretyak. Has neutrinoless double beta decay of ge-76 been really observed? *Phys. Lett.*, B546:206–215, 2002. 26

[69] A. M. Bakalyarov, A. Ya. Balysh, S. T. Belyaev, V. I. Lebedev, and S. V. Zhukov. Results of the experiment on investigation of germanium-76 double beta decay. *Phys. Part. Nucl. Lett.*, 2:77–81, 2005. 26

[70] X. Sarazin and D. Lalanne. Status report on the double-beta decay experiment nemo-3. 2000. 27

[71] R. Arnold et al. Limits on different majoron decay modes of mo-100 and se-82 for neutrinoless double beta decays in the nemo-3 experiment. *Nucl. Phys.*, A765:483–494, 2006. 27

[72] H. Ejiri. Double beta decays and neutrino nuclear responses. *Nucl. Phys. Proc. Suppl.*, 77:346–351, 1999. 27

[73] J. Farine. Search for beta beta decay in xe-136: Gotthard results. Prepared for 17th International Conference on Neutrino Physics and Astrophysics (Neutrino 96), Helsinki, Finland, 13-20 Jun 1996. 27

[74] V. Artemiev et al. Track detector itep for investigation the double beta decay devis. ITEP-8-04. 28

[75] P. G. Bizzeti et al. New results of cd-116 beta beta decay experiment. *Nucl. Phys. Proc. Suppl.*, 110:389–391, 2002. 28

[76] M. Danilov et al. Detection of very small neutrino masses in double-beta decay using laser tagging. *Phys. Lett.*, B480:12–18, 2000. 28

[77] H. V. Klapdor-Kleingrothaus, L. Baudis, G. Heusser, B. Majorovits, and H. Pas. Genius: A supersensitive germanium detector system for rare events. 1999. 28

[78] H. V. Klapdor-Kleingrothaus, O. Chkvorez, I. V. Krivosheina, H. Strecker, and C. Tomei. Genius test-facility started operation in gran sasso: With first ten kg of naked germanium detectors in liquid nitrogen. *Nucl. Instrum. Meth.*, A511:341–346, 2003. 28

[79] H. Ejiri et al. Spectroscopy of double-beta and inverse-beta decays from mo-100 for neutrinos. *Phys. Rev. Lett.*, 85:2917–2920, 2000. 29

[80] G. L. Knoll. *Radiation detection and measurement*. Wiley & Sons, 1989. 33, 98

[81] Taylor B. et al. *Phys. Rev. Lett.*, 49:416, 1969. 35

[82] K. Irwin et al. *Rev. Sci. Instr.*, 66:5322, 1995. 35

[83] J. Mott, N. Davis. *Phil. Mag.*, B42:845, 1980. 36

[84] E. Miller, A. Abrahams. *Phys. Rev.*, 120:761, 1961. 36

[85] E. Haller. *J. Appl. Phys.*, 77:2857, 1995. 36, 44, 66

[86] T. Fiorini, E. Niinikoski. *Nucl. Instr. and Meth. A*, 24:224, 1984. 41

[87] G. Gervasio et al. *Nucl. Phys. A*, 663:873, 2000. 42

[88] A. Alessandrello et al. *Proc. of the Int.Workshop on Therm. Detectors*, page 91, 1992. 45

[89] A. Alessandrello et al. New experimental results on double beta decay of te-130. *Phys. Lett.*, B486:13–21, 2000. 46

[90] F. Pobell. *Matter and Methods at Low Temperatures*. Springer - Verlag, Berlin, 1992. 47

[91] A. Alessandrello et al. *IEEE Trans. Nucl. Sci.*, 44:416, 1997. 48, 49

[92] A. Alessandrello et al. *Nucl. Instrum. Methods*, 444:111, 2000. 48, 49

[93] G. Pessina. *Nucl. Instrum. Methods*, 444:132, 2000. 48

[94] G. Pessina. *Rev. Sci. Instrum.*, 70:3473, 1999. 49

[95] C. Arnaboldi et al. *Nucl. Instrum. Methods A*, 520:578–580, 2004. 50, 122

[96] E. Gatti and P. F. Manfredi. Processing the signals from solid state detectors in elementary particle physics. *Riv. Nuovo Cim.*, 9N1:1–146, 1986. 51

[97] W. H. Press et al. *Numerical Recipes in C , The Art of Scientific Computing*. 1991. 52

[98] A. Alessandrello et al. Methods for response stabilization in bolometers for rare decays. *Nucl. Instrum. Meth.*, A412:454–464, 1998. 52

[99] S. Baker and P.D. Cousins. *Nucl. Instr. Methods*, 522:437, 1984. 62

[100] R. M. Barnett et al. *Phys. Rev. D*, 54:1, 1996. 62

[101] C. Arnaboldi et al. 62

[102] Klapdor-Kleingrothaus et al. *Nucl. Instr. Methods*, 522:367, 2004. 62

[103] M. Barucci et al. *J. Low Temp. Phys.*, 123:303, 2001. 67

[104] R. Ardito et al. 2005. 67

[105] G. Heusser. Private communication. 75

[106] M. Laubenstein. Private communication. 75

[107] R. Ardito et al. Cuore: A cryogenic underground observatory for rare events. 2005. 77, 93, 111

[108] R. Silberberg and R. Tsao. *Astrophys. J. Suppl. Ser.*, 220:315, 1973. 78

[109] F. Arneodo et al. Neutron background measurements in the hall c of the gran sasso laboratory. *Nuovo Cim.*, A112:819–831, 1999. 79, 105

[110] P. Belli et al. Search for wimps with enriched xenon at gran sasso. *Nuovo Cim.*, C19:537–544, 1996. 79, 85

[111] Neta A. Bahcall, Jeremiah P. Ostriker, Saul Perlmutter, and Paul J. Steinhardt. The cosmic triangle: Revealing the state of the universe. *Science*, 284:1481–1488, 1999. 83

[112] O. Elgaroy et al. A new limit on the total neutrino mass from the 2df galaxy redshift survey. *Phys. Rev. Lett.*, 89:061301, 2002. 83

[113] Rupert A. C. Croft, Wayne Hu, and Romeel Dave. Cosmological limits on the neutrino mass from the ly alpha forest. *Phys. Rev. Lett.*, 83:1092–1095, 1999. 83

[114] R. Bernabei. Dark matter search. *Prog. Part. Nucl. Phys.*, 48:263–282, 2002. 83

[115] Gerard Jungman, Marc Kamionkowski, and Kim Griest. Supersymmetric dark matter. *Phys. Rept.*, 267:195–373, 1996. 83

[116] Angel Morales. Direct detection of wimp dark matter. *Nucl. Phys. Proc. Suppl.*, 87:477–488, 2000. 83

[117] John R. Ellis, Andrew Ferstl, and Keith A. Olive. Exploration of elastic scattering rates for supersymmetric dark matter. *Phys. Rev.*, D63:065016, 2001. 83

[118] A. Bottino, F. Donato, N. Fornengo, and S. Scopel. Probing the supersymmetric parameter space by wimp direct detection. *Phys. Rev.*, D63:125003, 2001. 83

[119] Lars Bergstrom. Non-baryonic dark matter: Observational evidence and detection methods. *Rept. Prog. Phys.*, 63:793, 2000. 83

[120] O. Besida. *The dark side of the Universe*. World Sc., 1994. 85

[121] Snowden-Ifft et al. *The identification of Dark Matter*. World Sc., 2000. 85

[122] J. I. Collar and F. T. Avignone. Diurnal modulation effects in cold dark matter experiments. *Phys. Lett.*, B275:181–185, 1992. 85

[123] M. L. Sarsa et al. Searching for annual modulations of wimps with nai scintillators. *Phys. Lett.*, B386:458–462, 1996. 85

[124] D. Abriola et al. Search for an annual modulation of dark-matter signals with a germanium spectrometer at the sierra grande laboratory. *Astropart. Phys.*, 10:133–139, 1999. 85

[125] D. S. Akerib et al. First results from the cryogenic dark matter search in the soudan underground lab. *Phys. Rev. Lett.*, 93:211301, 2004. 87, 174

[126] A. Bottino, F. Donato, N. Fornengo, and S. Scopel. Indirect signals from light neutralinos in supersymmetric models without gaugino mass unification. *Phys. Rev.*, D70:015005, 2004. 87, 174

[127] John R. Ellis, J. S. Hagelin, D. V. Nanopoulos, Keith A. Olive, and M. Srednicki. Supersymmetric relics from the big bang. *Nucl. Phys.*, B238:453–476, 1984. 87, 174

[128] Paolo Gondolo and Graciela Gelmini. Compatibility of dama dark matter detection with other searches. *Phys. Rev.*, D71:123520, 2005. 87, 174

[129] R. Bernabei et al. New limits on wimp search with large-mass low-radioactivity nai(tl) set-up at gran sasso. *Phys. Lett.*, B389:757–766, 1996. 87, 174

[130] Veronique Sanglard et al. Final results of the edelweiss-i dark matter search with cryogenic heat-and-ionization ge detectors. *Phys. Rev.*, D71:122002, 2005. 87, 174

[131] G. J. Alner et al. First limits on nuclear recoil events from the zeplin i galactic dark matter detector. *Astropart. Phys.*, 23:444–462, 2005. 87, 174

[132] S. Cebrian et al. Sensitivity plots for wimp direct detection using the annual modulation signature. *Astropart. Phys.*, 14:339–350, 2001. 88, 89

[133] R. Bernabei et al. On a further search for a yearly modulation of the rate in particle dark matter direct search. *Phys. Lett.*, B450:448–455, 1999. 89, 174

[134] R. D. Peccei and Helen R. Quinn. Constraints imposed by cp conservation in the presence of instantons. *Phys. Rev.*, D16:1791–1797, 1977. 89

[135] K. van Bibber, P. M. McIntyre, D. E. Morris, and G. G. Raffelt. A practical laboratory detector for solar axions. *Phys. Rev.*, D39:2089, 1989. 90

[136] R. J. Creswick et al. Theory for the direct detection of solar axions by coherent primakoff conversion in germanium detectors. *Phys. Lett.*, B427:235–240, 1998. 90, 93

[137] E. A. Paschos and K. Zioutas. A proposal for solar axion detection via bragg scattering. *Phys. Lett.*, B323:367–372, 1994. 90

[138] III Avignone, F. T. et al. Experimental search for solar axions via coherent primakoff conversion in a germanium spectrometer. *Phys. Rev. Lett.*, 81:5068–5071, 1998. 90, 91

[139] A. Morales et al. Particle dark matter and solar axion searches with a small germanium detector at the canfranc underground laboratory. *Astropart. Phys.*, 16:325–332, 2002. 90, 91

[140] R. Bernabei et al. Search for solar axions by primakoff effect in nai crystals. *Phys. Lett.*, B515:6–12, 2001. 91

[141] F. T. Avignone et al. Solar axion experiments using coherent primakoff conversion in single crystals. *Nucl. Phys. Proc. Suppl.*, 72:176–182, 1999. 91, 92

[142] S. Cebrian et al. Prospects of solar axion searches with crystal detectors. *Astropart. Phys.*, 10:397–404, 1999. 91, 92

[143] P. R. Ehrenfreund E. Ewbank, M. D. Newman and W. A. Harrison. *J. Phys. Chem. Solids.*, 44:1157, 1983. 91

[144] A. Alessandrello et al. *Nucl. Phys. B (Proc. Suppl.)*, 35, 1994. 93

[145] F. A. Danevich et al. *Phys. At. Nucl.*, 59:1, 1995. 93

[146] P. de Marcillac et al. *Nature*, 422:876, 2003. 93

[147] F. A. Danevich et al. *Phys. Rev. C*, 67:014310, 2003. 93

[148] V. I. Tretyak and G. Zdesenko Yu. Tables of double beta decay data. *Atom. Data Nucl. Data Tabl.*, 61:43–90, 1995. 101

[149] A. Sh. Georgadze et al. *Phys. Atom. Nucl.*, 58:1093–1102, 1995. 101

[150] D. N. Watt and Glover R. N. *Phyl. Mag.*, 7:105, 1962. 102

[151] R. B. Baglin M. C. Firestone and Chau S. F. Tables of isotopes. *CD-ROM update*, 1998. 102

[152] A. Alessandrello et al. *Phys. Rev. Lett.*, 77:3319, 1996. 102, 103

[153] R. B. Firestone and V. S. Shirley. *Tables of Isotopes*. John Wiley and Sons, 1996. 105

[154] P. Belli et al. Deep underground neutron flux measurement with large bf-3 counters. *Nuovo Cim.*, A101:959–966, 1989. 105

[155] A. Alessandrello et al. The thermal detection efficiency for recoils induced by low energy nuclear reactions, neutrinos or weakly interacting massive particles. *Phys. Lett.*, B408:465–468, 1997. 107

[156] R. Michael Barnett et al. Review of particle physics. particle data group. *Phys. Rev.*, D54:1–720, 1996. 108

[157] Gary J. Feldman and Robert D. Cousins. A unified approach to the classical statistical analysis of small signals. *Phys. Rev.*, D57:3873–3889, 1998. 108

[158] R. Bernabei et al. Dark matter search. *Riv. Nuovo Cim.*, 26N1:1–73, 2003. 110

[159] National Instruments. Ni6289. `http://www.ni.com/pdf/products/us/04_4064_628x_MSeries.pdf`. 132

[160] Analog Devices. Ad7678 data sheets. 137, 141, 142, 147, 153

[161] Xilinx. Spartan-3 fpga family: Complete data sheet. `http://www.xilinx.com/bvdocs/publications/ds099.pdf`. 140

[162] Analog Devices. Ad8021 data sheets. `http://www.analog.com/UploadedFiles/Data_Sheets/289470949AD8021_e.pdf`. 141, 156

[163] Texas Instruments. Ina117 data sheets. `http://focus.ti.com/lit/ds/symlink/ina117.pdf`. 143, 153, 154, 156, 176

[164] Struck. Sis1100/3100. `http://www.struck.de`. 150

[165] Agilent Technologies. 34401a multimeter user-s guide. `http://cp.literature.agilent.com/litweb/pdf/34401-90004.pdf.98`. 152, 160

[166] Agilent Technologies. 33250a waveform generator user-s guide. `http://cp.literature.agilent.com/litweb/pdf/33250-90002.pdf.98`. 160

[167] `http://www.vita.com/specifications.html`. 167

[168] `http://www.ieee.org/web/standards/home/index.html`. 167